On the Way to the Superburst

A Numerical Simulation Study

Inauguraldissertation

zur
Erlangung der Würde eines Doktors der Philosophie

vorgelegt der

Philosophisch-Naturwissenschaftlichen Fakultät
der Universität Basel

von

Julia Reichert

aus Schwarzenberg Luzern

Basel, 2018

Genehmigt von der Philosophisch-Naturwissenschaftlichen Fakultät

auf Antrag von

Prof. Dr. Friedrich-Karl Thielemann

Dr. Laurens Keek

Basel, den 20.06.2017

Prof. Dr. Martin Spiess

Dedicated to

Alexandra Bucheli,

my family, and my dearest friends

Abstract

Regular X-ray bursts are the most prevalent thermonuclear stellar explosions observed in the Galaxy. They occur in accreting binary systems and provide important constraints about the physics of the involved neutron star – a highly compact object. The thermonuclear runaway is periodically triggered in the accreted shell in the atmosphere of the neutron star and can be observed for a few minutes as an intense increase of the luminosity. Observations have shown that, after thousands of X-ray bursts, a rare superburst event may take place. Having a day-long duration, it releases three orders of magnitude more energy. These superbursts are thought to be triggered by unstable carbon-burning in the ashes of the previous X-ray bursts. Nevertheless, they are not fully understood. Given that superbursts have a recurrence time of a few years, performing a self-consistent numerical simulation of the gradual build-up of ^{12}C up to the moment when it is ignited, is extremely expensive in terms of computational resources. Therefore, most simulations of superbursts start from artificial initial conditions, without simulating the thousands of Type I X-ray bursts that lead to a superburst. As a consequence, simulations are not yet capable of self-consistently reproducing the event of a superburst providing all its observable features.

In this thesis, we present a one-dimensional model which is capable of simulating thousands of Type I X-ray bursts in the surface layer of an accreting neutron star. Our code couples general relativistic hydrodynamics with a detailed nuclear reaction network to investigate the scenario of Type I X-ray bursts. Consequently, we are able to make predictions for the evolution of the composition of the ashes of Type I X-ray bursts. Various parameters influence the ignition of an X-ray burst and the resulting layer of ashes. Therefore, we perform an ambitious parameter study, focussing mainly on accretion rates and crustal heating, to find fitting sets for a superburst simulation. Investigating the change of these parameters, we find three different burning regimes and, being one of them the most promisingly consistent with observations, we provide useful constraints in the range of usable parameter sets for self-consistent superburst simulations.

Contents

1 Introduction

> *"A new type of time variation of cosmic X-ray sources has been found from the Astronomical Netherlands Satellite (ANS) observations of the source 3U 1820-30 associated with the globular cluster NGC 6624."*
>
> **— Grindlay et al.**
> [1]

Approximately forty years ago, the first X-ray bursts were discovered [1]. Even some years earlier, another X-ray burst at Cen X-4 had been observed, but it was only related to this type of events in 1976. Subsequently to the discovery of the first (nowadays known as) Type I X-ray burst, Woosley & Taam (1976, [2]) associated these events with a thermonuclear runaway predicted from Hansen and Van Horn (1975, [3]).

Since then, over one hundred sources of Type I X-ray bursts have been identified[1] and they are the most frequently observed thermonuclear explosion in the Milkyway (see e.g. [4, 5, 6]). We discuss observations of Type I X-ray bursts in Section 1.1. Generally speaking, observations provide important insights about the behaviour of Type I X-ray burst and the sites where they occur, as discussed in Section 1.2.

In order to simulate a self-consistent superburst, the abundance of ^{12}C in the ashes is a crucial factor. Recent investigations identify the minimal required mass fraction of ^{12}C to be at least 10% [7]. Many variables and conditions play a role during the ignition and the evolution of a Type I X-ray burst, some of them are the accretion rate, the heat conduction, the reaction rates, the composition of the ashes, the density profile, the underlying neutron star, the accretion composition, the convection, the temperature profile, and the crustal heating. Most of them are not yet fully understood and many of the variables and conditions are closely linked to each other. Some of the parameters, such as the accretion rate or the accretion composition,

[1] https://personal.sron.nl/~jeanz/bursterlist.html provides a list of Galactic Type-I X-ray bursters.

can be constrained by observations. Statistical simulations and experiments of the rp-process isotopes can constrain reaction rates, but still a large fraction of those reaction rates remain uncertain [8]. Therefore, we have to investigate a large parameter space.

In this thesis, we want to focus on the influence of the heat source at the bottom of our computational domain and the accretion rate of the donor star to find fitting parameter sets for simulating a self-consistent superburst. We do this for two different compositions of accreted material: one with solar abundances (in Section 3.3) and one for helium-rich composition (in Section 3.4). For both compositions, we identify different burning regimes. One of our aims is to find the right parameter set to produce a self-consistent superburst. Simulations of superbursts with accretion of the required amount of carbon have shown that a superburst successfully ignites due to a thermonuclear runaway in the carbon layer [9, 10]. Simplified superburst simulations have further confirmed that at least 10% of the mass fraction of the layer at the ignition depth is needed. Our study of Type I X-ray bursts allows us to identify promising parameter sets for further superburst ignition studies. Due to high computational need of the code, performing a self-consistent superburst ignition, we develop a method for a speed-up of the shift-down of the simulated ashes but keeping the conditions of the runs already obtained, see Section 3.6. Using this method we can two times faster state if the simulation could lead to an ignition of the carbon layer or if the conditions lead to stable carbon burning, which has been found by [10].

Various groups are working on numerical simulations of Type I X-ray bursts. The models that are used can be grouped into three main classes: the first predicts the recurrence time, energetics, and determines the ignition conditions for given accretion rate and fuel composition without following the time-dependent compositional structure of the atmosphere. This model has been used for comparisons to observations at low accretion rates [11] and has originally been developed to compare with the atmospheric expansion during a burst, suggested by measurements of burst oscillations [12]. The second class are one-zone time-dependent codes. They simulate some fraction of the nuclear reaction network and are used to demonstrate the extent of the rp-process – the power source of mixed H/He bursts [13]. Furthermore, they are used to probe the sensitivity of the light curves to single reaction rates [14]. The state of the art for modelling X-ray bursts are one-dimensional multi-zone hydrodynamics codes, which track the nuclear reaction network, such as `KEPLER` [15, 16], or `MESA` [17]. These models have been used for detailed comparisons to observations, e.g. [18, 19, 20].

The model used for this thesis belongs to the last of the afore-mentioned class. It is a numerical model similar to that of J. Fisker [21], who coupled the general relativistic hydrodynamic code AGILE (see, i.e. [22, 23]) with the nuclear reaction network provided by Thielemann and Hix [24]. In 2015, Fehlmann parallelized the code using an hybrid approach using OpenMP/MPI [25]. Additionally, the number of zones in the model was increased from 129 to 218 grid zones in order to also include the region of superburst ignition in the domain. The model is explained in detail in Chapter 2 of this thesis. In Chapter 3, we present our results of our parameter study with varying accretion rate and crustal heating. We present the results for two different accretion compositions, since X-ray burst observations have provided different accretion compositions for sites of superbursts. One of the main problems in simulating a superburst is to get the right amount of carbon into the deep layer close to the crust of the neutron star, where it is thought to ignite. Our aim is to identify the best parameter set, in terms of regular burst behaviour and carbon production during bursts, for future simulations of superbursts, as discussed in Section 3.6.

1.1 Observations of X-Ray Bursts and Superbursts

"Stars - In your multitudes - Scarce to be counted
Filling the darkness - With order and light..."

— Javert
Les Misérable

Due to the fact that Type I X-ray bursts are the most common thermonuclear explosions in the Galaxy, they have been and are still tracked by an enormous number of satellites[2]. Even on the ISS, MAXI[3] (**M**onitor of **A**ll-sky **X**-ray **I**mage) was installed and NICER[4] (**N**eutron star **I**nterior **C**omposition **E**xplorer) is planned to be installed there in 2017.

Usually, Type I X-ray burst sources are either named using letters of the satellites which have observed them in combination with a number-code for the galactic position or after the constellation and the order in that they were discovered [6]. As an example, for one of the first detections the X-ray source 3U 1820-30 published in the paper of Grindlay et al. (1976, [1]) was discovered by the satellite Uhuru –filed in the 3rd catalogue of it– and his coordinates in the sky are in right ascension 18 hours and 20 minutes in addition a declination of -30 degrees. The first Type I X-ray burst was also observed from this source.

Since the seventies, about 107 Type I X-ray burst sources have been found and observed. They show a broad range of variation in behaviour, such as recurrence time, that gives the time from one burst to the next burst. The recurrence time can vary from the common 2 to 4 hours (see e.g. [26, 27, 28, 29]), that is consistent with the ignition model predictions, but can also be much shorter, in the range of 10 minutes or even shorter (shortest of 3.8 minutes, see [30]). Even some of the sources turn silent for a time and those sources are called transient X-ray sources [31]. Type I X-ray bursts show the same global burst behaviour as their luminosity rises to its peak fast in a few seconds and then decays exponentially. The entire event lasts from seconds to tens of minutes. Between bursts there is a *persistent luminosity* – most sources show $L_{pers} \approx 10^{36-37}$erg s^{-1} – and for some sources (e.g. 4U 1705-44, see [32, 33]), the persistent luminosity seems to be correlated to the recurrence time. The light curve can look different not only from one source to another, but also from the same source each burst can have their individual shape. Fig. (1.1) shows bursts from three different sources. In the top box of Fig. 1.1 is one

[2] Some of the satellites are Vela(1969), Uhuru(1970), ANS(1974), EXOSAT(1983), RXTE(1995), BeppoSAX(1996), Chandra(1999), Integral(2002), NuSTAR(2012) and far more.
[3] https://www.nasa.gov/mission_pages/station/research/experiments/603.html
[4] https://www.nasa.gov/content/about-nicer

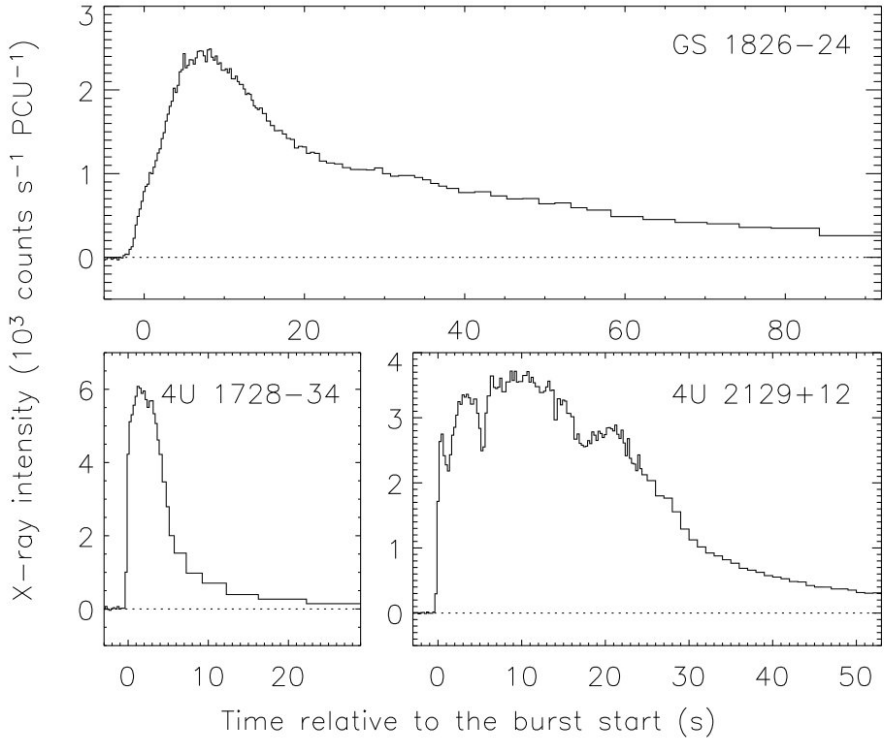

Fig. 1.1.: These light curves show three different Type I X-ray bursts, observed at three different sites, which are labelled at the panels right top. The *x*-axis shows the time starting at the beginning of the burst. The *y*-axis shows the X-ray intensity, the persisting level of X-ray intensity has been subtracted (dotted line). The top panel shows a long Type I X-ray burst observed in 1998, the lower left shows a short burst observed in 1999, and the lower right shows an intermediate duration burst observed in 2000 [27].

Type I X-ray burst of one of the outstanding sources of Type I X-ray bursts sources. It is the source GS 1826-24, which is also called the *clocked burster* or the *textbook burster* (see e.g. [34, 35]). This burster is remarkable because it exhibits extremely regular bursting behaviour over a long time period. The reason for this is believed to be a very stable accretion flow [36]. Therefore, GS 1826-24 is the only source which fits the thermonuclear flash model well [37].

Observations of Type I X-ray bursts and the found observable quantities, like recurrence time or burst duration, are important for comparing results from models and calculations with the reality [38]. Some of those quantities are listed in Tab. (1.1) with their range. Furthermore, they are also very important for understanding the physics of the ocean/surface[5] of a neutron star better. Observations of Type I X-ray bursts provide also a way of measuring neutron star's mass-radius relation and the distance to the source [28]. Over the last decade, a vast of observational data has

[5]Those are layers of the neutron star, explained in more detail in Sec. 1.2.3.

Observable quantity	Range of the quantity
Recurrence time t_{rec}	$2-4$h
Burst duration	tens to hundreds of seconds
Rise time t_{rise}	$\leq 1-10$s
Decay time t_{decay}	hundreds of seconds
Burst maximum L_{peak}	$\sim 10^{38}$erg s^{-1}
Persistent luminosity	$\sim 10^{36-37}$erg s^{-1}
α parameter	$\sim 10-100$

Tab. 1.1.: Observed quantities from X-ray bursters and their ranges.

been collected (see, e.g. [27]), one of them is the MINBAR[6] data base (short for: The **M**ulti- textbfInstrument **B**urst **Ar**chive) which will cover data from RXTE, BeppoSAX, and INTEGRAL JEM-X and will contain over 5000 Type I X-ray bursts [39].

Apart from the recurrence time and the burst duration, also the above-mentioned rise-time t_{rise}, as seen from infinity, of an Type I X-ray burst, can be calculated from the numerical simulations output and therefore compared to observational data. It is defined as follows,

$$t_{rise} \equiv t_{L=L_{peak}} - t_{L=0.02\cdot L_{peak}}, \tag{1.1}$$

where L_{peak} is the bust peak luminosity. The decay time t_{decay} or also called e-folding time, again seen from infinity, is an additional quantity which can be compared to observations and is given by

$$t_{decay} \equiv t_{\ln(L_{peak}/L)=1} - t_{L=L_{peak}}. \tag{1.2}$$

But one of the foremost important observable parameters is the so-called α-value, which gives the energy release per gram and is defined by the ratio of the persistent fluence, E_p, to the burst fluence, E_b, and is given by

$$\alpha \equiv \frac{E_p}{E_b} = \frac{\int_t^{t+\Delta t} F_p dt}{\int_t^{t+\Delta t} F_b dt} \approx \frac{GM/R}{Q_{nuc}} \tag{1.3}$$

where Δt is the recurrence time between two consecutive bursts, F_p is the persistent flux, and F_b is the burst flux. The last term relates the observations with the interpretation of the model, where G is the gravitational constant ($G = 6.673 \cdot$

[6] Geek-sidenote: The name MINBAR is inspired by the TV-show *Babylon 5* where it is the name of the homeplanet of an alien race, the minbari.

Source	Accretion rate [fraction of $\dot{M}_{Eddington}$]	Superburst	References
4U 0614+091	0.01	2	[46]
4U 1254-69	0.13	1	[47]
4U 1608-522	0.03	1	[48]
4U 1636-536	0.1	4	[49]
KS 1731-260	0.1	1	[50]
Swift J1734.5-3027	?	1 (?)	[51]
4U 1735-44	0.25	1	[52]
XB 1745-248 (Terzan 5)	?	1	[53]
GX 3+1	0.2	1	[54]
SAX J1747.0-2853	?	1	[55]
GX 17+2	0.8	4	[56]
4U 1820-303 (NGC 6624)	0.1	2	[57]
SAX J1828.5-1037	?	1	[58]
Ser X-1	0.2	3	[59]

Tab. 1.2.: Observed superbursts with accretion rate and their reference. The question mark means that the accretion rate has not been observed from this site or is not given by literature and the question mark in brackets marks a possible superburst.

10^{-8} dyn cm^2 g^{-2}), M and R are the gravitational mass and local radius of the neutron star, respectively, and $GM/R \sim 180$ MeV nuc^{-1}, Q_{nuc} is the nuclear energy release, which is for hydrogen burning ~ 8.4 MeV nuc^{-1}, and for helium burning ~ 1.7 MeV nuc^{-1} [40, 41]. Since the nuclear energy is stored and released in a burst – where it exceeds L_{pers} – this nuclear aspect of a site is observable. Observations provide us with values of $\alpha \sim 10 - 100$ [36]. We get values for α in the range of $\sim 70 - 130$. Many sources show that α is correlated with $\gamma \equiv F_p/max(F_b)$ and anti-correlated with the burst duration, $\tau \equiv E_b/max(F_b)$, [42]. There are several aspects which make the analysis of the observed data complicated as, e.g., possibility of false assumptions about the burst-disk interplay [42, 43], anisotropic flux [44], or reflection signal that evolves as the burst fades [45]. Therefore, comparing observations with theory is not trivial.

Some of the sources show a special event, the superburst. Over all, 24 superbursts have been detected in 14 X-ray sources, see Tab. (1.2). The first event called a “Super Burst” was detected 1984 [60] in the source 4U 1728-33. Fig. (1.2) shows that a “Super Burst” differs from normal Type I X-ray bursts, especially in the bolometric burst fluence E_b, which is the integrated burst flux. A superburst differs from a normal Type I X-ray burst in exceeding their duration several times – burst duration of an X-ray burst is from seconds to minutes, whereas a superburst lasts from hours to days [61]. Observations have shown that superbursts occur at the same source as previous Type I X-ray bursts after thousands of normal bursts. In terms of peak luminosity, they are not different from X-ray bursts, but their energy release is

with $\sim 10^{42}$ erg much higher than a normal Type I X-ray burst (typically 10^{39} erg). The light curve is characterised by a decay over several hours and after that the envelope has to cool down first before a sequence of Type I X-ray bursts can reappear. Therefore, no X-ray burst can be observed for weeks after a superburst [9].

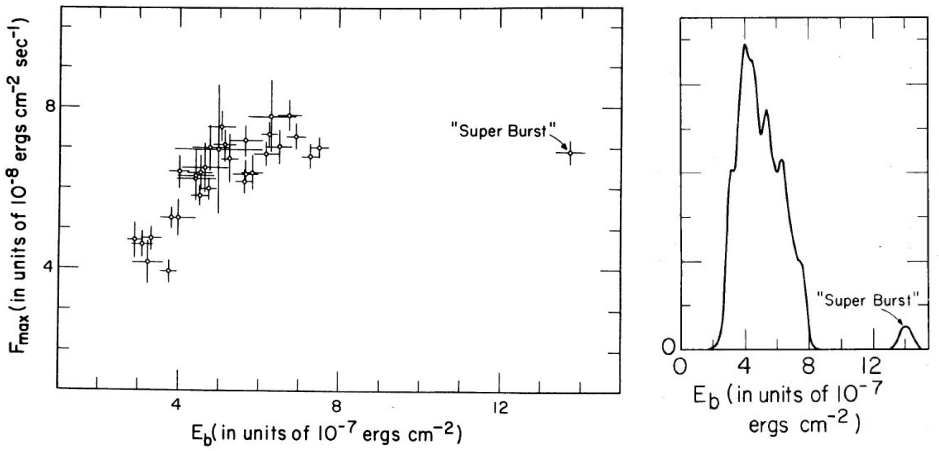

Fig. 1.2.: a) E_b is the bolometric burst fluence, F_{max} is the bolometric peak burst flux, which is the rate of the energy emission over the entire energy spectrum per unit area. The dots show the observed bursts. The short Type I X-ray bursts are all in the same area and show a linear relation between burst fluence and flux. The "Super Burst" is special and differs from the rest of the observations. b) This histogram shows the distribution of the bolometric burst flux, where a superburst is outstanding, is plotted here with given criterias from [60]. Both figures are taken from [60].

1.2 Theory

"Abandon all hope, ye who enter here."

— Dante Alighieri
Inferno

This section aims to explain what is thought to happen during an Type I X-ray burst, a superburst, and at which astrophysical site those phenomena are happening.

Thus, we will first discuss some basics about nucleosynthesis in Section 1.2.1, then we describe the evolution of stars in general in Section 1.2.2, then we focus on neutron stars in Section 1.2.3, because they – bound in a binary stellar system (discussed in Section 1.2.4) – are the sites for Type I X-ray bursts and superbursts. In Section 1.2.5, we will discuss Type I X-ray bursts and what is theoretically happening in the accreted shell of a neutron star. On average, after a few thousand Type I X-ray bursts, a special burst a so-called superburst can be observed. Those superbursts are discussed in Section 1.2.6.

1.2.1 Nucleosynthesis

The fast nucleosynthesis processes in a Type I X-ray burst are defined by an interplay of several charged-particle reactions and β^+-decays at characteristic densities and temperatures. This section gives an overview of the needed formalism to calculate reaction rates. For further detail, see [62, 63, 64, 65, 66, 67].

For all reactions $i(j,\,k)m$, where i is the heavier target nucleus, j the lighter incoming projectile, k the lighter outgoing particle (ejectile), and m the heavier residual nucleus, we can write down the rate r_{ij}, which is the number of reactions per volume and per time, in this way:

$$r_{ij} = \frac{1}{1+\delta_{ij}} n_i n_j \left\langle \sigma v \right\rangle_{ij} . \tag{1.4}$$

Here δ_{ij} is the Kronecker-Delta, which prevents the double counting of reactions with identical particles ($i = j$). For the species i and j, n denotes the number density

and $\langle \sigma v \rangle_{ij}$ is called reactivity, and gives the thermonuclear reaction rate per particle pair. It is given by:

$$\langle \sigma v \rangle_{ij} = \left(\frac{8}{\mu\pi}\right)^{\frac{1}{2}} \left(\frac{1}{kT}\right)^{\frac{3}{2}} \int_0^\infty \sigma(E) E \mathrm{e}^{-\frac{E}{kT}} \mathrm{d}E. \tag{1.5}$$

The reactivity includes the integral over all the possible kinetic energies E of the Maxwell-Boltzmann distribution $\mathrm{e}^{-\frac{E}{kT}}$, times the reaction cross section σ. The cross section is given by the number of reactions per target per time, divided by the flux of incoming projectiles. Therefore, σ has the dimension [cm^2]. The cross section can be written as $\frac{r_{ij}/n_i}{n_j v}$, where v is the relative velocity. If the participating nuclei obey Boltzmann statistics and the cross section is known (from experiments or theoretical calculations), $\langle \sigma v \rangle_{ij}$ can be determined easily.
Reaction rates can also be expressed in terms of the mean life times τ of a particle i against destruction by projectile j,

$$\tau_j(i) = \frac{1}{\langle \sigma v \rangle_{ij} n_i}. \tag{1.6}$$

We can now write the change of the number-densities of the different particles involved in the reaction. For the nuclei that are destroyed in the reaction, it has the form:

$$\left(\frac{\partial n_i}{\partial t}\right)_\rho = \left(\frac{\partial n_j}{\partial t}\right)_\rho = -r_{ij}, \tag{1.7}$$

and for the nuclei that are produced in the reaction

$$\left(\frac{\partial n_k}{\partial t}\right)_\rho = \left(\frac{\partial n_m}{\partial t}\right)_\rho = +r_{ij}, \tag{1.8}$$

where the index ρ means that we assume constant density, because the reaction timescale is much shorter than the dynamical timescale in which the density could change. Now we use the abundances Y_i to avoid the dependency on density fluctuations. Y_i can be written as $Y_i = \frac{X_i}{A_i}$, where X_i is the mass fraction and A_i is the mass number. The connection between abundances and number densities is given by

$$n_i = n_i(Y_i(t),\, \rho(t)) = \rho N_A Y_i, \tag{1.9}$$

where N_A stands for the Avogadro-constant, $N_A = 6.02214 \cdot 10^{23}\mathrm{mol}^{-1}$. We are interested in the changes of the number density or the abundance over time. Using the product rule for the total differential,

$$\frac{\mathrm{d}n}{\mathrm{d}t} = \frac{\partial n}{\partial Y}\frac{\partial Y}{\partial t} + \frac{\partial n}{\partial \rho}\frac{\partial \rho}{\partial t}, \tag{1.10}$$

we can write the temporal change of the number density

$$\dot{n}_i = \frac{\mathrm{d}n_i}{\mathrm{d}t} = \left(\frac{\partial n_i}{\partial t}\right)_\rho + \left(\frac{\partial n_i}{\partial t}\right)_{Y_i} = \left(\frac{\partial n_i}{\partial t}\right)_\rho + n_i \frac{\dot{\rho}}{\rho}. \tag{1.11}$$

Rewritten for the change of the abundances in Eq. (1.9), we get

$$\dot{Y}_i = \frac{\dot{n}_i}{\rho N_A} - \frac{n_i}{\rho N_A}\frac{\dot{\rho}}{\rho}. \tag{1.12}$$

If we insert Eq. (1.12) into the original differential Eq. (1.7), we get for the temporal change of the abundances

$$\dot{Y}_i = \frac{1}{\rho N_A}\left(\frac{\partial n_i}{\partial t}\right)_\rho = -\frac{r_{ij}}{\rho N_A}, \tag{1.13}$$

where r_{ij} is the already known rate given in Eq. (1.4), which we insert together with Eq. (1.9) into Eq. (1.13) to obtain

$$\dot{Y}_i = -\frac{1}{1+\delta_{ij}}\rho N_A \langle\sigma v\rangle_{ij} Y_i Y_j. \tag{1.14}$$

This can be done for all the participating nuclei in the reaction. For the example $i(j,\,k)m$, we will then get three more changes of abundances in addition to Eq. (1.14), i.e.

$$\dot{Y}_j = -\frac{1}{1+\delta_{ij}}\rho N_A \langle\sigma v\rangle_{ij} Y_i Y_j, \tag{1.15}$$

$$\dot{Y}_k = \frac{1}{1+\delta_{ij}}\rho N_A \langle\sigma v\rangle_{ij} Y_i Y_j, \tag{1.16}$$

$$\dot{Y}_m = \frac{1}{1+\delta_{ij}}\rho N_A \langle\sigma v\rangle_{ij} Y_i Y_j, \tag{1.17}$$

where we can see that the nuclei i and j get destroyed and the nuclei k and m are produced in this reaction.
For decays $i \to m$ the rate can be written as

$$r_i = n_i \lambda_i, \tag{1.18}$$

which gives us the number of reactions per time and per target nucleus i. The λ_i is the decay-constant for the nucleus i. Additionally to decays, we can calculate the change of the abundances for photodisintegration, electron-capture, etc. in a similar way and get

$$\dot{Y}_i = \frac{1}{\rho N_A}\left(\frac{\partial n_i}{\partial t}\right)_\rho = -\frac{r_i}{\rho N_A}. \tag{1.19}$$

Again, with the already known rate, we can insert Eq. (1.18) into Eq. (1.19) and find

$$\dot{Y}_i = -\lambda_i Y_i. \tag{1.20}$$

In a similar way, we get the change of the abundance for the produced nuclei m in the case of the decay

$$\dot{Y}_m = \lambda_i Y_i. \tag{1.21}$$

For normal decays, like β-decays or α-decays, there is another characteristic quantity which describes the decay. It is called the half-life $\tau_{1/2}$, and can be expressed in relation to the decay-constant λ_i of the decay

$$\lambda_i = \frac{\ln 2}{\tau_{1/2,\,i}}. \tag{1.22}$$

In an astrophysical plasma, multiple reactions occur at the same time, so for each nucleus we can write down the change of the number densities over time

$$\left(\frac{\partial n_i}{\partial t}\right)_\rho = \sum_j N_j^i r_j + \sum_{j,\,k} N_{j,\,k}^i r_{jk} + \sum_{j,\,k,\,l} \cdots + \ldots etc., \tag{1.23}$$

where N^i is the number of the nucleus species i, which is destroyed during the reaction. The summation indices refer to the residual nuclei that are produced. The first term describes all possible decays which produce or destroy the nucleus i, the second term is the sum of all possible two-particle reactions, the third term is the sum over all possible three-particle reactions, and so on for higher particle-number reactions which are usually negligible. Three-particle reactions are actually a sequence of two two-particle reactions with an intermediate reaction product which is destroyed on extremely short timescales, and hence, can mathematically be written like a three-particle reaction. The most important three-particle reaction is the triple-α reaction [68]. Here, all the other three-particle reactions are insignificant, because they are very improbable, even at very high densities.
Again, we can write Eq. (1.23) as the change of the abundances

$$\dot{Y}_i = \sum_j N_j^i \lambda_j Y_j + \sum_{j,\,k} \frac{N_{j,\,k}^i}{1+\delta_{jk}} \rho N_A \langle \sigma v \rangle_{jk} Y_j Y_k (+\ldots). \tag{1.24}$$

The only three-particle reaction which cannot be neglected is the already mentioned triple-α process, which occurs during He-burning, as discussed in Section 1.2.2. Under the conditions of He-burning, the triple-α process is the only possible reaction to overcome the gap in the row of stable nuclei at $A = 5$ and $A = 8$. The first step in the triple-α-process is ^{4}He $+^4$ He $\rightleftharpoons^8$ Be. ^{8}Be is also unstable and will decay on a timescale of about 2.6×10^{-16}s [62]. But with increasing temperatures and densities,more and more ^{8}Be nuclei are produced and a small abundance of them

remains in a chemical equilibrium. Because of the equilibrium, the temporal change of ^{8}Be is equal to zero,

$$\dot{Y}_{^8\mathrm{Be}} = \frac{1}{2}\rho N_A \langle \alpha, \alpha \rangle Y_\alpha^2 - \lambda_{^8\mathrm{Be}} Y_{^8\mathrm{Be}} = 0, \tag{1.25}$$

where $\lambda_{^8\mathrm{Be}}$ is the decay-rate of ^{8}Be and this is equal to $\tau_{^8\mathrm{Be}}^{-1} = \frac{\Gamma_{^8\mathrm{Be}}}{\hbar}$, where $\Gamma_{^8\mathrm{Be}}$ is the width of the ground state. With Eq. (1.25) and the given circumscriptions of $\lambda_{^8\mathrm{Be}}$, we can write down the equilibrium abundance of ^{8}Be,

$$Y_{^8\mathrm{Be}} = \frac{\hbar}{2\Gamma_{^8\mathrm{Be}}}\rho N_A \langle \alpha, \alpha \rangle Y_\alpha^2. \tag{1.26}$$

The next step in the triple-α process is the capture of another α-particle to the existing ^{8}Be, i.e. $^8\mathrm{Be} +^4 \mathrm{He} \rightarrow^{12}$ C. We can again write the temporal change of the abundance of ^{12}C, like we have done before for ^{8}Be, with the exception that this reaction is not in an equilibrium.

$$\dot{Y}_{^{12}\mathrm{C}} = \rho N_A \langle \alpha, {}^8\mathrm{Be} \rangle Y_\alpha Y_{^8\mathrm{Be}}, \tag{1.27}$$

where we can insert Eq. (1.26) to get

$$\dot{Y}_{^{12}\mathrm{C}} = \frac{\hbar}{2\Gamma_{^8\mathrm{Be}}}\rho^2 N_A^2 \langle \alpha, \alpha \rangle \langle \alpha, {}^8\mathrm{Be} \rangle Y_\alpha^3 \tag{1.28}$$

$$\equiv \frac{1}{3!}\rho^2 N_A^2 \langle \alpha, \alpha, \alpha \rangle Y_\alpha^3. \tag{1.29}$$

From Eq. (1.28) to Eq. (1.29), we treat the two step reaction like a three-particle reaction. We can see in Eq. (1.29), if we insert $\frac{n_i}{\rho N_A} = Y_i$, that the number density of α-particles - here n_α^3 - influences the abundance change of ^{12}C strongly. This is the reason why the triple-α process is so sensitive to the number density of α-particles.

1.2.2 Stellar Evolution

Stars of different initial masses live through different burning stages due to diverse central temperatures and will end up as different final objects. Therefore, the evolution of stars are linked strongly to their initial masses. Those mass ranges are shown in Tab. (1.3). $0.08M_{\odot}$ is the limit for hydrogen ignition in an objects and those below $0.08M_{\odot}$ never reach the central temperatures needed to ignite H-burning in the core. Slightly more massive stars with up to $2M_{\odot}$ are so called low-mass stars. They undergo H-burning and a helium white dwarf is left over because the conditions for helium burning is never reached. Intermediate-mass stars run through hydrogen, helium and carbon burning stages in the core and release a planetary nebula in their last stages of living. The remnant is then a CO white dwarf or even a more massive ONe white dwarf. Objects over $11M_{\odot}$ are called massive stars, they go through all the hydrostatic burning stages and will end their lives with an explosive event, the *core collapse supernova*. The mass limit between massive stars which end as neutron stars and those which end as black holes is not known exactly. We note that the precise mass limits depend on the metallicity of the star. One aim in astrophysics is to explain the solar abundances (see Fig. (1.4)) with different events, which give matter back into the universe. The longest part of their lives, stars will

Initial Masses [$M_{\odot}$]	Core Burning Stages	Shell Burning	Remnant
0.08-0.4	H	-	He white dwarfs
0.4-2	H, He	H, He	CO white dwarfs
2-11	H, He, C	H, He	CO withe dwarfs or ONe white dwarfs
11-25	H, He, C, Ne, O, Si	H, He, C, Ne, O	Neutron stars
> 25	H, He, C, Ne, O, Si	H, He, C, Ne, O	Black hole

Tab. 1.3.: The initial masses, burning stages in core and shells of the stars, and their remnants [64].

stay in hydrostatic burning stages. The fascinating end of a star just happens in a wink compared with the rest of its lifetime.

Hydrostatic Burning Stages

As shown in Tab. (1.3), a star, depending on its initial mass, can undergo different burning stages. These stages are named after the main nuclear fuel used in the corresponding phase, as shown in the last column of Tab. (1.4). The thermonuclear reactions of these nuclei release energy which counteracts the self-gravity of the star. The series of these stages are in the following order:

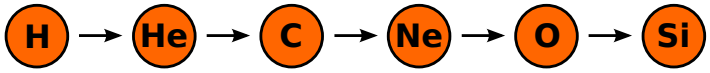

and get faster and faster because the nuclear reaction produces less and less energy the more massive the fused nucleus becomes. For heavier isotopes it gets harder to overcome the Coulomb barrier. The timescales of the different burning stages are also shown in Tab. (1.4) in the fourth column. There, the first two rows correspond to a $1M_\odot$ star, while the last six present the burning stages of a more massive $20M_\odot$ star.

Burning stages	ρ_c [g cm^{-3}]	T_c [GK]	τ [yr]	L_{photo} [ergs/s]	L_ν [ergs/s]	Primary Reactions
Hydrogen	150	0.015	1×10^{10}	3.9×10^{33}	-	pp-chain
Helium	2.0×10^{5}	0.15	4×10^{8}	1.6×10^{35}	-	Triple α
Hydrogen	5.6	0.040	1×10^{7}	2.7×10^{38}	-	CNO-cycle
Helium	9.4×10^{2}	0.19	9.5×10^{5}	5.3×10^{38}	$<\times10^{36}$	Triple α
Carbon	2.7×10^{5}	0.81	3.0×10^{2}	4.3×10^{38}	7.4×10^{39}	^{12}C+^{12}C $\rightarrow$ ^{20}Ne+α
Neon	4.0×10^{6}	1.7	0.4	4.4×10^{38}	1.2×10^{43}	^{20}Ne+γ $\rightarrow$ ^{16}O+α
Oxygen	6.0×10^{6}	2.1	0.5	4.4×10^{38}	7.4×10^{43}	^{16}O+^{16}O $\rightarrow$ ^{28}Si+α
Silicon	4.9×10^{7}	3.7	0.01	4.4×10^{38}	3.1×10^{45}	^{28}Si+7α $\rightarrow$ ^{56}Ni

Tab. 1.4.: Stellar burning stages and their center conditions for a $1M_\odot$ star from [69] and for a $20M_\odot$ star from [70]. This table is taken from [24].

The first burning stage is the hydrogen-burning stage. As soon as the conditions for the H-burning in the centre are reached, the reaction ignites. Typical temperatures for core H-burning are $0.008 - 0.055$GK. Depending on the mass of the star and, consequentially, on the temperature as well as on the metallicity, the H-burning takes place in two different ways: the pp-chain or the CNO-cycle. In both cases, the net reaction is $4\text{p} \rightarrow {}^4\text{He} + 2e^+ + 2\nu_e$. The pp-chain first builds up deuterium due to the reaction ^{1}H(p, $e^+\nu_e$)^{2}H. The formed deuterium reacts with another proton, ^{2}H(p, γ)^{3}He, and builds up ^{3}He releasing a photon. If two ^{3}He are built, they can undergo the reaction ^{3}He(^{3}He, 2p)^{4}He and finally produce ^{4}He. The CNO-cycle converts also ^{1}H into ^{4}He, but it needs the nuclei C, N and O as catalysts. They undergo a sequence of (p, γ) and (p, α) reactions with subsequent β-decays of unstable isotopes.

It depends on the characteristics of a star, which path is preferred and produces the most energy. For example, in the sun the main part of the energy is generated by pp-chain reactions. Additionally to the condition of having enough of the CNO-nuclei there is a critical mass limit above which the CNO-cycle is getting more important for the energy generation. In Fig. (1.3), the two curves of the CNO-cycle and the pp-chain are shown. The dot indicates the properties of the sun. The two curves show which process, pp-chain or CNO-cycle, dominates the energy production depending on the temperature. In Fig. (1.3), the *y*-axis is the logarithm of luminosity L relative

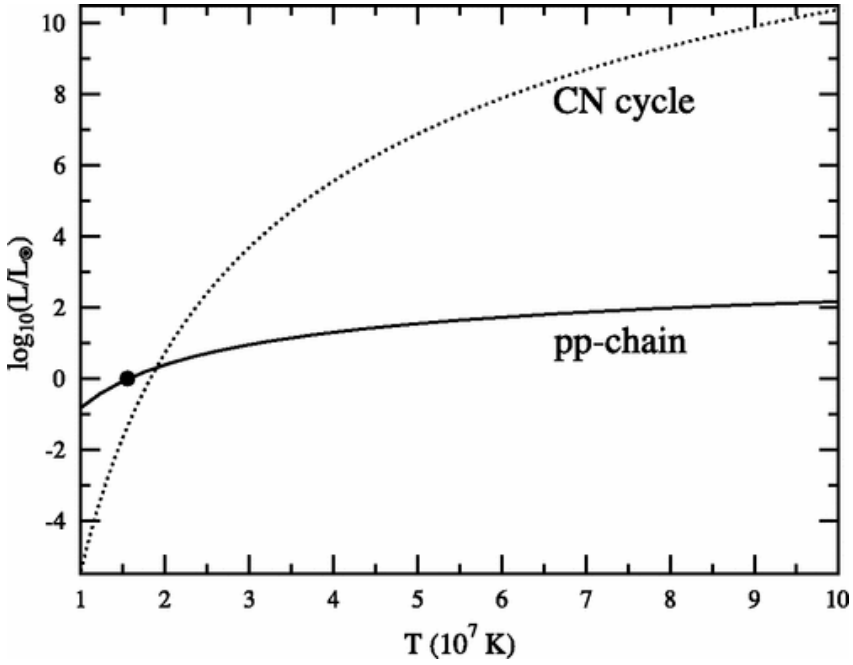

Fig. 1.3.: The logarithm of the normalized luminosity, i.e. $\log_{10}(L/L_{\odot})$, as a function of temperature. The solid line represents the pp-chain, the dashed line indicates the CNO-cycle. The black dot marks the properties of the sun, where most of the energy is produced by the pp-chain reactions. This figure is taken from [71].

to the solar luminosity $L_{\odot}$. The *x*-axis shows the temperature. The comparison of the two gradients of the curves shows that the CNO-cycle is much more temperature sensitive than the pp-chain.

Helium-burning follows the hydrogen-burning stage in the life of a star. After the H-burning, the reactions cannot follow-up with simple proton or neutron captures because there is a gap in the row of stable nuclei at $A = 5$ and $A = 8$. Therefore, there must be a reaction that overcomes this obstacle. This is the early mentioned triple-α reaction [68]. The net reaction of the He-burning is $3^4\text{He} \rightarrow {}^{12}\text{C}$. This can be split up in two reactions: $2^4\text{He} \rightarrow {}^8\text{Be}$ and ${}^8\text{Be} + {}^4\text{He} \rightarrow {}^{12}\text{C}$. The triple-$\alpha$ reaction rate is extremely sensitive to the number density of ${}^4\text{He}$, which has been discussed in detail in Section 1.2.1. Temperatures during core helium burning are in the range of $0.1 - 0.4$GK [64].

After the He fuel has been consumed, the carbon-burning stage ignites. The carbon-burning takes place at temperatures of $0.6 - 1.0$GK. During this stage ${}^{12}\text{C}$ can be burnt by two different reactions: one is ${}^{12}\text{C}({}^{12}\text{C}, \alpha){}^{20}\text{Ne}$, which is the main reaction, and the second one is ${}^{12}\text{C}({}^{12}\text{C}, \text{p}){}^{23}\text{Na}$, which is responsible for only a small fraction of carbon depletion. These two reactions release free protons and α-particles, which are important for further reactions and dominate the energy production. Those

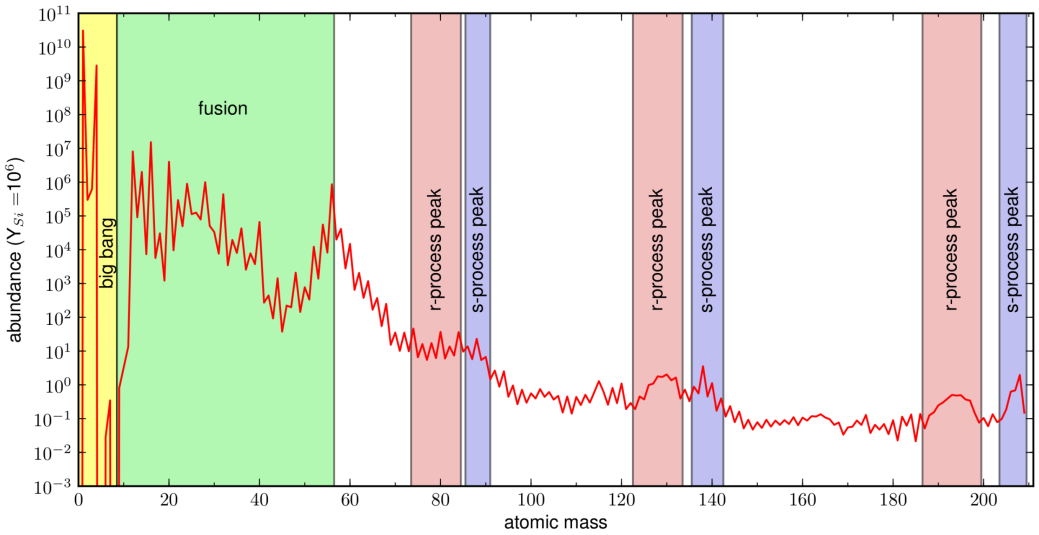

Fig. 1.4.: Solar abundances from [72] with silicon abundance normalized to 10^6. This figure is taken from [73]

following reactions are ^{23}Na(p, α)^{20}Ne, ^{23}Na(p, γ)^{24}Mg, and ^{12}C(α, γ)^{16}O.

Before the needed temperature for oxygen fusion is reached, the thermal photon bath reaches an energy level that makes photodisintegration of ^{20}Ne possible. During core neon-burning, temperatures of $1.2 - 1.8$GK occur. The main reaction during neon-burning is ^{20}Ne(γ, α)^{16}O. The α-particle that is freed by this reaction can be captured by other ^{20}Ne and produces ^{24}Mg. This can be written as ^{20}Ne(α, γ)^{24}Mg.

The next burning stage is the oxygen-burning stage because the fusion of oxygen has now the lowest Coulomb barrier. Its usual core temperature is between $1.5 - 2.7$GK. The three main reactions of oxygen-burning are: ^{16}O(^{16}O, p)^{31}P, ^{16}O(^{16}O, α)^{28}Si, and ^{16}O(^{16}O, n)^{31}S(β^+)^{31}P. The most abundant nuclei after the oxygen-burning are ^{28}Si and ^{32}S.

The last possible hydrostatical burning stage is the silicon-burning stage. Temperatures during core silicon-burning are in the range of $2.8 - 4.1$GK. Similar to neon-burning, silicon-burning also starts with the photodisintegration of its fuel and releases protons, neutrons and α-particles which can be captured by the other nuclei in the plasma. The reactions of two silicon nuclei, ^{28}Si+^{28}Si, or a silicon nucleus with a sulphur nucleus, ^{28}Si+^{32}S, are rather improbable because of the high Coulomb barrier. But the high temperature allows the capture of protons and α-particles, since they are energetic enough to overcome the Coulomb barrier. Neutrons have no charge and therefore the Coulomb barrier is never an obstacle for them. The following nucleosynthesis that transforms the existing nuclei to nuclei of the iron peak (around $A = 60$) is quite complex. First, a so-called QSE

(**q**uasi-**s**tatistical **e**quilibrium) occurs and builds up two main clusters of nuclei at $A = 24 - 43$ and $A = 50 - 67$, which will merge with rising temperatures. At the end of the silicon-burning stage, the high temperatures allow all nuclei to be in a large quasi-equilibrium group of strong and electromagnetic reactions from protons, neutrons, α-particles up to the iron peak nuclei. This is called NSE (**n**uclear **s**tatistical **e**quilibrium).

During He-burning in the core and the shell, it is possible that the existing neutron rich nuclei reacts with α-particles, releasing a single neutron, (α, n). These free neutrons can subsequently be captured by pre-existing nuclei up to iron and, over a sequence of neutron capture and β-decays, heavier nuclei are synthesised, up to Pb and Bi. This is called the s-process and occurs under conditions with a low photodisintegration level.

Explosive Burning

Even if most of the isotopes of Fig. (1.4) are produced in stars during the hydrostatic burning stages, they are still bound in the gravitational potential well of the stars. An event that releases the isotopes out into space is needed and for this task a huge amount of energy is required, like an explosive event would release. The most famous explosive event is a supernova that highlights the end of a massive star. The last stage of such a star is the Si-burning stage, which produces nuclei of the Fe-peak. These Fe-peak nuclei are the strongest bound elements - less or more massive nuclei are bound more weakly. Therefore, all reactions involving Fe-peak elements are endothermic meaning that, when the Si fuel is depleted, the iron core contracts because it cannot sustain the self-gravitation of the star. This contraction turns into a collapse until the matter of the core is so dense that the degenerate nucleon pressure halts the collapse. The material from outer regions of the star still falls on the compact core, which is called proto-neutron star, and bounces off. The formed shock wave runs outwards through the overlying layers. It comes to a halt after a few ms and is supposedly revived by neutrinos from the hot underlying proto-neutron star. The shock wave then passes through the layers, heats them up, accelerates and unbinds most of the material so it can escape into space. This event is known as a core-collapse supernova (also called CCSN or Type II SN). When the shock wave propagates through the layers it heats them up to several GK and causes further nucleosynthesis [24]. Many of the reactions happening in this scenario are similar to the corresponding reactions in the hydrostatical burning stages, but they occur at higher temperatures and on shorter timescales. Hydrodynamic models and nuclear reaction networks for CCSN are an active field of recent research and will not be discussed in this thesis in more detail. But we address the reader to the following

reviews on the topic [74, 75, 76].

A second type of supernova is the thermonuclear explosion of a white dwarf (or Type I SN). The explosive C-burning of the white dwarf can happen in two ways. Both ways include mass transfer from a companion in a binary system (see Section 1.2.4), e.g. an AGB star. One possible scenario occurs when the white dwarf accretes mass from a donor star and exceeds the maximum stable mass for white dwarfs, the so-called Chandrasekhar-mass (approximately $1.4M_{\odot}$). When approaching the Chandrasekhar-mass, the star becomes unstable and collapses, heating up the CO core and igniting carbon under degenerate conditions. The other way leading to the thermonuclear explosion of a white dwarf is that it accretes a He-layer from a companion star. This accreted layer undergoes a thermonuclear runaway, which results in the explosion of the white dwarf. In both cases the triggered flame front of the thermonuclear explosion disrupts the entire white dwarf and leaves a composition of matter dominated by Fe-peak and intermediate nuclei.

Another event involving a white dwarf typically bound in a binary system is the so-called nova. The white dwarf slowly accretes material from the hydrogen shell from its companion star, and if the conditions for temperature and density of H-burning are reached, the accreted hydrogen ignites in a layer on the surface of the white dwarf. The conditions of the environment on the surface of the white dwarf lead to explosive hydrogen burning via the hot CNO-cycle (HCNO). A nova releases about $10^{46} - 10^{47}$ergs in $100 - 1000$s and reaches temperatures of $0.2 - 0.3$GK [24]. An similar event, but happening on the surface of a neutron star, is a Type I X-ray burst, see Section (1.2.4) for more details.

Explosive nucleosynthesis is similar to stable burning but happens in a smaller timescale, under extremely high temperatures and high densities. The conditions of explosive burning leads to new reaction paths. One possible process is the r-process (rapid neutron capture), which is like the s-process (slow neutron capture) in the hydrostatical nucleosynthesis, but the neutron capture happens faster, which leads to heavy neutron-rich nuclei. The r-process occurs only in events with high neutron concentrations and comes very close to the neutron dripline. The required large neutron concentration for the r-process could occur in the innermost regions of CCSN ejecta or in the decompression of neutron star matter [24].

In explosive hydrogen burning in an environment, with a significant fraction of CNO-nuclei, the hot CNO cycles occur. The temperatures needed for these cycles are over 0.1GK. Each hot CNO-cycle transforms four protons into an α-particle, the hot CNO-nuclei act as catalysts and their total number, if no other reactions occur, remains nearly constant. Disparate to the CNO-cycle, where all unstable nuclei

undergo β-decay, in the hot CNO-cycle the produced unstable nuclei can undergo additional reactions, such as (p, γ) or (p, α). At "low" temperatures only isotopes of mass numbers $A < 20$ are included. If the temperature rises over 0.4GK, α-particle-induced reactions are more likely to happen and through a breakout sequence the production of heavier nuclei begins [64]. The hot CNO-cycle, and other proton and α-particle consuming reactions are discussed in more detail in Section 1.2.5, because they play an important role for Type I X-ray bursts.

1.2.3 Neutron Stars

> *"... the phenomenon of a super-nova represents the transition of an ordinary star into a body of considerably smaller mass."*
>
> **— W. Baade and F. Zwicky**
> [77]

Neutron stars, amongst the directly observable objects, are the most compact ones. As we have mentioned in Sec. (1.2.2), neutron stars are the remnants of supernovae: the death of massive stars ($8M_\odot < M_{\text{initial}} \leq 25M_\odot$). Already in 1934, Baade and Zwicky proposed the idea of a neutron star as a remnant of a supernova, having a very small radius and high density [78]. Another possible way of forming a neutron star is through the accretion-induced collapse of a white dwarf in a binary system. The event is also a supernova and depending on how much energy is released during the event, the white dwarf either collapses to a neutron star or is completely destroyed [79].

A typical neutron star has a radius of $\sim 10-15$km and a mass of $\sim 1.4M_\odot$, but exotic extremes up to $3.2M_\odot$ are theoretically possible, but ruled out by observations (see e.g. [80]). A neutron star is gravitationally very strongly bound. The gravity at the surface is about 10^{11} times bigger than on the surface of the earth, and the neutron star has a strong magnetic field on its surface of up to 10^{12}Gauss [81]. The material of a neutron star consists primarily of neutrons because under the conditions found in a neutron star, it is energetically favorable to combine protons and electrons to form neutrons and neutrinos. Under the condition of not reaching higher masses, a neutron star cannot further collapse because of the Pauli principle that states that two fermionic particles - in this case the neutrons - cannot occupy the same place and quantum state at the same time, i.e. the degeneracy prevents the further collapse. Otherwise, it could build a quarkstar or a blackhole. The interior of a neutron star is highly theoretical and not well known. Conditions such as in the core of a neutron star are no where else in the universe observable and certainly not on earth. Due to different constituent particles and theoretical phases, the interior of the neutron star can be split into different parts (shown in Fig. (1.5); see e.g. [82, 83, 84]). Those parts are the core, the crust, the ocean, the atmosphere and the photosphere. The ocean and the atmosphere are also in some literature combined mentioned as the envelope. The depth in Fig. (1.5) is given in meters and in terms of the column

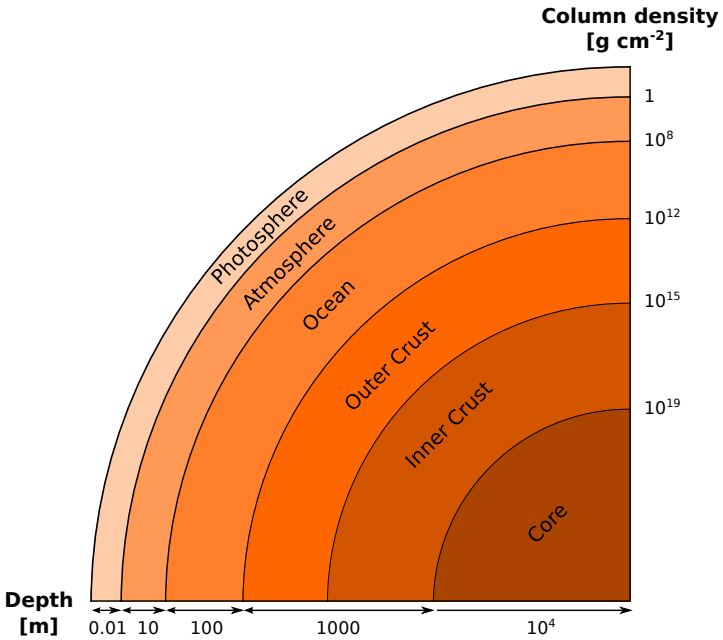

Fig. 1.5.: A sketch of the structure of a $1.4M_{\odot}$ neutron star with a 10km radius. Shown are the thickness of the different shells and the column density at their boundaries.

density, which is a common quantity in the studies of X-ray bursts. Inside a neutron star with a radius R, the relativistic column density y, at a radius r is given as

$$y(r) = \int_{R-r}^{R} \rho(r') \frac{dr'}{\Gamma}, \tag{1.30}$$

where ρ is the density and Γ is defined as

$$\Gamma = \sqrt{1 - \frac{2GM}{Rc^2}}, \tag{1.31}$$

with c being the speed of light, $G = 6.673 \cdot 10^{-8}$ dyn cm^2 g^{-2} is the gravitational constant, and M is the mass of the neutron star.

1.2.4 Binary Systems

Roughly every tenth known neutron star in our Galaxy is found in a X-ray binary ([85]). Observations have shown that more than half of the stars of our galaxy are found in binary or multiple star systems (mentioned in e.g. [64, 86]). If the stars are far enough away from each other, they hardly have any influence on each other. But if they are members of a close binary system, they will considerably affect each other's evolution. In extreme cases of closeness, the two stars are so nearby that they can share a common envelope. They are then called *contact binaries*. A binary system has a Roche Lobe, which is an equipotential surface of the gravitational field around both stars that touches at the Inner Lagrangian point where the effects of gravity and rotation cancel each other (see Fig. (1.6)). If one star reaches the Inner Lagrangian point, it will lead to mass exchange from the donor to the accretor of the binary system. This can happen through two events: One is that the binary system loses energy through gravitational waves and the stars get closer until one reaches the Inner Lagrangian point, or one of the stars evolves and expands until its envelope touches the Inner Lagrangian point.

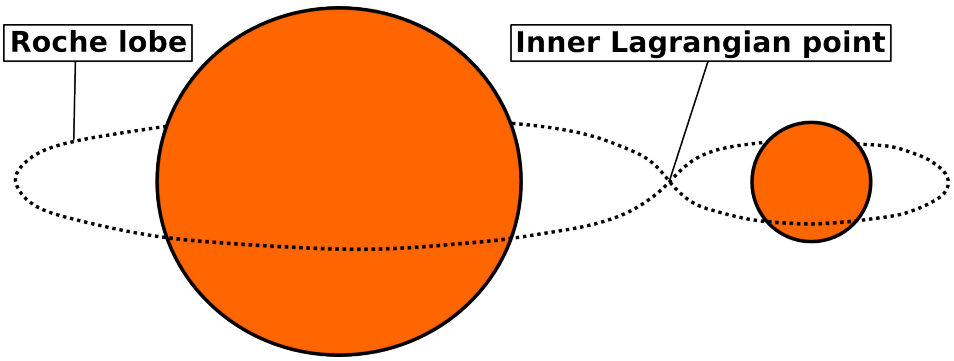

Fig. 1.6.: Sketch of a binary star system. Each star is surrounded by the Roche Lobe. The dashed lines show the equatorial belt of the Roche Lobe.

This mass transfer can lead to explosive events, the most common ones are type Ia supernovae[7] and classical novae, where the mass is transferred onto a white dwarf, or X-ray bursts where the mass is transferred onto a neutron star. The mass that is exchanged consists mostly of H and/or He because the matter is from the outer envelope of the binary companion, which is usually unburnt stellar material. The overflowing matter does not fall directly onto the surface of the accretor, but forms a accretion disk around it. If the angular momentum of the thin stream of matter, which is transferred through the Inner Lagrangian point (see Fig. (1.6)) of an accreting binary system, exceeds $\sim r_I c$ (where r_I is the radius of the innermost

[7] Type Ia supernovae are different from the other two events since the explosion disrupts the white dwarf and, in general, neither a neutron star nor a black hole is left behind, whereas the other two events are repetitive and the accretor survives.

stable orbit), and consequently it forms an accretion disk [87]. The matter of the disk then may even burn [88], may fall onto the accretor, may go back to the donor or may even leave the system completely through the second Lagrangian point [82]. A fraction of the matter of the accretion disk spirals inward and accumulates unburnt or can burn steadily during the accretion on the accretor's surface, where it builds up a new shell of ashes. A binary star system, with a neutron star as an accretor that emits most of its radiation in X-rays, is called an X-ray binary system and is class-divided depending on the mass of the donor star. Usually, X-ray burst sources have a short orbital period (between 0.2 and 15h [6]), because the involved stars are close.

1.2.5 X-ray Bursts

X-ray Binaries

X-ray binaries are close binary star systems where the compact accretor is a neutron star or a black hole. Those binary systems can be split into three different classes concerning the mass of the donor of the system. These classes are shown in Tab. (1.5). The donor can be, e.g., a main sequence star, a red giant, or a white dwarf. Most of the known LMXBs are perpetual active X-ray sources [5]. The transient X-ray sources give indication that the accretion rate from the disk onto the compact object is not constant. Most LMXBs are discovered in stages of emitting a persistent luminosity in the range of $0.001 - 0.1 L_{Edd}$ (L_{Edd} is given in Eq. (1.38)). Only few Type I X-ray bursts have been detected in quiescent phases [89].

Class of X-ray binary	Mass of the donor star
high-mass X-ray binaries (HMXBs)	$\geq 5 M_{\odot}$
intermediate-mass X-ray binaries (IMXBs)	$5 M_{\odot} \geq M_{donor} \geq 1 M_{\odot}$
low-mass X-ray binaries (LMXBs)	$\leq 1 M_{\odot}$

Tab. 1.5.: Classes of X-ray binaries in dependence of the mass of the donor star.

X-ray Burst Classes

The X-ray burst itself is characterised by a sudden increase in the radiation intensity compared to the normal level, see Fig. (1.1) for Type I X-ray bursts. All the X-ray bursts are classified into two types, Type I X-ray bursts and Type II X-ray bursts. Type I X-ray bursts are again sub-classified in short X-ray bursts and superbursts, as the sketch shows in Fig. (1.7). All Type I X-ray bursts and, therefore, also all superbursts, take place in LMXBs because they ignite at the same site.

The light curve of the two types of X-ray bursts is substantially different. The tail of a Type I X-ray burst light curve, after a sudden increase, decays softly - in contrast to the tail of the light curve of a Type II X-ray burst which decays more rapidly [27]. The duration of a Type II X-ray burst ranges from ~ 2s up to ~ 700s with intervals between the bursts from only ~ 7s up to ~ 1h [6]. The reason for the unequal light curves is that the two different types occur at different sites. It is believed that the Type II bursts occur due to sudden changes in the accretion rate in a X-ray binary system [27]. The smooth decay of the light curve of a Type I X-ray burst allows to infer that the site must be on the surface of a neutron star. The decay indicates the cooling of the material on the neutron star after a thermonuclear flash. The time until the light curve reaches its maximum varies between 1s and 10s, while the decay afterwards happens on a timescale of about 10s to 100s. Three different Type I X-ray

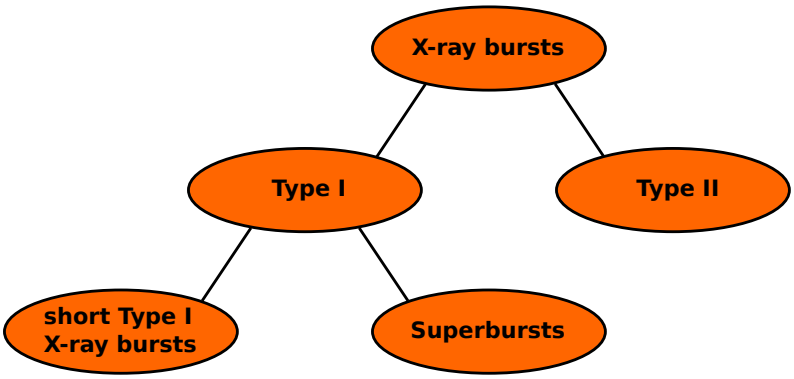

Fig. 1.7.: The classification of X-ray bursts into Type I and Type II bursts with respect to the site of the burst. Type I sub-classifies in short X-ray bursts and superbursts depending on the duration of the burst and the thermonuclear processes taking place.

burst light curves are shown in Fig. (1.1). The shape of the light curves gives a hint to what is the primary fuel of the thermonuclear runaway. Fast rises in the burst light curve are an indicator for mainly explosive He-burning, whereas slow rising intensities and slow decays in light curve are characteristics indicating a fuel mixed with H and He [27]. The energy release of a typical Type I X-ray burst is in the range of $10^{39} - 10^{40}$erg (for comparison a nova releases $10^{46} - 10^{47}$erg and a supernova $\sim 10^{51}$erg [24]).

Type I X-ray Bursts

In this thesis, we will focus only on Type I X-ray bursts and superbursts. In an accreting binary system with an accretion disk, where we observe Type I X-ray bursts, the accretion rate has to be below the Eddington critical accretion rate, otherwise the system does not survive long enough to be observed [90]. The Eddington critical accretion rate depends on the composition of the accreted material and is defined as

$$\dot{M}_{Edd} = \frac{4\pi GM}{c\kappa_0 \eta}, \tag{1.32}$$

where G is the gravitational constant, M is the mass of the neutron star, c is the speed of light, η is the accretion efficiency given by $\eta = \frac{GM}{Rc^2}$, and κ_0 is the Thomson opacity described as

$$\kappa_0 = \frac{8\pi}{3}\left(\frac{e^2}{m_e c^2}\right)^2 \frac{1}{m_u}\sum_i \frac{Z_i}{A_i} X_i, \tag{1.33}$$

where e is the electron charge, m_e is the electron mass, and m_u is the mass unit. In the sum over all nuclei of the accreted matter, Z_i is the proton number, A_i is the

mass number, and X_i is the mass fraction of the isotope i. This leads for a $1.4 M_\odot$ neutron star with accreting solar abundances (71% hydrogen, and 27% helium) to a Eddington critical accretion rate of approximately:

$$\dot{M}_{Edd} \approx 2 \times 10^{-8} M_\odot \text{yr}^{-1} = 1.3 \times 10^{18} \text{g s}^{-1}. \tag{1.34}$$

If the donor star has lost the outer envelope during its life or is a white dwarf (e.g. the case of an ultra-compact binary in [91]), the composition of the accreted matter is hydrogen-deficient (as in [91]) and therefore the Eddington critical accretion rate is shifted to higher values,

$$\dot{M}_{Edd} \approx 3 \times 10^{-8} M_\odot \text{yr}^{-1} = 1.9 \times 10^{18} \text{g s}^{-1}. \tag{1.35}$$

As already mentioned in Section (1.2.3), the gravity at the surface of the neutron star is in the order of 10^{14} cm s^{-2}. Therefore, in-falling matter sets a big amount of gravitational energy free. This energy heats the in-falling matter itself and the accretion disk, which results in fully ionization of the in-falling matter when it reaches the neutron star. This heating of both explains the persistently observed X-ray emission between the bursts [3]. Under the assumption that matter falls from infinity, the total energy release from mass transfer is given by

$$L = \left(1 - \sqrt{1 - \frac{2GM}{Rc^2}}\right) \dot{M}c^2 \approx \frac{GM}{R}\dot{M}, \tag{1.36}$$

where $\dot{M}$ is the total mass transfer. The total persistent luminosity observed from X-ray binaries consists (beside the luminosity from the mass transfer) additionally from the disk luminosity. This disk luminosity can exceed $> 10\%$ of the total persistent luminosity and depends on the geometry of the accretion flow. Therefore, the persistent luminosity can not be taken as a precise indicator of the instantaneous accretion rate [92].

For a Type I X-ray burst to occur, the material has to be transferred primarily unburned, but fully ionized, onto the surface of the neutron star, where it is accreted and undergoes gradual compression due to more matter being continuously piled on top of it (as shown in Fig. (1.8a)). Under the prevailing conditions of the atmosphere, in contrast to the nucleons, the electrons are degenerated and described as a Fermi-Dirac gas while the nuclei on the other hand behave like a temperature dependent ideal gas, but the partial pressure of the electrons is bigger compared to the partial pressure of the nuclei, therefore the total pressure of the matter at ignition depth behaves like a degenerated gas. By definition, a degenerated gas does not respond to temperature changes by expansion or contraction, the degenerated gas can only transport heat through radiation, conduction, or convection. The accreted

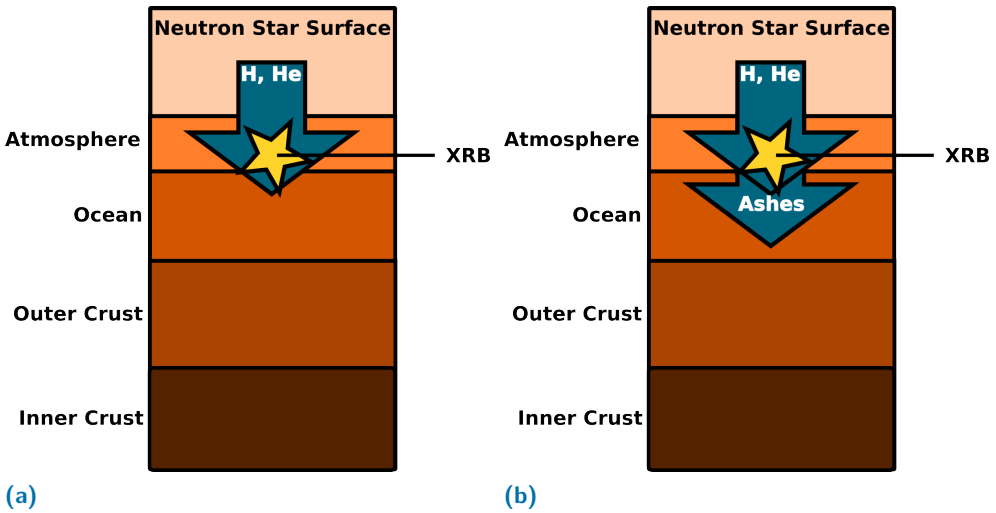

Fig. 1.8.: On the left side in (a) it is shown by the big arrow how the accreted matter reaches higher densities due to that more and more matter is accreted on top, until it reaches the density regime of about 10^6g cm^{-3} where the rp-process is thought kick in and an X-ray burst appears. On the right side in (b) it is shown how then the ashes of each X-ray burst is shifted into regimes of higher densities. These figures are adapted from [86].

matter forms a thin shell in the lower atmosphere, until the critical mass M_{critical} is reached. Then, close to the surface of the neutron star where the matter is dense and degenerated, a thermonuclear runaway occurs due to the ignition of the nuclear fuel. Because of the degeneracy at the beginning of the event, the material cannot expand and heats up due to the energy generation through nuclear reactions. This thin-shell thermal instability – first discussed by [3] and connected as the cause of observable Type I X-ray bursts by [2] – causes a nuclear runaway if the nuclear energy release rate becomes more sensitive to temperature changes than the corresponding cooling rate [93, 94]

$$\frac{d\epsilon_{nuc}}{dT} \geq \frac{d\epsilon_{cool}}{dT}, \tag{1.37}$$

where ϵ_{cool} is the divergence of the heat flux and ϵ_{nuc} is the time rate of the nuclear energy release. This leads to explosive hydrogen-, helium-burning, or burning of the H/He mixture of the accreted shell on the neutron star, which in this case is called a Type I X-ray burst. The ashes of the X-ray burst are moved down into the ocean, as more matter piles up again through the accretion from the companion star (as shown in Fig. (1.8b)).

As mentioned before, there is a maximum limit for accretion rates of matter, Eq. (1.32). This limit for the accretion rate is assumed to be set by the so-called Eddington limit [6]. Because if the luminosity exceeds the Eddington limit, it means that the radiative force of the burst exceeds the gravitational force, and thus the

atmosphere gets unstable to plasma outflow. The Eddington limit is a given limit for the maximum luminosity, L_{Edd}, given as

$$L_{Edd} = \frac{4\pi c G M m_p}{\sigma_0}, \tag{1.38}$$

where σ_0 is the Thomson scattering cross section and m_p is the proton mass. Furthermore, the Eddington limit has the following relation

$$L_{Edd} \cong 3.2 \times 10^4 \left(\frac{M}{M_\odot}\right) L_\odot, \tag{1.39}$$

where M is the mass of the neutron star, $M_\odot$ is the solar mass, and $L_\odot$ is the luminosity of the sun. According to Parikh et al. (2012) [6], with different total mass accretion rate $\dot{M}$, different burning-stages are allowed to burn stable or unstable. For a mass accretion rate of $< 2 \times 10^{-10} M_\odot \mathrm{yr}^{-1} = 1.3 \times 10^{16} \mathrm{g\ s}^{-1}$, He-burning is triggered by thermally unstable ignition of H-burning. The needed temperature for stable hydrogen-burning between the bursts is not reached and therefore, when the hydrogen ignites and triggers the helium-burning, a Type I X-ray burst occurs. If the mass accretion rate is $2 \times 10^{-10} M_\odot \mathrm{yr}^{-1} < \dot{M} < (4.4 - 11.1) \times 10^{-10} M_\odot \mathrm{yr}^{-1} = (2.8 - 7) \times 10^{16} \mathrm{g\ s}^{-1}$, the temperature in the accreted shell is higher than in the previous case. Therefore, hydrogen can burn stable to helium between the various Type I X-ray bursts. The Type I X-ray burst occurs when the He ignites and is characterised by a fast rise and a bright peak luminosity. The next regime of mass accretion rate is $\dot{M} > (4.4 - 11.1) \times 10^{-10} M_\odot \mathrm{yr}^{-1}$ where He ignites in a mixture of H/He, because the accretion supplies more unburned hydrogen than can be burnt steadily between the bursts. This last mass accretion regime leads to Type I X-ray bursts of long duration. Although an X-ray burst is an immense explosive event, it does not release enough energy, to throw the mass from the shell out of the gravitational pull of the neutron star. This is due to the small hydrogen layer ($\sim 10^{-12} M_\odot$), hence the mass bounces back to the shell after the event. Therefore, the neutron star shell does not lose material through this event and the ashes of the explosive hydrogen-burning come back to the shell, where it sinks down to the ocean of the neutron star. In an accreting system, the ocean consists more and more out of the ashes produced by each Type I X-ray burst, and with time even parts of the outer crust are infested with burnt material. If the neutron star is in a long-lived binary system, the entire crust can be replaced with by the accreted matter. If there is no heat source in the crust, the crust itself is the most sensitive to the neutrino cooling. The non-isolated neutron star's crust has a composition set by the nuclear history of the accreted material and is not in a statistical nuclear equilibrium [95, 96, 97, 98, 99]. The accreted matter induces nonequilibrium reactions that release heat. An additional heating source can increase the amount of carbon, which is produced during Type I X-ray bursts and is needed for superburst ignition. Calculations of [100] indicate that this heating source has to be located

in the ignition region of superbursts, because the heating source is independent of the URCA process in the crust. Literature gives the range of this crustal heating Q_b in the range of $0.1 - 1.5$ MeV nuc^{-1} [7, 101, 102]. Not only theory suggests this additional crustal heating, observations of thermal relaxations of neutron stars hint that this additional heating is needed to reproduce the cooling correctly [103].

Quiescent Burning

In between bursts, quiescent burning is happening because there is constantly matter accreted that heats up, being shifted down into the atmosphere of the neutron star. As this matter – mostly hydrogen, helium and metals – is pushed into the atmosphere of the neutron star, it can undergo stable burning as soon as the conditions are given. Depending on the accretion rate, this can destroy a certain amount of the accreted isotopes. For an accretion rate of $\dot{m}_{acc} = 5 \times 10^{16}$ g s^{-1} Fisker et al. (2004) [104] shows that, where the ignition occurs, all the hydrogen has already burnt stably into helium. For a higher accretion rate $\dot{m}_{acc} = 1 \times 10^{17}$ g s^{-1}, which corresponds to the accretion rate of the textbook burster GS 1826-24, Fisker et al. (2005) [105] shows that quiescent hydrogen burning happens through the hot CNO-cycle, which produces helium, which in this case is burned through triple-α-reactions.

The Triple-α Reaction, the αp-Process, and the rp-Process

A Type I X-ray burst is a thermonuclear shell flash occuring close beneath the surface of the neutron star. As already mentioned, the Type I X-ray bursts are powered by explosive H/He burning, more specifically by the triple-α reaction, the αp-process, and the rp-process (see for rp-process, e.g.: [13, 16, 106, 107, 108, 109, 110]), those three processes are shown in Fig. (1.10).

The rp-process, or hot explosive hydrogen burning, take place in a number of astrophysical sites, the most prominent ones are Novas and X-ray bursts. But how is the burst triggered? Prior to the ignition, the most important process is the hot CNO cycle (see [112], the hot CNO cycle is shown in Fig. (1.9) as the dark green arrow), whose net reaction is $4^1\text{H} \rightarrow {}^4\text{He} + 2\bar{\nu}_e$, which consumes hydrogen and produces helium. At the surface of the neutron star, the temperature is in a range of $0.1 - 0.2$ GK. In that condition, proton capture is much faster than the β^+-decays of the long-lived oxygen-isotopes of the hot CNO cycle. Therefore, the cycle is rapidly saturated and becomes temperature independent, but for a thermal runaway to happen, the reactions have to become thermally sensitive. Therefore, the triple-α reaction or the rp-process is essential. How exactly is the burst triggered depends on the material composition at the ignition depth, which again depends on the

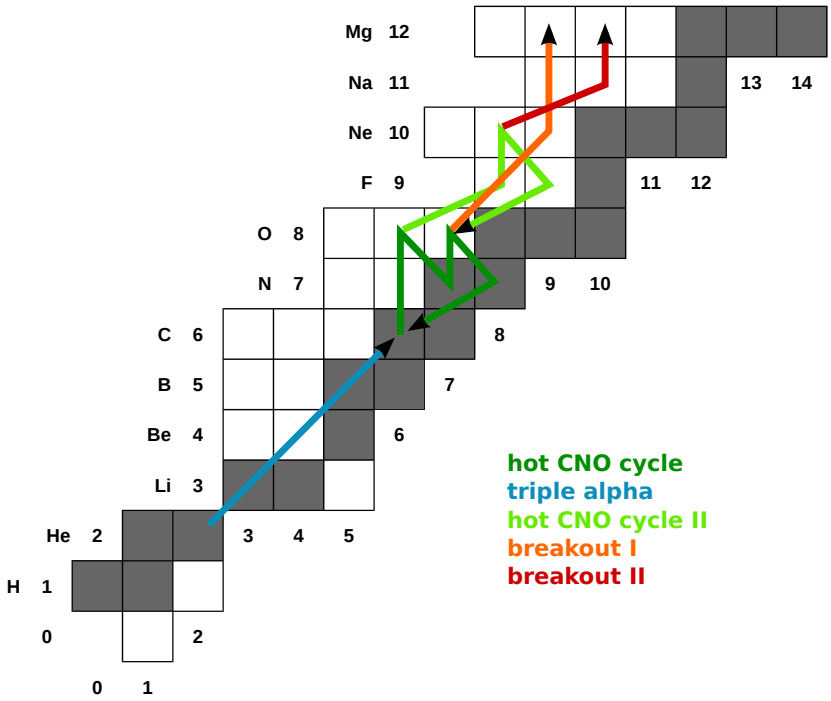

Fig. 1.9.: Prior to ignition, the hot CNO cycle (dark green arrow) catalyses four H nuclei in one ^{4}He. The triple-α (blue arrow) kicks in and initiates the ignition. Additionally, the hot CNO cycle two (light green arrow) is possible. At slightly higher temperatures, the breakout reaction ^{15}O(α,γ) is possible (orange arrow) and only $\sim$ 50ms after breakout 1 the temperatures for breakout reaction two ^{18}Ne(α,p) (red arrow) is reached, which leads to the rp-process. The gray-shaded squares are stable isotopes. This figure is adapted from talks given by H. Schatz.

accretion rate, the neutron star mass, and its radius [113]. The triple-α (the blue arrow in Fig. (1.9)) ignites at about $\sim$ 0.2GK and heats the matter. When it reaches $\sim$ 0.3 GK, the breakout reaction ^{15}O(α,γ) (the orange arrow in Fig. (1.9)) starts and only $\sim$ 50 ms later, at $\sim$ 0.6 GK, ^{18}Ne(α,p) (the red arrow in Fig. (1.9)) follows, and the subsequent flow up to ^{40}Ca is determined by the competition between the αp-process and the rp-process. The αp-process is a series of alternating (α, p) and (p, γ) reactions – for each proton capture there is an (α, p) reaction releasing a proton, therefore the net effect is pure helium burning. The rp-process is a sequence of proton capture and β^{+}-decays. The αp-process is very temperature dependent because of the strong Coulomb-barrier against the α-capture and can only reach up to Sc. Whereas the rp-process is an interplay between fast proton captures and β^{+}-decays and the temperature influences the ratio of the proton-rich isotopes within an isotone and thus which isotopes β^{+}-decays, but it can produce nuclei up to and beyond the Fe-peak. The produced nuclei are proton-rich and highly unstable, close to the proton dripline. As long as there is fuel for the rp-process, i.e. hydrogen, the process runs, until the end-point at ^{107}Te and ^{108}Te (see insert in Fig. (1.10)), where Sn-Sb-Te cycle can further produce α-particles via photodisintegration. During a Type I X-ray burst high temperatures in the range of $1-2$GK are reached on a short timescale ($1-10$s) and therefore it enables those fast proton captures [13].

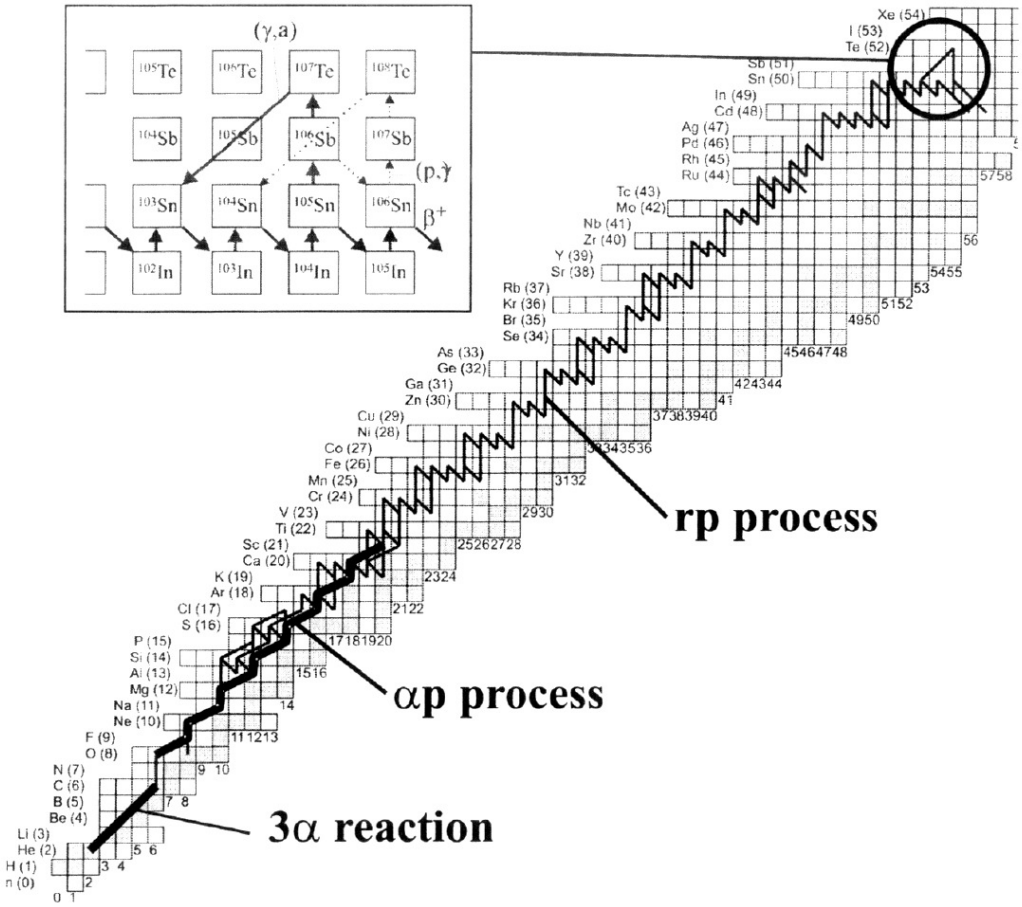

Fig. 1.10.: This figure shows the reaction flow time integrated over a complete Type I X-ray burst. Therefore, it shows the full sequence of nuclear reactions powering it. The three processes which fuses helium and hydrogen to heavier isotopes are shown here. The inset shows the endpoint of the rp-process – the Sn-Sb-Te cycle. This figure is taken from [111] and the calculations were made with a one zone model couples self-consistently to a complete reaction network (see [13]).

1.2.6 Superbursts

> *"There is one burst (we call it the "super burst") which is about 3 times more energetic than the average burst from his source [4U 1728-33]."*
>
> **— E. M. Basinska et al.**
> [60]

Superbursts are thought to be triggered by a carbon flash in the ocean of an accreting neutron star [114]. One of the main goals of this thesis is to consistently perform a simulation of thousands of X-ray bursts, in order to acummulate enough ^{12}C at the base of the ocean of the neutron star, so that a so-called superburst would be triggered. Observations have shown that superbursts occur at the same site after about thousands of normal Type I X-ray bursts, with a recurrence time of around a year, which is vaguely estimated due to limited observable data [115]. Fig. (1.11) shows the measurements of a superburst detected at the site KS 1731-260. Tab. (1.2) shows all the observed superbursts. There are only few observed events, because it is a rather newly discovered phenomenon and rare. The first superburst has been detected by Cornelisse et al. (2000) [52] in 1996 at the site 4U 1735-444. Since then, only a few more events have been found.

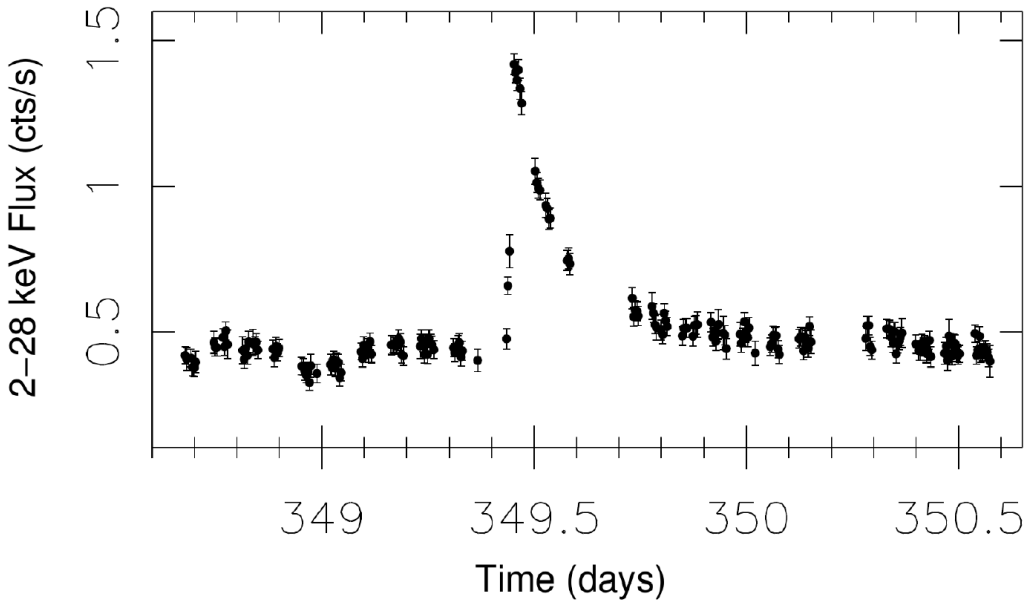

Fig. 1.11.: Measurements of a superburst – which lasted around half a day – from the site KS 1731-260. Taken from [50].

The leading theory suggests that a superburst occurs due to explosive carbon-burning [114], as discussed in Section 1.2.2, in deeper regions of the neutron star (see Fig. (1.12)). Carbon is one of the ashes of explosive hydrogen- and helium-burning from Type I X-ray bursts. Simulations of superbursts have confirmed the connection between superbursts and unstable burning of carbon [9]. Fig. (1.2) shows that a "Super Burst" differs from normal Type I X-ray bursts especially in the bolometric burst fluence E_b, which is the integrated burst flux. A superburst is roughly one thousand times more energetic than a normal Type I X-ray burst ($\sim 10^{38-39}$erg s^{-1}), coming both from the same source, an accreting binary system (see Section 1.2.4). Therefore, in the range of $\sim 10^{42}$ergs, and of longer duration [61] through longer radiation transport, due to the ignition depth. As a consequence, the light curve is characterized by a decay of several hours. After a superburst occurs, the envelope has to cool down before the sequence of Type I X-ray bursts can re-appear [9]. As long as the envelope is too hot, the newly accreted material undergoes stable burning at the same rate it is accreted [50, 52, 114]. Those quenching times are predicted to be as long as one week or even several weeks [116], while the recurrence times for superbursts are of the order of several years because it takes long time to accumulate enough carbon in the depth of the ignition.

The ignition of the carbon flash is thought to take place at the bottom of the ocean at column depths around $0.1 - 5 \times 10^{12}$g cm^{-2} [116, 117]. Studies on an additional heating source from the crust of the neutron star showed it has influence on the recurrence time through the effects of the heating flux on the ignition depth [10]. The ignition depth is sensitive to crustal heating and neutrino cooling of the core

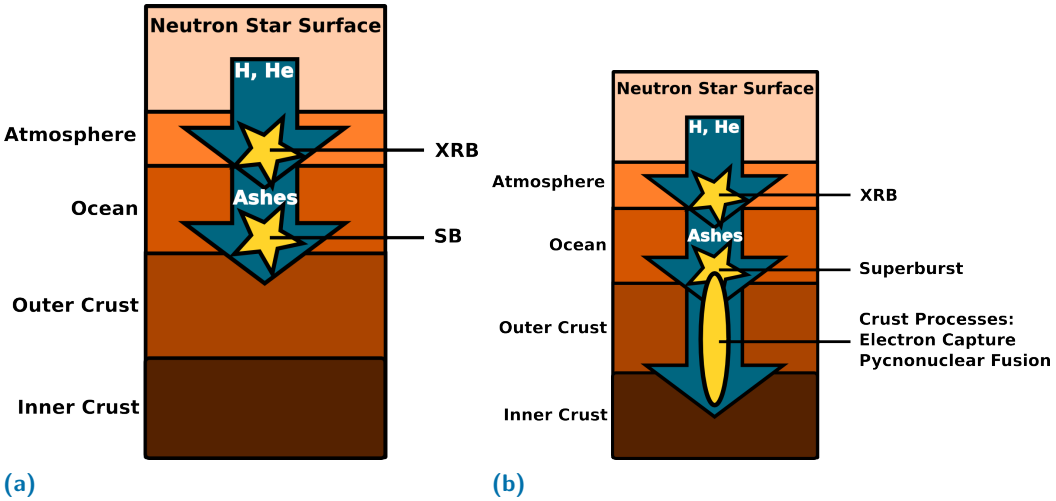

Fig. 1.12.: a) Due to prior Type I X-ray bursts, the ashes are accumulated at the bottom of the ocean and form a layer where the ignition of thermonuclear carbon flash is thought to happen. b) As the material is shifted to higher densities, electron-capture and pycnonuclear fusions are releasing an additional heat flux. Electron-captures can build very neutron rich nuclei. This figure is adapted from [86].

because of the high temperature dependence of the carbon burning rate [118]. Due to the depth of the superburst, it provides the opportunity to probe the properties of the neutron star crust, such as thermal structure and conductivity [7, 119] or more insight in the interface between the ocean and the crust [120, 121]. At that depth, the surrounding material consists of the ashes of previous Type I X-ray bursts, where the rp-process plays an important role, and those heavy proton rich nuclei provide up to half of the observed energy through photodisintegration [122]. Therefore, it is crucial to simulate the superburst not only with enough produced carbon from the Type I X-ray bursts, but also with the resulting composition from the bursts.

2 Code

"I almost wish I hadn't gone down the rabbit-hole - and yet- and yet- it's rather curious, you know, this sort of life!"

— **Alice**
Lewis Carroll

We present in this thesis the results using a one-dimensional code that is used for simulating recurring thermonuclear Type I X-ray bursts in the surface layers of an accreting neutron star and is capable of simulating superbursts. This code couples a general relativistic hydrodynamics code from M. Liebendörfer, called `AGILE` (see e.g. [22, 23]), with a nuclear reaction network from F.-K. Thielemann and W. R. Hix [24]. The code was initially programmed by J. Fisker 2006 [21] and has been updated and optimized by S. Fehlmann in 2015 [25]. The `AGILE` code had to be modified in this thesis to perform X-ray burst and superburst simulations, since `AGILE` was formerly created for numerical supernova simulations. Originally, it included the zones of the region where X-ray bursts are happening and the upper part of the ocean, where the ashes of X-ray bursts are accumulated. Now it includes not only these regions, but also the regions where a superburst is expected to be initiated. This means that our computational domain reaches a column density roughly of the order of $\sim 10^{13}$ g cm^{-2}, so that the ignition depth of a superburst is included (see Fig. (2.2) for an illustration of the regions which are included in our computational domain – box in the figure). The reaction network and the hydrodynamics of the

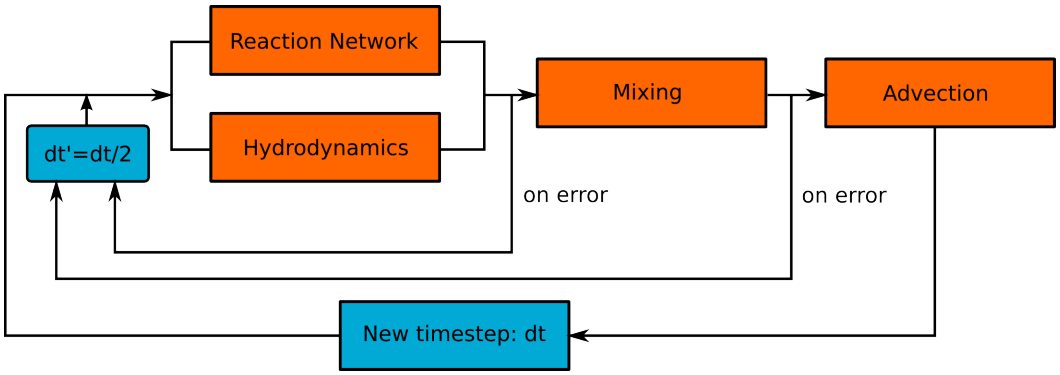

Fig. 2.1.: This figure shows the schematic view of the calculation method. The reaction network and the hydrodynamics element are parallelized. This scheme is adapted from [25].

code are parallelized (see Fig. (2.1)) to reduce the calculation time. For doing this, OpenMP as well as MPI was used. For each new time step (blue box at the bottom in Fig. (2.1)) the solution is divided into four submatrices (orange boxes in Fig. (2.1)): nuclear reactions, hydrodynamics, mixing, and advection.

We use the fast `PARDISO` solver [123] for the hydrodynamics and the nuclear reaction network because the implicit scheme requires the inversion of the Jacobian matrix which is connected to the independent variables of the system of equations. First, the nuclear reaction network and the hydrodynamics are solved in parallel for each timestep dt, this timestep will be on error divided in half and a new iteration with a new timestep $dt' = dt/2$ is started, until both solvers succeed. Then the convection solver returns the convected isotopes, or on error, divides the timestep again by a factor of two and another iteration begins with the new time step. The same procedure is in place for the advection solver.
In the following, we will discuss the single parts shortly in a bit more detail (for full details read the appendix of [21] or Section 2 of [25] and references therein).

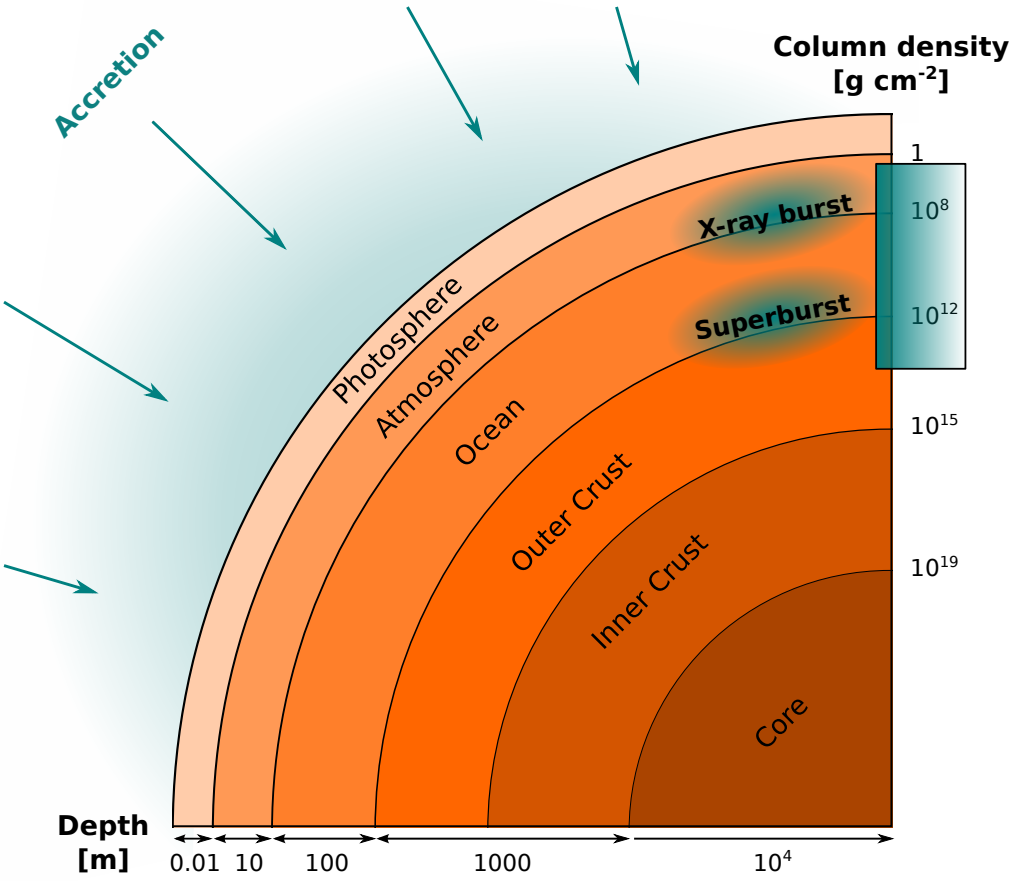

Fig. 2.2.: This figure shows a schematic view of an accreting neutron star, the different layers are in different shades of orange, the accretion is indicated with blue arrows. The depth of Type I X-ray bursts and superbursts are drawn in blue spheres. The range of our computational domain is presented as a blue box at the right corner.

2.1 Nuclear Reaction Network

At each timestep, we solve the reaction Equation (1.24) introduced in Section 1.2.1 for every single isotope i of our network, which includes 304 isotopes (see Tab. (2.1)). For up to three-particle reactions, this equation is given by

$$\dot{Y}_i = \sum_j N_j^i \lambda_j Y_j + \sum_{j,k} \frac{N_{j,k}^i}{1+\delta_{jk}} \rho N_A \langle \sigma v \rangle_{jk} Y_j Y_k + \sum_{j,k,l} \frac{N_{j,k,l}^i}{1+\delta_{jkl}} \rho^2 N_A^2 \langle \sigma v \rangle_{jkl} Y_j Y_k Y_l. \tag{2.1}$$

We include three possible reactions: one particle reactions (which includes photodisintegration, β-decays, electron or positron capture, and neutrino induced reactions), two particle reactions (proton- or α-capture), and three particle reactions (triple-α process). The reaction rates are from the latest `JINA REACLIB` version v2.0 [124].

Element	Z	A	Element	Z	A
n	0	1	Co	27	51-57
H	1	1-3	Ni	28	52-62
He	2	3-4	Cu	29	54-63
Li	3	7	Zn	30	55-66
Be	4	7-8	Ga	31	59-67
B	5	8, 11	Ge	32	60-68
C	6	9-10, 12	As	33	64-69
N	7	12-15	Se	34	65-72
O	8	13-18	Br	35	68-73
F	9	17-19	Kr	36	69-74
Ne	10	18-21	Rb	37	73-77
Na	11	20-23	Sr	38	74-78
Mg	12	21-25	Y	39	77-82
Al	13	22-27	Zr	40	78-83
Si	14	24-30	Nb	41	81-85
P	15	26-31	Mo	42	82-86
S	16	27-34	Tc	43	85-88
Cl	17	30-35	Ru	44	86-91
Ar	18	31-38	Rh	45	89-93
K	19	35-39	Pd	46	90-94
Ca	20	36-44	Ag	47	94-98
Sc	21	39-45	Cd	48	95-99
Ti	22	40-47	In	49	98-104
V	23	43-49	Sn	50	99-105
Cr	24	44-52	Sb	51	106
Mn	25	47-53	Te	52	107
Fe	26	48-56			

Tab. 2.1.: This table lists the isotopes which are used for our calculations in this thesis. It is the same network described in [21]. It ends with Te, because this element is the endpoint of the rp-process which is described in Section 1.2.5.

Solving Eq. (2.1) results in a change of the composition of the matter of each zone and therefore, also changes the total binding energy. Neutrino emissions can also change the energy. To include those changes, one has to correct the specific energy in the following way:

$$\epsilon \rightarrow \epsilon - \sum_{k} N_A \dot{Y}_k B_k + \sum_{weak} N_A \dot{Y}_i E_{\nu i} + \epsilon_{\text{Bremsstrahlung}}, \tag{2.2}$$

where $E_{\nu i}$ is the specific energy loss from neutrino emission due to the *ith* weak interaction, $\epsilon_{\text{Bremsstrahlung}}$ is the fraction of energy loss via neutrino emission due to neutrino bremsstrahlung, B_k is the binding energy of the isotope k and is defined as:

$$B_k = (N m_n + Z m_p - m_k) c^2, \tag{2.3}$$

where N is the neutron number of isotope k and Z its proton number and m_k is the mass of the isotope k. Due to the parallelization scheme, the isotopes of a zone can not interact with isotopes from a neighbouring zone. Note that the nuclear reaction network solver is the slowest part of the code.

2.2 Hydrodynamics

The Einstein field equation(s) determine the macroscopic motion of matter in a gravitationally dominated field and are given by,

$$G_{\mu\nu} = 8\pi T_{\mu\nu}, \tag{2.4}$$

where G is the Einstein curvature tensor and T is the stress-energy tensor. To solve the set of stress-tensors in spherical symmetry for an ideal fluid with radiation in co-moving coordinates (given by [125]) we assume a spherically symmetric metric,

$$ds^2 = -\alpha^2 c^2 dt^2 + \left(\frac{1}{\Gamma}\frac{\partial r}{\partial a}\right)^2 da^2 + r^2(d\vartheta^2 + sin^2\vartheta d\varphi^2), \tag{2.5}$$

where the radial coordinate is represented by a and attached to co-moving matter, r is the areal radius of the sphere enclosing a, and α is the proper time correction (redshift) of the coordinate time lapse dt of an observer following the motion of the matter attached to a as seen from infinity, Γ is a factor which in the special relativistic limit becomes the boost factor between the inertial system and the co-moving system, and is given by,

$$\Gamma = \sqrt{1 + \frac{u^2}{c^2} - \frac{2Gm}{rc^2}}, \tag{2.6}$$

where u is the matter velocity as seen from a frame with constant radius and m is the gravitational mass contained in a radius r. Note that Γ, in the static limit,

relates to the volume correction of the Schwarzschild metric. Using the stress-energy tensors and the given metric, Liebendörfer et al. (2001) derived a set of conservation equation from the Einstein field equations for the dynamical motion, which must be extended with the appropriate energy terms for nuclear and non-nuclear neutrino emission as follows

$$\frac{\partial}{c^2 \partial t}\left(\frac{1}{D}\right) = \frac{\partial}{\partial a}(4\pi r^2 \alpha u) \tag{2.7}$$

$$\frac{\partial \tau}{\partial t} = -\frac{\partial}{\partial a}(4\pi r^2 \alpha (up + \Gamma q)) - \Gamma \frac{\partial \epsilon}{\partial t} \tag{2.8}$$

$$\begin{aligned}\frac{\partial S}{\partial t} =& -\frac{\partial}{\partial a}(4\pi r^2 \alpha(\Gamma p + uq/c^2)) \\ & -\frac{\alpha}{r}\left[\left(1 + \frac{e}{c^2} + \frac{3p}{\rho c^2}\right)\frac{Gm}{r} + \frac{8\pi G r^2}{\rho c^2}\left(p\left(1 + \frac{e}{c^2}\right)\rho - \frac{q^2}{c^4}\right) - \frac{2p}{\rho}\right]\end{aligned} \tag{2.9}$$

$$\frac{\partial V}{\partial a} = \frac{4\pi}{3}\frac{\partial r^3}{\partial a} = \frac{1}{D} \tag{2.10}$$

$$\frac{\partial m}{\partial a} = 1 + \frac{\tau}{c^2} \tag{2.11}$$

$$\frac{\partial}{\partial t}\left(\frac{1q}{4\pi r^2 c^4 \rho^2}\right) = -\left(1 + \frac{e}{c^2}\right)\frac{\partial \alpha}{\partial a} - \frac{1}{\rho c^2}\frac{\partial}{\partial a}(\alpha p), \tag{2.12}$$

where D is a specific rest mass density, τ is the specific total energy density, and S is the specific momentum density, defined as followed:

$$D = \frac{\rho}{\Gamma} \tag{2.13}$$

$$\tau = \Gamma e + \frac{2}{\Gamma + 1}\left(\frac{1}{2}u^2 - \frac{Gm}{r}\right) + \frac{uq}{\rho c^2} = \Gamma\left(c^2 + e\right) - c^2 + \frac{uq}{\rho c^2} \tag{2.14}$$

$$S = u\left(1 + \frac{e}{c^2}\right) + \Gamma\frac{q}{\rho c^2}, \tag{2.15}$$

where $p = p_{\text{matter}} + p_{\text{rad}}$ is the pressure, $e = e_{\text{matter}} - B(X_j)c^2 + e_{\text{rad}}$ is the specific internal energy, $q = L/(4\pi r^2)$ is the energy flux, and V is the enclosed volume. In the Newtonian limit where $\alpha \to 1$, $\Gamma \to 1$, and $c \to \infty$, the Eq. (2.7-2.9) are reduced to the Euler equations in the Lagrangian formulation and the Eq. (2.10-2.12) are reduced to trivial identities.

We have now seven dependent variables from Eq. (2.7-2.12), one independent variable t, and one adaptive grid equation (will be introduced below). Because hydrodynamics are sensitive to efficient convective heat transport – which depends

on the physical transport of the composition (which is held constant during one hydrodynamics time step) – one has to consider three more equations:

$$\frac{\partial \Gamma Y_e}{\partial t} = -\frac{\partial}{\partial a}\left(4\pi r^2 \rho \alpha \Gamma \left(-4\pi r^2 \rho D \frac{\partial}{\alpha \partial d}(\alpha Y_e)\right)\right) \tag{2.16}$$

$$\frac{\partial \mu^{-1}}{\partial t} = -\frac{\partial}{\partial a}\left(4\pi r^2 \rho \alpha \Gamma \left(-4\pi r^2 \rho D \frac{\partial}{\alpha \partial d}(\alpha \mu^{-1})\right)\right) \tag{2.17}$$

$$\frac{\partial \Gamma Y_{e^2}}{\partial t} = -\frac{\partial}{\partial a}\left(4\pi r^2 \rho \alpha \Gamma \left(-4\pi r^2 \rho D \frac{\partial}{\alpha \partial d}(\alpha Y_{e^2})\right)\right), \tag{2.18}$$

where Y_e is the electron abundance, Y_{e^2} is the second momentum abundance ($Y_{e^2} = \sum X_j Z_j^2 / A_j$), and μ^{-1} is the mean molecular weight ($\mu^{-1} = Y_e + \sum X_j / A_j$).

Those sets of equations Eq. (2.7-2.12) and Eq. (2.16-2.18) and the adaptive grid equation have to be solved each time step using:

$$\delta y = \left(\frac{\partial f}{\partial y}\right)^{-1} y, \tag{2.19}$$

the Newton-Raphson method [126], where y is the array containing the hydrodynamical variables.

Adaptive Grid

Using the adaptive grid from `AGILE`, one has to make some modifications of it, since the simulation of Type I X-ray bursts has to handle both resolving a thin shell for the helium runaway, which has typical masses of $\sim 10^{-15} M_\odot$, and very thick shells for studies of the ashes of the bursts, which have typical masses of $\sim 10^{-5} M_\odot$. Therefore, the code used here has to have modified discretization of the Poisson equation to handle zone variable differing over many orders of magnitude.

$$m_{i+1}^{t+\Delta t} - m_i^{t+\Delta t} = \Gamma_{i'}^{t+\Delta t}\left(1 + \frac{e_{i'}^{t+\Delta t}}{c^2}\right) da_{i'}^{t+\Delta t}, \tag{2.20}$$

where $m_i^{t+\Delta t}$ is the total gravitational mass inside the gravitational radius $r_i^{t+\Delta t}$, $\Gamma_{i'}^{t+\Delta t} = \sqrt{1 + (u_i^{t+\Delta t}/c^2) + 2Gm_i^{t+\Delta t}/r_i^{t+\Delta t} c^2}$, $e_{i'}^{t+\Delta t}$ is the internal energy of a zone, and $da_{i'}^{t+\Delta t} = a_{i+1}^{t+\Delta t} - a_i^{t+\Delta t}$ is the rest mass of a zone. Primed indices mean that the variable is defined on the center-grid, while the others mean that the variable is defined on the edge-grid. The adaptive grid (even compiled with double precision) delivers numerical results with a maximum of 15 decimals of precision. This is insufficient to solve the thin shells at the surface of the neutron star. The left side of Eq. (2.20) and the definition of $da_{i'}^{t+\Delta t}$ cause problems because two large numbers

are subtracted, giving a result which is several orders of magnitude smaller. To readjust the adaptive grid, the following shift vectors are introduced:

$$m_i^{t+\Delta t} = m_i^t + \Delta m_i^{t+\Delta t} \tag{2.21}$$

$$r_i^{t+\Delta t} = r_i^t + \Delta r_i^{t+\Delta t} \tag{2.22}$$

$$da_i^{t+\Delta t} = da_i^t + \Delta da_{i+1}^{t+\Delta t} - \Delta da_i^{t+\Delta t}. \tag{2.23}$$

For substitution of the shift vectors into Eq. (2.20), we get then:

$$(m_{i+1}^t - m_i^t) + (\Delta m_{i+1}^{t+\Delta t} - \Delta m_i^{t+\Delta t}) = \Gamma_{i'} \left(1 + \frac{e_{i'}}{c^2}\right) (da_i^t + \Delta da_{i+1}^{t+\Delta t} - \Delta da_i^{t+\Delta t}). \tag{2.24}$$

With this change, the precision, which was lost before, is restored and the grid can handle large variable ranges.

To handle both, simulations of thousands of X-ray bursts and a possible superburst ignition, one needs to choose the grid location carefully. Furthermore, to make the new generalized adaptive grid capable of shock capturing, one has to use a logarithmic mass zone distribution. For this, we introduce $N_i = \Delta a_i$ which is the mass of the zone i, and $n_i = a_i^{t+\Delta t} - a_{i-1}^{t+\Delta t}$ is the mass which is advected into zone i during the time step Δi. N_i and n_i are both having the units of mass per zone. Let $X_i = k^i$ be a logarithmic series with k being a constant. We define $\hat{N}_i = N_i/X_i$ and $\hat{n}_i = n_i/X_i$. The desired resolution, for generalizing the grid equation and making it independent of variables, looks like:

$$R_i^{grid} = \sqrt{1 + \sum_j \left(w_j \frac{N_{scale}}{F_{scale}^j} \frac{f_i^j - f_{i-1}^j}{N_i} \right)^2}, \tag{2.25}$$

where the sum is over all other independent variables, w_j gives a weight factor to determine the significance of the variable. Both N_{scale} and F_{scale}^j are scales for the independent variables, and f_i^j is the value of the variable j itself at the grid point i. In a next step, we normalize R_i^{grid} ($\rightarrow \hat{R}_i^{grid}$) and link it to the old resolution:

$$R_i = (1 - sloth)\hat{R}_i^{grid} + sloth \frac{max_i(\hat{N}_i X_i)}{\hat{N}_i}, \tag{2.26}$$

where $sloth$ is a variable that determines how the resolutions are mixed. Using the code for X-ray burst simulations, we choose $sloth = \exp(-dt/0.1)$, where 0.1 is a chosen parameter and dt is the time step. For large time steps, the desired resolution will determine how the grid moves, and in the case of small time steps it

will maintain the current grid spacing. Finally the adaptive grid equation becomes

$$\left(\hat{N}_i R_i - \hat{N}_{i-1} R_{i-1}\right) + \left(\hat{n}_i R_i - \hat{n}_{i-1} R_{i-1}\right) = 0, \tag{2.27}$$

where the first and big parenthesis contain constant large terms, while the second, small parenthesis determines how the grid points need to be moved. In case that the terms in the first parenthesis cancel each other out, the grid points will not move because the current resolution is already the desired resolution. In its present form, the grid equation will keep a logarithmic profile of the mass zones and therefore advect newly accreted mass towards the centre of the neutron star.

Equation of State

For the equation of state, we adopted the EoS code from K. Nomoto. Type I X-ray bursts occur in the atmosphere of an accreting neutron star. As already mentioned before, the accreted atoms are assumed to be fully ionized and the composition of the matter sets Y_e. The contribution of the electrons to the pressure and the internal energy is calculated under the assumption of a relativistic degenerated gas. The contribution of the baryons is described as an ideal gas. The mean free path for photons is relatively short and therefore, one can assume that they are in a local thermodynamical equilibrium. Hence, their contribution to the pressure is given by $P_\gamma = a_{rad} T^4/3$. All those contributions are taken into account by K. Nomoto's code.

Heat Transport

The total heat transport is a combination of the radiative/conductive heat transport, q_γ, and the convective heat transport, q_c

$$q = q_\gamma + q_c. \tag{2.28}$$

The heat transport over convection is much more efficient than over radiation or conduction in the density regime of X-ray bursts. If we consider a bubble of matter and want to determine if this bubble stays stable against convection or not, one has to look at the Schwarzschild-Ledoux criteria, which also holds relativistically, due to the fact, that it is a local criteria [127]. The Schwarzschild-Ledoux criteria is given by

$$\left(\frac{d\ln T}{d\ln P}\right)_\star \leq \left(\frac{d\ln T}{d\ln P}\right)_{bubble} - \sum_{x\in\{Y_e, Y_e^2, \dots\}} \frac{\chi_x}{\chi_T}\left(\frac{d\ln x}{d\ln P}\right)_\star, \tag{2.29}$$

where the index $\star$ accounts for a derivative in the stellar profile and χ_x is given by

$$\chi_x = \left(\frac{\partial \ln P}{\partial \ln x}\right). \tag{2.30}$$

During a X-ray burst, the temperature rises fast and violates Eq. (2.29). Therefore, the steep gradient of temperature produces convective bubbles. These bubbles of matter rise with a characteristic mixing length, Λ, until they stop their rise, get dissolved, and release their heat to the circumjacent material. This heat transport smooths the temperature gradient until convection no longer occurs. The convective heat flux can be estimated by the formula given by [128]

$$q_c = \frac{1}{2} c_p \bar{v} \rho \Lambda \Gamma \left(\left. \frac{dT}{dr} \right|_\star - \left. \frac{dT}{dr} \right|_{bubble} \right), \tag{2.31}$$

where c_p is the specific heat capacity and $\bar{v}$ is the averaged velocity of rising (or descending) bubbles, which can be obtained by using the following relation

$$\bar{v}^2 = \frac{1}{8} \frac{Gm}{r^2} \Lambda^2 Q \frac{1}{T} \left(\left. \frac{dT}{dr} \right|_\star - \left. \frac{dT}{dr} \right|_{bubble} \right), \tag{2.32}$$

with

$$Q = - \left(\frac{\partial \ln \rho}{\partial \ln T} \right)_{P, Y_e, Y_e^2, \mu^{-1}}. \tag{2.33}$$

Heat transport via radiation or conduction is less efficient than via convection, but those not only appear due to the steep temperature gradient of a X-ray burst. In the region where an X-ray burst takes place, the mean free path of photons and electrons is small and thus many collisions occur. Heat transport follows Fourier's law and Fick's law since both electrons and photons are in a local thermodynamical equilibrium. For a spherical symmetric system, the heat transport equation is given by [125]

$$\frac{q_\gamma}{c} r^2 \left(\frac{1}{\Gamma} \frac{\partial r}{\partial a} \right)^2 + \frac{1}{\rho \kappa} \frac{\partial}{\alpha c \partial t} \left(\frac{q_\gamma}{c} r^2 \left(\frac{1}{\Gamma} \frac{\partial r}{\partial a} \right)^2 \right) = - \frac{4 a_{rad} c}{3} \frac{r^2}{\rho \kappa} \left(\frac{1}{\Gamma} \frac{\partial r}{\partial a} \right) T^3 \frac{\partial}{\alpha \partial a} (\alpha T), \tag{2.34}$$

where q_γ is the heat flux by radiation and conduction, κ is the opacity, and $(\rho\kappa)^{-1} = l$ is the length of the mean free path. Using $\frac{\partial r}{\partial a} = \frac{\Gamma}{4\pi r^2 \rho}$ we get

$$q_\gamma + \frac{(4\pi r^2 \rho)^2}{r^2} \frac{1}{\rho \kappa} \frac{\partial}{\alpha c \partial t} \left(q_\gamma \frac{r^2}{(4\pi r^2 \rho)^2} \right) = - \frac{4 a_{rad} c}{3} \frac{\Gamma}{\rho \kappa} T^3 \frac{\partial}{\alpha \partial r} (\alpha T). \tag{2.35}$$

Because the mean free path of the photons is only $\sim 10^{-1}$cm, which is much shorter than the distance a photon can roam in a time specified by the rise time of a burst, one can neglect the time-dependent term

$$q_\gamma = - \frac{4 a_{rad} c}{3} \frac{T^3}{\rho \kappa} \Gamma \frac{\partial}{\alpha \partial r} (\alpha T). \tag{2.36}$$

Using again the definition for $\frac{\partial r}{\partial a} = \frac{\Gamma}{4\pi r^2 \rho}$ we get for the radiative/conductive heat flux

$$q_\gamma = -\frac{16\pi a_{rad} c}{3} \frac{T^3}{\kappa} r^2 \frac{\partial}{\alpha \partial a}(\alpha T). \tag{2.37}$$

Boundary Conditions

In order to solve all the equations of the hydrodynamics part of the code, one has to set some boundary values, for both, the outer boundary conditions and the inner boundary conditions. Some boundary conditions have to be fixed, such as the gravitational mass and the radius of the underlying neutron star, are given as hard inner boundary conditions. In general, it can be stated that if a variable has a ghost zone, von Neumann boundary conditions are used, but if a variable has no ghost zone, Dirichlet boundary conditions are used instead. For each time step, we accrete matter at the surface of our model and therefore, the same amount advect into the innermost ghost zone in order to keep the total mass of the model constant. This means:

$$\Delta da_{nq}^{t+\Delta t} = \dot{M} \Delta t = \Delta da_1^{t+\Delta t}, \tag{2.38}$$

where the indice nq stays for the outermost surface zone and the indice 1 marks the innermost ghost zone.

Due to the existence of a ghost zone, we use of von Neumann boundary conditions to constrain the lapse function, the temperature, and the density at the inner boundary. The luminosity from the layers beyond our zones enters our calculations as an inner boundary luminosity, also called crustal heating, Q_b, given in units of MeV nuc^{-1} and results from electron captures and pycnonuclear energy generation as mentioned in Section 1.2.5.

At the surface are the outer boundary conditions for the lapse function and the redshift set to match the Schwarzschild solution (as in [23]). The pressure at the outer boundary is given by Dirichlet boundary conditions. The temperature and density at the surface are determined by radiative zero boundary condition or also a so-called grey photosphere. The Tolman-Oppenheimer-Volkoff equation describes – under the assumption of hydrostatic equilibrium – the structure of a spherically symmetric body [129], given by

$$\frac{\partial P}{\partial r} = \frac{-Gm\rho \left(1 + \frac{P}{\rho c^2}\right) \left(1 + \frac{4\pi r^3 P}{mc^2}\right)}{r^2 \left(1 - \frac{2Gm}{rc^2}\right)}, \tag{2.39}$$

where m is the gravitational mass and ρ is the density of the rest mass. One can simplify this equation by assuming that the energy density of the pressure is very

low compared to the rest mass density and therefore, we get for the simplified TOV-equation

$$\frac{\partial P}{\partial r} = \frac{-Gm\rho}{r^2\left(1-\frac{2Gm}{rc^2}\right)}. \tag{2.40}$$

The temperature of the neutron star is described by [130]

$$\frac{d}{dt}\left(Te^{\phi}\right) = \frac{-3\kappa\rho L_{\gamma}e^{\phi}}{16\pi acT^3r^2\sqrt{1-\frac{2Gm}{rc^2}}}, \tag{2.41}$$

where e^{ϕ} is the redshift correction factor, L_{γ} is the photon luminosity, and a is the radiation constant. For the thin photosphere, one can assume that the gravitational field stays constant and therefore, one can divide e^{ϕ} out because it is constant. We then get:

$$\frac{\partial T}{\partial r} = \frac{-3\kappa\rho L_{\gamma}}{16\pi acT^3r^2\sqrt{1-\frac{2Gm}{rc^2}}} \tag{2.42}$$

Combining the two simplified equations (2.40) and (2.42) we get

$$\frac{\partial P}{\partial T} = \frac{16\pi GacmT^3}{3\kappa L_{\gamma}\sqrt{1-\frac{2Gm}{rc^2}}}. \tag{2.43}$$

We can now integrate Eq. (2.43) from the zero boundary condition ($P = 0$ and $T = 0$) assuming that the opacity remains constant in the photosphere and that the release of nuclear energy is zero, thus the luminosity will be constant.

$$\int_0^{P_{surf}} dP = \int_0^{T_{surf}} \frac{4\pi Gacm}{3\kappa L_{\gamma}\sqrt{1-\frac{2Gm}{rc^2}}} dT^4 \tag{2.44}$$

and thus

$$P_{surf} = \frac{4\pi GacmT_{surf}^4}{3\kappa L_{\gamma}\sqrt{1-\frac{2Gm}{rc^2}}}. \tag{2.45}$$

The surface pressure is a hard outer boundary and therefore the equation above can be discretized as

$$P_{surf} = \frac{4\pi Gacm_{nq}T_{nq}^4}{3\kappa_{nq}L_{\gamma,nq-1}\sqrt{1-\frac{2Gm_{nq}}{r_{nq}c^2}}}, \tag{2.46}$$

where we have to use $L_{\gamma,nq-1}$ because $L_{\gamma,nq}$ is not defined and consequently $L_{\gamma,nq} = L_{\gamma,nq-1}$. With the assumption of radiative zero condition, one can not reach peak luminosities at the Eddington limit, which could be reached, but violates the assumption itself.

2.3 Mixing

The convective mixing, which is a multi-dimensional phenomenon and therefore not occuring in one dimensional simulations, has to be included in an effective way to account for composition mixing in the surface layers of a neutron star. Heat transport via convection is already calculated during a hydrodynamics timestep. The convective mixing of the composition is here approximated using Böhm-Vitense's stellar adaption of Prandtl's mixing length theory [131], including the Schwarzschild-Ledoux (Eq. (2.29)) instability criteria as in [127]. The convective mixing is described by

$$\frac{\partial \Gamma X_i}{\partial t} = \frac{\partial}{\partial a}\left(4\pi r^2 \rho \alpha \Gamma \left(4\pi r^2 \rho D \frac{\partial}{\alpha \partial a}(a X_i)\right)\right), \tag{2.47}$$

which is a relativistic version of the Lagrangian time dependent diffusion equation [132], where D is the diffusion constant, defined as $D = \bar{v}\Lambda/3$. In the surface zones of an accreting neutron star, the turnover timescale $\tau \sim \Lambda/\bar{v}$ is much shorter than the nuclear timescale and, thus, convective mixing plays a major role in these zones.

2.4 Advection

After the hydrodynamical calculation, where the adaptive grid properly handles the advection of all variables based on motion of a, the grid variable, one has to apply a corresponding advection for the composition before one time step is finished. After all, the ignition of a X-ray burst and, even more, the ignition of a superburst depends strongly on the composition in the region of the ignition depth. Our model uses a conservative second order formulation for calculating the flux of the isotopes at the edges of the zones based on an upwind total variation dimishing scheme, which is based on a Van Leer limiter.

3 Numerical Simulations

"To boldly go where no man has gone before."

— Gene Roddenberry
Star Trek

In this section we present the results of our X-ray burst study. First, we will present in Section 3.1 our choice of boundary conditions and how the initialization is done. Then in Section 3.2, we will present an enlarged network and how we chose the included isotopes.
We work in this thesis with a large number of grid zones, exactly 218[1], which include not only the column density range of the ignition of X-ray bursts ($y = 10^8$g cm^{-2}), but also the theoretically estimated column density of the ignition of a superburst ($y = 10^{11} - 10^{12}$g cm^{-2}) to see if the produced ^{12}C survives until it reaches those densities and if we can produce the needed amount of carbon (as already mentioned in Section 1.2.6 the mass fraction of ^{12}C should be bigger than 0.1).
We provide in this section a large parameter space study, varying the accretion rate, and the crustal heating for two different compositions of accreted matter. We choose the range for the accretion rate such that it covers the values around $0.1\dot{M}_{Edd}$. The range of the crustal heating was chosen to cover theoretically expected values. We choose to vary the composition because some of the detected superbursts are observed in ultra compact X-ray binaries (e.g. 4U 0614+91 [133] or 4U 1820-30 [57]). Ultra compact X-ray binaries are characterised by a very low orbital period, where the donor is a compact object with no hydrogen envelope. Thus one has to consider the change of the composition of the accreted matter towards hydrogen-poor and helium-rich, to study superburst ignition in those binary systems. For both compositions we found three different burning regimes in the parameter space, which are discussed in Section 3.3 for solar abundances and in Section 3.4 for helium-rich abundances.
In Section 3.6 we will present a concept to speed up the calculations of one parameter set, to accelerate the possible ignition of a superburst.
We will show in the last section of this chapter a short comparison with observations.

[1] In the thesis of J.Fisker [21] the calculations were made with 129 grid zones and also in most calculations of S.Fehlmann's thesis [25].

3.1 Initial Model

Our computational domain consists of $5.2 \cdot 10^{25}$ g within a thickness of $8.5 \cdot 10^{3}$ cm. As a fixed inner boundary condition, we consider an underlying neutron star with a mass of $1.41 M_{\odot}$ and a radius of $1.12 \cdot 10^{6}$ cm. The surface pressure as an outer boundary condition is chosen to be $5 \cdot 10^{18}$ erg cm^{-3}. For the mixing length we choose 1 cm. We constantly accrete matter at the surface with accretion rates between $0.1 - 1.5 \cdot 10^{17}$ g s^{-1} as observed from infinity, which corresponds to an Eddington accretion rate of $\sim 0.01 - 0.12 \dot{M}_{Edd}$. If we compare our range of accretion rates with those from observations of superbursting sources in Tab. (1.2) we cover nearly half of them. The local accretion rate, $\dot{M}^{0}_{acc}$, and the one seen from infinity, $\dot{M}^{\infty}_{acc}$, are connected to each other by the redshift

$$\dot{M}^{0}_{acc} = (1+z)\dot{M}^{\infty}_{acc}, \tag{3.1}$$

where $(1+z)$ is the redshift and defined by

$$(1+z) = \frac{1}{\sqrt{1 - \frac{2GM}{Rc^2}}}. \tag{3.2}$$

Here, M is the mass of the neutron star added to the mass of our computational domain, and likewise is R the combined radius of the neutron star with the domain. Another fixed inner boundary condition is the heat source coming from the crust, Q_b. This heat source is thought to come from pycnonuclear reactions, neutrino cooling, and heat transport from the crust. It enters our calculations as a crust luminosity, seen from infinity, L_{crust}, which is linked to the crustal heating as

$$L_{crust} = \frac{Q_b}{m_u}\dot{M}_{acc}c^2, \tag{3.3}$$

where Q_b is the crustal heating in units of MeV per accreted nucleon, and m_u is the atomic mass unit. Due to the enhancement of the number of grid zones and, more important, the enhancement of the mass contained in our computational domain, we have to shift the crustal heating used with the smaller amount of grid zones. This shift has to be done in the following way

$$Q_b^{SB} = Q_b^{XRB} + \Delta Q_b, \tag{3.4}$$

where Q_b^{SB} denotes for the crustal heating we use in the simulations presented in this thesis (later it will only be called Q_b), Q_b^{XRB} stands for the crustal heating which was used in former works with previous versions of this code (see results in [25]), and ΔQ_b is the shift of the crustal heating. This is essential in the beginning of this work to compare results with those presented in [25]. Comparisons in [25] have shown, that ΔQ_b is in the range of ~ -0.5 MeV/nuc.

Furthermore, we can choose the composition of the accreted matter. Fujimoto et al. [134] observed a strong dependence of the burst behaviour on the abundance of hot CNO-elements. For the first part of our simulations, we consider solar abundances from Anders & Grevesse [135]. The reason for this is, that most X-ray bursting neutron stars accrete matter from an unevolved star [136]. The second part is done with a helium-rich composition, since the companion star in high compact X-ray binaries has lost parts of his hydrogen shell during the evolution of the binary system.

Starting our simulations, the initial composition in our domain is artificially set to only ^{54}Fe (see top box in Fig. (3.1)). Instead of accreting at the beginning onto this iron-atmosphere for each run, the composition is shifted towards the inner boundary (as shown in the lower part of Fig. (3.1)), but not so far that it influences the region where a superburst ignites. This shift shortens the runtime because, we do not have to wait until the accreted matter reaches the depth of the first X-ray burst, but start with the first X-ray burst ignition in reasonable time. This also makes sure that the simulation of the X-ray bursts are independent of the initial conditions.

In the beginning of our work we were able to simulate ~ 8 bursts a day. Now we are capable of simulating $\sim 30 - 40$ bursts a day. This number is dependent on the recurrence time of the bursts and can therefore vary. Furthermore, the simulation-times are also dependent on the accretion composition. We find, that with solar abundance we can simulate a factor $\frac{3}{2}$ longer simulation-times than with helium-rich abundances.

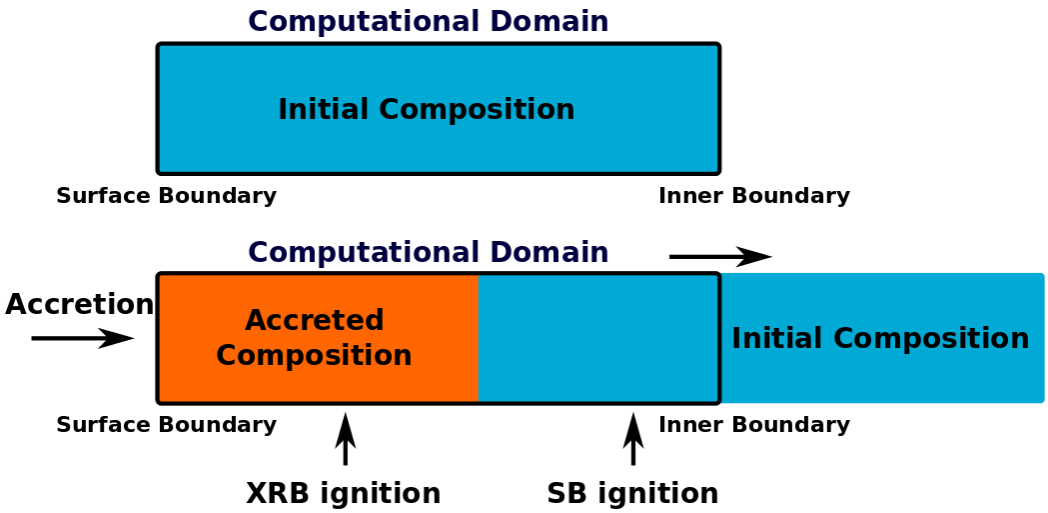

Fig. 3.1.: The initial progenitor file consists artificially only of ^{54}Fe. The code initially shifts the initial composition out of our computational domain and replaces it with the accreted composition until it reaches a depth, where only the ashes of Type I X-ray bursts (XRBs) are present. The two arrows show the region of the roughly estimated depth of the ignition of X-ray bursts and superbursts (SBs).

3.2 Enlarged Network

We provided an enlarged network for comparison of the full network and the slightly smaller one already used by J.Fisker in his thesis in 2006 [21]. The original 304-isotopes network includes all the nuclei which are produced in the main processes during and between bursts, such as the hot CNO-cycle nuclei, the αp-process, and the rp-process. Furthermore, it contains the fuels which drive those processes (see the orange boxes in Fig. (3.48)). We enlarged the network to include (1) all the nuclei down to the valley of instability and (2) up until they become either p-decay unstable or α-decay unstable. The reason for (1) was to include also the nuclei, which are produced through β^+-decay of the heavy proton-rich rp-process nuclei close to the proton drip-line. The reason for (2) was to include the nuclei, which are favourable p-decay or α-decay unstable, to check if they could be produced during a burst and then would liberate an α-particle or a proton. The result was a larger network, which consists of 561 isotopes (see Tab. (3.1), where all the used isotopes are listed).

To compare the impact of using two different networks, the recurrence time, the peak luminosity, the minimal luminosity, and the burst duration are taken into account for two different accretion rates (once with $0.1\dot{M}_{Edd}$ and once $0.025\dot{M}_{Edd}$). The reason for this choice is that those quantities depend either strongly on the conditions at

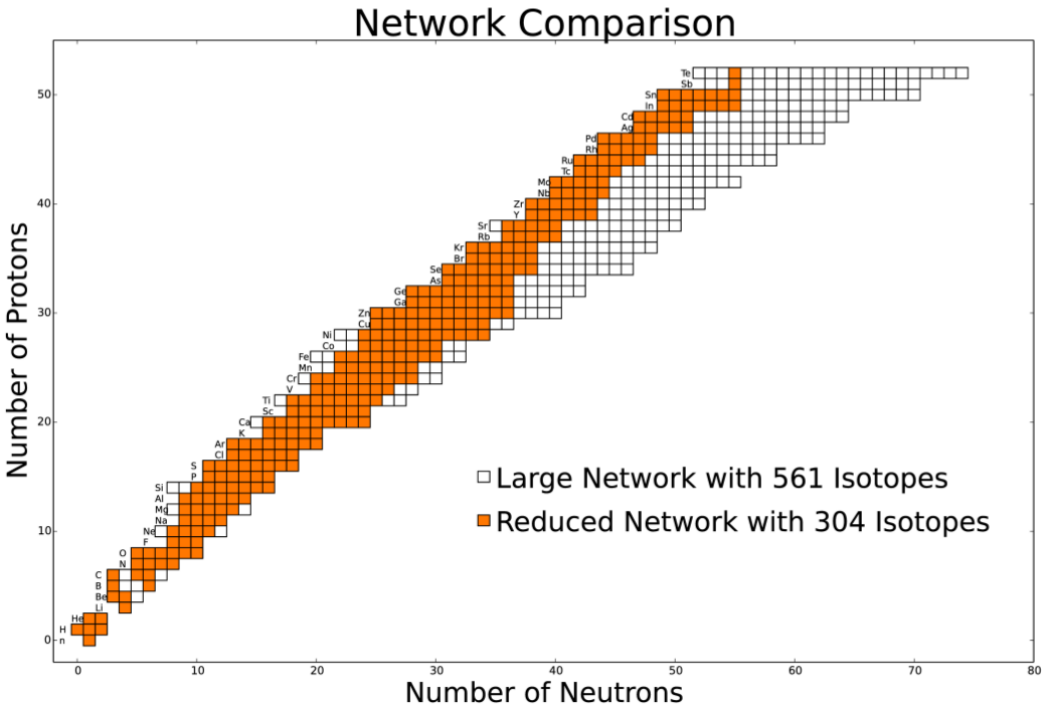

Fig. 3.2.: A comparison in nuclear chart form of the network with 561 isotopes (orange boxes plus the white boxes) and the network with 304 isotopes (orange boxes). Taken from [25].

the ignition depth, such as heat transport and thus temperature, or can indicate how much hydrogen and helium is burned during a burst or during the quiescent phase. The results of the comparison between those two different networks in case of both accretion rates show no larger deviation than a few percent [25], and therefore, we can safely rely on the smaller network. For a self-consistent superburst simulation, the larger network could be important. Since half of the energy released during this extreme event is thought to be provided from a photodisintegration runaway of heavy nuclei made during prior rp-process burning of hydrogen and helium [122]. Though, the main reason for taking the smaller network is, that the reaction network is the slowest part of this code and, therefore, a larger network would be the decisive factor, considerably slowing down the simulations. In the following, our results are based on simulations with the smaller network.

Element	Z	A	Element	Z	A
n	0	1	Co	27	50-59
H	1	1-3	Ni	28	50-62
He	2	3-4	Cu	29	55-65
Li	3	7	Zn	30	55-70
Be	4	7-9	Ga	31	60-71
B	5	8, 10, 11	Ge	32	60-74
C	6	9-13	As	33	64-75
N	7	12-15	Se	34	65-80
O	8	13-18	Br	35	70-81
F	9	17-19	Kr	36	69-84
Ne	10	17-22	Rb	37	74-85
Na	11	20-23	Sr	38	73-88
Mg	12	20-26	Y	39	77-89
Al	13	22-27	Zr	40	78-92
Si	14	22-30	Nb	41	81-93
P	15	26-31	Mo	42	82-97
S	16	27-34	Tc	43	85-97
Cl	17	31-35	Ru	44	86-102
Ar	18	31-38	Rh	45	89-103
K	19	35-39	Pd	46	90-108
Ca	20	35-44	Ag	47	94-109
Sc	21	40-45	Cd	48	95-112
Ti	22	39-49	In	49	98-113
V	23	43-51	Sn	50	99-120
Cr	24	43-54	Sb	51	104-121
Mn	25	46-55	Te	52	104-126
Fe	26	46-58			

Tab. 3.1.: This table lists all the isotopes of the enlarged – 561 isotopes – network.

3.3 Three Burning Regimes with Solar Abundances as Accretion Composition

In this section, we discuss the results of our simulations with solar abundances. In Tab. (3.2) we show how the mass fractions for hydrogen, helium, and the metals are distributed. We varied the accretion rate in the range of $0.1 - 1.5 \cdot 10^{17}$g s^{-1} (i.e. $\sim 0.008 - 0.12 \dot{M}_{Edd}$) in steps of $0.1 \cdot 10^{17}$g s^{-1}, and the crustal heating Q_b in the range of $0.1 - 1.5$ MeV nuc^{-1}, in steps of 0.1 MeV nuc^{-1}. This range of crustal heating is taken from literature [7, 101, 102]. In total, we cover the parameter space with 225 individual simulations for Q_b and $\dot{M}_{acc}$ as shown in Fig. (3.3), where each dot represents one set of chosen parameters.

Model	X(H)	X(^{4}He)	X(Z)
solar abundances	0.706	0.275	0.019

Tab. 3.2.: The hydrogen and helium mass fractions, and the remaining mass fraction of all metals, that we included in our solar abundances simulations.

We want to make a parameter space exploration finding possible parameter sets which could be used for self-consistent superburst simulations. We find three different burning regimes in the results of our numerical simulations. Fig. 3.3 shows these three burning regimes: red dots correspond to runs leading to stable burning, the turquoise dots indicate irregular bursts, and the violet dots regular burst behaviour. Only simulations that show at least two bursts were classified into the regular and the irregular burst regime. If results show none or one burst, we classify them as belonging to the stable burning regime. We simulate at least $\sim 10^6$ seconds simulation time to be sure that no burst was found in our results. In the next three subsections, we will discuss these three regimes in more detail.

We can see that smaller accretion rates ($\dot{M}_{acc} \leq 0.7 \cdot 10^{17}$g s^{-1}) lead to stable burning. With intermediate accretion rates ($0.8 - 1.0 \cdot 10^{17}$g s^{-1}) and high values for Q_b ($\gtrsim 1.1$ MeV nuc^{-1}) we find irregular burst behaviour and with intermediate and low Q_b values ($\lesssim 1.1$ MeV nuc^{-1}), or large accretion rates ($\dot{M}_{acc} \geq 1.1 \cdot 10^{17}$g s^{-1}), we find regular burst behaviour. The additional crustal heating source at the base of our computational domain seems to influence the burning regimes only in the upper middle part of the parameter space. There it seems that with higher Q_b, the irregular burst regime spreads into higher accretion rates. The accretion rate around $0.7 \cdot 10^{17}$g s^{-1} seems to be a transition region between regular bursts and stable burning. We want to point out that this accretion rate leads to only one burst at the beginning of our calculations and is thus categorized as stable burning. The simulated light curve of the irregular burst regime undergo a phase of Type I X-ray bursts before they end up in stable burning.

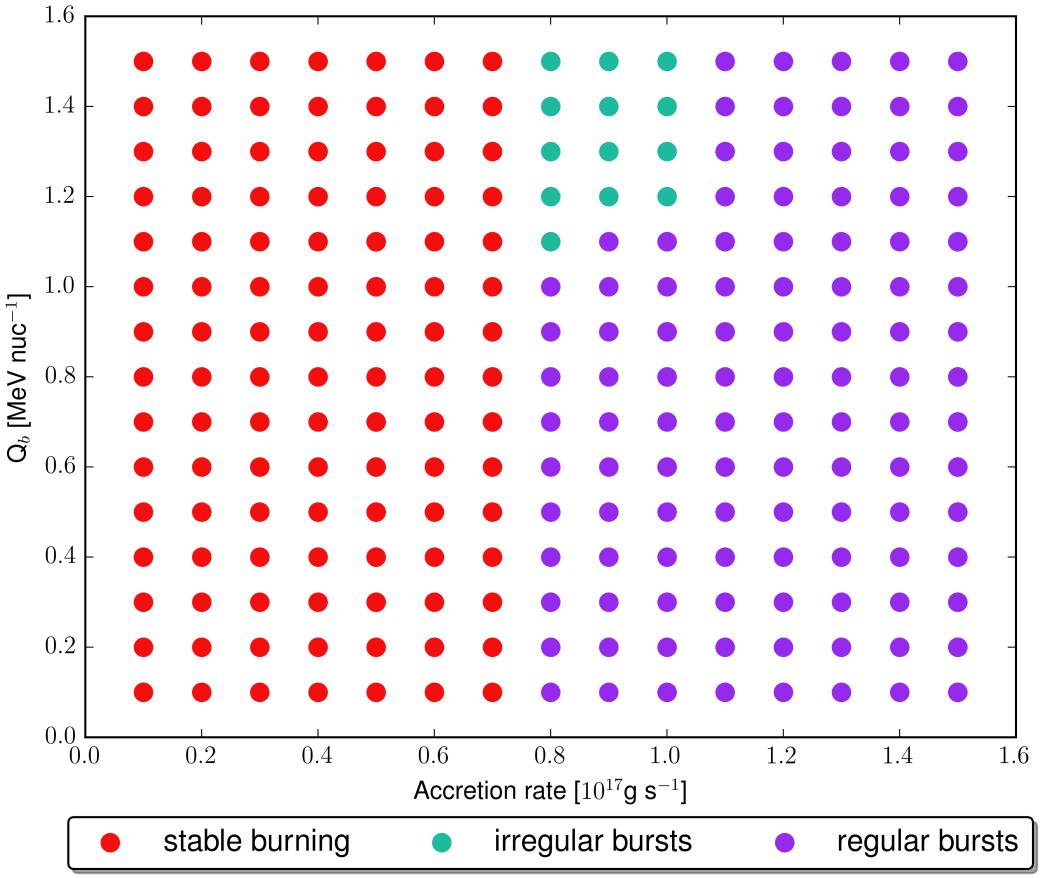

Fig. 3.3.: This plot shows the parameter space of our study with solar accretion composition, where Q_b is plotted against the accretion rate. It shows the three different burning regimes found in our work. The red dots are the parameter sets which lead to stable burning, the turquoise dots represent irregular bursts, and the violet ones regular burst behaviour. Note that for an accretion rate of $0.7 \cdot 10^{17}$g s^{-1} (for all shown values of Q_b) and for an accretion rate of $0.4 \cdot 10^{17}$g s^{-1} and Q_b of 0.8 MeV nuc^{-1}, a single burst occurs at the beginning of the run, but then shows stable burning. Those points were still categorized as stable burning.

3.3.1 Stable Burning Regime

For all numerical simulations with accretion rate conditions with $0.7 \cdot 10^{17}$g s^{-1} ($\approx 0.05\ \dot{M}_{Edd}$) and less, we get a regime of stable burning. Fig. (3.4) shows an example light curve of this burning regime.

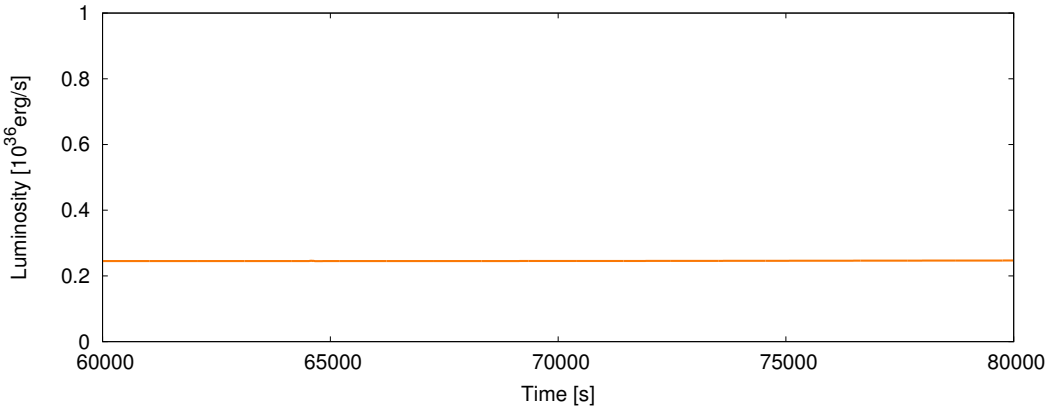

Fig. 3.4.: This is an example light curve from the simulation with $\dot{M}_{acc} = 0.2 \cdot 10^{17}$g s^{-1} and $Q_b = 1.2$ MeV nuc^{-1}.

Stable burning is assumed from the non-appearance of bursts at high accretion rates. The limit for that is $\sim 0.3\ \dot{M}_{Edd}$ [26, 42]. At those high accretion rates, the thermonuclear runaway is not triggered and hydrogen and helium are burned constantly in a steady state. Due to the stable burning, a large amount of carbon is produced and builds a carbon-rich layer underneath the burning region. Since a thermonuclear runaway of carbon fusion is thought to power a superburst and thus, carbon production of over 0.1 mass fraction is needed. This could be a possible scenario of producing enough carbon for ignition of a superburst.

In our simulations, stable burning also occurs, but in a regime with lower accretion rates (see red dots in Fig. (3.3)). The region for stable burning with high accretion rates is not in our parameter space, since we simulated only up to an accretion rate of $\sim 0.12\dot{M}_{Edd}$. Keek & Heger 2015 [137] found a new steady state regime of stable burning at low accretion rates with $\dot{m} = 0.02\dot{m}_{Edd}$ ($\approx 0.26 \cdot 10^{17}$ g s^{-1}) and crustal heating $Q_b = 0.75$ MeV u^{-1}, using the KEPLER code. This parameter set also lies in our parameter space in the regime of stable burning.

Fig. (3.5) shows the mass fractions for ^{1}H (red line), ^{4}He (green line), ^{12}C (blue line), ^{14}O (bright turquoise line), ^{15}O (orange line), and ^{16}O (black line) dependent on the column density for two different parameter sets. In the left plot, we show the results from the simulation with the parameters $\dot{M}_{acc} = 0.7 \cdot 10^{17}$g s^{-1} and $Q_b = 0.8$ MeV nuc^{-1}, and in the right plot the results from the simulation with the parameters $\dot{M}_{acc} = 0.2 \cdot 10^{17}$g s^{-1}, and $Q_b = 1.2$ MeV nuc^{-1} are presented. We see that in both

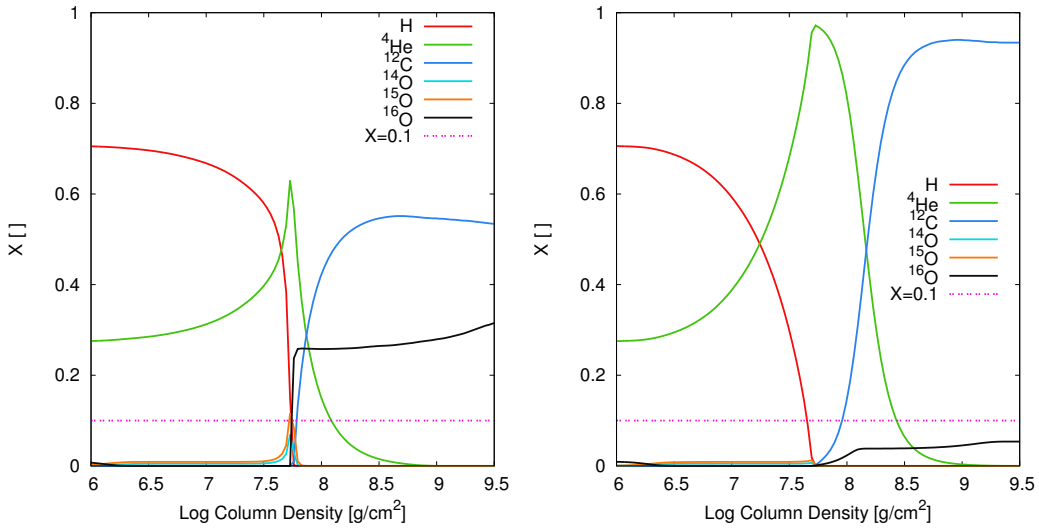

Fig. 3.5.: The mass fractions of hydrogen (red line), ^{4}He (green line), ^{12}C (blue line), ^{14}O (bright turquoise line), ^{15}O (orange line), ^{16}O (black line), and the minimal mass fraction of 0.1 (pink dashed line) which is needed for the successful ignition of a superburst.
a) shows the results from the simulation with an accretion rate of $0.7 \cdot 10^{17}$g s^{-1} and a crustal heating of 0.8 MeV nuc^{-1}.
b) shows the results for the run with an accretion rate of $0.2 \cdot 10^{17}$g s^{-1} and a crustal heating of 1.2 MeV nuc^{-1}.

cases, all hydrogen and all helium are consumed and a large amount of carbon is produced. This is the steady state burning of both hydrogen and helium because the stable burning of hydrogen heats up the sinking material and helium is burned in a stable way before it reaches the ignition conditions for a thermonuclear runaway. At these densities and temperatures, stable hydrogen burning happens through the hot CNO-cycle. The bottleneck reactions (meaning the slowest) of the hot CNO-cycle are the β^+-decays of the unstable oxygen isotopes, ^{14}O and ^{15}O, due to their considerable large half-lifes ($T_{1/2}(^{14}\text{O}) = 70.62$ s and $T_{1/2}(^{15}\text{O}) = 122.24$ s). Therefore, the combined mass fraction of the hot CNO-cycle particles is shifted to those isotopes during the hot CNO, which enters then the beta-limited equilibrium cycle. The produced α-particles from the hot CNO are converted into ^{12}C over the triple-alpha reaction. As long as hydrogen is not yet depleted, carbon isotopes capture quickly two protons to form ^{14}O. Those two processes, the triple-alpha reaction and the hot CNO-cycle, feed each other with new isotopes. This leads to an increase of ^{14}O and ^{15}O, as we can see in the middle of Fig. (3.5a), but not so intense in Fig. (3.5b).

To gain more insight in the differences between those two simulations, we take a closer look at the temperature profile and the burn rate in Fig. (3.6). The burn rate

is linked to the energy release E_{nuc} due to nuclear burning of a zone in the following way as

$$r_{burn} = \frac{E_{nuc}}{\Delta m c^2 \Delta t}, \tag{3.5}$$

where Δm is the mass of the zone, c is the speed of light, and Δt is the time step. Therefore, the burn rate gives an indication of how active a zone is in terms of nuclear energy production. In Fig. (3.6a), we see that the burn rate (black line) has one peak, which implies that the triple-alpha reaction indeed feeds the hot CNO-cycle in the same zone. Thus, in this case, we have mixed hydrogen- and helium-burning in a stable way. With higher temperatures (red line), the produced ^{12}C can capture an α-particle and produce the stable isotope ^{16}O[2]. Due to the higher temperature profile this is more probable in the case of Fig. (3.5a) than in case of Fig. (3.5b). In Fig. (3.6b), the stable hydrogen-burning produces a huge amount of helium (first peak in the burn rate), which sinks in regions with higher column density, where it is heated by the hydrogen-burning and undergoes stable burning (second peak in the burn rate), where it produces nearly purely carbon ashes, with a

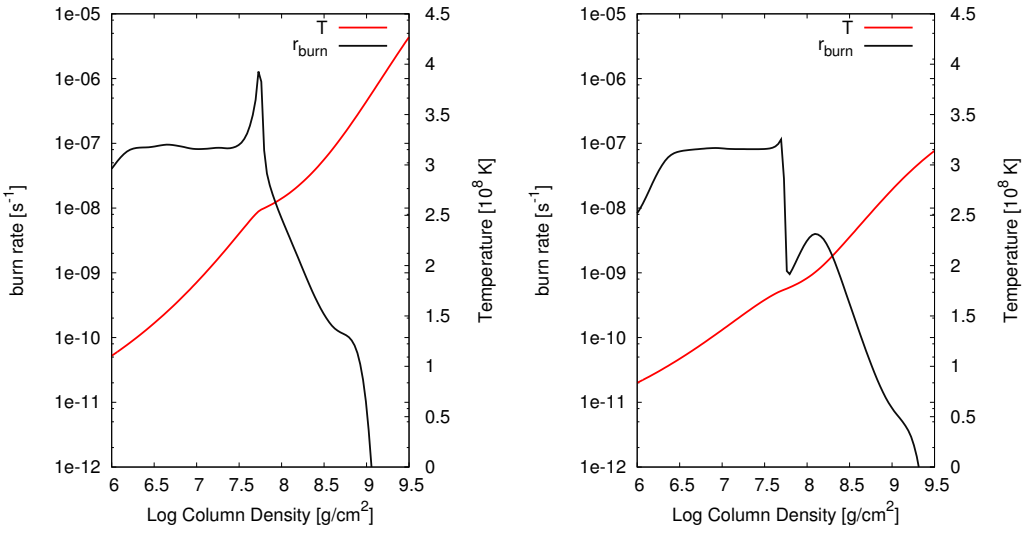

Fig. 3.6.: These two plots show the burn rate and the temperature of the regions where stable burning occurs.
a) shows the results from the simulation with an accretion rate of $0.7 \cdot 10^{17}$g s^{-1} and a crustal heating of 0.8 MeV nuc^{-1}.
b) shows the results for the run with an accretion rate of $0.2 \cdot 10^{17}$g s^{-1} and a crustal heating of 1.2 MeV nuc^{-1}.

[2]The reaction rate of ^{12}C$(\alpha, \gamma)^{16}$O is one of the most important, yet uncertain reaction rates, because its cross section is small and, at the energies needed for astrophysical use, not measurable and complicated to calculate, because of interferences of resonances.

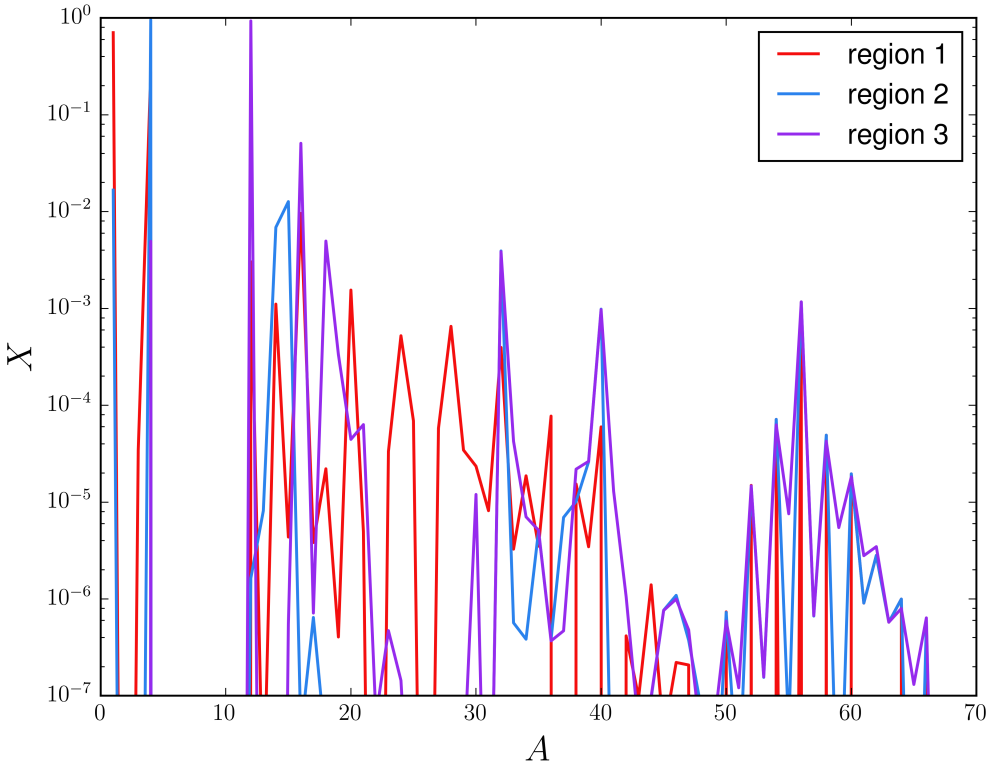

Fig. 3.7.: The composition of three different regions of the results from the simulation with $Q_b = 1.2$ MeV nuc^{-1} and $\dot{M}_{acc} = 0.2 \cdot 10^{17}$ g s^{-1}. The red line, region one, is one of the outermost zones in our domain. Region two, the blue line, is the zone with the highest burn rate at a column density of $4.9 \cdot 10^{7}$ g cm^{-2} ($\log(y) \approx 7.7$). The violet line, region three, represents one of the zones below the stable burning, where a maximum of ^{12}C is reached at a column density of $8.4 \cdot 10^{8}$ g cm^{-2} ($\log(y) \approx 8.9$).

small amount of ^{16}O.

In Fig. (3.7) we consider the entire composition of three different regions: Region 1 (red line) is one of our outermost zones and illustrates the initial composition of the accreted matter. Region 2 (blue line) is the zone with the highest burn rate at a column density of $4.9 \cdot 10^{7}$ g cm^{-2} ($\log(y) \approx 7.7$). Region 3 (violet line) is one of the zones below the burning regimes, where ^{12}C already reached its maximum at a column density of $8.4 \cdot 10^{8}$ g cm^{-2} ($\log(y) \approx 8.9$).

Besides the above mentioned changes in the mass fraction of hydrogen, helium, carbon and various oxygen isotopes, it can be seen in Fig. (3.7), that also other changes of the composition happen, mainly in the region $20 \lesssim$ A $\lesssim 30$, and around the iron peak. All isotopes with mass numbers between 20 and 30 have been destroyed during stable hydrogen-burning. One possibility is that they underwent a series of (p, γ) and β^{+} decays up to heavier isotopes around the iron-peak. The

absence of ^{15}O and ^{14}O in the region where hydrogen burns (see Fig. (3.5b)) confirms this assumption.

We now want to find out whether the change of the accretion rate or the change of the crustal heating has a stronger influence on the profile of the burn rate. If we vary the Q_b values from $0.1 - 1.5$ MeV nuc^{-1} while keeping the accretion rate fixed, the burn rate shows hardly any changes (see Fig. (3.8a)). However, if we change the accretion rate for a fixed Q_b value, we see a huge difference in the burn rate, which is shown in Fig. (3.8c). We see that only for accretion rates of 0.1 and $0.2 \cdot 10^{17}$g s^{-1}, we find two strictly separated regions for stable burning of hydrogen and helium that enables the production of a huge amount of ^{12}C. In contrast, at higher accretion rates, those two burning regions merge to one region, where mixed hydrogen- and helium burning occurs and carbon production becomes less efficient. In Fig. (3.8d), we see that with increasing accretion rate, also the temperature profile changes and goes towards higher values.

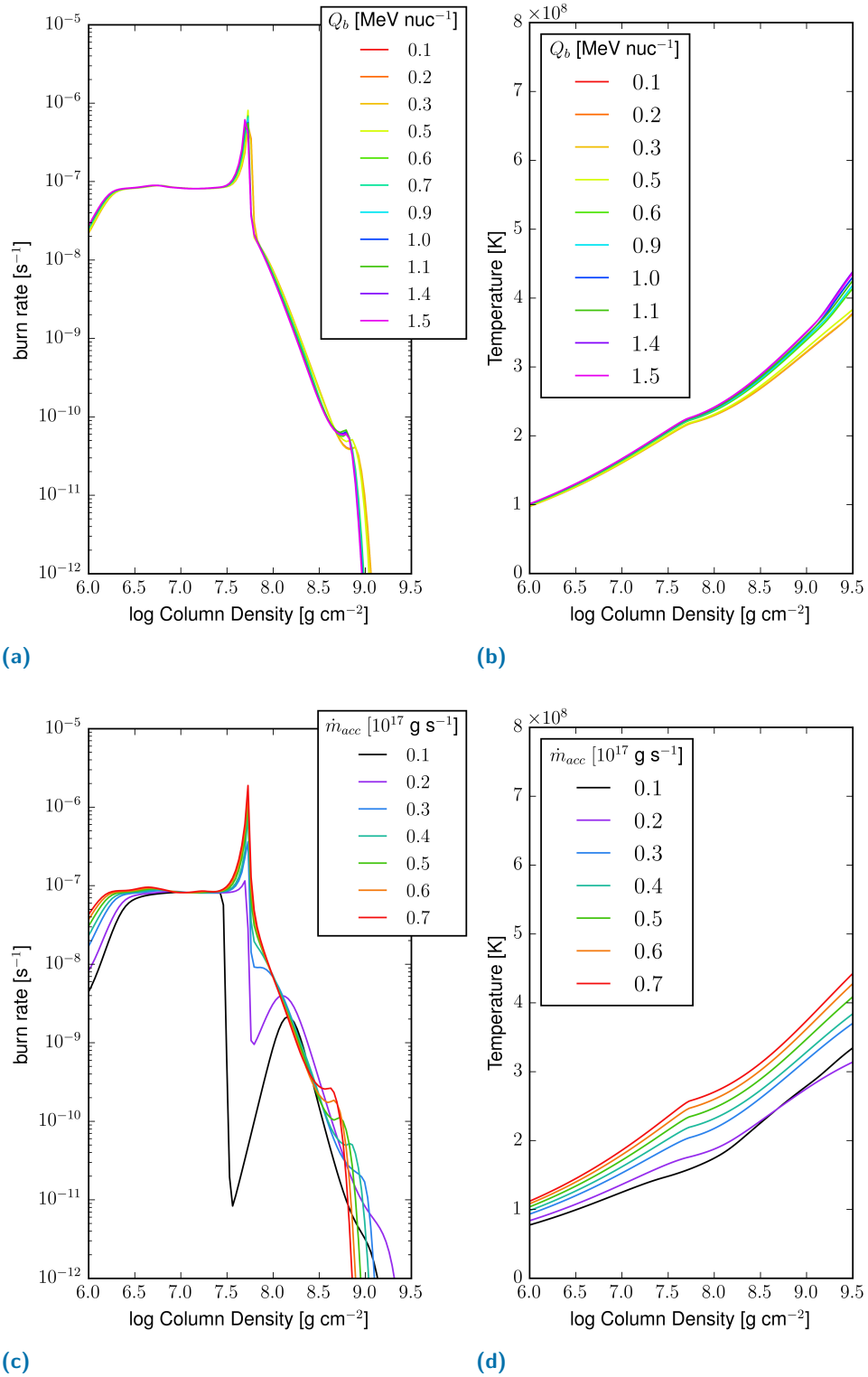

Fig. 3.8.: Figures a) and b) show the burn rate and the temperature for runs with fixed accretion rate of $0.4 \cdot 10^{17}$g s^{-1}, but with different crustal heat of $0.1 - 1.5$ MeV nuc^{-1}, see legend for color code.
Figures c) and d) show the burn rate and the temperature for runs with fixed crustal heating of 1.2 MeV nuc^{-1}, but with different accretion rates of $0.1 - 0.7 \cdot 10^{17}$g s^{-1}, see legend for color code.
a) and c) show the burn rate and the logarithm of the column density. We see that the accretion rate has a bigger influence on the burn rate than the crustal heat.
b) and d) show the temperature and the logarithm of the column density. We see that the accretion rate has a bigger influence on the temperature than the crustal heat.

3.3.2 Irregular Bursts Regime

In our numerical simulations with accretion rate conditions between $0.8 \cdot 10^{17}$ g s^{-1} and $1.0 \cdot 10^{17}$ g s^{-1} and high Q_b values, in the range of 1.1 MeV nuc^{-1} until 1.5 MeV nuc^{-1}, we find an irregular burst regime (see turquoise dots in Fig. (3.3)). This means that the results from the simulations show first burst behaviour in an irregular fashion and then "fall" into a stable burning phase without any further bursts.

For convenience, we label our simulations as follows:

$$x\, yyQ\, zza, \tag{3.6}$$

where x denotes the composition of the accreted material, e.g. s corresponds to solar abundances, yyQ denotes the values for Q_b, e.g. 11Q represents $Q_b = 1.1$ MeV nuc^{-1}, zza denotes the values for the accretion rate, e.g. 08a represents $\dot{M}_{acc} = 0.8 \cdot 10^{17}$ g s^{-1}.

In Fig. (3.9), we show two examples of light curves of this regime. Both of these plots are obtained from simulations with the same accretion rate, namely $\dot{M}_{acc} = 0.9 \cdot 10^{17}$g s^{-1}. We show the light curve of a simulation with crustal heating of 1.2 MeV nuc^{-1} in Fig. (3.9a), while the crustal heating is 1.4 MeV nuc^{-1} in Fig. (3.9b). We can see that for the same accretion rate, but with higher Q_b-values, the number of bursts gets smaller and the sequence of bursts shorter. In the two tables, Tab. (3.3) and (3.4), some properties of the irregular burst regime are listed. The first column in both table contains the identification name of the simulation, which describes the accretion rate and the crustal heat. The case of $Q_b = 1.1$ MeV nuc^{-1} and $\dot{M}_{acc} = 0.8 \cdot 10^{17}$ g s^{-1} is an exception from the behaviour of the values in dependency on the chosen parameter set. In the following section, we describe the general behaviour of all other simulations.

The averaged values of observational properties in Tab. (3.3) have been calculated with the `KEPLER analyser` (written by N. Lampe, private communications with L. Keek). This table shows that with increasing Q_b values, the number of bursts N$_{burst}$ (second column) decreases, since Q_b influences the ignition depth in a decreasing fashion, as shown in [25]. With increasing accretion rate, more fuel for bursts is provided in shorter time and thus the number of bursts increases. The peak luminosity in the third column (L$_{peak}$), averaged over the burst number[3], shows an decrease for increasing accretion rate, while the crustal heating does not seem to make a difference. The recurrence time in the fourth column (t_{rec} in hours), decreases also with increasing accretion rate. The recurrence time is determined

[3] In cases of more than 100 bursts, the average is over the first 100 bursts

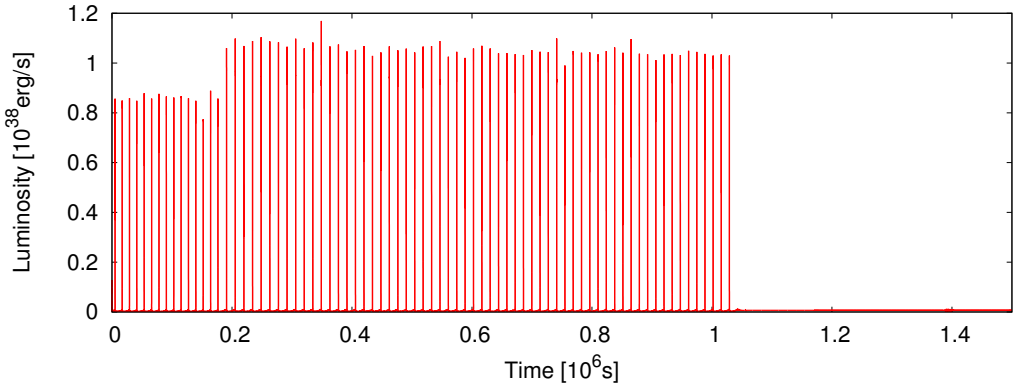

(a)

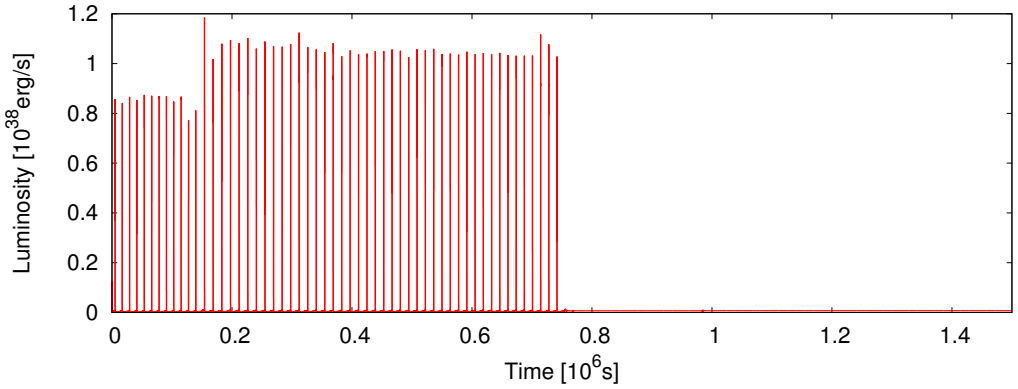

(b)

Fig. 3.9.: The simulated light curve from two runs, both with accretion rate of $0.9 \cdot 10^{17}$g s^{-1}.
a) corresponds to a crustal heating value of 1.2 MeV nuc^{-1}.
b) corresponds to a crustal heating value of 1.4 MeV nuc^{-1}.

by the time the system needs to accumulate enough fuel in the ignition region, this time is also called t_{fuel}, and is given by

$$t_{fuel} = \frac{4\pi R^2 y_{ignition}}{\dot{M}_{acc}}, \tag{3.7}$$

where R is the radius of the ignition zone and $y_{ignition}$ is the column density of the ignition zone. Thus, increasing the accretion rate leads to a faster refill of the fuel, and the burst can occur earlier. The given t_{rise} is defined here as the time it takes for the luminosity to rise from 10% up to 90% of the peak luminosity. The burst time increases with increasing accretion rate. The interplay of trends in burst time, recurrence time, and peak luminosity influences the α-parameter – see Eq. (1.3) – in a decreasing manner (last column).

run	N_{burst}	L_{peak} [erg s^{-1}]	t_{rec} [h]	t_{rise} [s]	t_{decay} [s]	α-value
s11Q08a	27	$1.17 \cdot 10^{38}$	4.49	2.16	74.0	132.1
s12Q08a	35	$1.16 \cdot 10^{38}$	4.47	2.23	72.6	132.4
s12Q09a	80	$1.01 \cdot 10^{38}$	3.60	2.65	78.9	124.1
s12Q10a	133	$8.46 \cdot 10^{37}$	3.01	3.63	88.2	111.7
s13Q08a	30	$1.15 \cdot 10^{38}$	4.47	2.25	71.4	138.9
s13Q09a	62	$1.05 \cdot 10^{38}$	3.88	2.47	78.2	126.8
s13Q10a	121	$8.63 \cdot 10^{37}$	3.06	3.51	88.3	111.6
s14Q08a	25	$1.17 \cdot 10^{38}$	4.47	2.19	69.9	138.0
s14Q09a	55	$1.02 \cdot 10^{38}$	3.80	2.67	81.0	122.8
s14Q10a	94	$8.74 \cdot 10^{37}$	3.09	3.37	86.4	114.1
s15Q08a	25	$1.15 \cdot 10^{38}$	4.46	2.31	71.2	137.4
s15Q09a	48	$9.94 \cdot 10^{37}$	3.75	2.81	79.7	123.6
s15Q10a	85	$8.52 \cdot 10^{37}$	3.03	3.37	88.7	111.0

Tab. 3.3.: The values in this table are averaged over all bursts. If a simulation shows more than 100 bursts, it is averaged over the first 100 bursts. The first column gives the simulation conditions. The first character, s, denotes accreted solar abundance, the next three digits represent the Q_b values, e.g. 11Q means $Q_b = 1.1$ MeV nuc^{-1}, the last three digits represent the accretion rate, e.g 08a means $0.8 \cdot 10^{17}$ g s^{-1}.

run	t_{trans} [h]	$L_{quiescent}$ [erg s^{-1}]	L_{stable} [erg s^{-1}]	$y_{ignition}$ [10^7 g cm^{-2}]	$y_{stableburning}$ [10^7 g cm^{-2}]
s11Q08a	123.7	$3.73 \cdot 10^{35}$	$6.22 \cdot 10^{35}$	5.3374	5.3408
s12Q08a	158.7	$3.68 \cdot 10^{35}$	$5.79 \cdot 10^{35}$	5.7636	5.3406
s12Q09a	289.6	$4.13 \cdot 10^{35}$	$6.70 \cdot 10^{35}$	5.7637	5.3401
s12Q10a	409.0	$4.31 \cdot 10^{35}$	$7.58 \cdot 10^{35}$	5.3375	5.3404
s13Q08a	136.3	$3.72 \cdot 10^{35}$	$6.21 \cdot 10^{35}$	5.7636	5.3404
s13Q09a	241.1	$4.01 \cdot 10^{35}$	$6.87 \cdot 10^{35}$	5.7637	5.3402
s13Q10a	378.7	$4.97 \cdot 10^{35}$	$7.58 \cdot 10^{35}$	5.7638	5.3399
s14Q08a	114.0	$3.50 \cdot 10^{35}$	$6.30 \cdot 10^{35}$	5.7636	5.3407
s14Q09a	209.8	$4.06 \cdot 10^{35}$	$6.62 \cdot 10^{35}$	5.7637	5.3402
s14Q10a	291.8	$4.59 \cdot 10^{35}$	$7.43 \cdot 10^{35}$	5.7639	5.3403
s15Q08a	113.7	$3.50 \cdot 10^{35}$	$5.76 \cdot 10^{35}$	5.7636	5.3407
s15Q09a	181.0	$4.41 \cdot 10^{35}$	$6.60 \cdot 10^{35}$	5.7637	5.3406
s15Q10a	258.7	$4.60 \cdot 10^{35}$	$7.55 \cdot 10^{35}$	5.7638	5.3406

Tab. 3.4.: Values of the transition from the bursting phase to stable burning. After the last burst, all runs show a "trying" ignition of a further burst which fails. We take this failed ignition as the time of transition t_{trans} between bursts and show it in the second column. The next two columns show the quiescent luminosity between two bursts and the luminosity of the stable burning after the transition. The second column, $y_{ignition}$, gives the ignition depth of one of the last bursts, the third column, $y_{stableburning}$, gives the column density of the stable burning, where the burn rate is the highest.

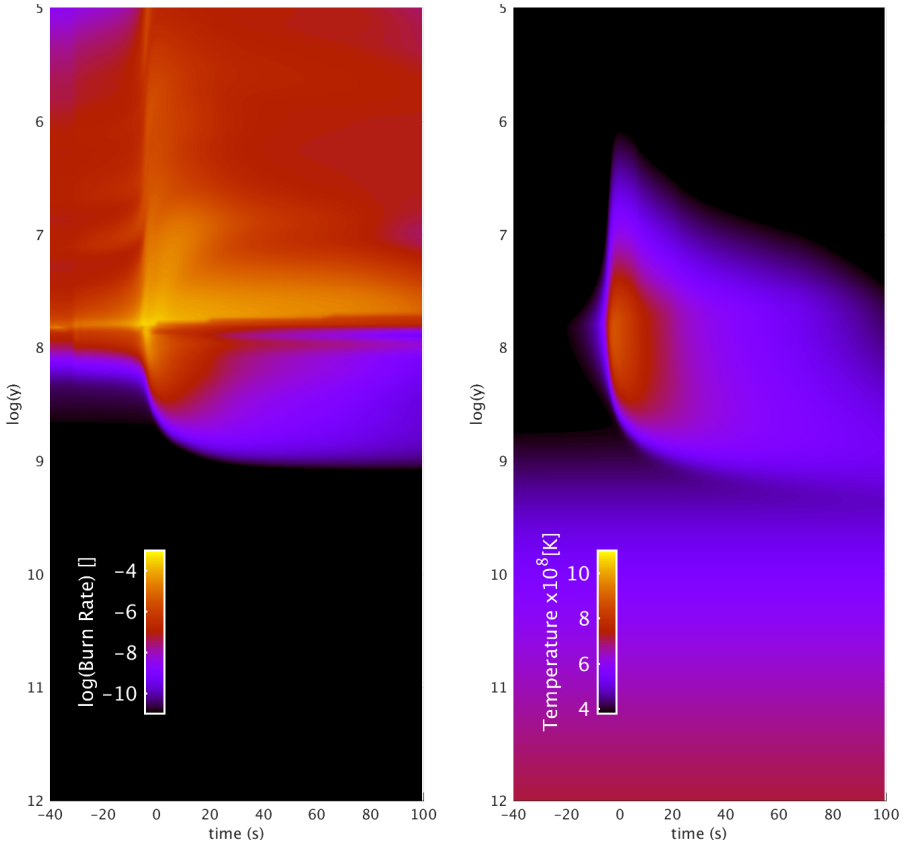

(a)

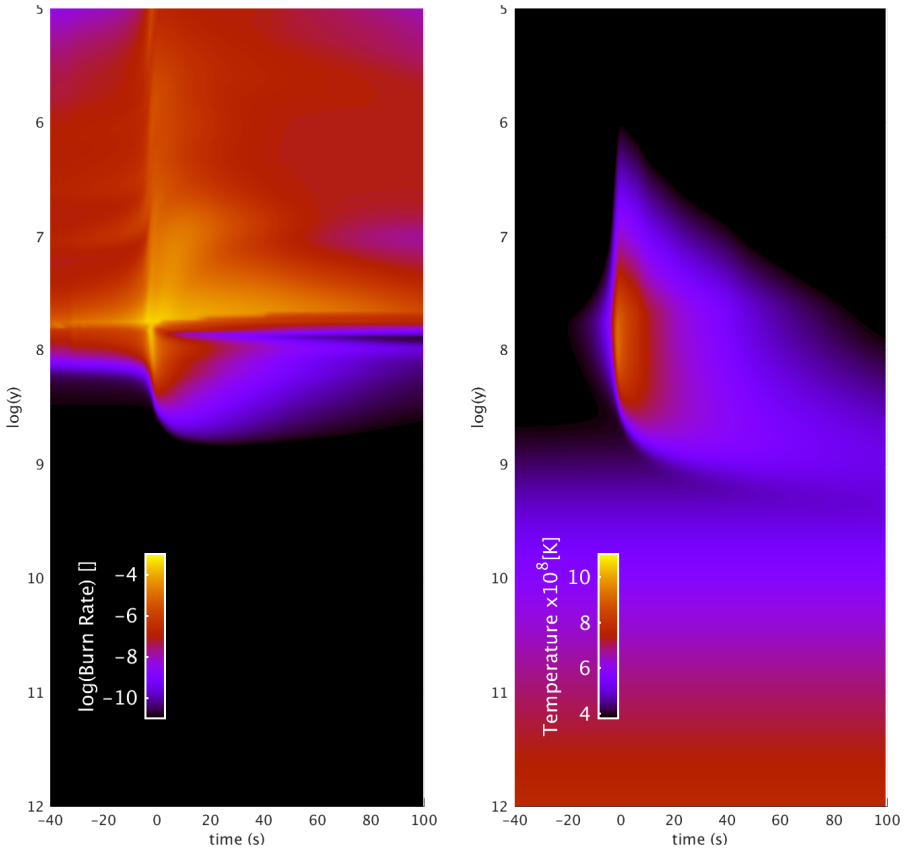

(b)

Fig. 3.10.: These four figures show the burn rate over one burst (left column) and the temperature over one burst (right column). Here the simulation of $Q_b = 1.2$ MeV nuc^{-1} and $\dot{M}_{acc} = 0.9 \cdot 10^{17}$g s^{-1} are shown. L_{peak} is chosen to be at $t = 0$ s. a) shows the results of the fifth burst. b) shows the results of the last burst.

Tab. (3.4) shows transition values from the change of the bursting phase to the stable burning phase. The second column shows the time t_{trans}, which marks the time of the transition from bursts to stable burning. This time is taken after the last burst, when a next burst seems to start, but fails to ignite. This transition time increases with increasing accretion rate and decreases with increasing crustal heating. The next two columns give the quiescent luminosity ($L_{quiescent}$) between bursts and the luminosity of the stable burning phase (L_{stable}). There, we see an increase from quiescent luminosity to the luminosity of the stable burning phase. The quiescent luminosity and the luminosity of stable burning are influenced by the accretion rate and increase with increasing accretion rate. In the last two column, we show the column density of the most active regions. The ignition depth of one of last the bursts is given by $y_{ignition}$. The column density of stable burning after the last burst is given by $y_{stableburning}$. If we compare early bursts with the last burst, we see that the last burst ignites at lower column density, at higher density (5th burst: $2.83 \cdot 10^5$g cm^{-3}, last burst: $3.09 \cdot 10^5$g cm^{-3}) and at higher temperatures (5th burst: $3.2 \cdot 10^8$ K, last burst: $3.4 \cdot 10^8$ K). This leads to more and more ineffective bursts, where the state of the matter behaving as a degenerate gas gets shorter. After the last burst, conditions for a thermonuclear runaway are not given anymore and stable burning occur. Additionally, when the ignition depth is shifted more and more into higher layers of the neutron star, the convection contributes a bigger part, since [25] showed that those layers are affected by convection. Fig. (3.10) shows in the two top plots, the time evolution of the burn rate (top left) and the temperature (top right) over the fifth burst of the simulation with crustal heating of 1.2 MeV nuc^{-1} and an accretion rate of $0.9 \cdot 10^{17}$ g s^{-1}. The two bottom plots show the same values for the last burst from the same simulation. If we compare the top with the bottom plots, we can see that the last burst does not induce nuclear reactions in the same extent as the fifth burst. The burn rate in the top plot stays longer at high values in the region above and below the burst. The layers above the ignition zone are not as long heated in the bottom plot than in the top plot. This shows, that the last burst is already less effective and a next burst can not ignite.

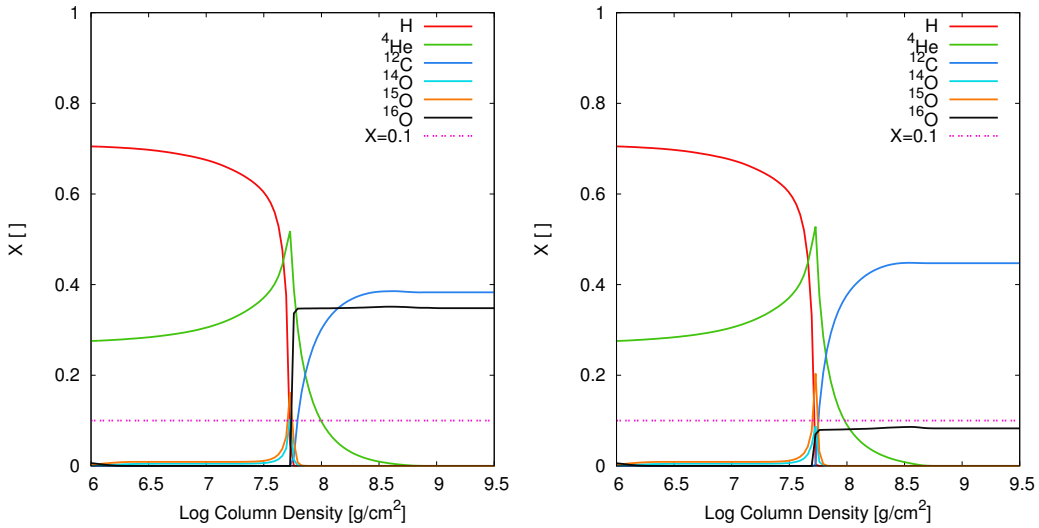

Fig. 3.11.: These two plots show the mass fractions of hydrogen (red line), ^{4}He (green line), ^{12}C (blue line), ^{14}O (bright turquoise line), ^{15}O (orange line), ^{16}O (black line) and the minimal mass fraction of 0.1 (pink dashed line), which would be needed for the successful ignition of a superburst.
a) shows the results from the simulation with an accretion rate of $0.9 \cdot 10^{17}$g s^{-1} and a crustal heating of 1.2 MeV nuc^{-1}.
b) shows the results for the run with an accretion rate of $0.9 \cdot 10^{17}$g s^{-1} and a crustal heating of 1.4 MeV nuc^{-1}.

In Fig. (3.11), we take a closer look at the mass fraction of hydrogen (red line), helium (green line), carbon (blue line), and three different isotopes of oxygen (bright turquoise, orange, and black line) dependent on the column density. Both plots show the results from simulations with accretion rate $0.9 \cdot 10^{17}$g s^{-1}, the left one with crustal heating of 1.2 MeV nuc^{-1} and the right one with 1.4 MeV nuc^{-1}. We see that in both cases, a rather large amount of ^{12}C and ^{16}O is produced. Hydrogen burns over the hot CNO-cycle, mixed with helium burning via the triple-alpha-reaction, which results in the increased mass fraction of ^{14}O and ^{15}O. In hydrogen depleted regions below the stable burning zone ^{16}O is produced, and, a bit deeper, ^{12}C.

In the composition plot in Fig. (3.12), we see the overall composition distribution of three regions of the simulation with $Q_b = 1.2$ MeV nuc^{-1} and $\dot{M}_{acc} = 0.9 \cdot 10^{17}$ g s^{-1}. The red line shows the composition of one of our outermost layers, which consists mostly out of the accreted matter. The blue line denotes the region with the highest burn rate, and therefore, the most active zone in terms of nuclear energy production. The violet line represents a region below the main active region and consists purely of ashes from the stable burning. Two main differences to the composition of the ashes from the pure stable burning (compared to Fig. (3.7)) are the regions of $20 \lesssim A \lesssim 30$ and $40 \lesssim A \lesssim 55$. The first mass-region is here present (while it is

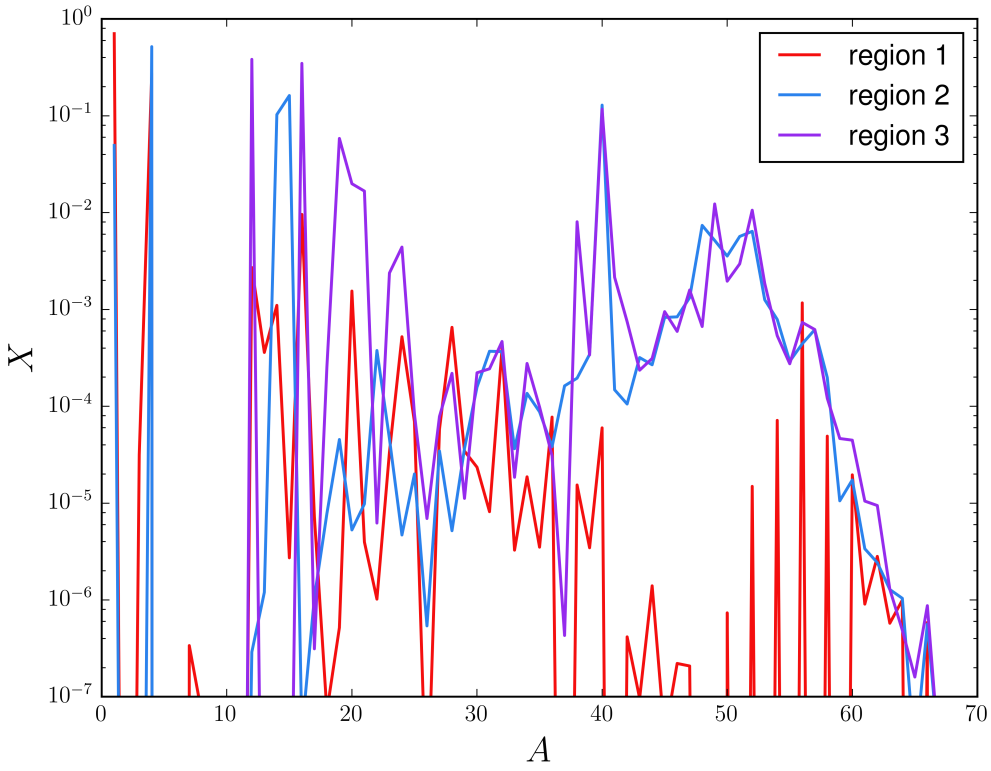

Fig. 3.12.: The composition of three different regions of the results from the simulation with $Q_b = 1.2$ MeV nuc^{-1} and $\dot{M}_{acc} = 0.9 \cdot 10^{17}$ g s^{-1}. The red line, region one, is one of the outermost zones in our domain. Region two, the blue line, is the zone with the highest burn rate at a column density of $5.34 \cdot 10^7$ g cm^{-2} ($\log(y) \approx 7.7$). The violet line, region three, represents one of the zones below the stable burning, where a maximum of ^{12}C is reached at a column density of $1.8 \cdot 10^9$ g cm^{-2} ($\log(y) \approx 9.3$).

missing in Fig. (3.7)) and the isotopes of the second mass-region are more abundant than before in the stable burning regime. Therefore, during the stable hydrogen- and helium-burning, the proton- and α-captures on the lighter nuclei are stronger present, and lead to a more balanced distribution of the mass fraction. Nuclei with $A \gtrsim 65$ can not be produced, as they would need explosive burning.

The burn rate and the temperature profile present no large change if we increase the accretion rate or the crustal heating (see Fig. (3.13), where in the left plot the burn rate and in the right plot the temperature profile is shown). Compared to the temperature profile of the stable burning regime in Fig. (3.8), we find slightly higher values for the temperature in the irregular bursting regime.

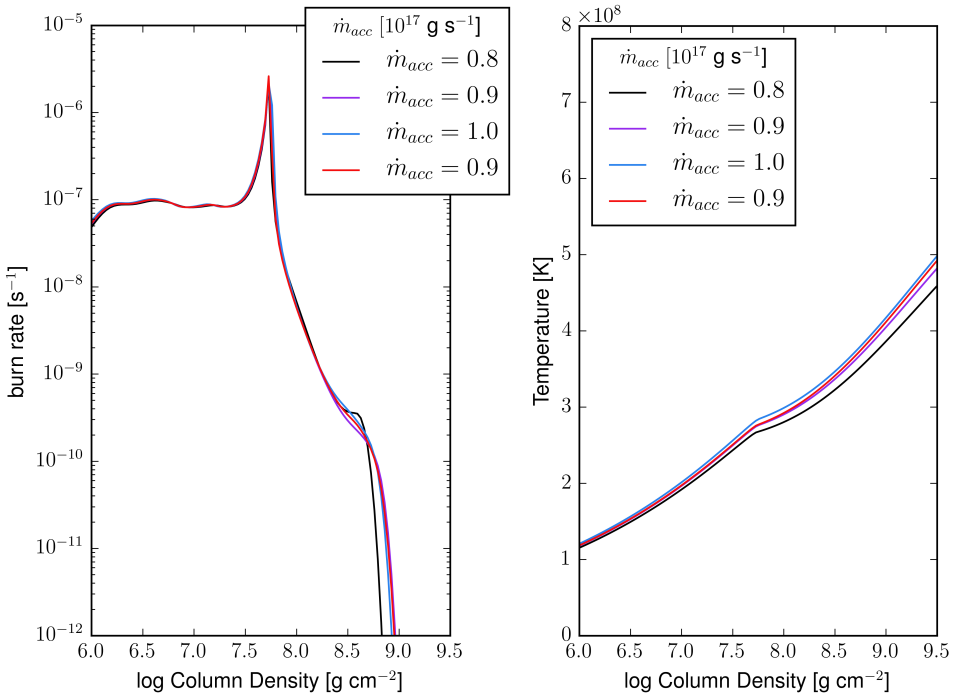

(a) (b)

Fig. 3.13.: The burn rate and the temperature for runs with fixed crustal heating of 1.2 MeV nuc^{-1}, but with different accretion rates of $0.8 \cdot 10^{17}$g s^{-1} (black line), of $0.9 \cdot 10^{17}$g s^{-1} (violet line), and of $1.0 \cdot 10^{17}$g s^{-1} (blue line). The red line additionally presents the results for the simulation with 1.4 MeV nuc^{-1} and an accretion rate of $0.9 \cdot 10^{17}$g s^{-1}.
a) The burn rate as a function of the logarithm of the column density. The increase of the accretion rate or of crustal heating has no significant influence on the burn rate.
b) The temperature profile of the different simulations.

3.3.3 Regular Burst Regime

For our numerical simulations with accretion rate conditions between $0.8 \cdot 10^{17}$ g s^{-1} and $1.5 \cdot 10^{17}$ g s^{-1} and for all Q_b values, except the ones described in Section 3.3.2, we find a regular burst regime (see violet dots in Fig. (3.3)). This means that over long time the results from the simulations show a regular burst behaviour.

Here we show the results of five numerical simulations (all results can be found in the Appendix A.1.1). We choose one parameter set with high Q_b value ($= 1.5$ MeV nuc^{-1}) and large $\dot{M}_{acc}$ ($= 1.5 \cdot 10^{17}$g s^{-1}), one set with intermediate Q_b value ($= 0.6$ MeV nuc^{-1}) and intermediate $\dot{M}_{acc}$ ($= 1.0 \cdot 10^{17}$g s^{-1}), and three parameter sets with low $\dot{M}_{acc}$ ($= 0.8 \cdot 10^{17}$g s^{-1}) for three different Q_b-values (0.1, 0.4, and 0.8 MeV nuc^{-1}).

In Fig. (3.14), we present the light curve of these simulations over a short period of time (~ 14 hours). The simulations with low accretion rate (green, light turquoise, and violet lines in the figure) show higher peak luminosities ($\sim 1.2 \cdot 10^{38}$ erg s^{-1}) and long recurrence times (~ 4.5 h), whereas simulations with higher accretion rate (red and orange lines) show lower peak luminosities ($\sim 7 - 9 \cdot 10^{37}$ erg s^{-1}) and shorter recurrence times ($\sim 1.5 - 3$ h). The recurrence time of Type I X-ray bursts is very sensitive to ignition conditions. Lower accretion rates lead to lower ignition depths [25, 138], and therefore, the bursts ignite at lower temperatures and lower densities. At these lower accretion rates, a helium dominated burst occurs, whereas at high accretion rate, a mixed hydrogen/helium burst takes place [139].

In Tab. (3.5), we show the observable burst parameters given as the values from our simulations averaged over the number of bursts. In the second column, N$_{burst}$ is the

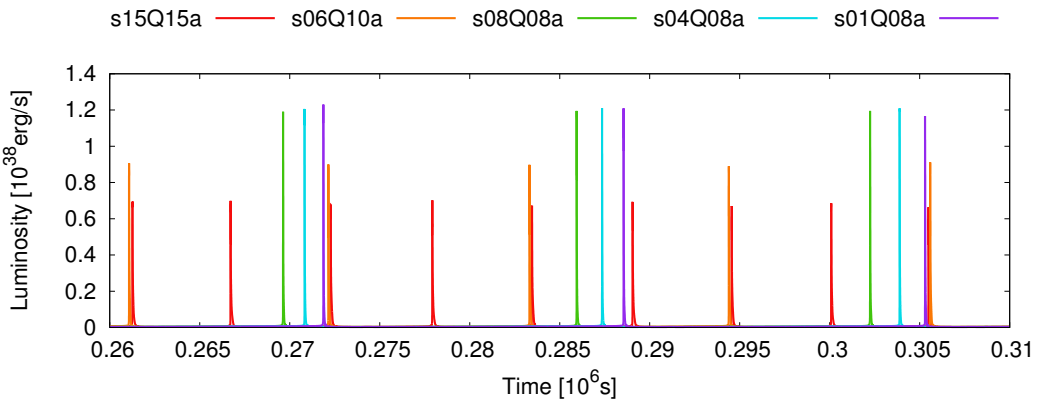

Fig. 3.14.: This figure shows the light curves of five simulations over a time of roughly 13.9 hours. The colour affiliation to the parameter sets are given in the legend above the plot. As before, we use the nomenclature described in Eq. (3.6).

run	N_{burst}	L_{peak} [erg s^{-1}]	t_{rec} [h]	t_{rise} [s]	$t_{duration}$ [s]	α-value
s15Q15a	83	$6.97 \cdot 10^{37}$	1.56	5.45	126.80	74.9
s06Q10a	2807	$8.92 \cdot 10^{37}$	3.09	3.62	97.24	100
s08Q08a	2331	$1.18 \cdot 10^{38}$	4.52	2.18	73.53	136.1
s04Q08a	1180	$1.24 \cdot 10^{38}$	4.70	1.74	74.74	131.1
s01Q08a	61	$1.25 \cdot 10^{38}$	4.72	1.70	74.68	130.4

Tab. 3.5.: The values in this table are averaged over all bursts, if a simulation shows more than 100 bursts, it is averaged over the first 100 bursts. The first column specifies the simulation conditions.

number of bursts, the third column L_{peak} gives the maximum in the luminosity of the simulations, the fourth column t_{rec} gives the recurrence time, the fifth column t_{rise} gives the rise times, the sixth column $t_{duration}$ gives the burst time, and the last column gives the α-values. In Sec. 3.7 we will compare our results to observations.

Fig. (3.15) shows a comparison of one single burst from each simulation of our five chosen parameter sets. The time is shifted, so that the steep rise of the bursts occur simultaneously. This point is also marked as time equals zero. This figure shows the differences in the behaviour of one single burst between the simulations. The high-accretion-rate-bursts rise not so steeply and to an overall lower maximum luminosity, which is reached later, and decay more shallowly (red and orange line), than the luminosities of the other simulations. The simulations with low accretion

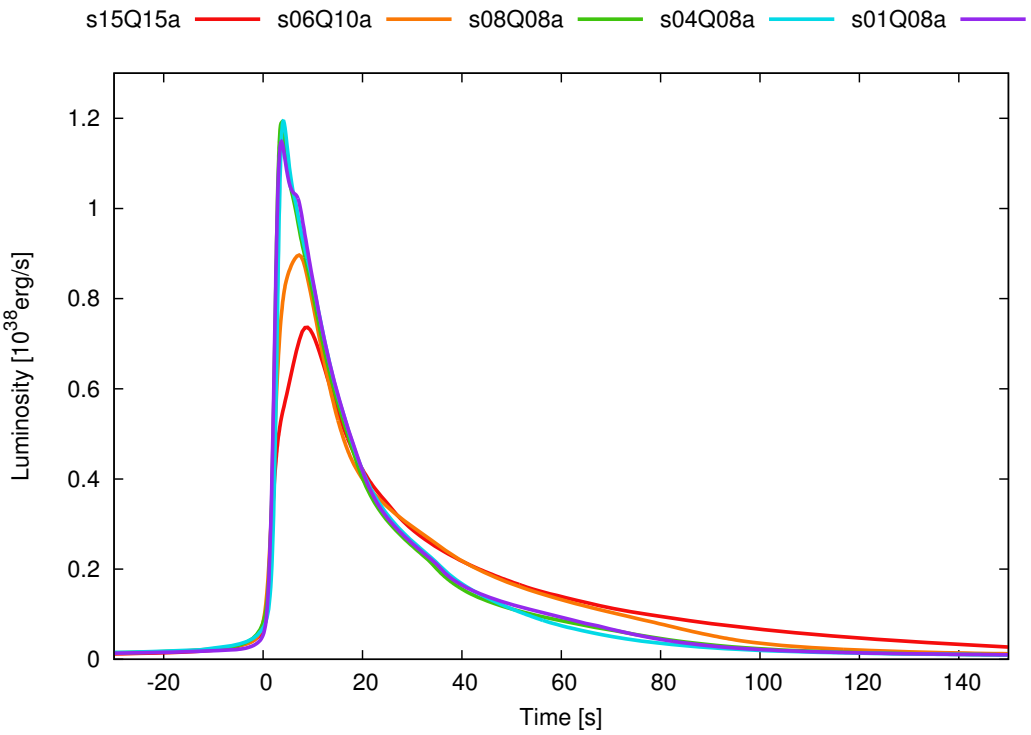

Fig. 3.15.: The light curves of one representative burst for each of our five parameter sets. The times have been shifted such that the steep rise of the curves lay on top of each other.

rate show a steep rise to a high peak luminosity and decay faster (violet, light turquoise, and green line). For all simulations with low accretion rate, the crustal heating has no strong impact on the results and the lines lay nearly on top of each other. It has to be noted, that here we show one specific example of a burst for each of our parameters. The bursts of one simulation can vary, but the general behaviour is represented by these examples.

Fig. (3.16) shows the dependency of the accretion rate and the crustal heating on the peak luminosity and the recurrence time. We show here average values of the represented quantities. The two top plots show the change of the peak luminosity (in units of 10^{38} erg s^{-1}) in dependence on the crustal heating (top left) and on the accretion rate (top right). The two bottom plots show the change of the recurrence time (in units of hours) in dependence on the crustal heating (bottom left) and on

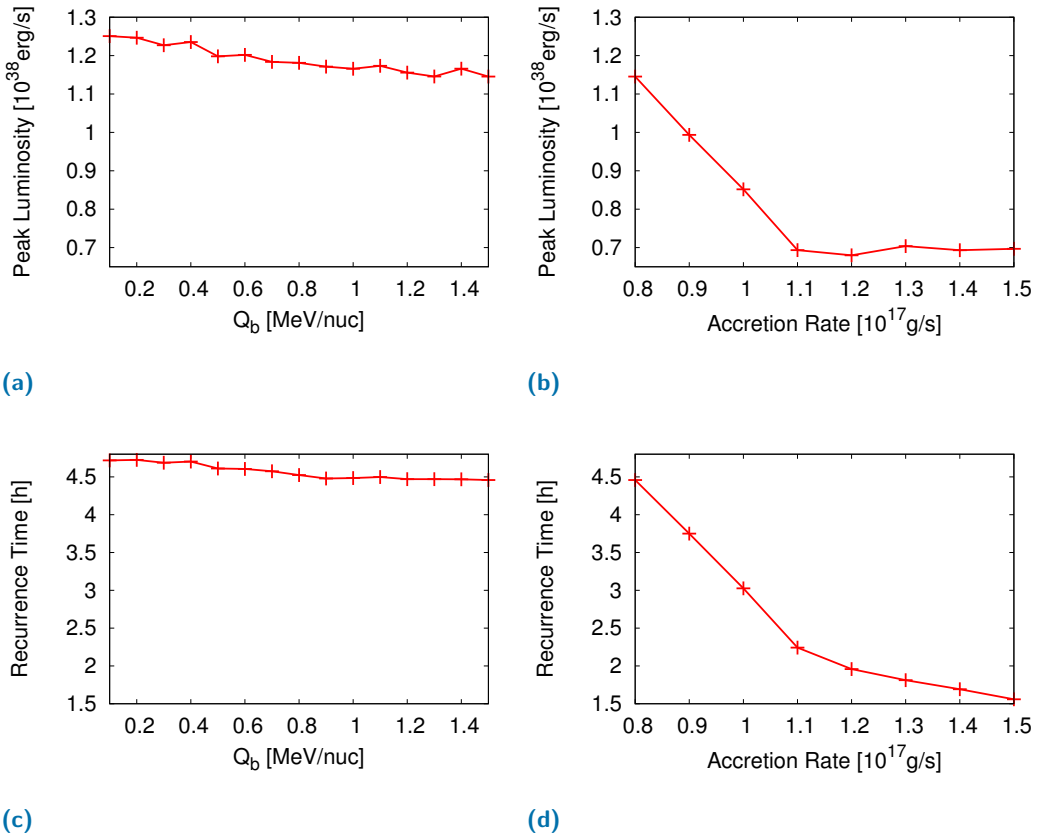

Fig. 3.16.: a) The top left plot shows the peak luminosity in dependence on the crustal heating. The accretion rate is fixed at $0.8 \cdot 10^{17}$g s^{-1}.
b) The top right plot shows the peak luminosity in dependence on the accretion rate. The crustal heating is fixed at 1.5 MeV nuc^{-1}.
c) The bottom left plot shows the recurrence time in dependence on the crustal heating. The accretion rate is fixed at $0.8 \cdot 10^{17}$g s^{-1}.
d) The bottom right plot shows the recurrence time in dependence on the accretion rate. The crustal heating is fixed at 1.5 MeV nuc^{-1}.

the accretion rate (bottom right). The left plots correspond to simulations with a fixed accretion rate of $0.8 \cdot 10^{17}$g s^{-1}. The right plots correspond to simulations with a fixed crustal heating of 1.5 MeV nuc^{-1}. In both cases (the top and the bottom plots), we choose the same range for the *y*-axis (displaying either peak luminosity or recurrence time) to compare them easily. All four plots show a decreasing behaviour. However, the accretion rate has a much bigger influence on the peak luminosity and on the recurrence time than the crustal heating. Since the change in recurrence times hints that the ignition depth of the burst has been shifted to other conditions. We see in the same fashion a decrease of the luminosity. This indicates that not the entire fraction of hydrogen and helium is depleted in the burst region for high accretion rates, as it is the case for low accretion rates, where a helium dominated burst occurs [25, 139].

The two plots in Fig. (3.17) are obtained at the time in between two bursts. Therefore, the previous burst does not influence these two distributions of the light isotopes over the column density. These light isotopes are important for hydrogen- and helium-burning during stable burning. In the left plot, we show the results from the simulation with a high accretion rate of $1.5 \cdot 10^{17}$g s^{-1} and Q_b of 1.5 MeV nuc^{-1}; in the right plot the results from the simulation with a low accretion rate of $0.8 \cdot 10^{17}$g

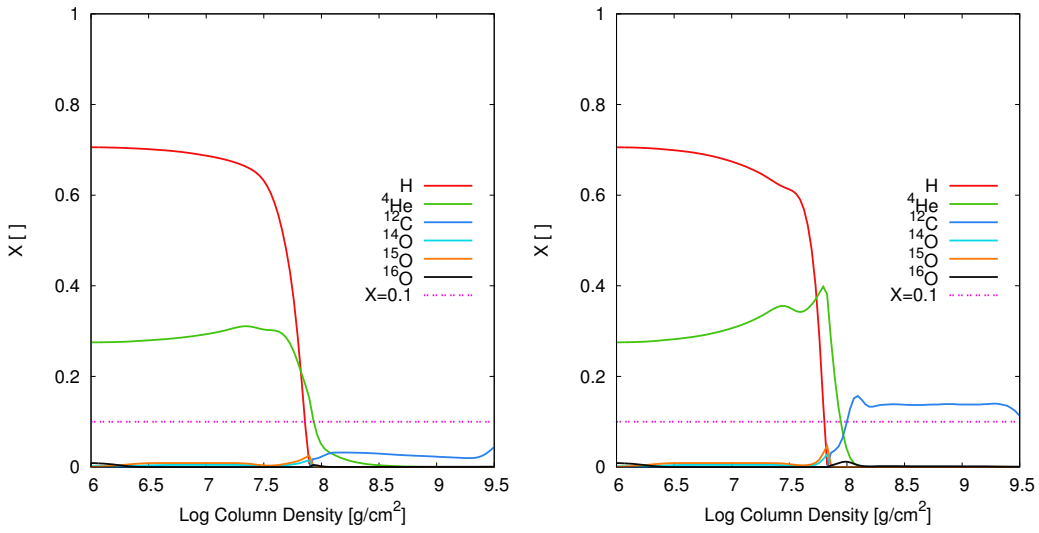

Fig. 3.17.: The mass fractions of hydrogen (red line), ^{4}He (green line), ^{12}C (blue line), ^{14}O (bright turquoise line), ^{15}O (orange line), ^{16}O (black line) and the minimal mass fraction of 0.1 (pink dashed line), which would be needed for the successful ignition of a superburst.
a) shows the results from the simulation with an accretion rate of $1.5 \cdot 10^{17}$g s^{-1} and a crustal heating of 1.5 MeV nuc^{-1}.
b) shows the results for the run with an accretion rate of $0.8 \cdot 10^{17}$g s^{-1} and a crustal heating of 0.1 MeV nuc^{-1}.

s^{-1} and Q_b of 0.1 MeV nuc^{-1}. Between two bursts, quiescent stable burning via the CNO-cycle and the triple-α reaction occurs. We can see that with low accretion rate, stable burning leads to more helium, which leads to a helium dominated burst with high peak luminosity and long recurrence time. Whereas, we can see for high accretion rate, less helium is produced in between bursts and a mixed hydrogen/helium burst occurs with lower peak luminosity and shorter recurrence time.

In Fig. (3.18), we show the burn rate and the temperature for different column densities. The left plot shows the results for the case with an accretion rate of $1.5 \cdot 10^{17}$g s^{-1} and a crustal heating of 1.5 MeV nuc^{-1}, the right plot shows the results for the case with an accretion rate of $0.8 \cdot 10^{17}$g s^{-1} and a crustal heating of 0.1 MeV nuc^{-1}. In Fig. (3.18a), we find that the temperature profile is steeper and rises to larger values than in the cases of stable burning in the irregular burst and in the stable burning regimes. The temperature profile in the right plot is similar to the ones in the irregular burst regime in Fig. (3.13b), but steeper than the ones of the stable burning regime in Fig. (3.8d). The burn rate in both cases show a valley besides the peak at lower column density. The small plateau in low column densities indicates hydrogen-burning via the hot CNO-cycle, whereas the peak indicates additional carbon production via triple-alpha reactions. Compared to the other two regimes, the burn rate has its peak at slightly higher column densities, but the peak itself is

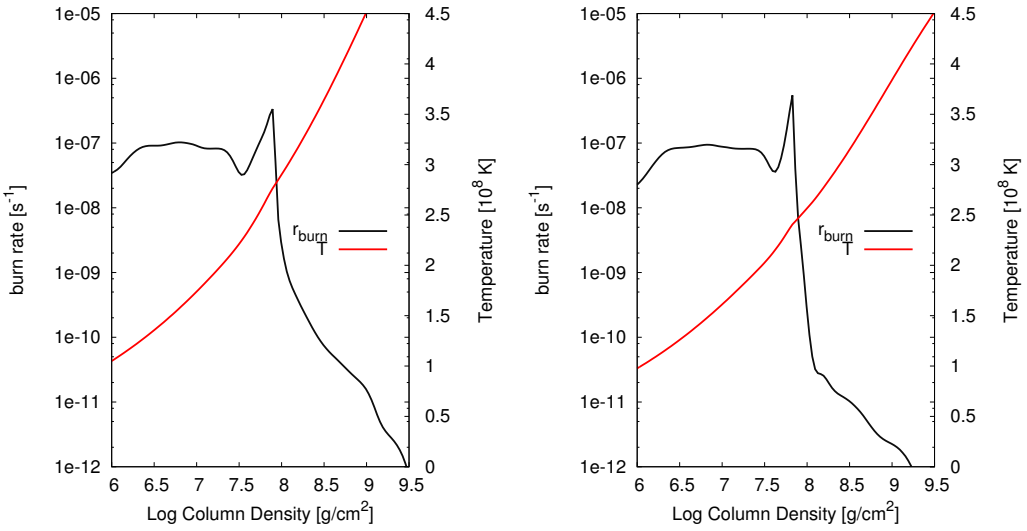

(a) (b)

Fig. 3.18.: The burn rate and the temperature of the regions where stable burning occurs.
a) shows the results from the simulation with an accretion rate of $1.5 \cdot 10^{17}$g s^{-1} and a crustal heating of 1.5 MeV nuc^{-1}.
b) shows the results for the run with an accretion rate of $0.8 \cdot 10^{17}$g s^{-1} and a crustal heating of 0.1 MeV nuc^{-1}.

smaller than the peaks in Fig. (3.13a). Both peaks in Fig. (3.18) decay faster than the peaks in the other burning regimes. While the hot CNO-cycle is temperature independent, the triple-α reaction is strongly dependent on temperature. Therefore, in the left plot, the triple-α reaction is reducing the helium production stronger than in the right plot.

In the composition plot in Fig. (3.19), we see the overall composition distribution of three regions of the simulation with the conditions $Q_b = 0.1$ MeV nuc^{-1}, and $\dot{M}_{acc} = 0.8 \cdot 10^{17}$ g s^{-1}. Note, that if we compare this figure with Fig. (3.7) or Fig. (3.12), we have to take into account that the *x*-axis (the mass number) includes here also larger values than before. In Fig. (3.19), the red line shows the composition of one of the outermost zones and represents the accreted composition. The blue line shows the composition of the region, where quiescent burning has a maximal burn rate, and consists out of newly accreted material and ashes from the previous

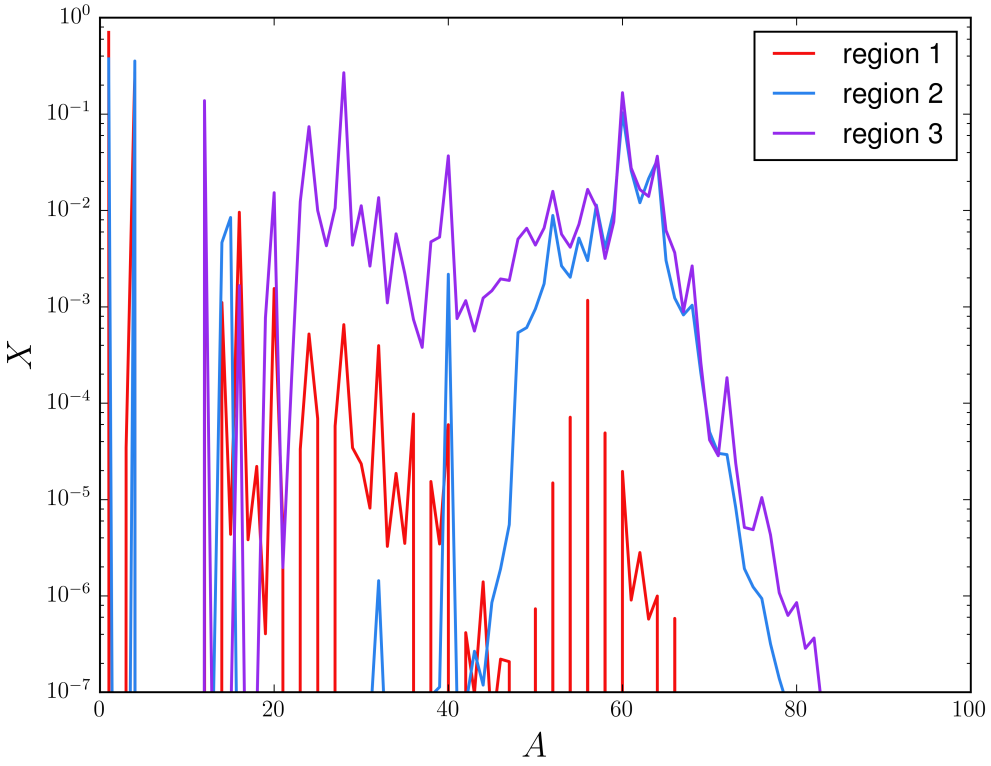

Fig. 3.19.: The composition of three different regions obtained from the simulation with $Q_b = 0.1$ MeV nuc^{-1} and $\dot{M}_{acc} = 0.8 \cdot 10^{17}$ g s^{-1}. The red line, region one, is one of the outermost zones in our domain. Region two, the blue line, is the zone with the highest burn rate between two bursts at a column density of $6.72 \cdot 10^7$ g cm^{-2} ($\log(y) \approx 7.8$). This region consists out of a mixture of newly accreted matter and traces of the ashes of the last burst. The violet line, region three, represents one of the zones below the stable burning, where the composition consists purely out of ashes of the previous bursts. This is at a column density of $1.06 \cdot 10^9$ g cm^{-2} ($\log(y) \approx 9.0$).

thermonuclear runaway. The violet line represents a deeper zone, which consists purely out of the composition of the ashes of the previous bursts. Region two consist out of some heavy isotopes, with peaks around $A \sim 65$, and $A \sim 40$, and lighter isotopes around oxygen, helium, and hydrogen. In the deepest region, all of the helium and hydrogen is depleted due to the reactions of the bursts. Isotopes up to a mass number of $A \sim 80$ have been produced, which are the products of the rp-process.

Fig. (3.20a) shows the burn rate (left plot) and the temperature (right plot) evolution over one burst. During a burst, the burn rate rises fast to high values and reaches out to lower and higher column densities. Due to the rise in the nuclear reaction activity, the temperature rises, which enables the αp and the rp-process. The temperature reaches values of $\sim 9.3 \cdot 10^8$ K at densities of $3 - 4 \cdot 10^5$ g cm^{-3} at the peak luminosity ($t = 0$ in these plots). At those conditions matter does not behave like a degenerate gas anymore and the reaction flow of the processes slows down. The hydrogen in the ignition region is completely depleted (Fig. (3.20b), left plot) whereas some fraction of helium (right plot) remains in the ignition zone, while it is immediately depleted in the zones below. Fig. (3.20) shows a burst of a simulation with low accretion rate and low crustal heating. Therefore, the burst ignition is helium dominated. This can also be seen in the middle plot of Fig. (3.21), where the helium mass fraction is higher than the hydrogen mass fraction. The three plots in Fig. (3.21) show the mass fractions as obtained from a simulation with the following conditions: $Q_b = 0.1$ MeV nuc^{-1} and $\dot{M}_{acc} = 0.8 \cdot 10^{17}$ g s^{-1}. Fig. (3.21b) shows the mass fraction of the composition in the ignition zone. This zone is chosen because it shows the highest burn rate at the peak luminosity. We choose to take a look at the time between $t_0 - 25$ s and $t_0 + 145$ s because for this parameter set, bursts have an average length of ~ 75 s, with a short rise time of only 1.7 s. The red line represents the mass fraction of hydrogen (H), the green line the mass fraction of helium (^{4}He), the dark blue line the mass fraction of carbon (^{12}C), black the mass fraction of oxygen (^{16}O), and the light turquoise line the mass fraction of silicon (^{28}Si). We choose $t = 0$ s as the time where the luminosity reaches its peak. Fig.(3.21a) shows the mass fraction in the zone above the ignition zone, whereas Fig. (3.21c) shows the mass fraction of the zone below the ignition zone. We see here in Fig. (3.21), that all hydrogen is depleted in all three zones. Furthermore, helium remains with a mass fraction of ~ 0.1. Carbon is only produced until shortly below 0.1, which is the needed mass fraction to ignite a superburst in deeper zones after thousands of bursts providing layers of ashes. Combined, the zones produce the mass fractions that were previously shown in Fig. (3.17b). So this simulation prooves to be a candidate for a self-consistent superburst ignition.

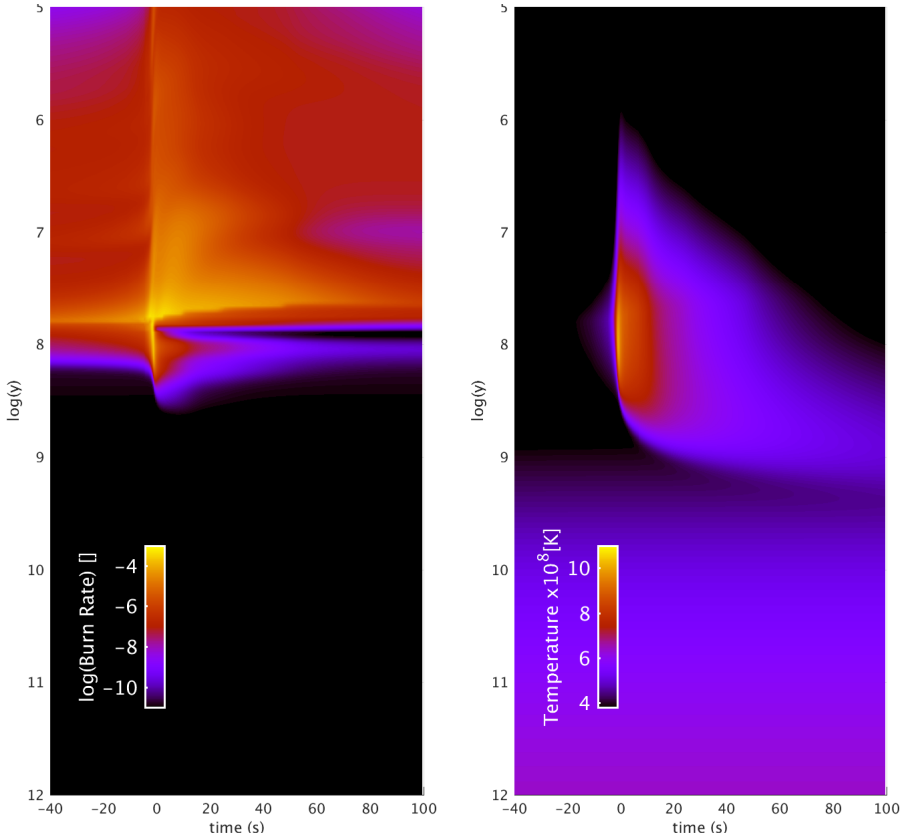

(a)

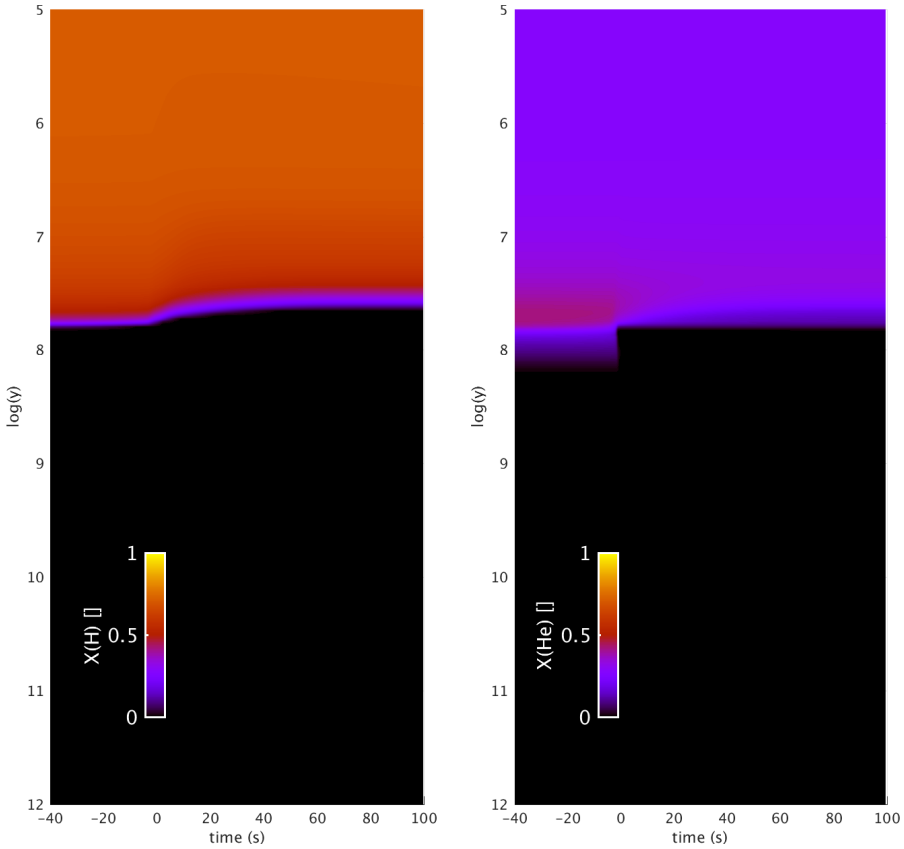

(b)

Fig. 3.20.: Here, the results from the simulation s01Q08a are shown. L_{peak} is chosen to be at $t = 0$ s. The figures in a) show the burn rate over one burst (left) and the temperature over one burst (right). The figures in b) show the mass fraction of H and He.

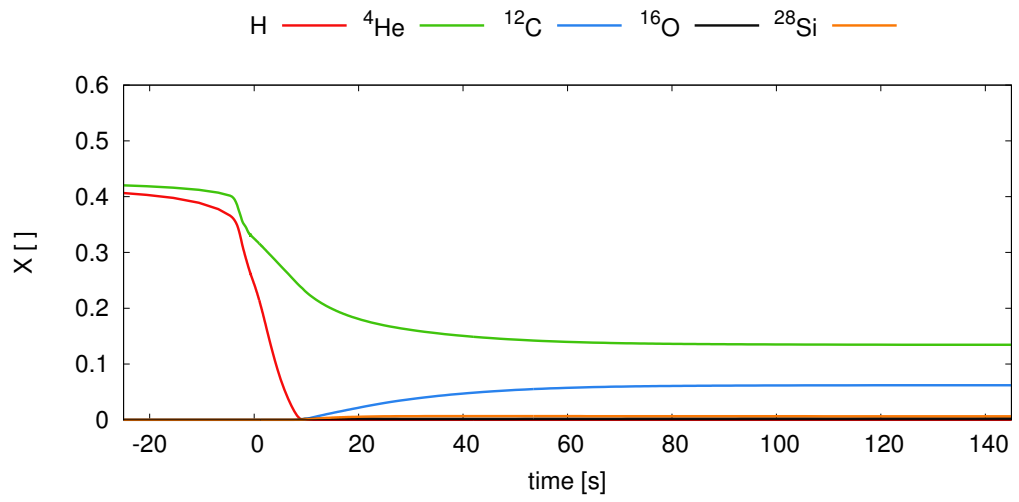

(a)

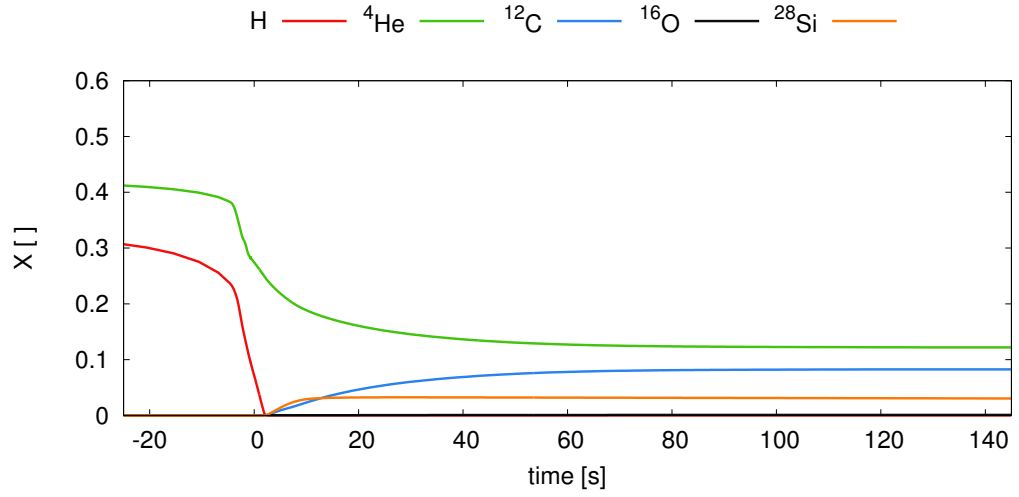

(b)

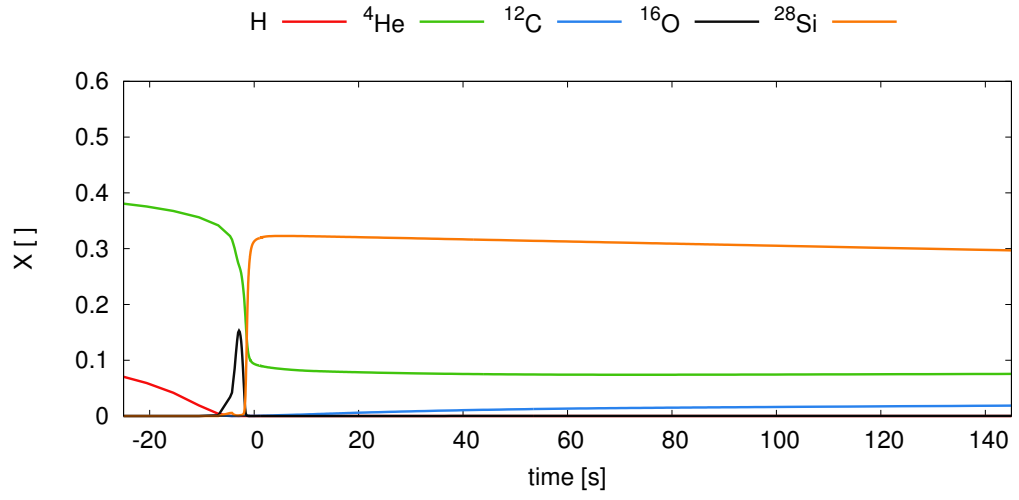

(c)

Fig. 3.21.: a) Shows the mass fraction from the zone above the ignition zone. b) Shows the evolution of the mass fraction of the zone, where the most nuclear energy is released at time $t = 0$, when the luminosity reaches its peak. This happens at a column density of $5.77 \cdot 10^7$ g cm^{-2} ($\log(y) = 7.76$). c) Shows the mass fraction from the zone below the ignition zone. The red line represents the mass fraction of hydrogen, the green line the mass fraction of helium, the dark blue line the mass fraction of carbon, black is the mass fraction of oxygen, and the light turquoise line the mass fraction of silicon.

3.3.4 Discussion of the Three Burning Regimes with Solar Abundances as Accretion Composition

We find for the burst behaviour in the irregular regime that with increasing accretion rate, the number of bursts increases, as well as the burst time, the transition time, and the luminosity of the stable burning and the quiescent burning between bursts. In contrast, the recurrence time, the α-parameter, and the peak luminosity decreases. With increasing crustal heat, the number of bursts decreases, as well as the transition time, whereas the peak luminosity remains more or less unchanged. At the range of Q_b values, where we find irregular burst behaviour, we find a shift of the ignition depth towards smaller values over time. Due to this shift, the ignition region rises upwards, where the conditions for a thermonuclear runaway are in the end not given anymore, and therefore, stable burning occurs.

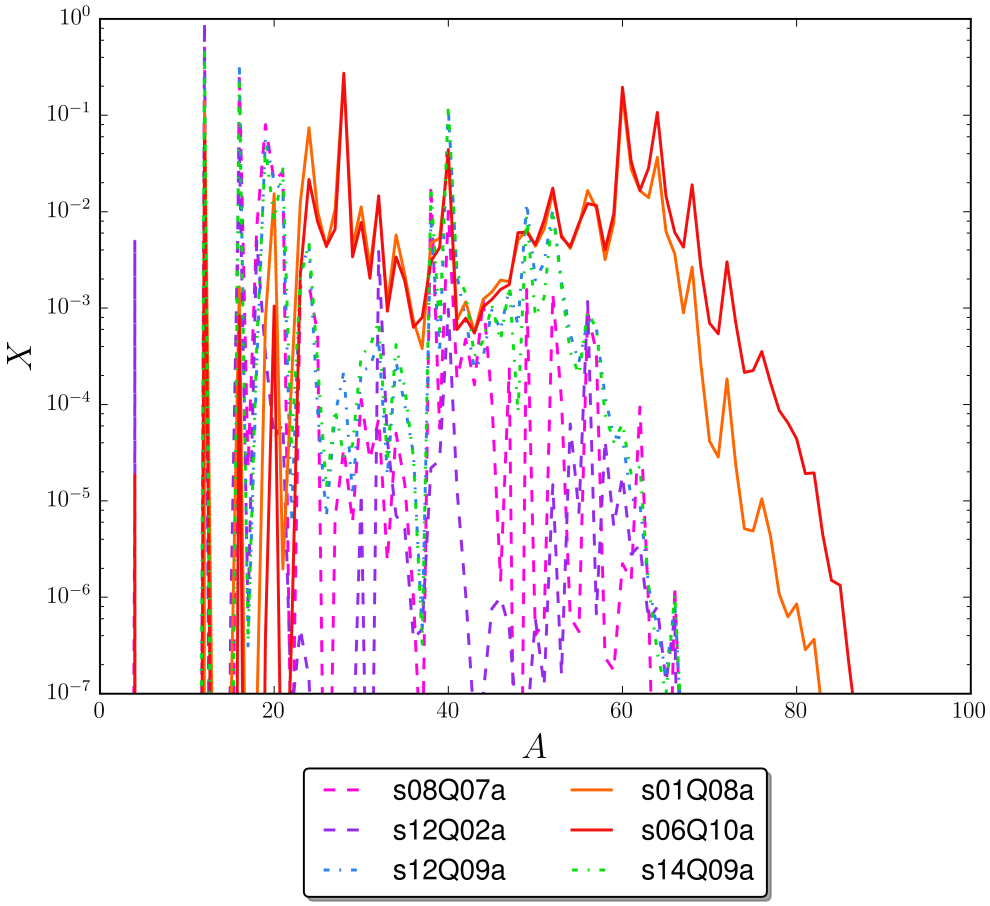

Fig. 3.22.: A comparison of the composition of two representative simulations for each burning regime (definition of the parameter set conditions of each simulation is given in the box below the figure). The solid lines represent the regular bursting regime, the dashed lines the irregular burst regime, and the dot-dashed lines the stable burning regime.

In the regular burst regime we see a major influence of the accretion rate on the peak luminosity and the recurrence time, which both decrease with increasing accretion rate. The rise time and the burst time tend to increase for increasing accretion rate, whereas the α-parameter decreases with increasing accretion rate. Increasing crustal heat leads to increasing α-parameters and rise times, but to decreasing burst times and peak luminosities. This is due to the rfact that with low accretion rates, we have more helium in the ignition zone and the burst ignitions are helium dominated. With high accretion rates, the helium fraction in the ignition zone is reduced and we find a mixed hydrogen/helium ignition.

For the three different burning regimes, we find differences in the stable and quiescent burning region, and therefore, differences in the composition of the ashes in a layer with column density of $\sim 1 \cdot 10^9$ g cm^{-2}. The composition of the ashes is presented in Fig. (3.22), where the solid lines represent two cases with regular burst behaviour, the dashed lines cases with stable burning behaviour, and the dot-dashed lines cases with irregular burst behaviour. All regions consisting of ashes are completely hydrogen depleted. We find that the mass fractions in the stable burning regime and the regular burst regime are shifted: in the stable burning regime the light isotopes dominate and only some heavier isotopes around the iron-peak appear. In contrast, in the regular burst regime, heavier isotopes up to $A \sim 80$ are found and lighter isotopes are less present.

In Fig. (3.23), we combine our results from the burning regimes with the amount of carbon found in the ashes of the different burning regimes. This is crucial for finding parameter sets which could be used for simulating a self-consistent ignition of a superburst. In the stable burning regime, higher accretion rates result in a steeper temperature profile and therefore mixed, stable H/He-burning. The temperature gradient enables α-capture on the produced ^{12}C, leading to less carbon than in cases with lower accretion rates, where an immense part of the produced carbon survives because the hydrogen and helium burning regimes are slightly parted. In the irregular burst regime, we find stable burning of hydrogen and in the layer consisting of ashes just below, helium burns stably to carbon. In some cases, e.g. s12Q09a, there is nearly as much ^{16}O production as ^{12}C production. In Fig. (3.23), we merge the results of the found carbon mass fraction in the layers consisting of ashes into our parameter space, which gives us the burning behaviour. The four shades of grey indicate the mass fraction of carbon. Going from a bright shade of grey to the darker shade means: $X_{^{12}C} > 0.1$, $X_{^{12}C} > 0.5$, $X_{^{12}C} > 0.7$, $X_{^{12}C} > 0.9$, whereas white means $X_{^{12}C} < 0.1$. We observe a small band of parameter sets, which show both, regular bursts (violet dots), and have layers of ashes, which consists of more than 10% carbon (in the grey area), and are therefore candidates for superburst simulations.

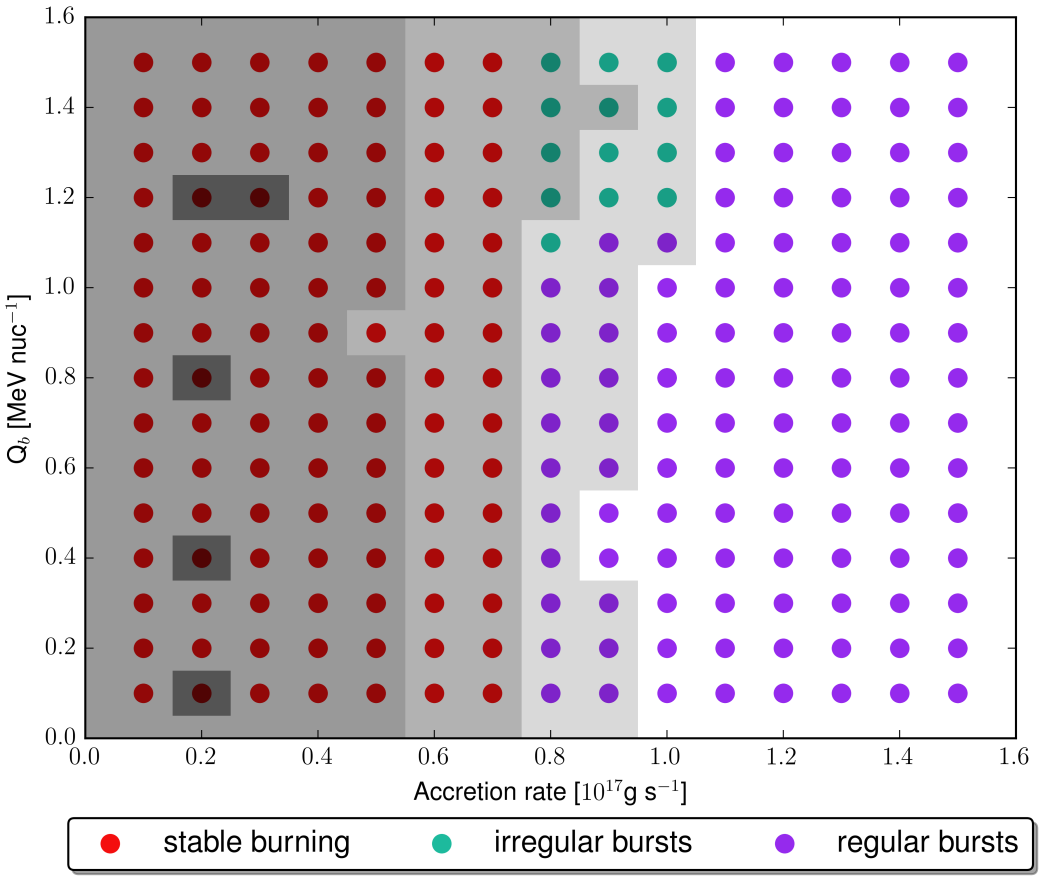

Fig. 3.23.: This plot shows the three different burning regimes found in our simulations. The red dots are the parameter set runs which lead to stable burning, the turquoise dots represent irregular bursts, and the violet ones regular burst behaviour. The mass fraction of ^{12}C is shown by the different shades of grey. From bright to dark: $X_{^{12}C} > 0.1$, $X_{^{12}C} > 0.5$, $X_{^{12}C} > 0.7$, $X_{^{12}C} > 0.9$ and white is $X_{^{12}C} < 0.1$.

3.4 Three Burning Regimes with Helium-Rich Abundances as Accretion Composition

In this section, we discuss the results of our numerical simulations with a helium rich accretion composition. Our interest for such helium-rich environments originates from two superbursts observations in ultra-compact X-ray binaries, cf. Tab. (1.2). Those two sites are 4U 0614+91 (see [46]) and 4U 1820-30 (see [57]). In such binaries, Roche-lobe overflow can only originate from an evolved star without a hydrogen envelope.

Model	X(H)	X(^{4}He)	X(Z)
helium-rich	0.471	0.510	0.019

Tab. 3.6.: The helium and hydrogen mass fractions, and the remaining mass fraction of all the metals, which were included in our helium-rich simulations.

We also want to make for helium-rich accretion composition a parameter space exploration, finding possible parameter sets, which could be used for self-consistent superburst simulations. Our simulations reveal three different burning regimes, which we show in Fig. (3.24): red dots represent stable burning, turquoise dots irregular bursts, and violet dots regular burst behaviour. We simulate at least $\sim 10^6$ seconds simulation time to be sure, that no burst was found in our results. In the next three subsections, we discuss these three regimes in more detail.

We can see that from smaller until intermediate accretion rates ($\dot{M}_{acc} = 0.1 - 1.1 \cdot 10^{17}$g s^{-1}), we find for all Q_b values stable burning. With higher accretion rates and higher base heating ($Q_b > 0.6$ MeV nuc^{-1}), we find irregular burst behaviour and with high accretion rates ($\dot{M}_{acc} > 1.2 \cdot 10^{17}$g s^{-1}) and low Q_b values ($Q_b \lesssim 0.6$ MeV nuc^{-1}), we find regular burst behaviour. The additional heat source at the base of our computational domain seems to influence the burning regimes only in the upper right part of Fig. (3.24): with a higher Q_b value, the region of the irregular burst regime spreads towards higher accretion rates. In the irregular burst regime, a phase of Type I X-ray bursts is followed by stable burning.

Note that the nomenclature in this section still follows the convention described in Eq. (3.6), but now the x, which represents the composition of the accreted matter, is now he, since we accrete helium-rich matter.

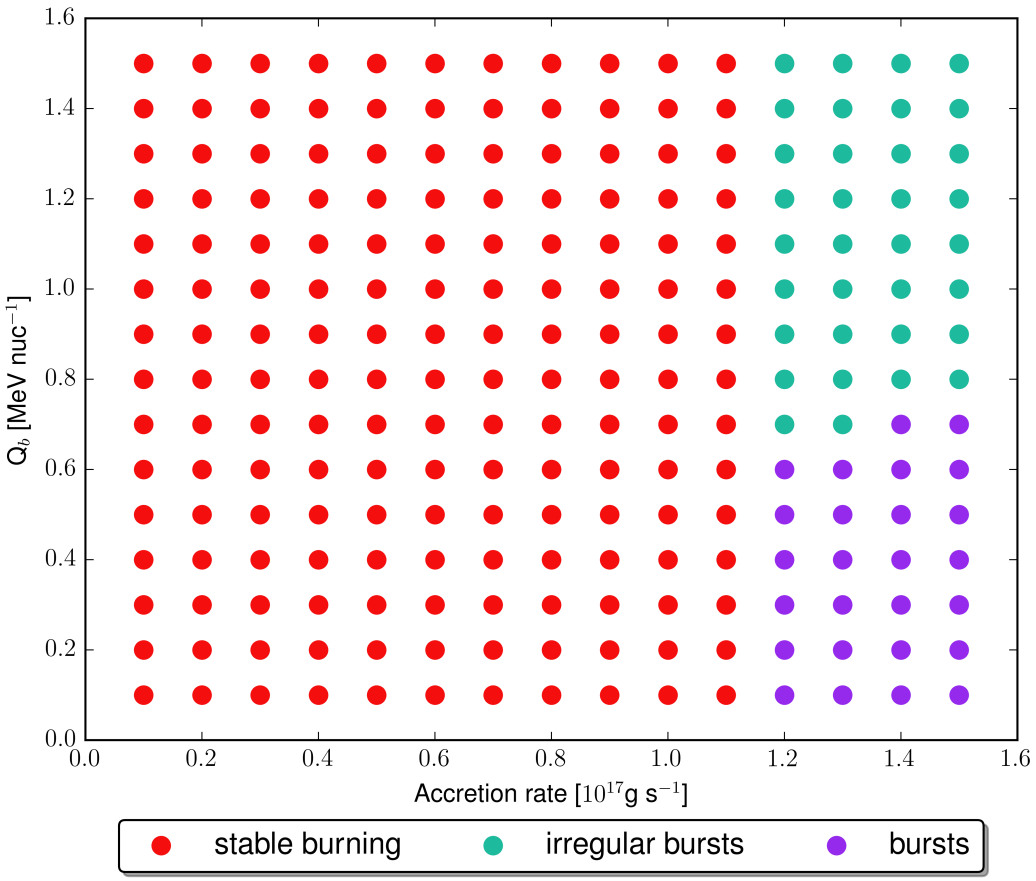

Fig. 3.24.: The three different burning regimes found in our study with helium-rich accretion composition, where the crustal heating Q_b is plotted versus the accretion rate. The red dots represent the parameter set runs, which lead to stable burning, the turquoise dots denote irregular bursts, and the violet ones regular burst behaviour.

3.4.1 Stable Burning Regime

In our simulations with helium-rich accretion composition, the upper limit for the stable burning regime of simulations with helium-rich accretion composition is found at an accretion rate of $1.1 \cdot 10^{17}$g s^{-1} (see red dots in Fig. (3.24)). Fig. (3.25) shows an example light curve of this burning regime.

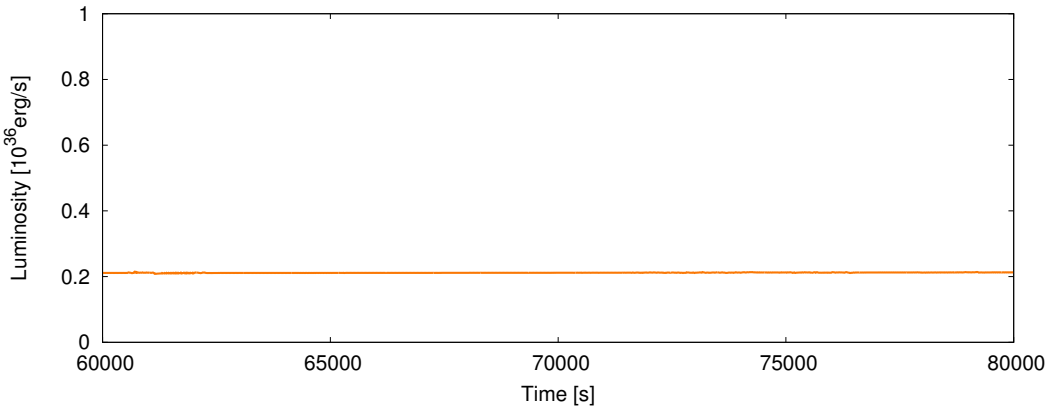

Fig. 3.25.: This is an example light curve from the simulation with $\dot{M}_{acc} = 0.2 \cdot 10^{17}$g s^{-1}, and $Q_b = 1.2$ MeV nuc^{-1}.

In Fig. (3.26), we show the results from the simulations with an accretion rate of $1.1 \cdot 10^{17}$g s^{-1} and a Q_b value of 0.9 MeV nuc^{-1} (left plot), and from the simulations with an accretion rate of $0.3 \cdot 10^{17}$g s^{-1} and a crustal heating of 0.9 MeV nuc^{-1} (right plot). Fig. (3.26) shows the mass fractions for ^{1}H (red line), ^{4}He (green line), ^{12}C (blue line), ^{14}O (light turquoise line), ^{15}O (orange line), and ^{16}O (black line) in dependence on the column density. In both cases, hydrogen is burning under stable conditions. We see that with high accretion rate, Fig. (3.26a), ^{4}He is burning stably in the lower part of the stable hydrogen burning region and produces ^{14}O and ^{15}O. In even deeper layers, where no hydrogen is available anymore, ^{16}O and ^{12}C are produced during hydrogen burning and build a layer of mainly carbon and oxygen. In contrast, if the accretion is low (Fig. 3.26b), the stable hydrogen burning builds up a rather thick layer of helium (as compared to Fig. (3.26a)), which burns at the lower part of the layer and builds a nearly pure ^{12}C layer.

Fig. (3.27) shows the burn rate and the temperature as a function of the column density. We show results for the same parameter sets as in Fig. (3.26). Fig. (3.27a) shows a plateau in the burn rate with a peak before it drops at higher column density. The plateau originates from stable hydrogen burning and the peak arises due to the higher activity of the zone where, additionally, ^{4}He burns to ^{12}C. This feeds the hot CNO cycle, which produces more ^{4}He, which then burns to ^{12}C, and so on, until one fuel is depleted, in this case hydrogen. In Fig. (3.27b), at low accretion rate, we

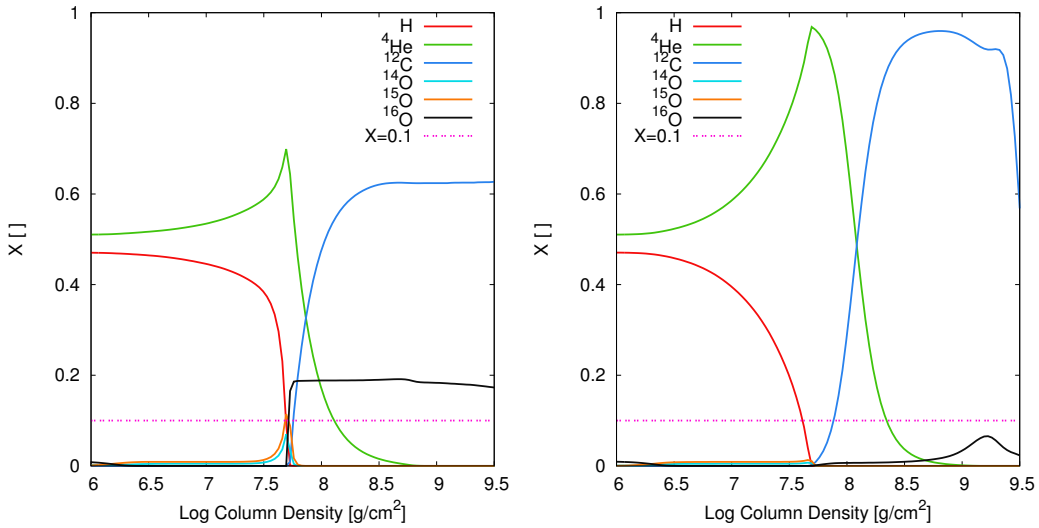

Fig. 3.26.: The mass fractions of hydrogen (red line), ^{4}He (green line), ^{12}C (blue line), ^{14}O (light turquoise line), ^{15}O (orange line), ^{16}O (black line), and the minimal mass fraction of 0.1 (pink dashed line), which would be needed for the successful ignition of a superburst.
a) Shows the results from the simulation with an accretion rate of $1.1 \cdot 10^{17}$g s^{-1} and a crustal heating of 0.9 MeV nuc^{-1}.
b) Shows the results for the run with an accretion rate of $0.3 \cdot 10^{17}$g s^{-1} and a crustal heating of 0.9 MeV nuc^{-1}.

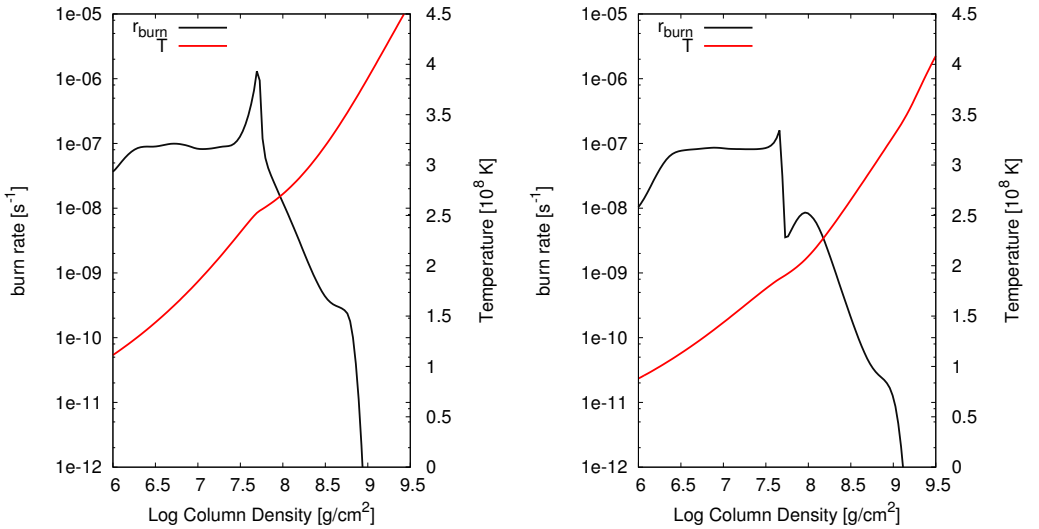

Fig. 3.27.: The burn rate and the temperature of the regions where stable burning occurs.
a) Shows the results from the simulation with an accretion rate of $1.1 \cdot 10^{17}$g s^{-1} and a crustal heating of 0.9 MeV nuc^{-1}.
b) Shows the results for the run with an accretion rate of $0.3 \cdot 10^{17}$g s^{-1} and a crustal heating of 0.9 MeV nuc^{-1}.

only see a small peak at the end of the plateau. This is in agreement with the small increase in the mass fraction of ^{14}O and ^{15}O in the zone at $\log(y) \sim 7.5$ g cm^{-2}, as seen in Fig. (3.26b), which corresponds to the triple-α-reaction feeding the hot CNO-cycle. Therefore, a thick layer of hydrogen burning ashes is produced. Helium burns stable in a deeper layer (at $\log(y) \sim 8$ g cm^{-2}) and produces carbon.

Fig. (3.28) shows the composition of three regions of the simulation with $Q_b = 0.9$ MeV nuc^{-1} and $\dot{M}_{acc} = 0.3 \cdot 10^{17}$ g s^{-1}. The *y*-axis indicates the mass fraction and the *x*-axis denotes the mass number of the isotopes in the composition. The red line shows the composition of the outermost zone, which consists purely out of accreted matter. The blue line shows the composition of the zone with the highest burn rate at a column density of $\sim 4.6 \cdot 10^7$ g cm^{-2} ($\log(y) \approx 7.7$). There we see that most of the mass fraction of hydrogen is already shifted to helium and, additionally, ^{14}O and ^{15}O. The violet line represents the zone at a column density of $\sim 8.4 \cdot 10^8$ g cm^{-2} ($\log(y) \approx 8.9$). In this zone, there is no hydrogen and only some helium is

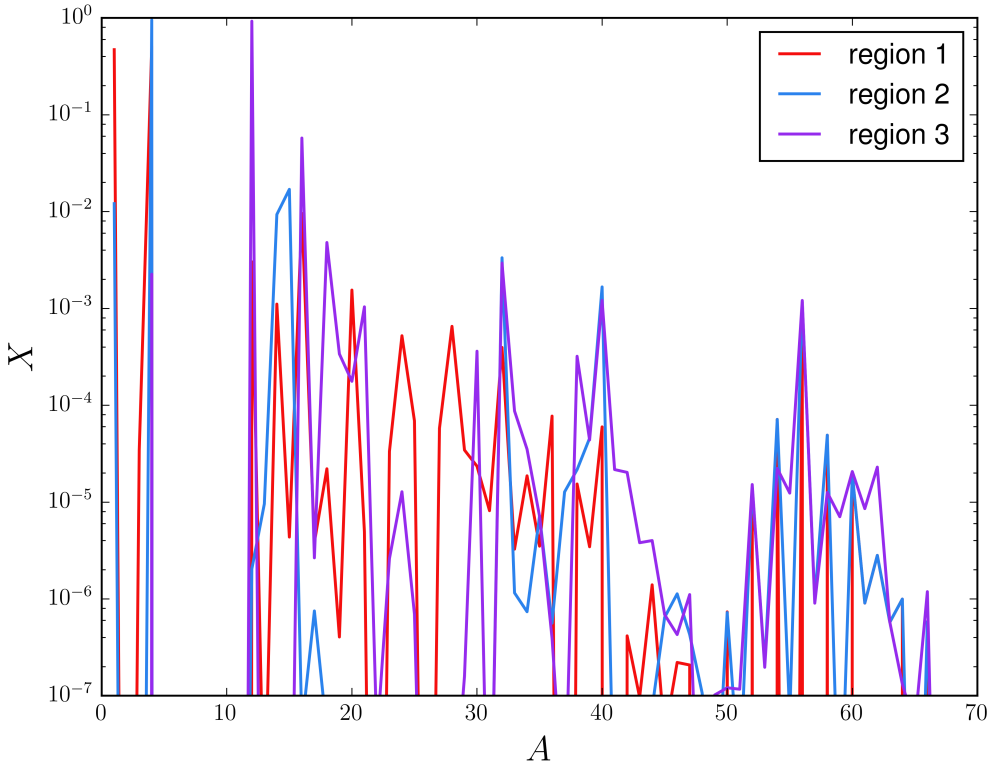

Fig. 3.28.: The composition of three different regions of the results from the simulation with $Q_b = 0.9$ MeV nuc^{-1} and $\dot{M}_{acc} = 0.3 \cdot 10^{17}$ g s^{-1}. The red line, region one, is one of the outermost zones in our domain. Region two, the blue line, is the zone with the highest burn rate at a column density of $4.6 \cdot 10^7$ g cm^{-2} ($\log(y) \approx 7.7$). The violet line, region three, represents one of the zones below the stable burning, where a maximum of ^{12}C is reached, at a column density of $8.4 \cdot 10^8$ g cm^{-2} ($\log(y) \approx 8.9$).

visible, since helium is burned in a layer underneath, as seen in Fig. (3.29a). Carbon dominates the composition with some isotopes at $A \sim 20$.

In Fig. (3.29), we investigate the influence of the accretion rate on the burn rate. In contrast, Q_b has merely any influence on the burn rate (as shown in the Fig. (3.8)) and is thus not shown. Similar to the results for stable burning with solar abundances in the accreted matter in Fig. (3.8), we see here in the left plot Fig. (3.29a), that with low accretion rates ($0.1- \sim 0.4 \cdot 10^{17}$g s^{-1}), two separated peaks in the burn rate appear. This separation of the burning hydrogen and helium region leads to the production of a large amount of carbon. A certain amount of helium survives the hydrogen burning and burns stably in a lower layer into carbon, without feeding the hot CNO, which would only lead to a single peak. In contrast, at higher accretion rates, we see a peak at the end of the plateau of the burn rate, where the triple-α process fuels the hot CNO with additional ^{12}C. This leads to hydrogen depletion and a layer of helium accumulates below the hydrogen burning layer. This layer burns in a stable way to carbon, but does not produce as much carbon as the case with two separated burning regions.

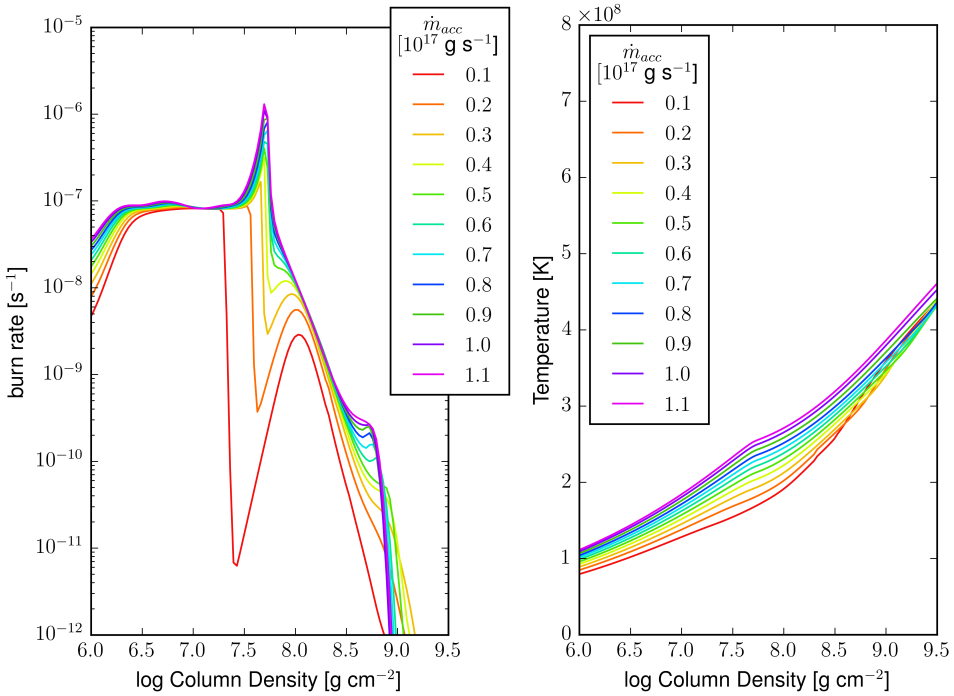

(a) (b)

Fig. 3.29.: The burn rate and the temperature for runs with fixed crustal heating of 0.9 MeV nuc^{-1}, but with different accretion rates from $0.1 \cdot 10^{17}$g s^{-1} (red line) until $1.1 \cdot 10^{17}$g s^{-1} (pink line).
a) Shows the burn rate as a function of the logarithmic column density. The increase of the accretion rate results in a higher burn rates at higher column densities.
b) Shows the temperature profile of the different simulations.

3.4.2 Irregular Bursts Regime

For our numerical simulations with accretion rates of $1.2 \cdot 10^{17}$g s$^{-1} \leq \dot{M}_{acc} \leq 1.5 \cdot 10^{17}$g s^{-1} and crustal heating in the range of 0.7 MeV nuc$^{-1} \leq Q_b \leq 1.5$ MeV nuc^{-1}, with exception of the simulations with crustal heating of 0.7 MeV nuc^{-1} with accretion rates of $1.4 - 1.5 \cdot 10^{17}$g s^{-1}, we get irregular burst behaviour. This means, that first we get for a certain time t_{trans} bursts and afterwards we get stable burning, while the bursts do not reappear. Those are the cases marked with turquoise dots in Fig. (3.24).

In Tab. (3.7), we listed the simulation name in the first column, the number of bursts before stable burning occurs in the second column N$_{burst}$, in the third column the averaged peak luminosity over the first hundred bursts, the fourth column shows the recurrence times of the bursts, the next two columns show the rise time and the burst time, and the last column shows the α-parameter of the bursting phase. We see that increasing accretion rate leads to increasing t_{rise}, increasing $t_{duration}$, and increasing number of bursts before the burning falls into stable burning, since more fuel for bursts is provided in a shorter time. Increasing accretion rate leads further to decreasing peak luminosities and decreasing t_{rec}. The interplay of trends in burst time, recurrence time, and peak luminosity influences the α-parameter in a decreasing manner. Furthermore, we find that with increasing crustal heating, the

run	N$_{burst}$	L$_{peak}$ [erg s^{-1}]	t_{rec} [h]	t_{rise} [s]	$t_{duration}$ [s]	α-value
he07Q12a	180	$2.40 \cdot 10^{38}$	3.24	1.04	42.21	132.2
he07Q13a	260	$2.29 \cdot 10^{38}$	2.89	1.11	43.68	123.3
he09Q12a	74	$2.38 \cdot 10^{38}$	3.22	1.10	41.49	134.0
he09Q13a	121	$2.23 \cdot 10^{38}$	2.86	1.20	43.42	124.1
he09Q14a	184	$2.13 \cdot 10^{38}$	2.59	1.26	45.16	116.1
he09Q15a	240	$2.02 \cdot 10^{38}$	2.36	1.32	46.90	109.5
he11Q12a	52	$2.37 \cdot 10^{38}$	3.22	1.14	41.85	133.3
he11Q13a	81	$2.22 \cdot 10^{38}$	2.85	1.24	42.99	126.1
he11Q14a	143	$2.08 \cdot 10^{38}$	2.56	1.33	45.03	117.3
he11Q15a	273	$1.97 \cdot 10^{38}$	2.34	1.41	46.54	111.3
he13Q12a	45	$2.35 \cdot 10^{38}$	3.23	1.12	41.40	136.5
he13Q13a	63	$2.18 \cdot 10^{38}$	2.86	1.35	43.36	126.6
he13Q14a	83	$2.05 \cdot 10^{38}$	2.56	1.43	44.80	119.3
he13Q15a	96	$1.94 \cdot 10^{38}$	2.32	1.38	46.85	109.4
he15Q12a	38	$2.36 \cdot 10^{38}$	3.23	1.20	41.80	134.2
he15Q13a	54	$2.21 \cdot 10^{38}$	2.85	1.29	43.21	125.5
he15Q14a	68	$2.08 \cdot 10^{38}$	2.56	1.37	44.90	117.9
he15Q15a	81	$1.95 \cdot 10^{38}$	2.33	1.44	46.32	112.6

Tab. 3.7.: The values in this table are averaged over all bursts. If a simulation shows more than 100 bursts, the average is taken over the first 100 bursts. The first column shows the simulation conditions.

number of bursts decreases, since Q_b influences the ignition depth in a decreasing fashion, as shown in [25].

In the next table (Tab. (3.8)), we show the values for the transition between bursts and stable burning. The table lists from left to right, the simulation identification, the transition time, the quiescent luminosity, and the luminosity in the stable phase L_{stable}. In the next two columns, we show the ignition column density $y_{ignition}$ of the burst phase and the column density of the stable burning $y_{stableburning}$, which is the column density of the zone where the burn rate is the highest. We find that with increasing crustal heating the t_{trans} decreases, while the quiescent luminosity and the luminosity during stable burning remain more or less unchanged. With increasing accretion rate, the transition time increases, as well as the quiescent luminosity and the luminosity of the stable burning system. The region where the burn rate peaks is neither largely influenced by the crustal heating nor the accretion rate. Nevertheless, if we compare early bursts with the last burst, we see that the last burst ignites at lower column density, at lower density (5th burst: $3.11 \cdot 10^5$g cm^{-3},

run	t_{trans} [h]	$L_{quiescent}$ [erg s^{-1}]	L_{stable} [erg s^{-1}]	$y_{ignition}$ [10^7 g cm^{-2}]	$y_{stableburning}$ [10^7 g cm^{-2}]
he07Q12a	572.5	$3.50 \cdot 10^{35}$	$6.49 \cdot 10^{35}$	4.2380	4.9459
he07Q13a	684.7	$3.58 \cdot 10^{35}$	$7.01 \cdot 10^{35}$	4.5766	5.3409
he09Q12a	238.0	$3.37 \cdot 10^{35}$	$6.51 \cdot 10^{35}$	4.5766	4.9456
he09Q13a	296.9	$3.59 \cdot 10^{35}$	$7.04 \cdot 10^{35}$	4.9423	4.9456
he09Q14a	371.3	$3.96 \cdot 10^{35}$	$7.63 \cdot 10^{35}$	4.5770	4.9457
he09Q15a	410.6	$4.23 \cdot 10^{35}$	$8.13 \cdot 10^{35}$	4.5771	4.9456
he11Q12a	167.4	$3.55 \cdot 10^{35}$	$6.53 \cdot 10^{35}$	4.9423	4.9457
he11Q13a	230.9	$3.66 \cdot 10^{35}$	$7.14 \cdot 10^{35}$	4.9423	4.9456
he11Q14a	261.2	$3.98 \cdot 10^{35}$	$7.73 \cdot 10^{35}$	4.5766	4.9456
he11Q15a	530.5	$4.69 \cdot 10^{35}$	$8.62 \cdot 10^{35}$	4.2386	4.9458
he13Q12a	144.9	$3.66 \cdot 10^{35}$	$6.55 \cdot 10^{35}$	4.9422	4.9461
he13Q13a	179.8	$3.72 \cdot 10^{35}$	$7.18 \cdot 10^{35}$	4.9423	4.9461
he13Q14a	212.6	$3.88 \cdot 10^{35}$	$7.75 \cdot 10^{35}$	4.9426	4.9460
he13Q15a	222.9	$4.11 \cdot 10^{35}$	$8.08 \cdot 10^{35}$	4.9427	4.9460
he15Q12a	122.3	$3.47 \cdot 10^{35}$	$6.60 \cdot 10^{35}$	4.5766	4.9455
he15Q13a	153.8	$3.82 \cdot 10^{35}$	$7.21 \cdot 10^{35}$	4.5768	4.9457
he15Q14a	174.2	$4.18 \cdot 10^{35}$	$7.77 \cdot 10^{35}$	4.5769	4.9456
he15Q15a	189.1	$4.42 \cdot 10^{35}$	$8.24 \cdot 10^{35}$	4.5769	4.9580

Tab. 3.8.: In this table, values for the change of the bursting phase to the stable burning phase are shown. The second column, t_{trans}, shows the time of the transition from bursts to stable burning. As all the runs show after the last burst a "trying" ignition of a further burst, which fails, we took this failed ignition as the time of transition. The next two columns show the quiescent luminosity between two bursts and the luminosity of the stable burning after the transition. The last two columns show the the ignition depth of one of the last bursts, $y_{ignition}$, and the column density of the stable burning, $y_{stableburning}$, where the burn rate is the highest.

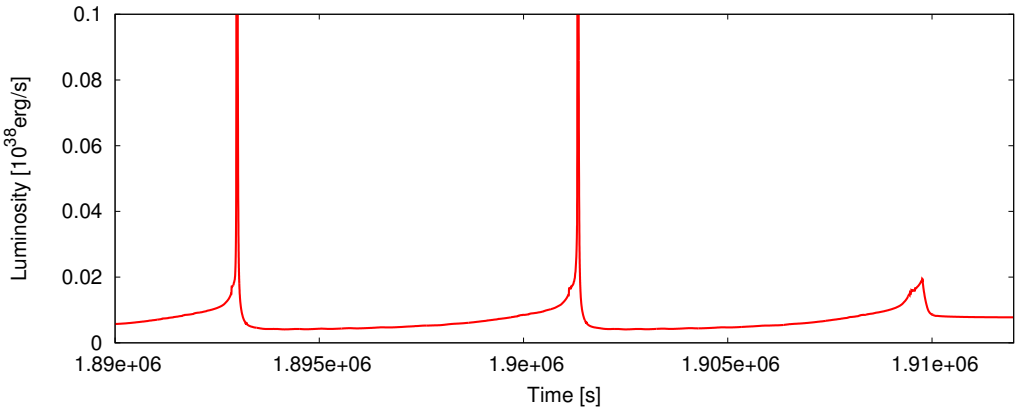

Fig. 3.30.: The light curve of the last two bursts and the failed burst, which initiate the stable burning phase of the irregular burst regime. This light curve is from the simulation with the condition for accretion rate of $1.5 \cdot 10^{17}$g s^{-1} and crustal heat of 1.1 MeV nuc^{-1}

last burst: $3.00 \cdot 10^{5}$g cm^{-3}) and at lower temperatures (5th burst: $3.2 \cdot 10^{8}$ K, last burst: $3.00 \cdot 10^{8}$ K). This leads to more and more ineffective bursts, where the state of the matter behaving as a degenerate gas gets shorter. After the last burst, conditions for a thermonuclear runaway are not given anymore and stable burning occur. Additionally, when the ignition depth is shifted more and more into higher layers of the neutron star, the convection contributes a bigger part, since [25] showed that those layers are affected by convection.

Fig. (3.30) shows the transition from bursts to stable burning for the simulation with crustal heat of 1.1 MeV nuc^{-1} and accretion rate of $1.5 \cdot 10^{17}$g s^{-1}. Already the bursts before do not show typical burst behaviour. The shape of the light curve does not show the typical fast rise and slow decay. The third burst visible in Fig. (3.30) is the “failed” burst, where the light curve shows the start of a rise, but the light curve does not reach the high luminosities of a full burst and soon decreases again to a stable value.

Fig. (3.31) shows in the two top plots the time evolution of the burn rate (top left) and the temperature (top right) over the fifth burst of the simulation with crustal heating of 1.1 MeV nuc^{-1} and an accretion rate of $1.3 \cdot 10^{17}$ g s^{-1}. The two bottom plots show the same values for the last burst from the same simulation. If we compare the top with the bottom plots, we can see that the last burst does not influence as much the layers underneath as the fifth burst. Additionally, those layers underneath the burst region already show more nuclear reaction activity than the same layers in the plot of the fifth burst. This shows that the last burst is already less effective, since fuel for the burst is burning stably and a next burst can not ignite. Both temperature plots are similar, with the exception that for the last burst, the lowest layers are heated due to crustal heating.

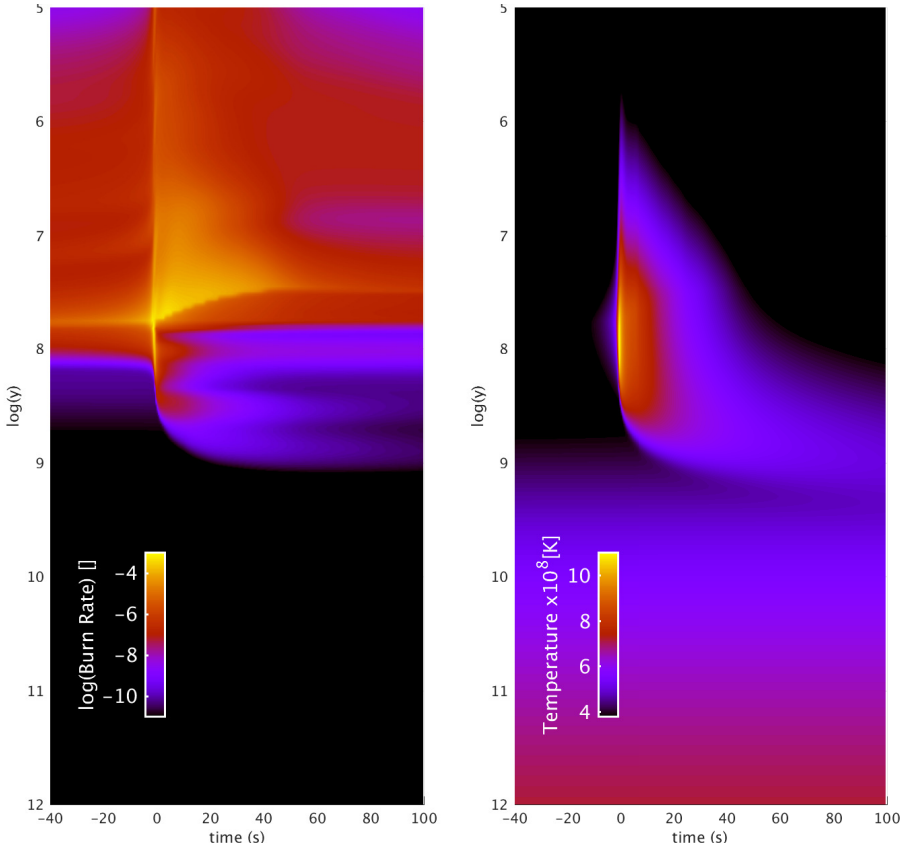

(a)

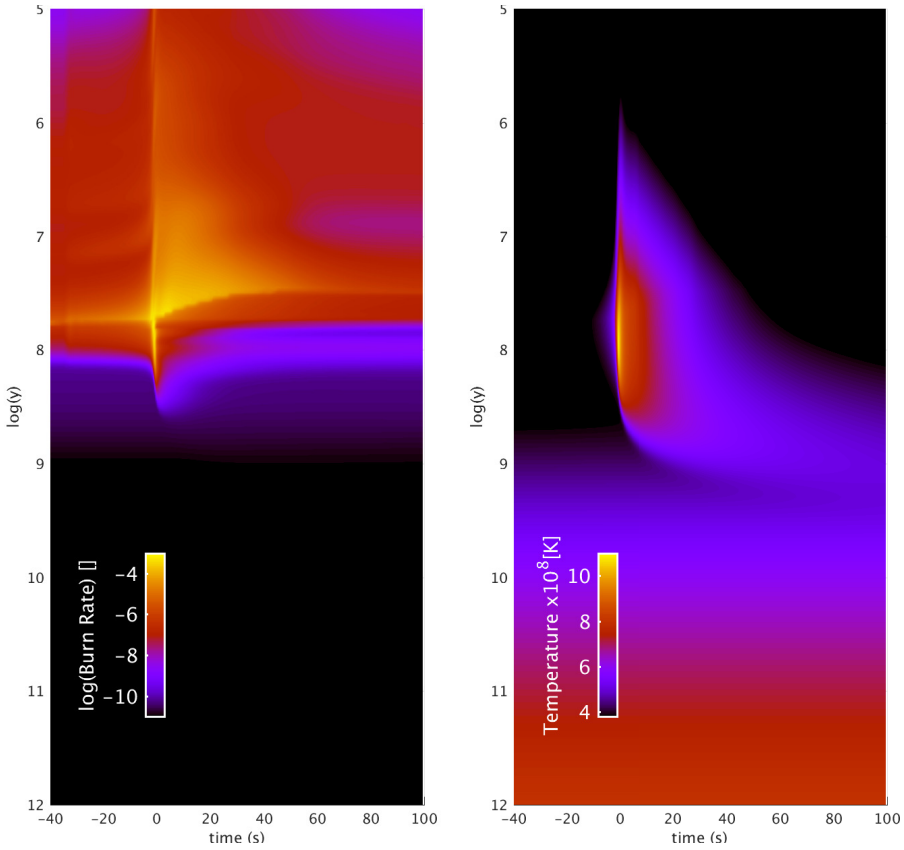

(b)

Fig. 3.31.: The results from the simulation he11Q13a are shown. L_{peak} is chosen to be at $t = 0$ s. These four figures show the burn rate over one burst (left figures) and the temperature over one burst (right figures).
a) Shows the results of the fifth burst. b) Shows the results of the last burst.

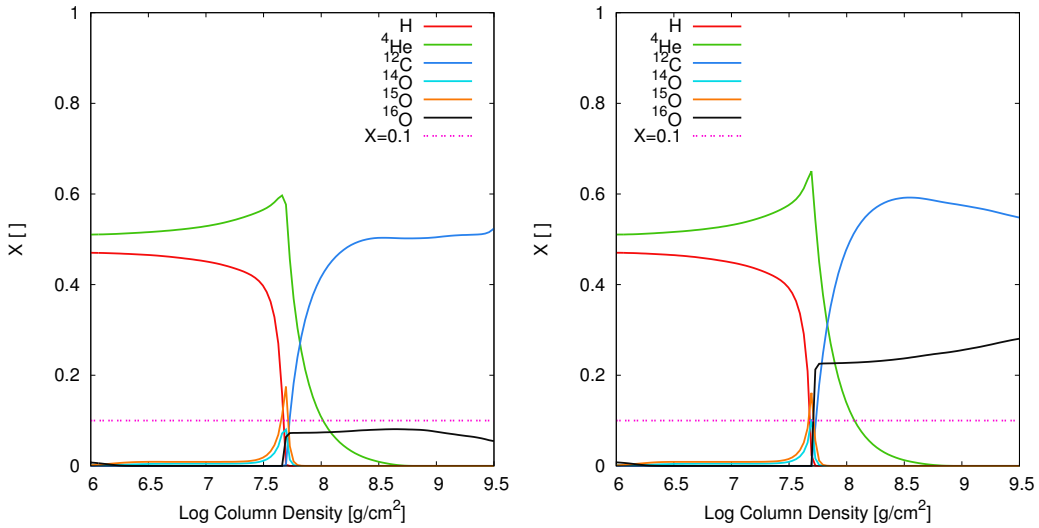

Fig. 3.32.: The mass fractions of hydrogen (red line), ^{4}He (green line), ^{12}C (blue line), ^{14}O (light turquoise line), ^{15}O (orange line), ^{16}O (black line), and the minimal mass fraction of 0.1 (pink dashed line), which would be needed for the successful ignition of a superburst.
a) Shows the results from the simulation with an accretion rate of $1.5 \cdot 10^{17}$g s^{-1} and a crustal heating of 1.1 MeV nuc^{-1}.
b) Shows the results for the run with an accretion rate of $1.3 \cdot 10^{17}$g s^{-1} and a crustal heating of 1.1 MeV nuc^{-1}.

In Fig. (3.32), we show the mass fraction of ^{1}H (red line), ^{4}He (green line), ^{12}C (blue line), ^{14}O (light turquoise line), ^{15}O (orange line), and ^{16}O (black line) in dependence of the column density for high accretion rate in the left plot and for slightly lower in the right. For both plots, a crustal heating of 1.1 MeV nuc^{-1} is used. The main difference between these two plots is in the stronger production of ^{16}O in the case with higher accretion rate in Fig. (3.32a). Both show an increase of hot CNO nuclei at the lower part of the hydrogen burning region of the accreted layer, which consists mainly out of helium and hydrogen. Also the profiles of the burn rates of these two situations look similar, as seen in Fig. (3.33), but for the higher accretion rate (Fig. (3.32a)) the burn rate drops at a smaller column density. The temperature profiles also show only small differences. Notably, the peak in the burn rate corresponds to a slightly higher temperature in the case of higher accretion rate, Fig. (3.33a), as compared to the situation with smaller accretion rate, Fig. (3.33b). Notably, at lower temperatures (Fig. (3.33b)), the region corresponding to the peak in the burn rate produces twice as much oxygen (black line in Fig. (3.32b)) than in the situation with higher temperatures (black line in Fig. (3.32a)).

Fig. (3.34) shows three regions of the simulation with the conditions $Q_b = 1.1$ MeV nuc^{-1} and $\dot{M}_{acc} = 1.3 \cdot 10^{17}$ g s^{-1}. The red line represents one of the outermost

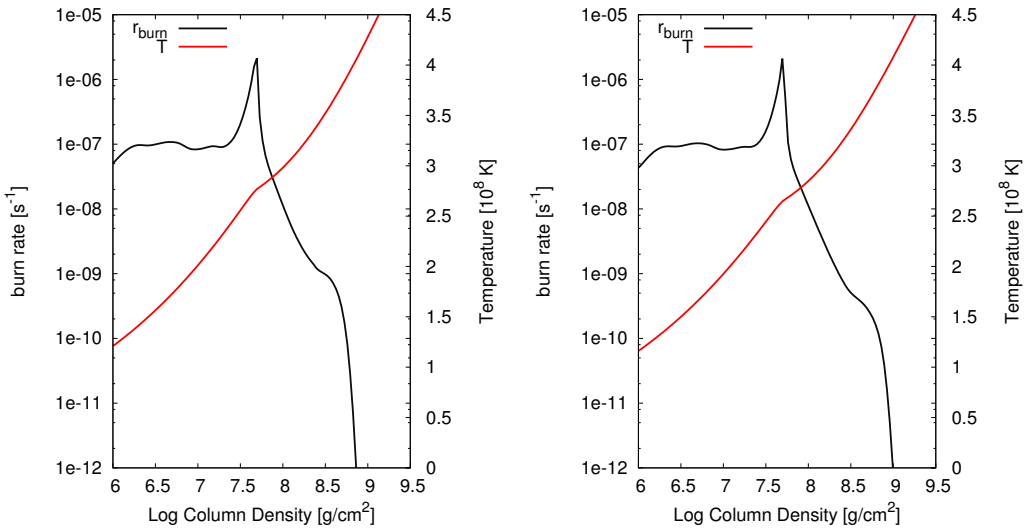

Fig. 3.33.: The burn rate and the temperature of the regions, where stable burning occurs. a) Shows the results from the simulation with an accretion rate of $1.5 \cdot 10^{17}$g s^{-1} and a crustal heating of 1.1 MeV nuc^{-1}.
b) Shows the results for the run with an accretion rate of $1.3 \cdot 10^{17}$g s^{-1} and a crustal heating of 1.1 MeV nuc^{-1}.

zones, which consists mainly out of accreted matter. The blue line shows the mass fractions of the composition of the zone with the highest burn rate at a column density of $4.9 \cdot 10^7$ g cm^{-2} ($\log(y) \approx 7.7$). Furthermore, the violet line represents the composition of a zone underneath the stable burning region at a column density of $1.8 \cdot 10^9$ g cm^{-2} ($\log(y) \approx 9.3$). In region 2 (blue line), we find mainly helium, oxygen isotopes (^{14}O and ^{15}O), and some heavier isotopes. In contrast, in the region of the ashes (violet line), ^{12}C and ^{16}O dominate the composition of less abundant heavier isotopes. Those heavier isotopes could be a remainder of the bursting phase of this simulation. However, since the time difference between the transition and the time at which this composition was taken is ~ 700 hours, this is highly improbable. Thus, the composition should consist of ashes, but due to advection mixing of the composition, one cannot exclude that still some isotopes from the bursting phase exist in this layer. Since heavier isotopes are also present in the burning region, one can conclude that they are produced during the stable burning and undergo reactions in the not so active zones below region 2.

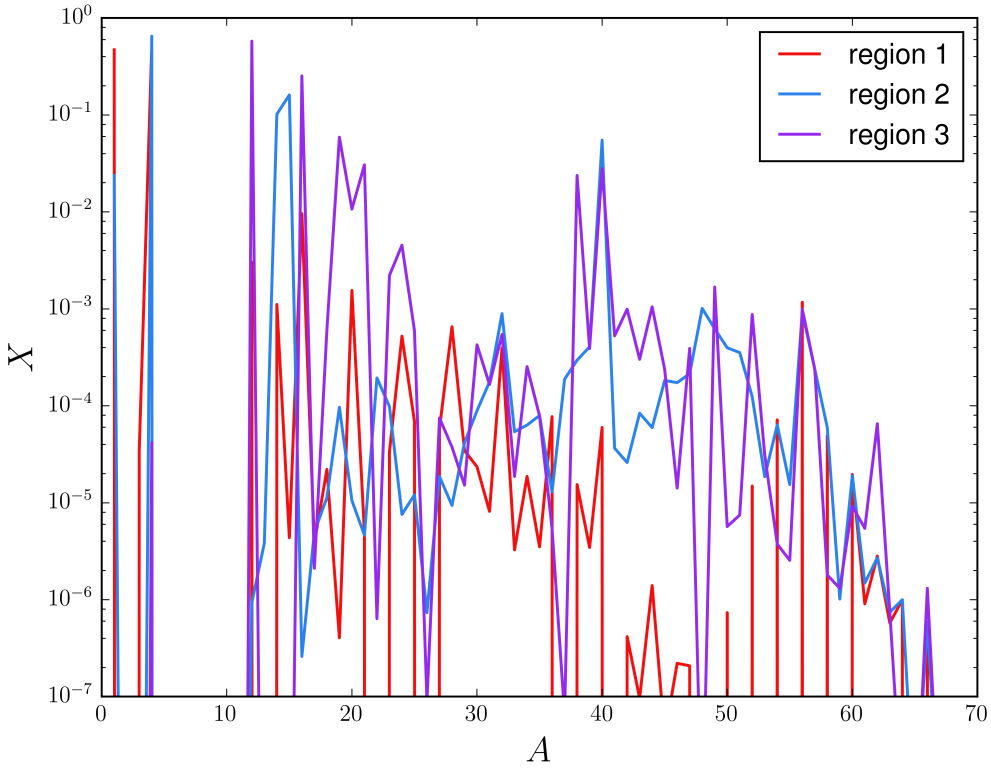

Fig. 3.34.: The composition of three different regions of the results from the simulation with $Q_b = 1.1$ MeV nuc^{-1} and $\dot{M}_{acc} = 1.3 \cdot 10^{17}$ g s^{-1}. The red line, region one, is one of the outermost zones in our domain. Region two, the blue line, is the zone with the highest burn rate at a column density of $4.9 \cdot 10^7$ g cm^{-2} ($\log(y) \approx 7.7$). The violet line, region three, represents one of the zones below the stable burning, where a maximum of ^{12}C is reached at a column density of $1.8 \cdot 10^9$ g cm^{-2} ($\log(y) \approx 9.3$).

3.4.3 Regular Burst Regime

For our numerical simulations with accretion rates of $1.2 \cdot 10^{17}$g s$^{-1} \leq \dot{M}_{acc} \leq 1.5 \cdot 10^{17}$g s^{-1} and crustal heating in the range of 0.1 MeV nuc$^{-1} \leq Q_b \leq 0.7$ MeV nuc^{-1}, with exception of the simulations with crustal heating of 0.7 MeV nuc^{-1} and accretion rates of $1.2 - 1.3 \cdot 10^{17}$g s^{-1}, we find regular burst behaviour. This is only a small area in our parameter space. The regular bursting conditions are represented by the violet dots in Fig. (3.24).

We show here the results of five numerical simulations (all results can be found in the Appendix A.1.2). We choose two parameter sets with low Q_b value ($= 0.1$ MeV nuc^{-1}) and accretion rates at the border of our regime ($= 1.2$ and $1.5 \cdot 10^{17}$ g s^{-1}), one set with intermediate Q_b value ($= 0.3$ MeV nuc^{-1}) and intermediate accretion rate ($= 1.3 \cdot 10^{17}$ g s^{-1}), and two sets with higher Q_b value ($= 0.5$ MeV nuc^{-1}) and accretion rates at the border of our regime ($= 1.2$ and $1.5 \cdot 10^{17}$ g s^{-1}).

In Fig. (3.35), we show the light curves of our five example simulations of this regime. This figure shows the luminosity in units of 10^{38} erg s^{-1} as a function of time covering ~ 13.9 hours. We see that simulations with higher accretion rate show lower peak luminosities ($\sim 2 \cdot 10^{38}$erg s^{-1}) and shorter recurrence times (~ 2.4 h) and are represented by the orange and the green line, respectively. In contrast, low accretion rates (red and violet line), i.e. low in terms of our range of this regime, show higher peak luminosities ($\sim 2.4 \cdot 10^{38}$erg s^{-1}) and longer recurrence times (~ 3.2 h). This behaviour reflects the results of [25, 138], since higher accretion rates shift the ignition depth of the burst to higher column densities, and therefore, the burst ignites at higher temperatures and higher densities. This leads to weaker

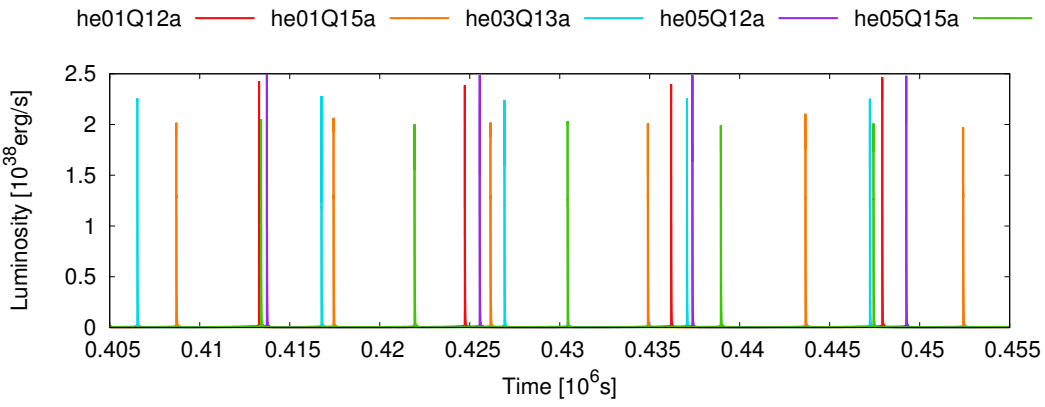

Fig. 3.35.: The light curves of five representative simulations over a time of roughly 13.9 hours. The colour affiliation to the parameter sets are given in the legend above the plot. We use the nomenclature stated in Eq. (3.6).

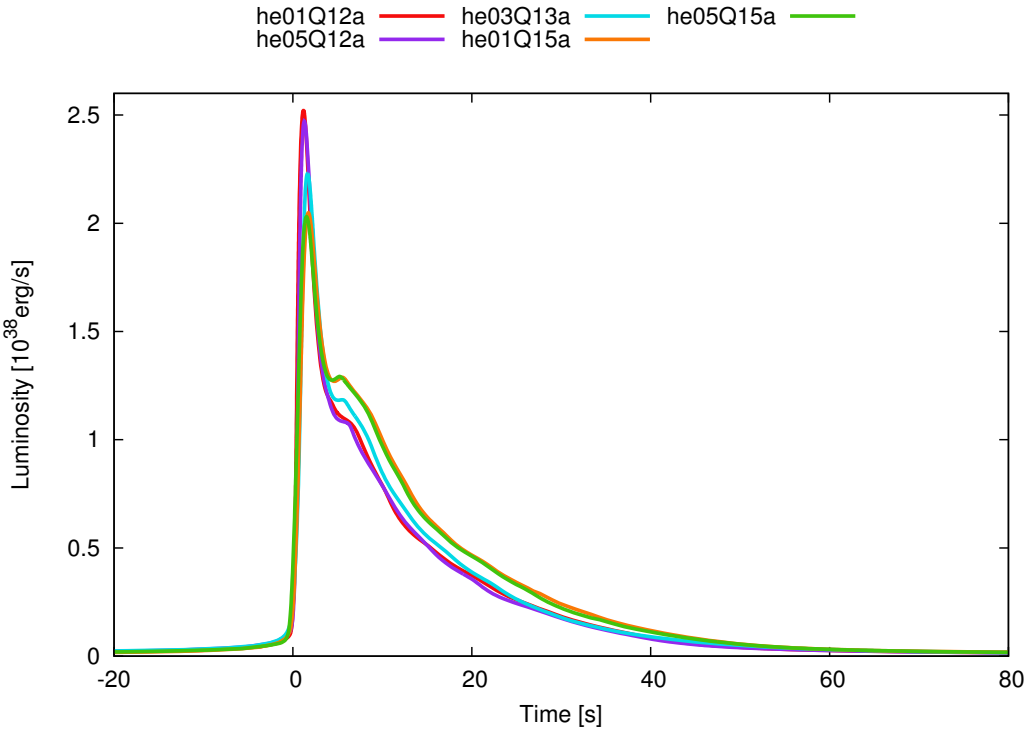

Fig. 3.36.: This figure shows the light curves of one example burst of our five chosen simulations. The times have been shifted so that the steep rise of the curves lay on each other.

bursts with shorter recurrence times.

Fig. (3.36) shows one burst from each of the previous five simulations. The colour-code is the same as in Fig. (3.35). We can see that the bursts show the typical fast rise to the peak luminosity, which increases with decreasing accretion rate (compare, e.g. violet, blue, and green line for increasing accretion rate). The bursts also show a longer decay with a peculiar small second peak, which appears at higher luminosities for larger accretion rates. It should be noted that we show here one specific example of a burst for each of our parameters. The bursts of one simulation can vary, but the general behaviour is represented by these examples.

In Tab. (3.9), we show the values averaged over 100 bursts of these five simulations. This table lists from left to right, the simulation name, the number of bursts, the peak luminosity, the recurrence time, the rise time, the burst duration, and the α-parameter. We see differences in the recurrence time in dependence on the accretion rate. The burst length ($t_{duration}$) shows decreasing behaviour with increasing crustal heat, but increasing tendency with increasing accretion rate. The α-parameter decreases with increasing crustal heat as well as with increasing accretion rate.

run	N_{burst}	L_{peak} [erg s^{-1}]	t_{rec} [h]	t_{rise} [s]	$t_{duration}$ [s]	α-value
he01Q12a	427	$2.42 \cdot 10^{38}$	3.2	0.93	43.45	121.2
he01Q15a	654	$2.05 \cdot 10^{38}$	2.43	1.26	48.60	101.5
he03Q13a	373	$2.25 \cdot 10^{38}$	2.83	1.04	45.06	111.7
he05Q12a	271	$2.47 \cdot 10^{38}$	3.28	0.94	41.99	131.7
he05Q15a	479	$2.02 \cdot 10^{38}$	2.36	1.31	47.85	103.7

Tab. 3.9.: The values in this table are averaged over all bursts. If a simulation shows more than 100 bursts, it is averaged over the first 100 bursts. The first column states the simulation conditions.

Fig. (3.37) shows the dependency of our simulations on the crustal heating and on the accretion rate. The top left and bottom left plot show the dependency of the peak luminosity (top) and the recurrence time on the crustal heat (bottom). We kept the value for the accretion rate fixed at $1.3 \cdot 10^{17}$g s^{-1}. We find that the crustal heating

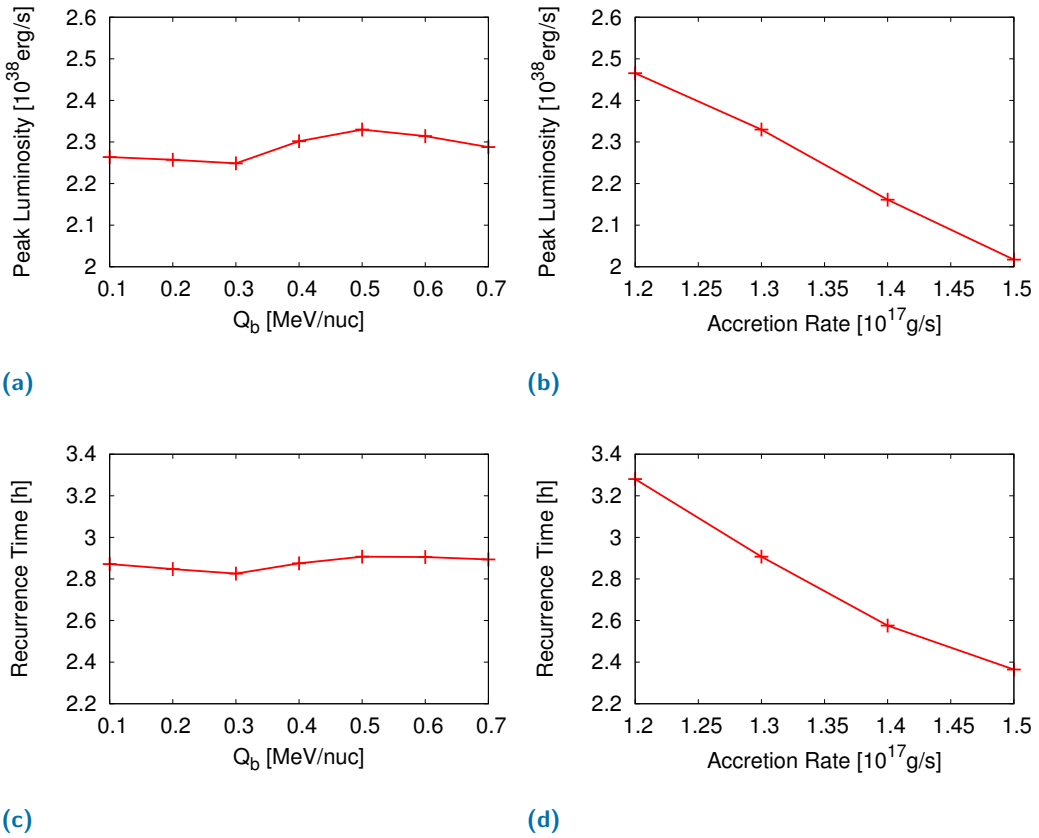

Fig. 3.37.: a) Shows the peak luminosity in dependence on the crustal heating. The accretion rate is fixed at $1.3 \cdot 10^{17}$g s^{-1}.
b) Shows the peak luminosity in dependence on the accretion rate. The crustal heating is fixed at 0.5 MeV nuc^{-1}.
c) Shows the recurrence time in dependence on the crustal heating. The accretion rate is fixed at $1.3 \cdot 10^{17}$g s^{-1}.
d) Shows the recurrence time in dependence on the accretion rate. The crustal heating is fixed at 0.5 MeV nuc^{-1}.

only has a minor influence on the recurrence time. In the right top and bottom plot, we show the peak luminosity (top) and the recurrence time (bottom) on dependency on the accretion rate. For those two plots, we fixed the crustal heating at a value of 0.5 MeV nuc^{-1}. We see that the accretion rate has a large influence on the peak luminosity and on the recurrence time: both decrease with increasing accretion rate. As already mentioned in Sec. 3.3, the change in recurrence times hints that the ignition depth of the burst has been shifted to other conditions. High accretion rates lead to lower recurrence times, which was also shown in [25]. We see in the same fashion a decrease of the luminosity. This indicates that not the entire fraction of fuel is depleted in the burst region for high accretion rates, as it is the case for low accretion rates, where a helium dominated burst occurs [25, 139].

In the following, we take a closer look at what is happening in the layers, where the bursts ignite and leave ashes, and in between bursts, when quiescent burning occurs. We do this to see if the accretion rate has any influence on the prevailing composition, as it was noted in [25]. In Fig. (3.38), we show the mass fraction as a function of the column density. The plots reveal the mass fractions of ^{1}H (red line), ^{4}He (green line), ^{12}C (blue line), ^{14}O (light turquoise line), ^{15}O (orange line), and ^{16}O (black line). The left plot (Fig. (3.38a)) shows the results of a simulation with

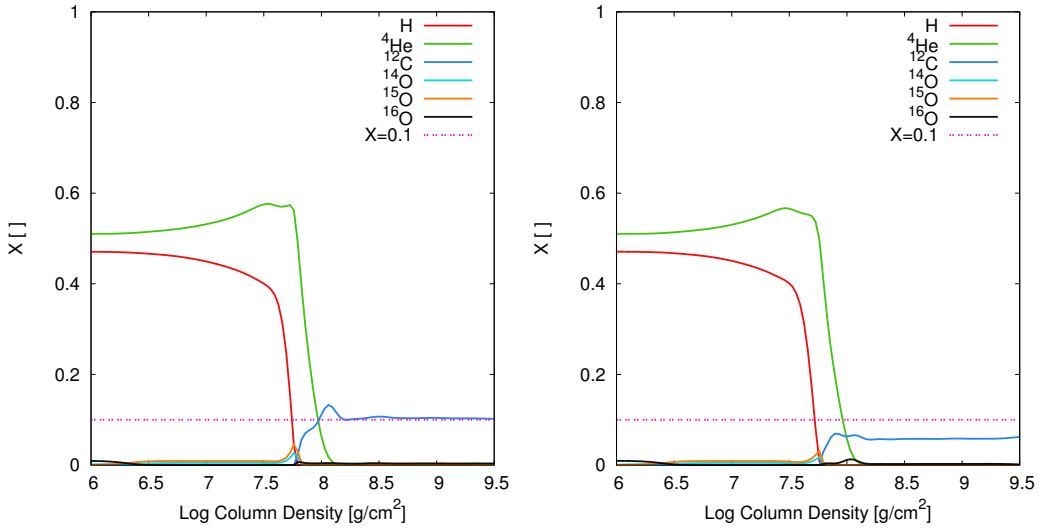

Fig. 3.38.: The mass fractions of hydrogen (red line), ^{4}He (green line), ^{12}C (blue line), ^{14}O (light turquoise line), ^{15}O (orange line), ^{16}O (black line), and the minimal mass fraction of 0.1 (pink dashed line), which would be needed for the successful ignition of a superburst.
a) Shows the results from the simulation with an accretion rate of $1.2 \cdot 10^{17}$g s^{-1} and a crustal heating of 0.5 MeV nuc^{-1}.
b) Shows the results for the run with an accretion rate of $1.5 \cdot 10^{17}$g s^{-1} and a crustal heating of 0.1 MeV nuc^{-1}.

an accretion rate of $1.2 \cdot 10^{17}$g s^{-1} and a crustal heating of 0.5 MeV nuc^{-1}, whereas the right plot (Fig. (3.38b)) shows the results of a simulation with an accretion rate of $1.5 \cdot 10^{17}$g s^{-1} and a crustal heating of 0.1 MeV nuc^{-1}. The layers of the range of $\log(y) \sim 7 - 8$ g cm^{-2} are mostly influenced by stable burning in the quiescent phase between bursts, whereas deeper layers consist mainly of ashes from previous bursts. Even if they look similar, a change in the ignition depth can have influences in the burst behaviour. The main difference is the amount of produced carbon. In Fig. (3.39a), we have a large amount of carbon in the ashes layers of the burst. This is favourable for superburst simulations, since the mass fraction of carbon exceeds 10%. The small peak in the carbon mass fraction comes from stable helium burning in this region. But this region is heated during a burst and the prevailing carbon is destroyed.

As we can see in Fig. (3.39), in this region of column density, the burn rate rises to high values and then decreases back to negligible values in deeper zones. This is between two bursts. We can hardly find a second peak, thus, there is only a thin shell of helium-rich matter below the mixed hydrogen and helium burning region. Therefore, the stable burning between bursts cannot produce much carbon.

In Fig. (3.40), we show the composition of three regions of the simulation with crustal heating of $Q_b = 0.5$ MeV nuc^{-1} and with an accretion rate of $\dot{M}_{acc} =$

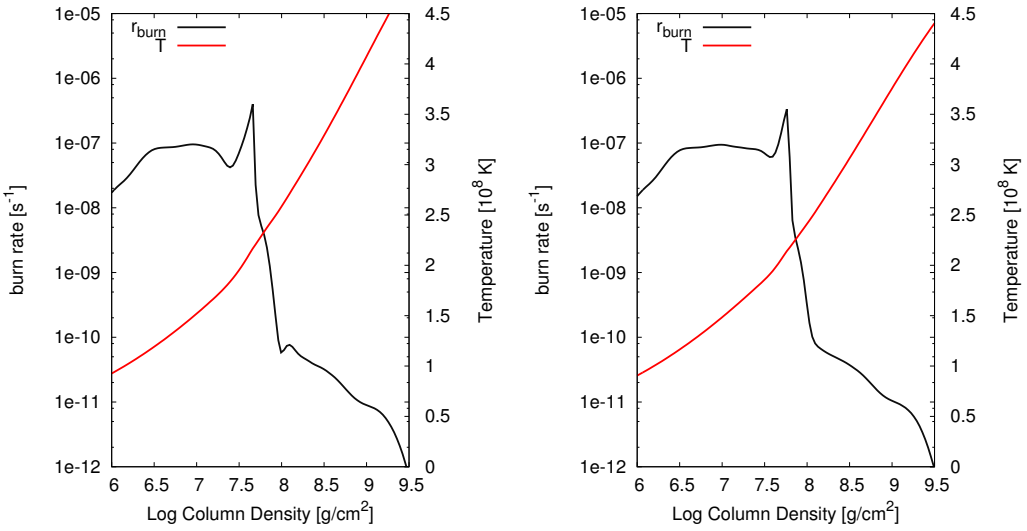

(a) (b)

Fig. 3.39.: The burn rate and the temperature of the regions where stable burning occurs.
a) Shows the results from the simulation with an accretion rate of $1.2 \cdot 10^{17}$g s^{-1} and a crustal heating of 0.5 MeV nuc^{-1}.
b) Shows the results for the run with an accretion rate of $1.5 \cdot 10^{17}$g s^{-1} and a crustal heating of 0.1 MeV nuc^{-1}.

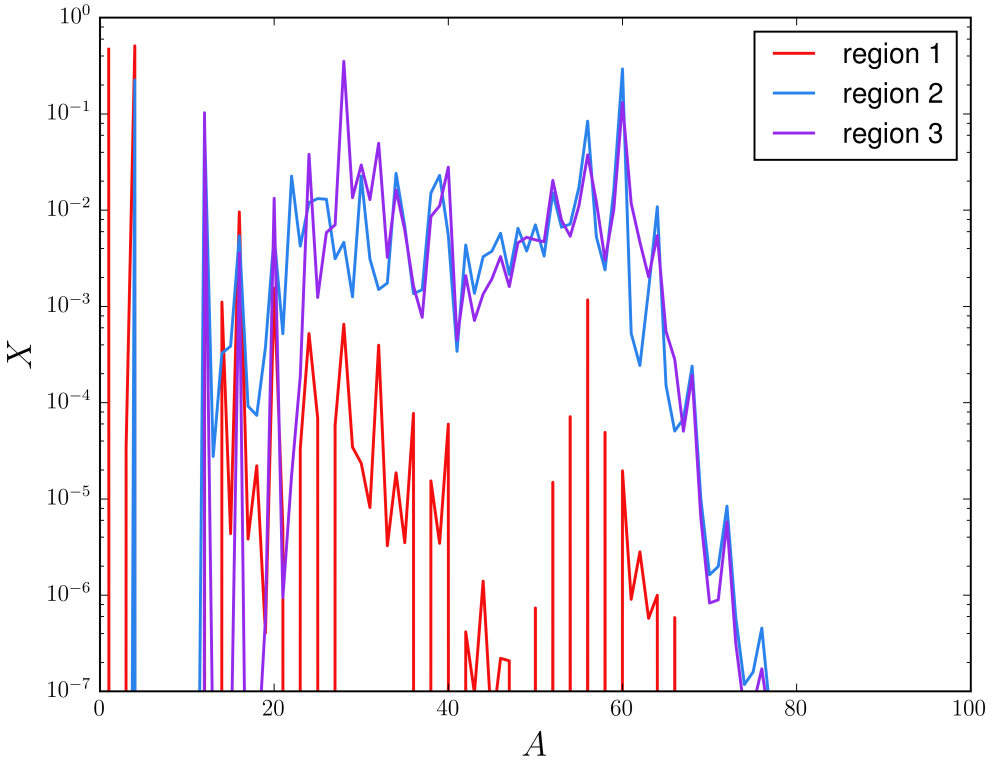

Fig. 3.40.: The composition of three different regions from the simulation with $Q_b = 0.5$ MeV nuc^{-1} and $\dot{M}_{acc} = 1.2 \cdot 10^{17}$ g s^{-1}. The red line, region one, is one of the outermost zones in our domain. Region two, the blue line, is the zone with the highest burn rate at a column density of $4.6 \cdot 10^7$ g cm^{-2} ($\log(y) \approx 7.7$). The violet line, region three, represents one of the zones below the stable burning, where a maximum of ^{12}C is reached at a column density of $1.8 \cdot 10^9$ g cm^{-2} ($\log(y) \approx 9.3$).

$1.2 \cdot 10^{17}$ g s^{-1}. The red line represents the composition of the outermost zone, and therefore, shows the composition of the accreted matter. The blue line represents the composition of the most active zone (in terms of burn rate) during the quiescent burning. This region is at a column density of $4.6 \cdot 10^7$ g cm^{-2} ($\log(y) \approx 7.7$). The violet line represents a zone beneath the quiescent burning and thus, a region which is not influenced by stable burning at a column density of $1.8 \cdot 10^9$ g cm^{-2} ($\log(y) \approx 9.3$). This violet line represents the ashes of the previous bursts, which sank into deeper layers. If we compare the composition of these three regions in our computational domain, we see that the most active zone of the quiescent burning (region 2, blue line) is dominated by heavier isotopes and lighter elements. Most of the heavier isotopes $20 \lesssim A \lesssim 70$ are produced during the bursts, whereas most of the light elements are either newly accreted or produced during stable burning. Here, hydrogen is absent since all of it is consumed in the quiescent burning. In the region of the ashes of Type I X-ray bursts (region 3), helium is absent, since it is completely destroyed during a burst in the layers underneath the ignition of a burst.

Fig. (3.41a) shows the burn rate (left plot) and the temperature (right plot) evolution over one burst. During a burst, the burn rate rises fast to high values and reaches out to lower and higher column densities. Due to the rise in the nuclear reaction activity, the temperature rises enabling the αp and the rp-process. The temperature reaches values of $\sim 1.0 \cdot 10^8$ K at densities of $3 - 4 \cdot 10^5$ g cm^{-3} at the peak luminosity ($t = 0$ in these plots). At these conditions, matter does not behave like a degenerate gas anymore and the reaction flow of the processes slows down. The hydrogen in the ignition region is completely depleted (Fig. (3.41b), left plot), whereas some fraction of helium (right plot) remains in the ignition zone, while in the zones below is immediately depleted. Fig. (3.41) shows a burst of a simulation with an accretion rate of $1.2 \cdot 10^{17}$ g s^{-1} and crustal heating of 0.5 MeV nuc^{-1}.

Fig. (3.42) shows the change of the mass fraction during a burst. The considered mass fractions are hydrogen (H, red line), helium (^{4}He, green line), carbon (^{12}C, blue line), oxygen (^{16}O, black line), and silicon (^{28}Si, orange line). The three plots of Fig. (3.42) are the results of the simulation with the conditions $Q_b = 0.5$ MeV nuc^{-1} and $\dot{M}_{acc} = 1.2 \cdot 10^{17}$ g s^{-1}. Fig. (3.42b) shows the mass fractions of the above mentioned isotopes of the ignition zone. This zone is chosen because at the time of the peak luminosity this zone shows the highest burn rate at a column density of $5.34 \cdot 10^7$ g cm^{-2} ($\log y = 7.73$). We show the same range of time as in Fig. (3.21), i.e. from $t_0 - 25$ s to $t_0 + 145$ s, where t_0 marks the time of the peak luminosity. Fig. (3.42a) shows the mass fractions of the zone above the burst zone and Fig. (3.42c) the results from the zone beneath the burst. In Fig. (3.42a), all hydrogen is depleted during the burst, ~ 4 seconds after the peak luminosity, and therefore, later than in the ignition zone, where hydrogen is already depleted in less than one second after reaching the peak luminosity. In the zone above the ignition zone, nearly a third of the mass fraction of helium survives the burst. Carbon and silicon are produced during the burst. In the ignition zone (Fig. (3.42b)), little hydrogen is available, which is fast consumed when the burst starts. Also, a huge amount of helium is consumed, but some mass fraction survives the burst. In this zone, carbon and silicon are produced. In the zone below the ignition zone, in Fig. (3.42c), only a small amount of hydrogen is present, which is then consumed. Helium has not been destroyed previously through quiescent burning. Shortly before reaching the peak luminosity, ^{16}O is produced in the zone below the ignition, but within 3 seconds is destroyed again through α-capture. After the burst, ^{28}Si represents nearly a third of the composition in the zone below the ignition.

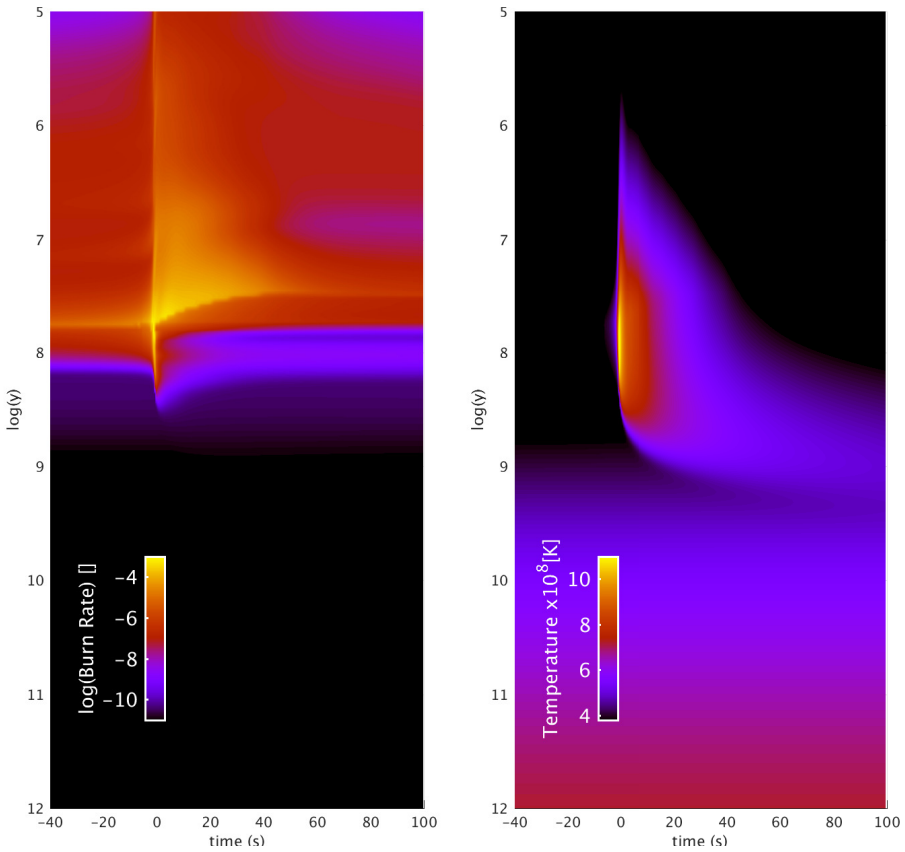

(a)

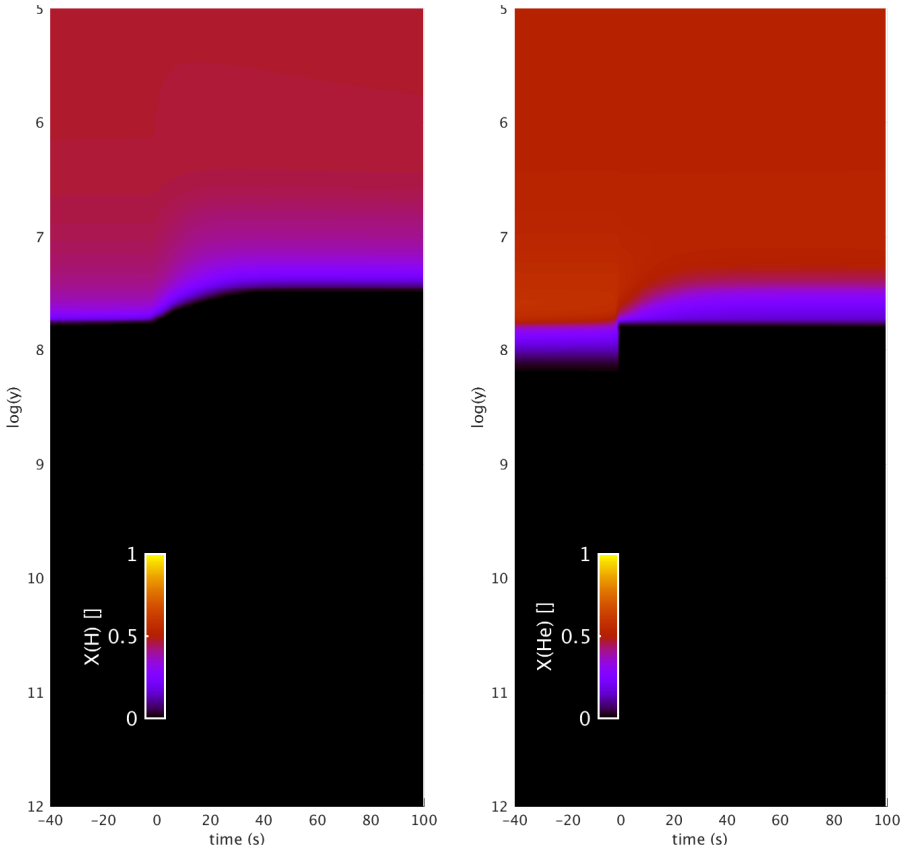

(b)

Fig. 3.41.: The results from the simulation he05Q12a are shown. L_{peak} is chosen to be at $t = 0$ s. The figures in a) show the burn rate over one burst (left) and the temperature over one burst (right). The figures in b) show the mass fraction of H and He.

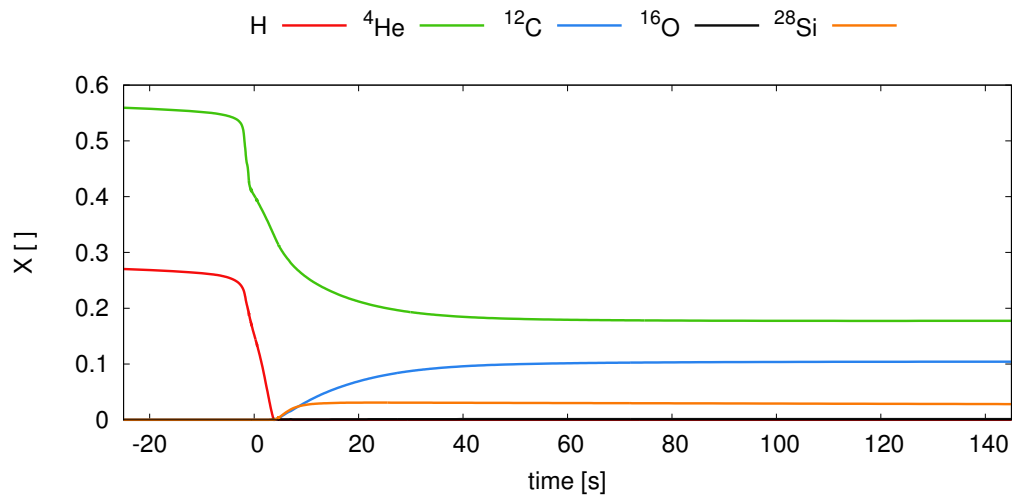

(a)

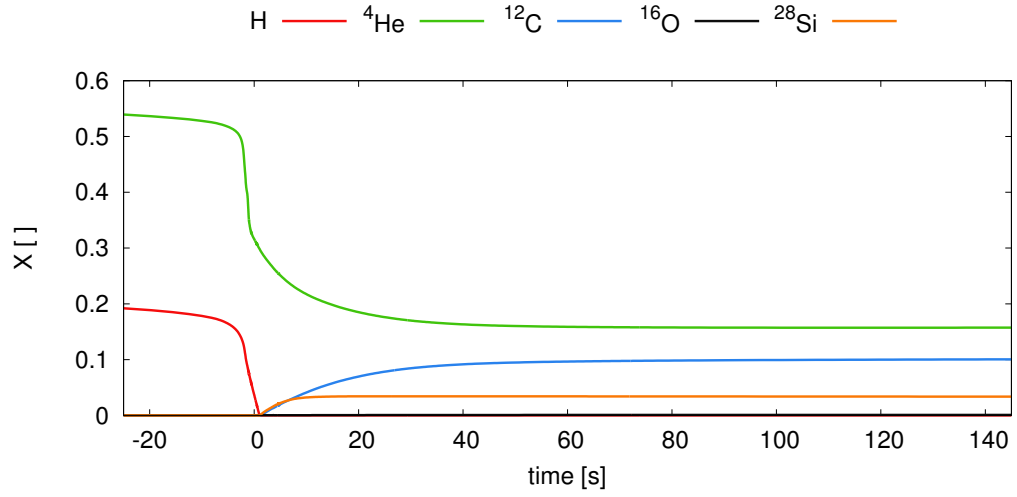

(b)

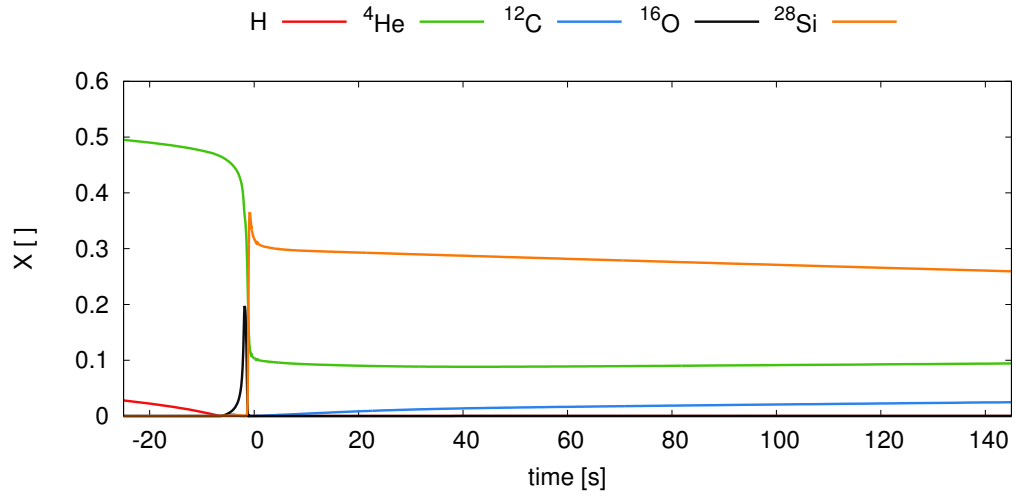

(c)

Fig. 3.42.: This figure shows in a) the evolution of mass fraction from the zone above the ignition zone. b) Shows the mass fraction of the zone, where the most nuclear energy is set free at time $t = 0$ when the luminosity reaches its peak. This happens at a column density of $5.34 \cdot 10^7$ g cm^{-2} ($\log y = 7.73$). c) Shows the mass fraction from the zone below the ignition zone. The red line represents the mass fraction of hydrogen, the green line the mass fraction of helium, the blue line the mass fraction of carbon, black shows the mass fraction of oxygen, and the orange line the mass fraction of silicon.

3.4.4 Discussion of the Three Burning Regimes with Helium-Rich Abundances as Accretion Composition

We find for the burst behaviour in the irregular burst regime that with increasing crustal heat, the number of bursts decreases before stable burning occurs. Thus, the transition time decreases as well. With increasing accretion rate, we see an increase of the rise time, the burst time, the number of bursts, as well as an increase in the transition time and the luminosities of the quiescent and the stable burning. Furthermore, we see a decrease in the recurrence time, the peak luminosity, and the α-parameter. At the range of Q_b values, where we find irregular burst behaviour, we find a shift of the ignition depth towards smaller values over time. Due to this shift, the ignition region rises upwards where the conditions for a thermonuclear runaway are in the end not given anymore, and therefore, stable burning occurs. Since Type I X-ray bursts are very sensitive to changes of the ignition conditions, a small shift is in this region of Q_b-values enough to cease bursts.

In the regular burst regime, we find a similar dependence of the accretion rate on the peak luminosity, the recurrence time, and the burst time. Increasing crustal heat leads to a decreasing burst time and α-parameter, since increasing crustal heating shifts the ignition conditions to lower column densities.

For the three different burning regimes, we find differences in the stable and quiescent burning region, and therefore, differences in the composition of the ashes in a layer with column density of $\sim 1 \cdot 10^9$ g cm^{-2}. The composition of the ashes is presented in Fig. (3.22), where the solid line stands for two examples showing regular burst behaviour, the dashed line for examples of stable burning behaviour, and the dot-dashed line for examples of irregular burst behaviour. All ashes regions are completely hydrogen depleted and only in the case of stable burning with low accretion rate do we still find a significant amount of helium. We observe a change of the mass fraction, which dominates at the light isotopes in the stable burning and irregular burst regime. Only some heavier isotopes around the iron peak contribute in these regimes. In contrast, heavier isotopes up to $A \lesssim 80$ dominate in the regular burst regime, where lighter isotopes are less present.

In Fig. (3.44), we combine our results from the burning regimes with the amount of carbon found in the ashes of the different burning regimes. This is crucial for finding parameter sets which could be used for self-consistent superburst simulations. In the regular bursting regime, we find that with higher accretion rate and lower crustal heating, the production of carbon decreases drastically. Therefore, we only find for simulation conditions close to the irregular and the stable burning regime mass fractions of carbon slightly above 0.1. This would just fulfil the condition

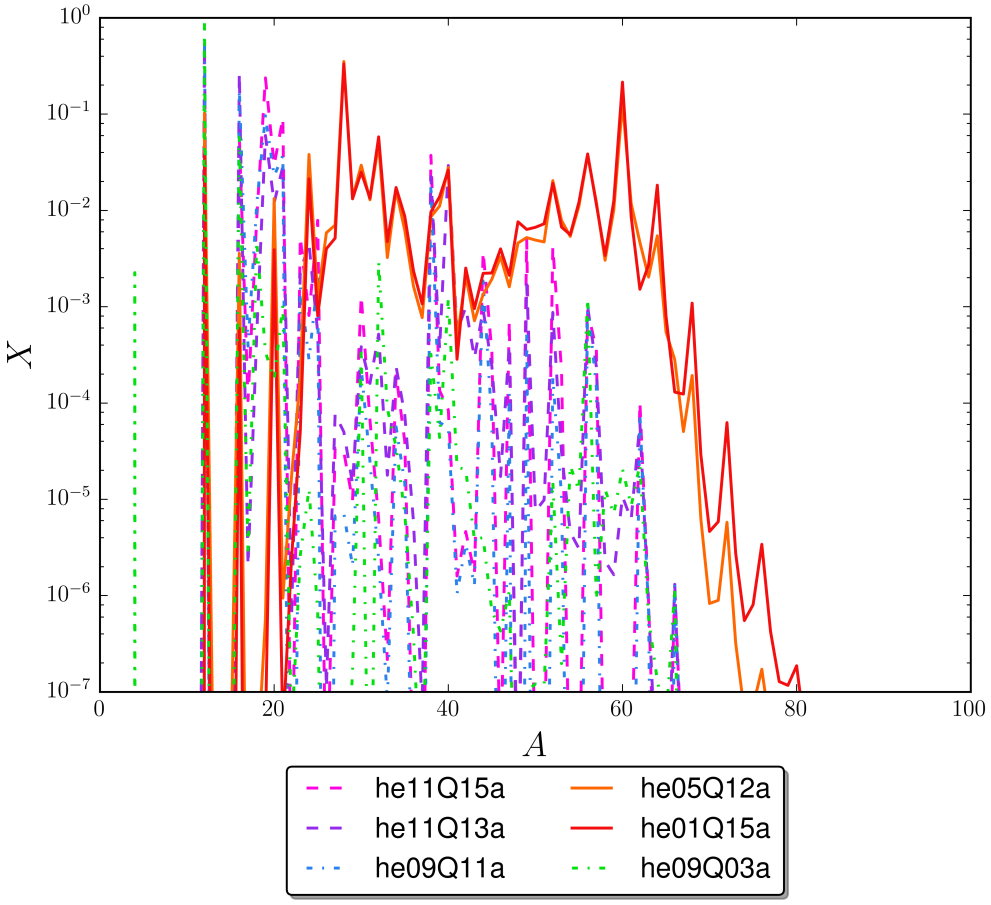

Fig. 3.43.: A comparison of the compositions of two representative simulations for each burning regime (definition of the parameter set conditions of each simulation is given in the box below the figure). The solid lines represent the regular bursting regime, the dashed lines the irregular burst regime, and the dot-dashed lines the stable burning regime.

of producing enough carbon for triggering a superburst. Furthermore, for stable burning, we find a huge area in which the carbon production is very effective. This results in the area of darkest grey in Fig. (3.44). This high mass fraction of carbon originates from two separate burning regions of helium and hydrogen, which enables the helium to build a nearly pure carbon layer via the triple-α reaction. In contrast, in regions of stable burning with higher accretion rates, those two burning regions merge and mixed hydrogen-helium-burning leads to ashes with mass fractions of carbon between 0.5 and 0.9 (the second brightest and second darkest shade of grey in Fig. (3.44)). In the irregular burning regime, we find intermediate mass fractions of carbon.

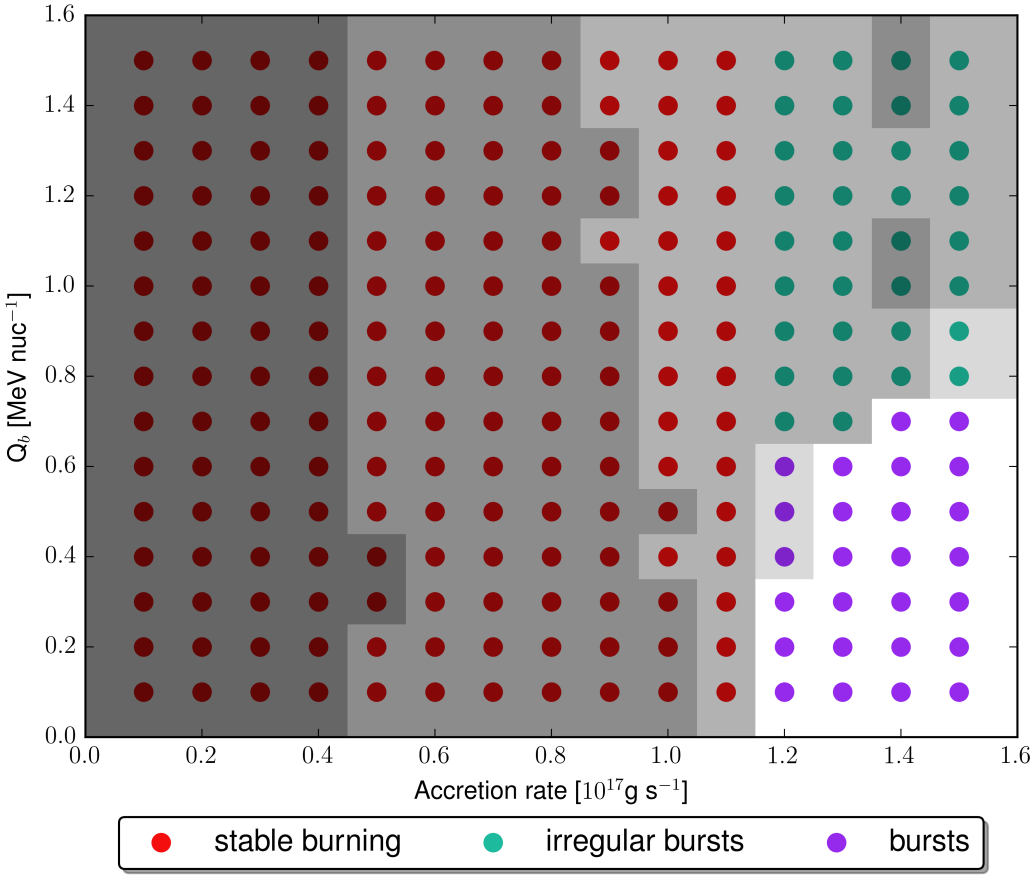

Fig. 3.44.: The three different burning regimes found in our simulations. The red dots represent the parameters of runs which lead to stable burning, the turquoise dots indicate irregular bursts behaviour and the violet ones regular burst behaviour. The different shades of grey correspond to the mass fraction of ^{12}C. From bright to dark: $X_{^{12}C} > 0.1$, $X_{^{12}C} > 0.5$, $X_{^{12}C} > 0.7$, $X_{^{12}C} > 0.9$, and white means $X_{^{12}C} < 0.1$.

3.5 Comparison of the Simulations with Solar Abundances Accretion Composition with the Simulations with Helium-Rich Accretion Composition

In this section, we compare the results of the simulations with solar abundances accretion composition from Section 3.3 to our findings with helium-rich accretion composition discussed in Section 3.4.

For both accretion compositions, we find three different regimes of burning behaviour. For low accretion rates, we find stable burning in all of our simulations. At the border to regular burst behaviour, we find a regime which shows irregular burst behaviour, i.e., first a series of bursts and eventually stable burning. Apart from that, we find regular burst behaviour at high accretion rates.

The exact location of the burning regimes in the parameter space depends on the composition of the accreted matter. Stable burning in the case of helium-rich accretion composition occurs for accretion rates up to $1.1 \cdot 10^{17}$ g s^{-1}, whereas in the case of accreting matter with solar abundances, a change of the burst behaviour already takes place slightly above $\sim 0.7 \cdot 10^{17}$ g s^{-1}. The irregular burst regime in the helium-rich situation appears above a crustal heating of ~ 0.7 MeV nuc^{-1}, while solar abundances lead to irregular burst behaviour for crustal heating above ~ 1.1 MeV nuc^{-1}. Notably, for solar abundances composition, only regular burst behaviour is observed if the accretion rate is larger than $1.0 \cdot 10^{17}$ g s^{-1}. Based on our simulations, we cannot conclude whether such an upper bound for irregular burst regime as a function of accretion rate exists in the helium-rich situation as well because our parameter space ends with accretion rates of $1.5 \cdot 10^{17}$ g s^{-1} where we still observe irregular burst behaviour.

The influence of the accretion rate and crustal heating on the observable properties of the irregular burst regime can be seen in Tabs. (3.3) & (3.4) for solar abundances and in Tabs. (3.7) & (3.8) for helium-rich abundances. Notably, the general dependences of these observable properties on the parameters crustal heating and accretion rate is similar for both types of abundances. A detailed comparison is not meaningful since the irregular burst regimes of the two situations cover different regions in parameter space and do not share the same initial conditions for a single simulation point. Nonetheless, we observe that the peak luminosities in the helium-rich situation are in general higher. Furthermore, the recurrence time, the rise time, and the burst time for simulations with helium-rich abundances are shorter, though the

α-parameters are in the same range. Another interesting observation is that the bursts in the helium-rich situation ignite closer to the surface (i.e. smaller $y_{ignition}$) and also the eventual stable burning occurs in higher layers than we observe it in the solar-abundances simulations. In contrast, we find that the luminosities of the stable phase and in between bursts are of the same order of magnitudes.

The mass fraction of the produced carbon varies, but the trend is similar, as we can see if we compare Fig. (3.23) with Fig. (3.44). In the stable burning regime at low accretion rates, we find ash layers of nearly pure carbon. In the helium-rich simulations, the region in the parameter space for getting ashes of nearly pure carbon is bigger and includes simulations with accretion rates up to $0.4 \cdot 10^{17}$ g s^{-1}, whereas only some parameter sets with solar abundances lead to such a large amount of carbon. In the irregular burst regime (for both types of abundance compositions), the carbon production is still high, since the bursts in this area cease and eventually stable burning occurs.

For self-consistent superburst simulations, the mass fraction of carbon in the ashes of Type I X-ray burst is the crucial factor. In the regular burst regime (for both type of accretion composition), the carbon production rarely exceeds the needed 10% for superburst ignition. Whereat simulations with solar abundances as accretion composition reveal more combinations of parameter sets resulting in more than 10% carbon in the ashes of the Type I X-ray bursts.

If we compare the composition of the ashes in the stable burning regime of both accretion composition conditions in Fig. (3.45), we find differences mainly concerning the heavier isotopes. This is due to the rp-process, which produces the heavier elements, which strongly depends on the number density of available hydrogen in the ignition region of the X-ray burst. In the case of helium-rich accretion composition, there is less hydrogen, and therefore, the rp-process is not as effective as if we accrete more hydrogen abundant matter. The ashes have been investigated at the same column density of $8.42 \cdot 10^8$ g cm^{-2} ($\log(y) \approx 8.93$) for all four cases in Fig. (3.45). The orange lines show the results of a simulations with 0.4 MeV nuc^{-1} and the turquoise lines show the results of a simulations with 0.6 MeV nuc^{-1}. All four cases correspond to an accretion rate of $1.2 \cdot 10^{17}$ g s^{-1}. The solid lines are the results from simulations with solar abundances and the dashed lines are the results from simulations with helium-rich accreted matter.

The regular burst regime observed in simulations with helium-rich accretion composition is small compared to that found for the solar abundance composition. Nevertheless, some overlap in parameters exists, i.e. we find regular burst behaviour for the same set of conditions (accretion rate and crustal heating) for both types of

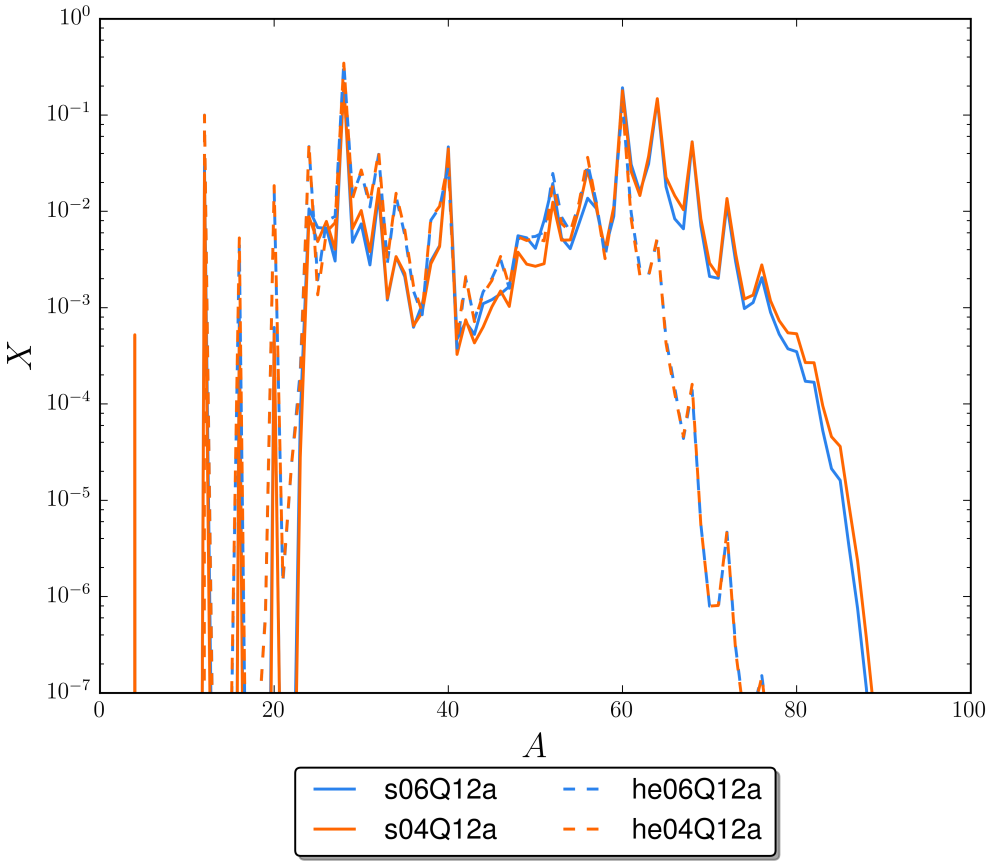

Fig. 3.45.: The composition of the ashes taken at a column density of $8.42 \cdot 10^8$ g cm^{-2} ($\log(y) \approx 8.93$). The solid lines are the results from simulations with solar abundances in the accreted matter, the dashed lines are the results from simulations with helium-rich accreted matter.

abundance compositions. In Fig. (3.46), we compare results from some of those simulations with the same conditions, but different accretion composition. Green and red lines represent the examples with helium-rich accretion composition, blue and black lines those with solar abundance accretion composition. In the two top plots, we fix the crustal heating at 0.1 MeV nuc^{-1} (blue and red line) and at 0.5 MeV nuc^{-1} (green and black line), and vary the accretion rate. For helium-rich accretion composition, there is no burst behaviour for accretion rates below $1.2 \cdot 10^{17}$ g s^{-1}. Therefore, only results from higher accretion rates are shown. In the two bottom plots, we fixed the accretion rate at $1.2 \cdot 10^{17}$ g s^{-1} (red and blue line) and at $1.5 \cdot 10^{17}$ g s^{-1} (green and black line), and vary the crustal heating. For helium-rich cases there is no regular burst behaviour for crustal heating above ~ 0.7 MeV nuc^{-1}. In Fig. (3.46a) and (3.46c), i.e. on the left side, we show the α-parameter. In Fig. (3.46b) and (3.46d), i.e. on the right side, we show the burst time. We find that both the burst time and α-parameter depend more on the accretion rate than on the crustal heating. Notably, the overall behaviour is independent on the accretion composition.

Even though the found peak luminosities in the helium-rich cases are higher than in solar cases[4], we find also shorter recurrence times[5], shorter rise times, and shorter burst times (see Fig. (3.46) the two plots on the right side). The interplay of those variables lead to higher α-parameters shown in Fig. (3.46) on the left side. For all four cases shown in Fig. (3.46a), we can see that with increasing accretion rate, the α-parameter is decreasing. In Fig. (3.46b), we see that with increasing accretion rate, the burst time rises. The bursts in helium-rich simulations are much shorter than in the case of solar abundances simulations, which coincides with observations.

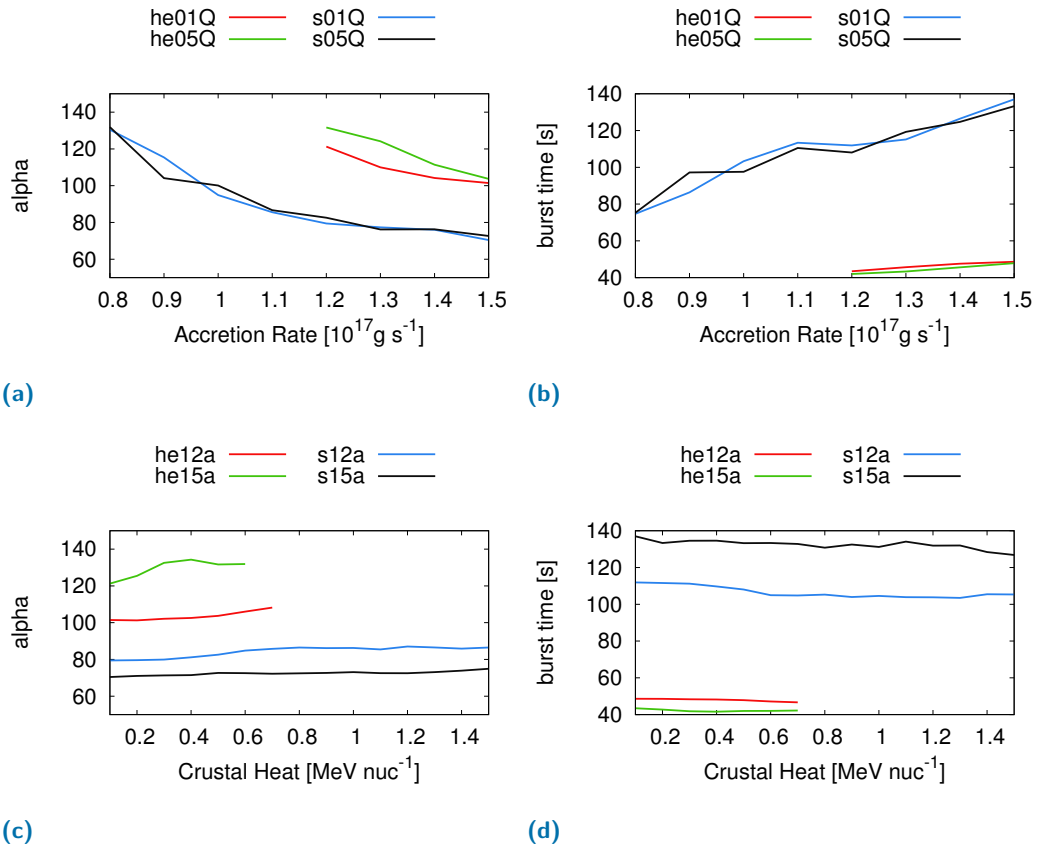

Fig. 3.46.: The crustal heating in a) and b) is fixed, whereas the accretion rate in c) and d) is fixed. Both values are given in the legends above the plots.
a) Shows the α-parameter in dependence on the accretion rate.
b) Shows the burst time in dependence on the crustal heating.
c) Shows the α-parameter in dependence on the accretion rate.
d) Shows the burst time in dependence on the crustal heating.

[4]Compare Fig. (3.37a) and Fig. (3.37b) with Fig. (3.16a) and Fig. (3.16b)

[5]For simulations with solar abundant accretion matter, we find roughly $2-5$ h, whereas for helium-rich simulations we get $2-3$ h.

3.6 Outlook for Superburst Simulations

"Make it so."

— Jean-Luc Picard
Star Trek

In Sections 3.3 and 3.4, we found 22 parameter sets in total where the simulations show regular burst behaviour and the produced amount of carbon in the ashes of the bursts exhibit more than 10% carbon mass fraction. These simulations and the produced amount of carbon are listed in Tab. (3.10).

One of the aims of this thesis was to self-consistently simulate a superburst. Due to the high computational needs of the code, we developed a method to speed up the process, but keeping the conditions of the runs already obtained. For these fast simulations, we decided to make a cut-off of the highest zones and accrete the composition of the ashes of the simulated X-ray bursts directly into a deeper layer of the computational domain. For these runs, we took one of the most promising simulations, which has provided enough carbon ($X(^{12}C) > 0.1$) and nevertheless, show regular bursts over a long period of time. Therefore, we decided to take the run s08Q08a as a template for this job. As we know, X-ray bursts heat the underlying layers during a burst and they cool down again between bursts as the heat is transported outwards. Therefore, we chose a layer for the cut, which is not heated during an X-ray burst. Sufficiently deep lying layers are never heated [140]. Another condition was that there is no (or negligible) nuclear reaction activity. Therefore, we explored the burn rate of the zones, see Eq. (3.5), to select a reasonable cut region.

simulation name	$X(^{12}C)$ at $y \approx 1.2 \cdot 10^9$	simulation name	$X(^{12}C)$ at $y \approx 1.2 \cdot 10^9$
he04Q12a	0.101	s06Q09a	0.118
he05Q12a	0.103	s07Q08a	0.136
he06Q12a	0.100	s07Q09a	0.116
s01Q08a	0.138	s08Q08a	0.132
s01Q09a	0.105	s08Q09a	0.118
s02Q08a	0.137	s09Q08a	0.131
s02Q09a	0.119	s09Q09a	0.123
s03Q08a	0.143	s10Q08a	0.139
s03Q09a	0.105[6]	s10Q09a	0.122
s05Q08a	0.138	s11Q09a	0.124
s06Q08a	0.137	s11Q10a	0.101[7]

Tab. 3.10.: This table lists all the possible superburst simulations and the corresponding mass fraction of ^{12}C at a column density of $1.2 \cdot 10^9$ g cm^{-2} ($\log(y) \approx 9.09$). [6] is taken at a column density of $2.1 \cdot 10^9$ g cm^{-2}, and [7] is taken at a column density of $7.2 \cdot 10^8$ g cm^{-2}.

Nevertheless, we did not want to take too many zones away, so that we still can see the impact of a possible explosive carbon ignition. For the case of s08Q08a, we chose a cut-off at zone 101 and kept the deepest 100 zones of our computational domain. Zone 100 has a column density of $1.8 \cdot 10^9$ g cm^{-2} ($\log(y) \approx 9.26$). Fig. (3.47) shows in the left plot, the burn rate in dependence on the column densities over the time of one burst. The right plot shows the corresponding temperatures over the time of one burst. Time $t = 0$ s lies at the time when the burst reaches its peak luminosity. As we can see in the right plot of Fig. (3.47), zone 100 just lies under the through the X-ray burst heated region. In the left plot of Fig. (3.47), we see that the significant burn rate does not reach regions with column densities of $\sim 10^9$ g cm^{-2} and consider that zone 100 lies in regions where the burn rate is insignificantly small. We took the same accretion rate as in the normal run, but changed the composition in a way such that the domain accretes the composition of the overlaying zone. In the case of the cut-off at zone 100, we accreted the composition of zone 101. The mass fraction of zone 101 is shown in Fig. (3.48). Here, we can see that no isotope lighter than carbon has a significant mass fraction in the new accretion composition. The

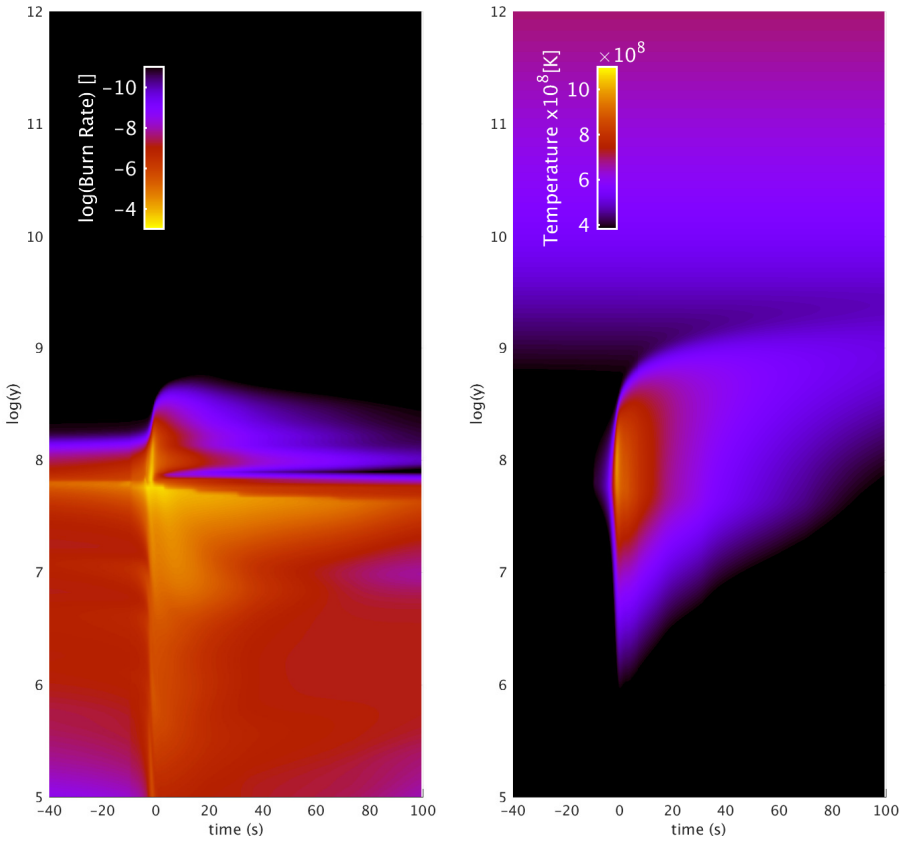

Fig. 3.47.: Time $t = 0$ s lies where the maximum luminosity of a burst is reached. The left plot shows the burnrate throughout the entire computational domain over one burst, whereas the right plot shows the corresponding temperatures in our domain over one burst.

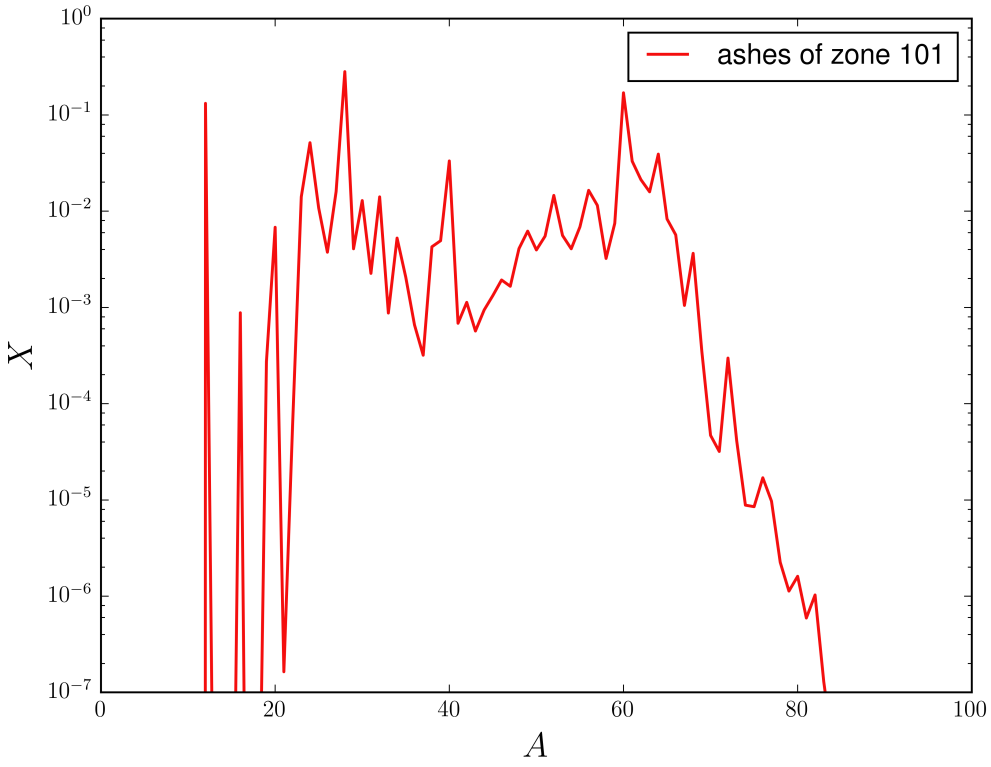

Fig. 3.48.: The composition of the ashes of X-ray bursts in the zone 101 are shown here. This is the new composition of the accreted matter for the cut-off simulation of s08Q08a.

largest mass fraction is, beside carbon ($\sim 13\%$), in isotopes such as silicon ($\sim 28\%$) and nickel ($\sim 17\%$), with smaller mass fraction, but still significant in this plot are isotopes around $A \sim 30$ and $A \sim 60$. The heavier isotopes were built through reactions of the rp-process. Additionally, we have to adjust the surface pressure P_{surf}, which is in our code an outerboundary condition. Likewise, the calculation of the column density from Eq. (1.30) has to be adjusted in this way:

$$y(r) = \int_{R-r}^{R} \rho(r) \frac{dr}{\Gamma} + y_{boundary}, \tag{3.8}$$

where $y_{boundary}$ is the column density of the zone 101. With these adaptations we speed up the runs by a factor of two. In Fig. (3.49), we compare the reached column density of carbon of the three different runs. In this figure, the black line represents the start of the simulations with the cut at zone 100. The blue line shows which column densities the mass fraction has reached in the normal run without the cut. This simulation has been done in parallel to the applied cut simulation. The red line shows the carbon mass fraction distribution of the cut-off simulation. We see that in one month wallclock-time, the full simulation of s08Q08a simulated from

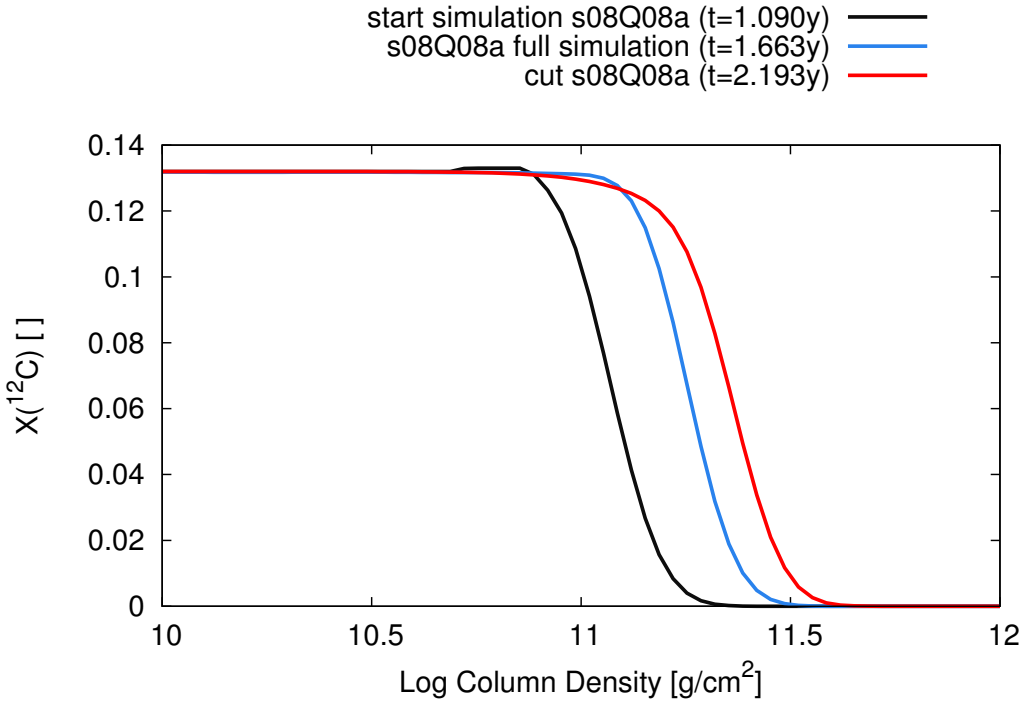

Fig. 3.49.: This figure shows the mass fraction of ^{12}C in dependency on the column density. The black line shows the start situation of the cut-off simulation. The blue line shows the simulation results of s08Q08a with no cut-off for comparison of how much faster the cut-off simulation (red line) runs. In parenthesis are the simulation times given.

the beginning of roughly one year to one and a half years, whereas the cut-off simulation reached simulation-times of over two years. Even with this speed up of the simulation, we could not simulate a superburst until the date of handing in this work.

3.7 Comparison with Observations

As already mentioned in the introduction (Section 1.1), observations provide constraints for certain quantities, see Tab. (1.1). For comparison, we listed in Tab. (3.11) the ranges for the same quantities obtained from our simulations. The left column of this table contains the observable quantity, the second column shows the range of our results of those quantities obtained from simulations with solar abundant accretion matter, whereas the next column lists the values obtained from simulations with helium-rich accreted matter, and the last shows the range of observed values. The range of our calculated values lies reasonably well in the range of the observed quantities. Only for the α-parameter generally we do find too large values, even though some of them lie in the observed range.

Tab. (3.12) shows some results from our simulations, where the first column identifies the simulation conditions and the other columns give some of the quantities from Tab. (3.11), averaged over the number of bursts (second column). If there are more than 100 bursts in a single simulation, the average is taken over the first one hundred bursts. The values for all our simulations can be found in the Appendix A.1.1 for solar abundances and in A.1.2 for helium-rich accretion composition.

Observable quantity	Range with solar abundances	Range with helium-rich abundances	Range of observations
t_{rec}	$\sim 1.6 - 4.7$ h	$\sim 2.3 - 3.3$ h	$2 - 4$h
$t_{duration}$	$\sim 70 - 140$ s	$\sim 40 - 50$ s	tens to hundreds sec
t_{rise}	$\sim 2 - 7$ s	$\sim 1 - 1.5$ s	$\leq 1 - 10$s
t_{decay}	$\sim 65 - 130$ s	$\sim 40 - 50$ s	hundreds of seconds
L_{peak}	$\sim 0.7 - 1.25 \cdot 10^{38}$erg s^{-1}	$\sim 2 - 2.5 \cdot 10^{38}$erg s^{-1}	$\sim 10^{38}$erg s^{-1}
L_{pers}	$\sim 1 - 3 \cdot 10^{36}$erg s^{-1}	$\sim 2 \cdot 10^{36}$erg s^{-1}	$\sim 10^{36-37}$erg s^{-1}
α	$\sim 70 - 140$	$\sim 100 - 140$	$\sim 10 - 100$

Tab. 3.11.: Observed quantities from typical X-ray bursts and the respective ranges as obtained from our simulations.

run	N_{burst}	L_{peak} [erg s^{-1}]	t_{rec} [h]	t_{rise} [s]	$t_{duration}$[s]	α-value
s06Q10a	2807	$8.92 \cdot 10^{37}$	3.1	3.62	97.24	99.98
s01Q08a	61	$1.25 \cdot 10^{38}$	4.7	1.70	74.68	130.44
s08Q08a	3172	$1.18 \cdot 10^{38}$	4.5	2.18	73.53	136.08
s15Q15a	83	$6.97 \cdot 10^{37}$	1.6	5.45	126.80	74.92
he04Q12a	232	$2.47 \cdot 10^{38}$	3.3	0.91	41.58	134.28
he07Q15a	251	$2.06 \cdot 10^{38}$	2.4	1.23	46.68	108.20

Tab. 3.12.: Some of the mentioned values in Tab. (3.11) for some of our simulations. All values are averaged over the number of bursts. If there are more than one hundred bursts, the average of the first 100 bursts is shown.

We now want to compare the results from our simulations directly to observation data from [141][8]. In order to compare the luminosities properly, we have to calculate the flux as given in [20],

$$F_x = \frac{L_x}{4\pi d^2 \xi_b (1+z)}, \tag{3.9}$$

where F_x is the observed flux, L_x is our simulated luminosity, d is the distance in cm, ξ_b takes into account the possible anisotropy of the burst flux, and $(1+z)$ denotes the redshift. We decided to compare some of our results with observation of the *textbook* burster GS 1826-24[9]. In Fig. (3.50), we show the data for GS 1826-24 given in [141] for three different phases of constant recurrence time (indicated in the legend of the figure as Δt). The blue line shows the light curve corresponding to the shortest recurrence time ($t_{rec} = 3.530$ h), the red line corresponds to a intermediate recurrence time ($t_{rec} = 4.177$ h), and the green line to the longest recurrence time ($t_{rec} = 5.14$ h). For comparison, we show data from one of our simulations (grey

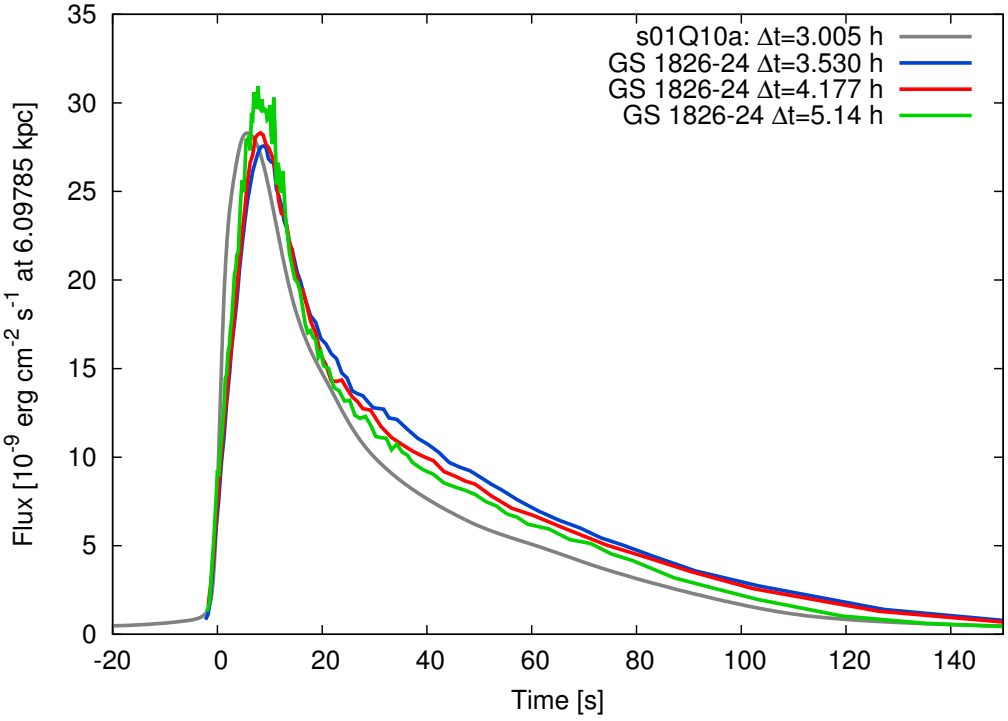

Fig. 3.50.: We compare the observational data from [141] with results of our simulations. The conditions of our simulations are shown in the legend in the upper right corner of the figure. The grey line corresponds to a simulation with an accretion rate of $1.0 \cdot 10^{17}$g s^{-1} and a crustal heating of 0.1 MeV nuc^{-1}. For ξ_b we choose a factor of 2/3. The chosen burst of the simulation in this figure is one which is close to the averaged value of its simulation.

[8] The data from the observations can be found here: https://burst.sci.monash.edu/reference [141]
[9] After consultation with D. Galloway at an ISSI meeting in Bern.

line). Since the accretion rate of this source does not vary much over short timescales, it remains within the range of $5 - 13\%\ \dot{m}_{Edd}$ [27, 142], and therefore, it is an appropriate X-ray burst source for comparison. We take the values for the distance from [141] and the references therein, additionally, we choose for ξ_b a value of 2/3, and show the comparison of the flux in Fig. (3.50). In particular, we have used an accretion rate of $1.0 \cdot 10^{17}$ g s^{-1} and a low crustal heating value of 0.1 MeV nuc^{-1}. Since the observations find an α-parameter of $\sim 34 - 39$, our simulated values are too high ($\alpha \approx 81 - 111$ with an average of 94.90). We can see in Fig. (3.50) that our simulated burst rises slightly faster and decays steeper than it is seen in the observed behaviour. The peak luminosity, however, is in the same order of magnitude. We obtain slightly shorter recurrence times($t_{rec} = 3.005$ h) than in the observations.

Two out of the four Type I X-ray burst sources described in [141] accrete helium-rich matter. Even though the mass fraction of our helium-rich simulations fit better to the source SAX J1808.4-3658, we compare our results to the data of 4U 1820-30 instead, see Fig. (3.51). The reason for this is that the accretion rate range corresponding to the observation of SAX J1808.4-3658 leads to stable burning, i.e. no bursts, in our simulations with helium-rich accretion composition. 4U 1820-30 accretes almost pure helium ($\gtrsim 90\%$), which is more than we use in our simulation (51%, cf.

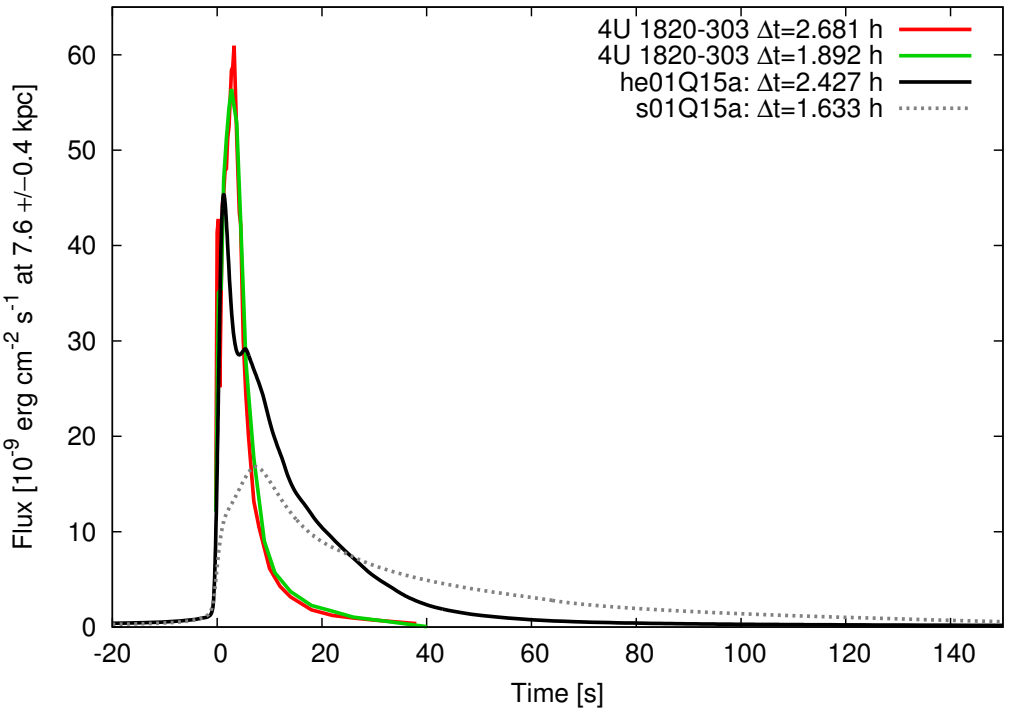

Fig. 3.51.: In this figure, we compare our simulation with helium-rich accretion composition, and high accretion rate (black line), with a simulation with solar abundances accretion condition, but otherwise the same parameters (grey dashed line) with given observational data (green and red lines).

Section 3.4). Furthermore, the accretion rate of $0.114\ \dot{m}_{Edd} \approx 1.9 \cdot 10^{17}$ g s^{-1} given in [141] is slightly larger than the largest value we used in simulations, i.e. $1.5 \cdot 10^{17}$ g s^{-1}. Nonetheless, as we can see in Fig. (3.51), we get the right trend in the flux, increasing the helium mass fraction. In Fig. (3.51) we show in red and green lines the observed data, in black we show results from one simulation with the highest accretion rate of our parameter space with helium-rich accretion composition. For comparison, we also show results from simulations with the same accretion rate and crustal heating, but solar abundances as accretion composition (grey dashed line). We clearly see that the black line is a much better prediction of the observations, i.e. the black line is much closer to the coloured lines than the grey dashed line.

Altogether, we can say that our simulations show the right behaviour and trends as observational data provide, but comparing the results one to one with observational examples show that our calculated light curves are slightly different. This could be due to the fact that we do not cover with our simulations the exact given accretion rates predicted from observations, and additionally the observed data does not make a statement about the possible crustal heating and the composition of the accreted matter is only given in terms of the mass fraction of hydrogen and of the CNO-cycle nuclei. Furthermore, we have as an inner boundary condition a neutron star with a radius of 11.2 km under our computational domain[10] and this is smaller than the given radii in [141]. For further comparisons with this set of observable data, we would need to adapt the given conditions from [141] and vary only the conditions, which are not provided by observations.

[10] Our computational domain has the thickness of $8.5 \cdot 10^3$ cm.

4 Summary of this Work

"I think nature's imagination is so much greater than man's, she's never going to let us relax."

— Richard P. Feynman

In this work we put together a set of tools that allow us to simulate several thousands of X-ray bursts within a reasonable amount of time ($\sim$ few months). This landmark opens the path to simulate consistently the emergence of a superburst; a task which until now was considered too computationally demanding. To do that, we built a scheme based on the works of J. Fisker [21] and S. Fehlmann [25], via extending the computational domain to include the superburst ignition depth – provided by theoretical suggestions and X-ray burst models [10, 114].

X-ray bursts, and consequently superbursts, depend very sensitively on many physical variables (accretion rate, composition, properties of the underlying neutron star, etc. ...). This leads to a huge parameter space, where not all combinations are suitable for triggering a superburst. Due to the computationally demanding calculation that is to simulate consistently a superburst, we performed a detailed parameter study over two relevant quantities: accretion rate ($0.1 - 1.5 \cdot 10^{17}$ g s^{-1}) and crustal heating ($0.1 - 1.5$ MeV nuc^{-1}). In fact, we duplicated this study to include also the effect of varying the composition of the accreted matter, using for that purpose solar composition and helium-rich composition. This leads to a total of 450 simulations of X-ray bursts, which in overall adds up to the order of more than a century in computational time. Since X-ray burst sources cover a large range of accretion rates, we chose a range that included observations of X-ray bursts and observations of superbursts. The crustal heating is needed for explaining observations of thermal relaxation of neutron stars [103, 143]. The location of this heating source is suggested to be in the region of the ignition of a superburst or below. We used a range for the crustal heating covering the theoretically suggested values [101, 102, 116]. As said above, this is done in this work for two different compositions of accreted matter. Once with solar abundances, in the other case with a helium-rich composition. The choice of solar abundances is done due to the fact, that most X-ray bursts and hence, most superbursts have been observed in low-mass X-ray binaries with an unevolved donor star. We also chose a helium-rich composition, since some superbursts have been observed in a ultra-compact

binary with a donor star, which lost its hydrogen envelope and helium-rich matter is accreted on the neutron star [57, 133].

As a result of this study, we found three different regimes: stable burning, where stable burning of hydrogen and helium occurs; irregular bursts, where we simulate a sequence of bursts, which change over to stable burning; and regular burst, which show a long sequence of bursts and are the target group to be the possible precursors to a superburst. For both accretion compositions, we found burning regimes, which are influenced by the choice of the accretion rate and the crustal heating. Varying those two parameters has influence on observable properties, summarized in Tab. (4.1). Those tendencies are for the two burst regimes, since stable burning does not provide us with observable burst properties.

Since one of our goals is to find suitable parameter sets, which could lead to a superburst ignition, we are focused on the the needed amount of carbon in the ashes of the bursts. Theory and other numerical calculations predict that the needed mass fraction is at least 10% [7]. We find for simulations with solar abundances and an accretion rate below $0.7 \cdot 10^{17}$ g s^{-1} a production of huge amounts of carbon, due to stable burning of hydrogen and helium. Decreasing accretion rate leads to an increase of carbon production. This is due to the separation of the hydrogen and

Observable quantity	Increasing crustal heating	Increasing accretion rate
Solar Abundances		
Recurrence time t_{rec}	–	decrease
Burst time $t_{duration}$	–	increase
Rise time t_{rise}	*increase*	increase
Decay time t_{decay}	–	increase
Peak luminosity L_{peak}	*decrease*	decrease
Persistent luminosity L_{pers}	*increase*	–
α-parameter	*increase*	decrease
Helium-rich Abundances		
Recurrence time t_{rec}	–	decrease
Burst time $t_{duration}$	decrease	increase
Rise time t_{rise}	increase	increase
Decay time t_{decay}	increase	increase
Peak luminosity L_{peak}	*decrease*	decrease
Persistent luminosity L_{pers}	*increase*	*decrease*
α-parameter	increase	decrease

Tab. 4.1.: A short summary of the influence of the accretion rate and the crustal heating on the observable quantities for both accretion compositions. – means that there is no significant influence seen. Tendencies written in italics only show a slight tendency.

helium stable burning region. In extreme cases of low accretion rate, the ashes of stable burning consist out of $> 90\%$ carbon. For helium-rich accretion composition, we obtain stable burning for a broader range of accretion rates, and therefore more cases with large production of carbon. This is caused by hydrogen depletion at lower column densities, since less hydrogen is in the accretion composition. A stable burning regime with production of a huge amount of carbon has also been seen from [137].

After all, for selecting a possible superburst parameter set, we need a set that resembles regular burst behaviour. This combined with the condition for $X(^{12}\mathrm{C})$, we obtain 22 matching parameter sets (three helium-rich cases, 19 solar abundances cases). After this work, the path to consistently simulate a superburst seems more reachable. The effort done here to constrain the parameter space can be of interest for the community and help to unveil the mysterious of this exciting scenario.

Simulations of a self-consisting ignition of a superburst have high computational costs and would still take several months of wallclock-time, even on highly parallelized machines. Due to this fact, we have not been able to present a self-consistently igniting superburst in this work. The required time is mainly needed for a shift-down of the produced carbon into higher column densities until it reaches the ignition depth of a superburst. Therefore, we developed a method for speeding up the shift-down of the produced carbon of X-ray burst simulations, cutting-off the zones of X-ray burst ignitions. Those zones are the most active zones in terms of nuclear reactions, and omitting them reduces the wallclock-time of the simulations. With this method, we were able to speed up the simulations by a factor two. Since we accrete the composition of the ashes of the previously simulated X-ray bursts, we are capable of keeping the conditions of the run already obtained. Nevertheless these simulations are still running, and not finished by the time of handing in this work.

Finally, we compared our results with observational data [141] and find that we lie in the general range of given observational properties, with the exception of slightly too high α-parameters. If we compare single bursts with solar accretion composition, they deviate slightly from the observed properties, mainly in faster rise and faster decay times. Nevertheless, we were able to reach the range of peak luminosities and were in a close range to the observed recurrence times. The comparison of helium-rich accretion composition show closer rise times to observations, but longer decay times. This is due to the fact that our helium and hydrogen mass fractions differ from the suggested ones of the observational data. Further investigation in fitting to these given data is needed, varying our input conditions.

5 Future Work

"There are only two days in the year that nothing can be done. One is called Yesterday and the other is called Tomorrow. Today is the right day to Love, Believe, Do and mostly Live."

— Tenzin Gyatso, the 14th Dalai Lama

In this work, we investigate the variation of the accretion rate and the crustal heating for two different composition of accreted matter. A more realistic comparison to observations could be achieved by adapting the accretion composition for the given observational data in [141]. Furthermore, we should also change the radius and the mass of the underlying neutron star to fit the suggested values of observations.

Additionally, we show that during quiescent state of an X-ray binary at low accretion rates, stable burning of hydrogen and helium produces a large amount of carbon. Since nature shows no X-ray burst source with a completely constant accretion rate, the influence of a time-varying accretion rate is crucial. If the ashes of stable burning sinks in the ocean before the accretion rate increases, a superburst ignition during the active bursting phase might occur. Therefore, a study of the effect of varying the accretion rate might provide relevant information about the emergence of a superburst.

Furthermore, our method, that speeds-up the down-shift of the ashes of X-ray bursts, could be used to determine the ignition depth of a possible superburst in our simulations. The theoretical range of the column depth of a superburst ignition lies in $10^{11} - 10^{12}$ g cm^{-2} [10, 116, 117]. With the information of a specific ignition depth in our simulations, we could constrain the possible parameter set to be further investigated and estimate a wallclock-time for those simulations. Also we may identify stable carbon burning in those depths much faster. Stable carbon burning is suggested in [10] to appear for high Q_b-values in dependency on the accretion rate.

Mass and reaction rate sensitivity studies have been performed and have shown a big influence for certain masses and reaction rates on the light curve and the ashes of an X-ray burst [117, 144, 145]. Our code could be used in future works for such studies. Furthermore, one has to stay up-to-date with the latest reaction rate library, as those works show that certain reactions have a large influence on the outcome of X-ray burst simulations.

Acknowledgements

"Live long and prosper!"

— Leonard Nimoy aka Spock
vulcan saying

The results presented in this doctoral thesis would not have been possible without the support of a variety of persons. I am grateful to those, who have contributed to this thesis, and want to thank:

First I want to thank Friedel Thielemann for giving me the chance to do my PhD in his group and under his supervision. I want to thank him for all his support, all the last minute meetings, giving me the opportunity to present my results at conferences and the ISSI meetings in Bern and at the research facility Riken, all the supportive gestures, and his comprehension.

Especially out of our group in Basel I want to thank Rubén Cabezón, who helped me with all my server problems and was a great source of inputs, tricks, and pushes (actually kicks, if needed) during my PhD time. He always took time to discuss and help. A most grateful "Thank you" to him. Furthermore, he introduced me to the world of boardgames, which was and still is a most welcome pastime.

I want to thank **ISSI** and the team of Duncan Galloway: **Nuclear Reactions in Superdense Matter – From the Laboratory to the Stars**. It was a wonderful opportunity for getting in contact with experts in the field and very nice persons. Every single talk was an inspiration, and the discussions with you were utile. Out of this team I want to thank especially: Duncan Galloway, Laurens Keek, Alexander Heger, Hendrik Schatz, Jérôme Chenevez, Andrew Cumming, and Edward Brown.

From the last active group members in Basel I want to thank: Kevin Ebinger for all the late-night-times and progenitor-drinks we shared together in the office, Maik Frensel for all the help and discussions, Oliver Heinimann, Matthias Hempel, Andreas Lohs, Benjamin Wehmeyer, and Tommy Rauscher, thanks for the shared time and the

fun we had together doing physics, BBQ-ing, and all the dinners and shared drinks. You were all a great company.

Additionally to the *active* members, I also want to thank the following former group members for welcoming me in the group and sharing some interesting science moments and evenings: Kuo-Chuan Pan, Takami Kuroda, Marco Pignatari, Nobuya Nishimura.

Working on my PhD-thesis, I got a lot of help, had a lot of interesting discussions, and fun with my former office mates and my actual office mates: Marius Eichler, Kevin Ebinger, Maik Frensel, Benjamin Wehmeyer, Eros Cazzato, and Francesco Cefala. We shared more or less time together, and I appreciate every single day with you. At this point, I want to thank Stefan Antusch and his group for including me in the last months of my PhD in their social activities over lunch breaks, and offering me a free table in his student's office. I really appreciate that.

From the former PhD students of our group, I would like to thank: Chiara Biscaro for all the cakes and being the social centre of the group for many years – long live the *Hinterbänkler*, the last row of the seminar, Marius Eichler, Umberto Battino, Dave Gobrecht, and Sofie Fehlmann.

I also want to thank some special friends in physics:
First Talitha Weiß, who studied physics in the bachelor and master with me in Basel. Already back then she was a source of calmness, ideas, long studying hours in the library, late night walks filled with discussions about physics, the world, the latest movie, god and everything in between. I am glad to call you my friend and still be in contact with you. I can only say: ToFlNiOwPh und blubb ;-)
My second fellow student, Bastian Schäfer, I want also thank for all the help back in the undergrad studies and also during my PhD-time. He was just one or two doors away, and always took time for discussions or questions.
One person, we found out, I know since childhood, but physics brought us a close friendship – Mara Batzer, I cannot thank you enough for all the walks, talks, hugs, and runs to clear my head.
Also I want to thank Olya Popova for the coffee breaks, and late evening talks and chats, for encouragements in all field of life, even if not always wanted, they brought me joy and some good laughs.
Further I want to thank Andrea Mehlin, who is a warm soul and always gives more than she ever can receive. I am so grateful for your support, your way of being perfectly organised, and the many talks we had. You are one of the best souls in this department.

The list must not lack following helpers, who proof-read my thesis in part or in full: Rubén Cabezón, Talitha Weiß, Dave Gobrecht, Oliver Müller, Francesco Cefala, Eros Cazzato, Kevin Ebinger, and Natalie Walford.

Also a great, and honest “Thank you!” to all my friends, you are the most wonderful persons I chose to have in my life, and hopefully you will continue to stay at my side in the unknown future.

Of course I also want to thank my entire family, which is pretty big and to mention everyone of my beloved, related ones, who supported me in one or another way, would fill countless pages. Therefore, I will mention only a short list of those, who where among the most important persons in my PhD-life. I want to thank my Grandmaman for all the candles she lit up in the church and for praying for me. Of course I can not thank my family and leave out my big brother, who shared the sufferings during a PhD for a good part of my PhD-time. I am really happy, that he’s back in Basel and shares once in a while a “Fyrobe-Bier” with his little sister. Furthermore, I want to thank my little sister for all the supportive conversations we had. She just started her university-time and I wish her good luck on this way. I also want to thank my father, who lives way too far away, but is always close in my heart. Further I want to thank my “jurassic”-clan, who always supported me, showed interest in my work, and shared their love, and warmth of hugs with me.

Last but not least. Especially I want to thank my mother, who was always there for me and granted me asylum back at home in times when I needed it. She was a source of warmth, support, long talks and handkerchiefs and a big hug, if needed. Without her I would not have managed these three years of PhD-time. BHAK!

Appendix

A

A.1 Tables of Results

As a reminder, we label our simulations as follows

$$x\,yyQ\,zza,$$

where x denotes the composition of the accreted material (s corresponds to solar abundances, he corresponds to helium-rich abundances), yyQ denotes the values for Q_b, e.g. 11Q represents $Q_b = 1.1$ MeV nuc^{-1}, zza denotes the values for the accretion rate, e.g. 08a represents $\dot{M}_{acc} = 0.8 \cdot 10^{17}$ g s^{-1}.

In the following tables are the results from our simulations listed. The tables list from left to right, the simulation names (*italics* written run names are from the irregular burst regime, the others are from the regular burst regime), the number of bursts, the peak luminosity, the recurrence time, the rise time, the burst length, and the α-parameter.

A.1.1 Solar Abundance Accretion Composition

run	N_{burst}	L_{peak} [erg s^{-1}]	t_{rec} [s]	t_{rise} [s]	$t_{duration}$ [s]	α-value
s01Q08a	61	$1.25 \cdot 10^{38}$	16983.54	1.70	74.68	130.44
s01Q09a	54	$1.03 \cdot 10^{38}$	13793.74	2.77	86.37	115.38
s01Q10a	126	$8.37 \cdot 10^{37}$	10818.29	3.53	103.33	94.90
s01Q11a	153	$7.54 \cdot 10^{37}$	8797.72	3.80	113.37	85.56
s01Q12a	53	$7.33 \cdot 10^{37}$	7331.21	5.69	111.89	79.47
s01Q13a	79	$7.24 \cdot 10^{37}$	6878.92	4.81	115.13	77.37
s01Q14a	78	$7.30 \cdot 10^{37}$	6357.51	5.00	126.44	76.05
s01Q15a	67	$7.47 \cdot 10^{37}$	5877.13	5.86	136.98	70.46
s02Q08a	73	$1.25 \cdot 10^{38}$	17007.64	1.69	75.14	130.39
s02Q09a	39	$1.07 \cdot 10^{38}$	14134.60	2.28	85.17	123.01
s02Q10a	135	$8.33 \cdot 10^{37}$	10669.42	3.54	103.53	94.53
s02Q11a	110	$7.46 \cdot 10^{37}$	8741.01	3.82	112.31	85.80
s02Q12a	83	$7.35 \cdot 10^{37}$	7377.48	5.75	111.56	79.63

Continued on the next page

Tab. A.1 – continued from previous page

run	N_{burst}	L_{peak} [erg s^{-1}]	t_{rec} [s]	t_{rise} [s]	$t_{duration}$ [s]	α-value
s02Q13a	94	$7.25 \cdot 10^{37}$	6958.05	4.84	119.63	76.64
s02Q14a	85	$7.27 \cdot 10^{37}$	6362.15	4.96	126.62	76.31
s02Q15a	56	$7.44 \cdot 10^{37}$	5846.84	5.84	133.35	71.06
s03Q08a	68	$1.23 \cdot 10^{38}$	16872.30	1.81	75.02	131.27
s03Q09a	81	$9.93 \cdot 10^{37}$	13511.90	2.83	91.18	113.85
s03Q10a	152	$8.49 \cdot 10^{37}$	10893.31	3.66	103.55	95.94
s03Q11a	189	$7.37 \cdot 10^{37}$	8658.10	3.80	111.92	85.76
s03Q12a	114	$7.33 \cdot 10^{37}$	7313.80	5.76	111.23	79.93
s03Q13a	90	$7.27 \cdot 10^{37}$	6925.20	4.92	120.90	76.21
s03Q14a	82	$7.24 \cdot 10^{37}$	6328.38	4.97	126.20	76.16
s03Q15a	77	$7.41 \cdot 10^{37}$	5831.67	5.81	134.57	71.33
s04Q08a	1180	$1.24 \cdot 10^{38}$	16930.06	1.74	74.74	131.11
s04Q09a	2234	$1.03 \cdot 10^{38}$	13837.75	2.68	89.13	117.10
s04Q10a	276	$9.02 \cdot 10^{37}$	11297.69	3.46	97.06	100.72
s04Q11a	178	$7.30 \cdot 10^{37}$	8588.06	3.80	112.08	85.30
s04Q12a	484	$7.31 \cdot 10^{37}$	7248.83	5.70	109.72	81.15
s04Q13a	85	$7.23 \cdot 10^{37}$	6885.87	4.91	119.20	75.93
s04Q14a	94	$7.19 \cdot 10^{37}$	6287.84	4.99	122.88	76.92
s04Q15a	38	$7.40 \cdot 10^{37}$	5825.82	5.78	134.62	71.47
s05Q08a	57	$1.20 \cdot 10^{38}$	16598.66	2.04	75.27	131.84
s05Q09a	176	$8.90 \cdot 10^{37}$	12694.37	3.59	97.22	104.12
s05Q10a	142	$9.02 \cdot 10^{37}$	11240.36	3.59	97.55	100.11
s05Q11a	106	$7.18 \cdot 10^{37}$	8509.45	4.10	110.50	86.67
s05Q12a	164	$7.25 \cdot 10^{37}$	7217.26	5.45	108.06	82.59
s05Q13a	163	$7.21 \cdot 10^{37}$	6853.49	5.09	119.28	76.18
s05Q14a	95	$7.18 \cdot 10^{37}$	6281.54	5.00	124.71	76.28
s05Q15a	106	$7.29 \cdot 10^{37}$	5773.21	5.64	133.26	72.66
s06Q08a	82	$1.20 \cdot 10^{38}$	16577.50	1.99	75.45	131.58
s06Q09a	56	$1.12 \cdot 10^{38}$	14606.43	2.07	77.89	130.97
s06Q10a	2807	$8.92 \cdot 10^{37}$	11108.27	3.62	97.24	99.98
s06Q11a	211	$7.15 \cdot 10^{37}$	8483.30	4.04	112.51	85.92
s06Q12a	125	$7.16 \cdot 10^{37}$	7205.44	5.15	104.96	84.83
s06Q13a	66	$7.18 \cdot 10^{37}$	6806.54	5.12	114.85	77.29
s06Q14a	84	$7.14 \cdot 10^{37}$	6242.44	5.03	122.86	76.60
s06Q15a	75	$7.30 \cdot 10^{37}$	5772.55	5.63	133.35	72.54
s07Q08a	106	$1.18 \cdot 10^{38}$	16467.30	2.18	75.34	130.60
s07Q09a	77	$1.09 \cdot 10^{38}$	14396.34	2.32	78.47	131.04
s07Q10a	140	$8.72 \cdot 10^{37}$	10897.93	3.67	100.06	99.28

Continued on the next page

Tab. A.1 – continued from previous page

run	N_{burst}	L_{peak} [erg s^{-1}]	t_{rec} [s]	t_{rise} [s]	$t_{duration}$ [s]	α-value
s07Q11a	165	$7.08 \cdot 10^{37}$	8394.14	4.29	110.50	86.86
s07Q12a	153	$7.10 \cdot 10^{37}$	7226.30	4.80	104.80	85.79
s07Q13a	89	$7.20 \cdot 10^{37}$	6736.96	5.32	120.57	75.92
s07Q14a	73	$7.12 \cdot 10^{37}$	6248.17	5.00	123.77	76.61
s07Q15a	63	$7.30 \cdot 10^{37}$	5756.65	5.65	132.81	72.21
s08Q08a	3172	$1.18 \cdot 10^{38}$	16286.31	2.18	73.53	136.08
s08Q09a	135	$1.09 \cdot 10^{38}$	14378.64	2.24	78.17	130.40
s08Q10a	205	$8.49 \cdot 10^{37}$	10743.40	3.71	102.19	99.16
s08Q11a	328	$7.05 \cdot 10^{37}$	8333.75	4.49	110.87	86.50
s08Q12a	219	$7.08 \cdot 10^{37}$	7257.29	4.51	105.24	86.49
s08Q13a	95	$7.12 \cdot 10^{37}$	6696.75	5.43	114.52	77.12
s08Q14a	49	$7.14 \cdot 10^{37}$	6255.45	5.05	121.78	77.14
s08Q15a	7	$7.33 \cdot 10^{37}$	7007.11	6.47	130.80	86.20
s09Q08a	93	$1.17 \cdot 10^{38}$	16124.50	2.17	75.10	131.61
s09Q09a	115	$1.07 \cdot 10^{38}$	14311.92	2.29	79.48	129.88
s09Q10a	145	$8.21 \cdot 10^{37}$	10549.77	3.67	101.80	100.19
s09Q11a	131	$7.01 \cdot 10^{37}$	8234.93	4.66	109.43	86.86
s09Q12a	96	$7.02 \cdot 10^{37}$	7206.69	4.63	103.96	86.18
s09Q13a	83	$7.12 \cdot 10^{37}$	6687.01	5.42	115.47	76.65
s09Q14a	62	$7.08 \cdot 10^{37}$	6241.69	5.00	123.17	76.71
s09Q15a	64	$7.25 \cdot 10^{37}$	5735.94	5.55	132.48	72.68
s10Q08a	44	$1.17 \cdot 10^{38}$	16144.51	2.28	74.73	135.10
s10Q09a	71	$1.07 \cdot 10^{38}$	14255.87	2.30	77.50	130.07
s10Q10a	143	$8.00 \cdot 10^{37}$	10351.92	3.86	99.66	102.55
s10Q11a	102	$6.96 \cdot 10^{37}$	8058.89	4.95	104.84	88.63
s10Q12a	82	$7.04 \cdot 10^{37}$	7206.98	4.58	104.57	86.25
s10Q13a	87	$7.09 \cdot 10^{37}$	6626.14	5.52	115.27	76.81
s10Q14a	88	$6.98 \cdot 10^{37}$	6158.28	5.12	119.96	77.16
s10Q15a	83	$7.17 \cdot 10^{37}$	5692.04	5.48	131.19	73.12
s11Q08a	27	$1.17 \cdot 10^{38}$	16192.26	2.16	76.21	132.10
s11Q09a	82	$1.01 \cdot 10^{38}$	13699.43	2.72	80.43	126.87
s11Q10a	112	$8.10 \cdot 10^{37}$	10472.91	3.70	97.56	104.57
s11Q11a	130	$7.02 \cdot 10^{37}$	8280.29	4.71	106.49	91.08
s11Q12a	116	$6.97 \cdot 10^{37}$	7120.06	4.50	103.86	85.46
s11Q13a	67	$7.11 \cdot 10^{37}$	6698.30	5.44	116.01	76.73
s11Q14a	95	$6.94 \cdot 10^{37}$	6114.95	5.21	119.08	77.13
s11Q15a	40	$7.29 \cdot 10^{37}$	5768.20	5.62	134.08	72.56
s12Q08a	35	$1.16 \cdot 10^{38}$	16090.07	2.23	74.79	132.40

Continued on the next page

Tab. A.1 – continued from previous page

run	N_{burst}	L_{peak} [erg s^{-1}]	t_{rec} [s]	t_{rise} [s]	$t_{duration}$ [s]	α-value
s12Q09a	76	$1.02 \cdot 10^{38}$	13676.94	2.65	81.55	124.11
s12Q10a	133	$8.46 \cdot 10^{37}$	10825.18	3.63	91.88	111.74
s12Q11a	281	$7.02 \cdot 10^{37}$	8279.72	4.52	105.98	92.00
s12Q12a	240	$6.89 \cdot 10^{37}$	7130.64	4.59	103.81	87.02
s12Q13a	71	$7.09 \cdot 10^{37}$	6627.41	5.52	114.20	77.16
s12Q14a	89	$6.94 \cdot 10^{37}$	6085.81	5.28	117.85	77.16
s12Q15a	50	$7.25 \cdot 10^{37}$	5732.25	5.59	131.91	72.49
s13Q08a	30	$1.15 \cdot 10^{38}$	16091.91	2.25	73.68	138.86
s13Q09a	62	$1.05 \cdot 10^{38}$	13954.59	2.47	80.70	126.79
s13Q10a	121	$8.63 \cdot 10^{37}$	10999.52	3.51	91.83	111.57
s13Q11a	565	$6.95 \cdot 10^{37}$	8030.61	5.12	104.66	89.86
s13Q12a	632	$6.86 \cdot 10^{37}$	7082.10	4.64	103.49	86.54
s13Q13a	86	$7.03 \cdot 10^{37}$	6507.32	5.62	112.36	77.54
s13Q14a	82	$6.95 \cdot 10^{37}$	6117.09	5.26	120.68	76.40
s13Q15a	52	$7.22 \cdot 10^{37}$	5724.95	5.50	132.00	73.11
s14Q08a	25	$1.17 \cdot 10^{38}$	16085.12	2.19	72.07	137.96
s14Q09a	55	$1.02 \cdot 10^{38}$	13673.55	2.67	83.72	122.75
s14Q10a	94	$8.74 \cdot 10^{37}$	11121.86	3.37	89.80	114.09
s14Q11a	555	$6.92 \cdot 10^{37}$	8193.98	4.53	104.53	93.91
s14Q12a	170	$6.84 \cdot 10^{37}$	7063.03	4.89	105.47	85.91
s14Q13a	198	$6.93 \cdot 10^{37}$	6436.44	5.57	109.71	79.76
s14Q14a	75	$6.96 \cdot 10^{37}$	6118.17	5.23	118.41	77.19
s14Q15a	67	$7.10 \cdot 10^{37}$	5657.59	5.46	128.40	73.91
s15Q08a	25	$1.15 \cdot 10^{38}$	16050.42	2.31	73.58	137.38
s15Q09a	48	$9.94 \cdot 10^{37}$	13498.01	2.81	82.53	123.61
s15Q10a	85	$8.52 \cdot 10^{37}$	10892.41	3.37	92.11	111.01
s15Q11a	75	$6.93 \cdot 10^{37}$	8071.00	4.94	104.84	90.39
s15Q12a	195	$6.80 \cdot 10^{37}$	7048.90	4.79	105.36	86.49
s15Q13a	73	$7.04 \cdot 10^{37}$	6521.28	5.62	112.75	77.24
s15Q14a	73	$6.93 \cdot 10^{37}$	6090.71	5.31	118.19	77.11
s15Q15a	83	$6.97 \cdot 10^{37}$	5611.78	5.45	126.80	74.92

Tab. A.1.: Results from Solar Abundance Accretion Composition, *italics* written run names are from the irregular burning regime.

A.1.2 Helium-rich Accretion Composition

run	N_{burst}	L_{peak} [erg s^{-1}]	t_{rec} [s]	t_{rise} [s]	$t_{duration}$ [s]	α-value
he01Q12a	427	$2.42 \cdot 10^{38}$	11609.19	0.93	43.45	121.25
he01Q13a	518	$2.26 \cdot 10^{38}$	10337.82	1.09	45.67	109.97
he01Q14a	567	$2.14 \cdot 10^{38}$	9479.50	1.23	47.60	104.18
he01Q15a	654	$2.05 \cdot 10^{38}$	8736.23	1.26	48.60	101.46
he02Q12a	402	$2.42 \cdot 10^{38}$	11622.57	0.93	42.73	125.47
he02Q13a	434	$2.26 \cdot 10^{38}$	10251.03	1.06	45.51	110.00
he02Q14a	577	$2.15 \cdot 10^{38}$	9415.26	1.23	47.16	105.45
he02Q15a	659	$2.03 \cdot 10^{38}$	8682.05	1.32	48.57	101.26
he03Q12a	314	$2.46 \cdot 10^{38}$	11812.83	0.93	41.84	132.52
he03Q13a	373	$2.27 \cdot 10^{38}$	10173.34	1.04	45.06	111.69
he03Q14a	366	$2.15 \cdot 10^{38}$	9342.00	1.20	46.64	106.50
he03Q15a	522	$2.03 \cdot 10^{38}$	8630.42	1.31	48.33	102.11
he04Q12a	232	$2.47 \cdot 10^{38}$	11844.00	0.91	41.58	134.28
he04Q13a	305	$2.30 \cdot 10^{38}$	10350.48	1.05	43.32	121.95
he04Q14a	483	$2.13 \cdot 10^{38}$	9273.11	1.20	46.57	107.47
he04Q15a	383	$2.02 \cdot 10^{38}$	8581.07	1.34	48.20	102.56
he05Q12a	271	$2.47 \cdot 10^{38}$	11808.75	0.94	41.99	131.67
he05Q13a	275	$2.33 \cdot 10^{38}$	10465.39	1.04	43.34	124.15
he05Q14a	450	$2.16 \cdot 10^{38}$	9273.39	1.14	45.61	111.40
he05Q15a	479	$2.02 \cdot 10^{38}$	8512.27	1.31	47.85	103.73
he06Q12a	266	$2.42 \cdot 10^{38}$	11734.76	1.04	42.01	131.90
he06Q13a	271	$2.31 \cdot 10^{38}$	10459.68	1.08	43.35	124.21
he06Q14a	317	$2.19 \cdot 10^{38}$	9342.31	1.13	45.15	114.43
he06Q15a	401	$2.04 \cdot 10^{38}$	8476.43	1.26	47.14	106.01
he07Q12a	180	$2.40 \cdot 10^{38}$	11650.59	1.04	42.21	132.21
he07Q13a	260	$2.29 \cdot 10^{38}$	10418.61	1.11	43.68	123.34
he07Q14a	290	$2.17 \cdot 10^{38}$	9366.83	1.17	45.33	114.44
he07Q15a	251	$2.06 \cdot 10^{38}$	8502.18	1.23	46.68	108.20
he08Q12a	98	$2.37 \cdot 10^{38}$	11577.82	1.10	41.61	134.72
he08Q13a	167	$2.26 \cdot 10^{38}$	10360.01	1.17	43.41	124.19
he08Q14a	240	$2.14 \cdot 10^{38}$	9350.68	1.23	45.37	115.69
he08Q15a	302	$2.04 \cdot 10^{38}$	8506.84	1.28	46.47	109.74
he09Q12a	74	$2.38 \cdot 10^{38}$	11590.63	1.10	41.49	133.99
he09Q13a	121	$2.23 \cdot 10^{38}$	10290.51	1.20	43.42	124.09
he09Q14a	184	$2.13 \cdot 10^{38}$	9310.75	1.26	45.16	116.09
he09Q15a	240	$2.02 \cdot 10^{38}$	8489.92	1.32	46.90	109.47
he10Q12a	62	$2.38 \cdot 10^{38}$	11593.75	1.11	41.73	133.45

Continued on the next page

Tab. A.2 – continued from previous page

run	N_{burst}	L_{peak} [erg s^{-1}]	t_{rec} [s]	t_{rise} [s]	$t_{duration}$ [s]	α-value
he10Q13a	95	$2.22 \cdot 10^{38}$	10264.17	1.23	43.05	125.46
he10Q14a	163	$2.11 \cdot 10^{38}$	9276.28	1.28	45.24	115.94
he10Q15a	204	$2.00 \cdot 10^{38}$	8468.31	1.34	46.69	110.31
he11Q12a	52	$2.37 \cdot 10^{38}$	11602.94	1.14	41.85	133.34
he11Q13a	81	$2.22 \cdot 10^{38}$	10270.85	1.24	42.99	126.10
he11Q14a	143	$2.08 \cdot 10^{38}$	9226.45	1.33	45.03	117.30
he11Q15a	273	$1.97 \cdot 10^{38}$	8432.95	1.41	46.54	111.34
he12Q12a	47	$2.38 \cdot 10^{38}$	11605.07	1.12	42.04	132.55
he12Q13a	72	$2.13 \cdot 10^{38}$	10259.84	1.49	43.15	126.56
he12Q14a	86	$2.08 \cdot 10^{38}$	9241.60	1.34	44.89	118.04
he12Q15a	169	$1.97 \cdot 10^{38}$	8396.82	1.34	46.88	109.85
he13Q12a	45	$2.35 \cdot 10^{38}$	11612.21	1.19	41.40	136.52
he13Q13a	63	$2.18 \cdot 10^{38}$	10280.59	1.35	43.36	126.59
he13Q14a	83	$2.05 \cdot 10^{38}$	9226.33	1.43	44.80	119.27
he13Q15a	96	$1.94 \cdot 10^{38}$	8360.02	1.38	46.85	109.44
he14Q12a	40	$2.38 \cdot 10^{38}$	11608.69	1.13	41.62	133.63
he14Q13a	56	$2.23 \cdot 10^{38}$	10289.27	1.25	43.45	124.52
he14Q14a	76	$2.07 \cdot 10^{38}$	9220.65	1.37	44.82	118.28
he14Q15a	175	$1.94 \cdot 10^{38}$	8422.51	1.46	45.80	116.55
he15Q12a	38	$2.36 \cdot 10^{38}$	11612.12	1.20	41.80	134.21
he15Q13a	54	$2.21 \cdot 10^{38}$	10270.05	1.28	43.21	125.52
he15Q14a	68	$2.08 \cdot 10^{38}$	9226.59	1.37	44.90	117.93
he15Q15a	81	$1.95 \cdot 10^{38}$	8392.88	1.44	46.32	112.57

Tab. A.2.: Results from Helium-rich Accretion Composition, *italics* written run names are from the irregular burning regime.

Curriculum Vitae

Julia Reichert

Personal Data

Address	Ryffstrasse 30
	4056 Basel
Phone	0041 78 859 14 31
E-mail	julia.reichert@yahoo.de
Date of Birth	19.6.1986
Place of Birth	Basel BS
Nationality	Swiss

Education

2013–2017	PhD at the University of Basel
	On the Way to the Superburst– A Numerical Simulation Study
	Supervisors: Prof. Friedrich-Karl Thielemann, Dr. Rubén M. Cabezón
2010–2013	Masters Degree in Physics at the University of Basel
2007–2010	Bachelors Degree in Physics at the University of Basel
2003–2006	Gymnasium Oberwil BL
	Major Subject: Applied Mathematics and Physics
1998–2003	Progymnasium Spiegelfeld, Binningen BL
	Major Subject: Mathematics
1992–1998	Primarschule Spiegelfeld, Binningen BL

Teaching Activities

2016	Teaching Assistant: Nuclear Astrophysics I & II University of Basel
2014–2015	Teaching Assistant: Electrodynamics, Mechanics University of Basel
2010–2013	(Undergraduate) Teaching Assistant: Introduction to Physics 1 - 4 University of Basel

Conferences

2017	ISSI meeting: Teamleader: D. Galloway, Bern
2016	Nuclei in Cosmos, Niigata, Japan
	ISSI meeting: Teamleader: D. Galloway, Tokyo Riken
2015	Nuclear Physics in Astrophysics, York
	ISSI meeting: Teamleader: D. Galloway, Bern

Languages

German	Native Language
English	Fluent in writing and speech
French	Basic Knowledge

Personal Interests

Travelling, Circus, Snowboarding, playing Darts, Boardgame association (Boardgame Basel), Drawing

Bibliography

"Who are you, who are so wise in the ways of science?"

— Sir Bedevere the Wise
Monty Python and the Holy Grail

[1] J. Grindlay, H. Gursky, H. Schnopper, D. R. Parsignault, J. Heise, A. C. Brinkman, and J. Schrijver. Discovery of intense X-ray bursts from the globular cluster NGC 6624. ApJ, 205:L127–L130, May 1976.

[2] S. E. Woosley and R. E. Taam. Gamma-ray bursts from thermonuclear explosions on neutron stars. Nature, 263:101–103, September 1976.

[3] C. J. Hansen and H. M. van Horn. Steady-state nuclear fusion in accreting neutron-star envelopes. ApJ, 195:735–741, February 1975.

[4] H. Schatz and K. E. Rehm. X-ray binaries. *Nuclear Physics A*, 777:601–622, October 2006.

[5] W. H. G. Lewin, J. van Paradijs, and R. E. Taam. X-Ray Bursts. Space Sci. Rev., 62:223–389, September 1993.

[6] A. Parikh, J. José, G. Sala, and C. Iliadis. Nucleosynthesis in type I X-ray bursts. *Progress in Particle and Nuclear Physics*, 69:225–253, March 2013.

[7] A. Cumming, J. Macbeth, J. J. M. in 't Zand, and D. Page. Long Type I X-Ray Bursts and Neutron Star Interior Physics. ApJ, 646:429–451, July 2006.

[8] A. M. Amthor, D. Galaviz, A. Heger, A. Sakharuk, H. Schatz, and K. Smith. Sensitivity of Type I X-Ray Bursts to rp-Process Reaction Rates. *ArXiv Astrophysics e-prints*, August 2006.

[9] L. Keek, A. Heger, and J. J. M. in't Zand. Superburst Models for Neutron Stars with Hydrogen- and Helium-rich Atmospheres. ApJ, 752:150, June 2012.

[10] L. Keek and A. Heger. Multi-zone Models of Superbursts from Accreting Neutron Stars. ApJ, 743:189, December 2011.

[11] D. K. Galloway and A. Cumming. Helium-rich Thermonuclear Bursts and the Distance to the Accretion-powered Millisecond Pulsar SAX J1808.4-3658. ApJ, 652:559–568, November 2006.

[12] A. Cumming and L. Bildsten. Rotational Evolution during Type I X-Ray Bursts. ApJ, 544:453–474, November 2000.

[13] H. Schatz, A. Aprahamian, V. Barnard, L. Bildsten, A. Cumming, M. Ouellette, T. Rauscher, F.-K. Thielemann, and M. Wiescher. End Point of the rp Process on Accreting Neutron Stars. *Physical Review Letters*, 86:3471–3474, April 2001.

[14] R. H. Cyburt, A. M. Amthor, A. Heger, E. Johnson, L. Keek, Z. Meisel, H. Schatz, and K. Smith. Dependence of X-Ray Burst Models on Nuclear Reaction Rates. ApJ, 830:55, October 2016.

[15] T. A. Weaver, G. B. Zimmerman, and S. E. Woosley. Presupernova evolution of massive stars. ApJ, 225:1021–1029, November 1978.

[16] S. E. Woosley, A. Heger, A. Cumming, R. D. Hoffman, J. Pruet, T. Rauscher, J. L. Fisker, H. Schatz, B. A. Brown, and M. Wiescher. Models for Type I X-Ray Bursts with Improved Nuclear Physics. ApJS, 151:75–102, March 2004.

[17] B. Paxton, P. Marchant, J. Schwab, E. B. Bauer, L. Bildsten, M. Cantiello, L. Dessart, R. Farmer, H. Hu, N. Langer, R. H. D. Townsend, D. M. Townsley, and F. X. Timmes. Modules for Experiments in Stellar Astrophysics (MESA): Binaries, Pulsations, and Explosions. ApJS, 220:15, September 2015.

[18] A. Heger, A. Cumming, D. K. Galloway, and S. E. Woosley. Models of Type I X-Ray Bursts from GS 1826-24: A Probe of rp-Process Hydrogen Burning. ApJ, 671:L141–L144, December 2007.

[19] M. Zamfir, A. Cumming, and D. K. Galloway. Constraints on Neutron Star Mass and Radius in GS 1826-24 from Sub-Eddington X-Ray Bursts. ApJ, 749:69, April 2012.

[20] D. K. Galloway, A. J. Goodwin, and L. Keek. Thermonuclear Burst Observations for Model Comparisons: A Reference Sample. PASA, 34:e019, April 2017.

[21] J. L. Fisker. *The reaction flow during explosive nuclear burning on an accreting neutron star*. PhD thesis, University of Basel, 2005.

[22] M. Liebendörfer, A. Mezzacappa, and F.-K. Thielemann. Conservative general relativistic radiation hydrodynamics in spherical symmetry and comoving coordinates. Phys. Rev. D, 63(10):104003, May 2001.

[23] M. Liebendörfer, S. Rosswog, and F.-K. Thielemann. An Adaptive Grid, Implicit Code for Spherically Symmetric, General Relativistic Hydrodynamics in Comoving Coordinates. ApJS, 141:229–246, July 2002.

[24] W. R. Hix and F.-K. Thielemann. Computational methods for nucleosynthesis and nuclear energy generation. *Journal of Computational and Applied Mathematics*, 109:321–351, September 1999.

[25] S. Fehlmann. *Simulations of X-ray Bursts and Superbursts*. PhD thesis, University of Basel, 2015.

[26] R. Cornelisse, J. J. M. in't Zand, F. Verbunt, E. Kuulkers, J. Heise, P. R. den Hartog, M. Cocchi, L. Natalucci, A. Bazzano, and P. Ubertini. Six years of BeppoSAX Wide Field Cameras observations of nine galactic type I X-ray bursters. A&A, 405:1033–1042, July 2003.

[27] D. K. Galloway, M. P. Muno, J. M. Hartman, D. Psaltis, and D. Chakrabarty. Thermonuclear (Type I) X-Ray Bursts Observed by the Rossi X-Ray Timing Explorer. ApJS, 179:360–422, December 2008.

[28] D. K. Galloway, F. Özel, and D. Psaltis. Biases for neutron star mass, radius and distance measurements from Eddington-limited X-ray bursts. MNRAS, 387:268–272, June 2008.

[29] L. Stella, W. Priedhorsky, and N. E. White. The discovery of a 685 second orbital period from the X-ray source 4U 1820 - 30 in the globular cluster NGC 6624. ApJ, 312:L17–L21, January 1987.

[30] L. Keek, D. K. Galloway, J. J. M. in't Zand, and A. Heger. Multi-instrument X-ray Observations of Thermonuclear Bursts with Short Recurrence Times. ApJ, 718:292–305, July 2010.

[31] W. H. G. Lewin and P. C. Joss. X-ray burst sources. Nature, 270:211–216, November 1977.

[32] M. Gottwald, F. Haberl, A. N. Parmar, and N. E. White. The bursting behavior of the transient X-ray burst source EXO 0748-676 - A dependence between the X-ray burst properties and the strength of the persistent emission. ApJ, 308:213–224, September 1986.

[33] A. Langmeier, M. Sztajno, G. Hasinger, J. Truemper, and M. Gottwald. EXOSAT observations of 4U 1705-44 - Type I bursts and persistent emission. ApJ, 323:288–293, December 1987.

[34] P. Ubertini, A. Bazzano, M. Cocchi, L. Natalucci, J. Heise, J. M. Muller, and J. J. M. in 't Zand. Bursts from GS 1826-238: A Clocked Thermonuclear Flashes Generator. ApJ, 514:L27–L30, March 1999.

[35] L. Bildsten. Theory and observations of Type I X-Ray bursts from neutron stars. In S. S. Holt and W. W. Zhang, editors, *American Institute of Physics Conference Series*, volume 522 of *American Institute of Physics Conference Series*, pages 359–369, June 2000.

[36] D. K. Galloway, A. Cumming, E. Kuulkers, L. Bildsten, D. Chakrabarty, and R. E. Rothschild. Periodic Thermonuclear X-Ray Bursts from GS 1826-24 and the Fuel Composition as a Function of Accretion Rate. ApJ, 601:466–473, January 2004.

[37] A. Cumming. Thermonuclear X-ray bursts: theory vs. observations. *Nuclear Physics B Proceedings Supplements*, 132:435–445, June 2004.

[38] A. Cumming. What can we learn from long term monitoring of X-ray bursters? In F. D'Amico, J. Braga, and R. E. Rothschild, editors, *The Transient Milky Way: A Perspective for MIRAX*, volume 840 of *American Institute of Physics Conference Series*, pages 55–59, June 2006.

[39] D. Galloway, J. in't Zand, J. Chenevez, L. Keek, and S. Brandt. The Multi-INstrument Burst ARchive (MINBAR). In *38th COSPAR Scientific Assembly*, volume 38 of *COSPAR Meeting*, page 6, 2010.

[40] W. H. G. Lewin, J. van Paradijs, and R. E. Taam. X-ray bursts. *X-ray Binaries*, pages 175–232, 1995.

[41] L. Bildsten. Thermonuclear Burning on Rapidly Accreting Neutron Stars. In R. Buccheri, J. van Paradijs, and A. Alpar, editors, *NATO Advanced Science Institutes (ASI) Series C*, volume 515 of *NATO Advanced Science Institutes (ASI) Series C*, page 419, 1998.

[42] J. van Paradijs, W. Penninx, and W. H. G. Lewin. On the relation between X-ray burst properties and the persistent X-ray luminosity. MNRAS, 233:437–450, July 1988.

[43] M. A. Walker and P. Meszaros. The dynamical influence of radiation in type 1 X-ray bursts. ApJ, 346:844–846, November 1989.

[44] M. Sztajno, M. Y. Fujimoto, J. van Paradijs, W. D. Vacca, W. H. G. Lewin, W. Penninx, and J. Trumper. Constraints on the mass-radius relation of the neutron star in 4U 1746-37/NGC 6441. MNRAS, 226:39–55, May 1987.

[45] L. Keek, Z. Wolf, and D. R. Ballantyne. Accretion Disk Signatures in Type I X-Ray Bursts: Prospects for Future Missions. ApJ, 826:79, July 2016.

[46] E. Kuulkers. Probable superbursts in 4U 0614+091 and 4U 1608-522. *The Astronomer's Telegram*, 483, May 2005.

[47] J. J. M. in't Zand, E. Kuulkers, F. Verbunt, J. Heise, and R. Cornelisse. A superburst from 4U 1254-69. A&A, 411:L487–L491, December 2003.

[48] R. Remillard, E. Morgan, and N. ASM Team at MIT. Superburst in 4U1608-52. *The Astronomer's Telegram*, 482, May 2005.

[49] R. Wijnands. Recurrent Very Long Type I X-Ray Bursts in the Low-Mass X-Ray Binary 4U 1636-53. ApJ, 554:L59–L62, June 2001.

[50] E. Kuulkers, J. J. M. in't Zand, M. H. van Kerkwijk, R. Cornelisse, D. A. Smith, J. Heise, A. Bazzano, M. Cocchi, L. Natalucci, and P. Ubertini. A half-a-day long thermonuclear X-ray burst from KS 1731-260. A&A, 382:503–512, February 2002.

[51] J. A. Kennea, D. N. Burrows, J. R. Cummings, C. B. Markwardt, N. Gehrels, T. N. Ukwatta, B. Sbarufatti, D. Malesani, and C. J. Mountford. Swift J1734.5-3027: Swift discovery of a possible new superbursting transient. *The Astronomer's Telegram*, 5354, September 2013.

[52] R. Cornelisse, J. Heise, E. Kuulkers, F. Verbunt, and J. J. M. in't Zand. The longest thermonuclear X-ray burst ever observed?. A BeppoSAX Wide Field Camera observation of 4U 1735-44. A&A, 357:L21–L24, May 2000.

[53] D. Altamirano, N. Degenaar, C. O. Heinke, J. Homan, D. Pooley, G. R. Sivakoff, and R. Wijnands. Swift and RXTE follow up observations of the transient currently active in the globular cluster Terzan 5. *The Astronomer's Telegram*, 3720, October 2011.

[54] E. Kuulkers. A superburst from GX 3+1. A&A, 383:L5–L8, February 2002.

[55] J. Chenevez, S. Brandt, E. Kuulkers, J. Alfonso-Garzon, V. Beckmann, T. Bird, T. Courvoisier, M. Del Santo, A. Domingo, K. Ebisawa, P. Jonker, P. Kretschmar, C. Markwardt, T. Oosterbroek, A. Paizis, K. Pottschmidt, C. Sanchez-Fernandez, and R. Wijnands. First superburst observed by INTEGRAL, from SAX J1747.0-2853. *The Astronomer's Telegram*, 3183, February 2011.

[56] J. J. M. in't Zand, R. Cornelisse, and A. Cumming. Superbursts at near-Eddington mass accretion rates. A&A, 426:257–265, October 2004.

[57] T. E. Strohmayer and E. F. Brown. A Remarkable 3 Hour Thermonuclear Burst from 4U 1820-30. ApJ, 566:1045–1059, February 2002.

[58] M. Asada, H. Negoro, M. Sugizaki, M. Matsuoka, T. Mihara, M. Serino, S. Nakahira, T. Yamamoto, T. Sootome, S. Ueno, H. Tomida, M. Kohama, M. Ishikawa, N. Kawai, M. Morii, K. Sugimori, R. Usui, T. Toizumi, Y. Aoki, S. Song, A. Yoshida, K. Yamaoka, H. Tsunemi, M. Kimura, H. Kitayama, M. Nakajima, F. Suwa, H. Sakakibara, Y. Ueda, K. Hiroi, M. Shidatsu, Y. Tsuboi, T. Matsumura, K. Y. M. Yamauchi, Y. Nishimura, and T. Hanayama. MAXI/GSC detection of a superburst from the neutron star SAX J1828.5-1037. *The Astronomer's Telegram*, 3760, November 2011.

[59] R. Cornelisse, E. Kuulkers, J. J. M. in't Zand, F. Verbunt, and J. Heise. A four-hours long burst from Serpens X-1. A&A, 382:174–177, January 2002.

[60] E. M. Basinska, W. H. G. Lewin, M. Sztajno, L. R. Cominsky, and F. J. Marshall. X-ray observations of the burst source MXB 1728 - 34. ApJ, 281:337–353, June 1984.

[61] J. José and C. Iliadis. Nuclear astrophysics: the unfinished quest for the origin of the elements. *Reports on Progress in Physics*, 74(9):096901, September 2011.

[62] Cowan, Thielemann, Truran. Nuclear evolution of the universe.

[63] M. Wiescher, F. Käppeler, and K. Langanke. Critical Reactions in Contemporary Nuclear Astrophysics. ARA&A, 50:165–210, September 2012.

[64] C. Iliadis. *Nuclear Physics of Stars*. Wiley-VCH, 2007.

[65] W. D. Arnett. Explosive Nucleosynthesis in Stars. ApJ, 157:1369, September 1969.

[66] T. Rauscher. Lecture Notes: Nuclear Astrophysics 1 & 2. 2010-2011.

[67] D. Arnett. *Supernovae and Nucleosynthesis*. Princton University Press, 1996.

[68] E. E. Salpeter. Nuclear Reactions in Stars Without Hydrogen. ApJ, 115:326–328, March 1952.

[69] J. N. Bahcall, W. F. Huebner, S. H. Lubow, P. D. Parker, and R. K. Ulrich. Standard solar models and the uncertainties in predicted capture rates of solar neutrinos. *Reviews of Modern Physics*, 54:767–799, July 1982.

[70] W. D. Arnett, J. N. Bahcall, R. P. Kirshner, and S. E. Woosley. Supernova 1987A. ARA&A, 27:629–700, 1989.

[71] E. G. Adelberger, A. García, R. G. H. Robertson, K. A. Snover, A. B. Balantekin, K. Heeger, M. J. Ramsey-Musolf, D. Bemmerer, A. Junghans, C. A. Bertulani, J.-W. Chen, H. Costantini, P. Prati, M. Couder, E. Uberseder, M. Wiescher, R. Cyburt, B. Davids, S. J. Freedman, M. Gai, D. Gazit, L. Gialanella, G. Imbriani, U. Greife, M. Hass, W. C. Haxton, T. Itahashi, K. Kubodera, K. Langanke, D. Leitner, M. Leitner, P. Vetter, L. Winslow, L. E. Marcucci, T. Motobayashi, A. Mukhamedzhanov, R. E. Tribble, K. M. Nollett, F. M. Nunes, T.-S. Park, P. D. Parker, R. Schiavilla, E. C. Simpson, C. Spitaleri, F. Strieder, H.-P. Trautvetter, K. Suemmerer, and S. Typel. Solar fusion cross sections. II. The pp chain and CNO cycles. *Reviews of Modern Physics*, 83:195–246, January 2011.

[72] N. Grevesse M. Asplund and A. J. Sauval. The solar chemical composition. In I. T. G. Barnes and F. N. Bash, editors, *Cosmic Abundances as Records of Stellar Evolution and Nucleosynthesis*, volume 336 of *Astronomical Society of the Pacific Conference Series*, page 25, 2005.

[73] C. Winteler. *Light Element Production in the Big Bang and the Synthesis of Heavy Elements in 3DMHD Jets from Core-Collapse Supernovae*. PhD thesis, 2013.

[74] H.-T. Janka. Explosion Mechanisms of Core-Collapse Supernovae. *Annual Review of Nuclear and Particle Science*, 62:407–451, November 2012.

[75] K. Nomoto. Core Collapse Supernova Models and Nucleosynthesis. In A. Ray and R. A. McCray, editors, *Supernova Environmental Impacts*, volume 296 of *IAU Symposium*, pages 27–36, January 2014.

[76] H.-T. Janka, T. Melson, and A. Summa. Physics of Core-Collapse Supernovae in Three Dimensions: A Sneak Preview. *Annual Review of Nuclear and Particle*

Science, 66:341–375, October 2016.

[77] W. Baade and F. Zwicky. On Super-novae. *Contributions from the Mount Wilson Observatory, vol. 3, pp.73-78*, 3:73–78, 1934.

[78] W. Baade and F. Zwicky. Cosmic Rays from Super-novae. *Proceedings of the National Academy of Science*, 20:259–263, May 1934.

[79] K. Nomoto and Y. Kondo. Conditions for accretion-induced collapse of white dwarfs. ApJ, 367:L19–L22, January 1991.

[80] B. Kiziltan, A. Kottas, M. De Yoreo, and S. E. Thorsett. The Neutron Star Mass Distribution. ApJ, 778:66, November 2013.

[81] M. Coleman Miller. Introduction to neutron stars. http://www.astro.umd.edu/ miller/nstar.html, 2.9.2013.

[82] Shapiro Stuart L. and Saul A. Teukolsky. *Black Holes, White Dwarfs, and Neutron Stars. The Physics of Compact Objects*. Wiley.

[83] D. Page and S. Reddy. Dense Matter in Compact Stars: Theoretical Developments and Observational Constraints. *Annual Review of Nuclear and Particle Science*, 56:327–374, November 2006.

[84] D. Page, J. M. Lattimer, M. Prakash, and A. W. Steiner. Stellar Superfluids. *ArXiv e-prints*, February 2013.

[85] Q. Z. Liu, J. van Paradijs, and E. P. J. van den Heuvel. A catalogue of low-mass X-ray binaries in the Galaxy, LMC, and SMC (Fourth edition). A&A, 469:807–810, July 2007.

[86] Richard N. Boyd. *An Introduction to Nuclear Astrophysics*. The University of Chicago Press, 2007.

[87] K. H. Prendergast and G. R. Burbidge. On the Nature of Some Galactic X-Ray Sources. ApJ, 151:L83, February 1968.

[88] R. E. Taam and B. A. Fryxell. The influence of nuclear burning on the stability of degenerate and nondegenerate accretion disks. ApJ, 294:303–309, July 1985.

[89] E. Kuulkers, J. J. M. in't Zand, and J.-P. Lasota. Restless quiescence: thermonuclear flashes between transient X-ray outbursts. A&A, 503:889–897, September 2009.

[90] E. P. J. van den Heuvel. Modes of mass transfer and classes of binary X-ray sources. ApJ, 198:L109–L112, June 1975.

[91] J. J. M. in't Zand, A. Cumming, M. V. van der Sluys, F. Verbunt, and O. R. Pols. On the possibility of a helium white dwarf donor in the presumed ultracompact binary 2S 0918-549. A&A, 441:675–684, October 2005.

[92] M. van der Klis, G. Hasinger, E. Damen, W. Penninx, J. van Paradijs, and W. H. G. Lewin. Correlation of X-ray burst properties with source state in the 'atoll' source 4U/MXB 1636 - 53. ApJ, 360:L19–L22, September 1990.

[93] G. Rakavy, G. Shaviv, and Z. Zinamon. Carbon and Oxygen Burning Stars and Pre-Supernova Models. ApJ, 150:131, October 1967.

[94] G. Rakavy and G. Shaviv. Nuclear Burning Stability and the Limitation of 'Thermal Runaways'. Ap&SS, 1:347–354, May 1968.

[95] O. Blaes, R. Blandford, P. Madau, and S. Koonin. Slowly accreting neutron stars and the origin of gamma-ray bursts. ApJ, 363:612–627, November 1990.

[96] O. M. Blaes, R. D. Blandford, P. Madau, and L. Yan. On the evolution of slowly accreting neutron stars. ApJ, 399:634–645, November 1992.

[97] P. Haensel and J. L. Zdunik. Equation of state and structure of the crust of an accreting neutron star. A&A, 229:117–122, March 1990.

[98] P. Haensel and J. L. Zdunik. Non-equilibrium processes in the crust of an accreting neutron star. A&A, 227:431–436, January 1990.

[99] K. Sato. Nuclear Compositions in the Inner Crust of Neutron Stars. *Progress of Theoretical Physics*, 62:957–968, October 1979.

[100] H. Schatz, S. Gupta, P. Möller, M. Beard, E. F. Brown, A. T. Deibel, L. R. Gasques, W. R. Hix, L. Keek, R. Lau, A. W. Steiner, and M. Wiescher. Strong neutrino cooling by cycles of electron capture and β^- decay in neutron star crusts. Nature, 505:62–65, January 2014.

[101] P. Haensel and J. L. Zdunik. Nuclear composition and heating in accreting neutron-star crusts. A&A, 404:L33–L36, June 2003.

[102] S. Gupta, E. F. Brown, H. Schatz, P. Möller, and K.-L. Kratz. Heating in the Accreted Neutron Star Ocean: Implications for Superburst Ignition. ApJ, 662:1188–1197, June 2007.

[103] P. S. Shternin, D. G. Yakovlev, P. Haensel, and A. Y. Potekhin. Neutron star cooling after deep crustal heating in the X-ray transient KS 1731-260. MNRAS, 382:L43–L47, November 2007.

[104] J. L. Fisker, E. Brown, M. Liebendörfer, H. Schatz, and F.-K. Thielemann. The nuclear reaction flow of type I X-ray bursts. *Nuclear Physics A*, 758:447–450, July 2005.

[105] J. L. Fisker, E. F. Brown, M. Liebendörfer, F.-K. Thielemann, and M. Wiescher. The reactions and ashes of thermonuclear explosions on neutron stars. *Nuclear Physics A*, 752:604–607, April 2005.

[106] R. K. Wallace and S. E. Woosley. Explosive hydrogen burning. ApJS, 45:389–420, February 1981.

[107] L. Van Wormer, J. Görres, C. Iliadis, M. Wiescher, and F.-K. Thielemann. Reaction Rates and Reaction Sequences in the rp-Process. ApJ, 432:326–350, 1994.

[108] H. Schatz, A. Aprahamian, J. Goerres, M. Wiescher, T. Rauscher, J. F. Rembges, F.-K. Thielemann, B. Pfeiffer, P. Moeller, K.-L. Kratz, H. Herndl, B. A. Brown, and H. Rebel. rp-Process Nucleosynthesis at Extreme Temperature and Density Conditions. Phys. Rep., 294, February 1998.

[109] J. L. Fisker, H. Schatz, and F.-K. Thielemann. Explosive Hydrogen Burning during Type I X-Ray Bursts. ApJS, 174:261–276, January 2008.

[110] J. José, F. Moreno, A. Parikh, and C. Iliadis. Hydrodynamic Models of Type I X-ray Bursts: Metallicity Effects. ApJS, 189:204–239, July 2010.

[111] H. Schatz, L. Bildsten, A. Cumming, and M. Ouellette. Nuclear physics in normal X-ray bursts and superblasts. *Nuclear Physics A*, 718:247–254, May 2003.

[112] J. Audouze, J. W. Truran, and B. A. Zimmerman. Hot CNO-Ne Cycle Hydrogen Burning. Thermonuclear Evolution at Constant Temperature and Density. ApJ, 184:493–516, September 1973.

[113] I. Fushiki and D. Q. Lamb. New insights from a global view of X-ray bursts. ApJ, 323:L55–L60, December 1987.

[114] A. Cumming and L. Bildsten. Carbon Flashes in the Heavy-Element Ocean on Accreting Neutron Stars. ApJ, 559:L127–L130, October 2001.

[115] L. Keek, J. J. M. in't Zand, and A. Cumming. The superburst recurrence time in luminous persistent LMXBs. A&A, 455:1031–1036, September 2006.

[116] A. Cumming and J. Macbeth. The Thermal Evolution following a Superburst on an Accreting Neutron Star. ApJ, 603:L37–L40, March 2004.

[117] J. Stevens, E. F. Brown, A. Cumming, R. Cyburt, and H. Schatz. Carbon Synthesis in Steady-state Hydrogen and Helium Burning on Accreting Neutron Stars. ApJ, 791:106, August 2014.

[118] G. R. Caughlan and W. A. Fowler. Thermonuclear Reaction Rates V. *Atomic Data and Nuclear Data Tables*, 40:283, 1988.

[119] E. F. Brown. Superburst Ignition and Implications for Neutron Star Interiors. ApJ, 614:L57–L60, October 2004.

[120] C. J. Horowitz, D. K. Berry, and E. F. Brown. Phase separation in the crust of accreting neutron stars. Phys. Rev. E, 75(6):066101, June 2007.

[121] Z. Medin and A. Cumming. Compositionally Driven Convection in the Oceans of Accreting Neutron Stars. ApJ, 730:97, April 2011.

[122] H. Schatz, L. Bildsten, and A. Cumming. Photodisintegration-triggered Nuclear Energy Release in Superbursts. ApJ, 583:L87–L90, February 2003.

[123] Olaf Schenk, Klaus Gärtner, Wolfgang Fichtner, and Andreas Stricker. PARDISO: a high-performance serial and parallel sparse linear solver in semiconductor device simulation. *Future Generation Comp. Syst.*, 18(1):69–78, 2001.

[124] R. H. Cyburt, A. M. Amthor, R. Ferguson, Z. Meisel, K. Smith, S. Warren, A. Heger, R. D. Hoffman, T. Rauscher, A. Sakharuk, H. Schatz, F. K. Thielemann, and M. Wiescher. The JINA REACLIB Database: Its Recent Updates and Impact on Type-I X-ray Bursts. ApJS, 189:240–252, July 2010.

[125] R. W. Lindquist. Relativistic transport theory. *Annals of Physics*, 37:487–518, May 1966.

[126] W. H. Press, S. A. Teukolsky, W. T. Vetterling, and B. P. Flannery. *Numerical recipes in FORTRAN. The art of scientific computing*. 1992.

[127] K. S. Thorne. Validity in General Relativity of the Schwarzschild Criterion for Convection. ApJ, 144:201, April 1966.

[128] K. S. Thorne. The relativistic equations of stellar structure and evolution. ApJ, 212:825–831, March 1977.

[129] J. R. Oppenheimer and G. M. Volkoff. On Massive Neutron Cores. *Physical Review*, 55:374–381, February 1939.

[130] G. Glen and P. Sutherland. On the cooling of neutron stars. ApJ, 239:671–684, July 1980.

[131] J. P. Cox and R. T. Giuli. *Principles of stellar structure* . 1968.

[132] N. Langer, M. F. El Eid, and K. J. Fricke. Evolution of massive stars with semiconvective diffusion. A&A, 145:179–191, April 1985.

[133] E. Kuulkers, J. J. M. in't Zand, J.-L. Atteia, A. M. Levine, S. Brandt, D. A. Smith, M. Linares, M. Falanga, C. Sánchez-Fernández, C. B. Markwardt, T. E. Strohmayer, A. Cumming, and M. Suzuki. What ignites on the neutron star of 4U 0614+091? A&A, 514:A65, May 2010.

[134] M. Y. Fujimoto, M. Sztajno, W. H. G. Lewin, and J. van Paradijs. On the theory of type I X-ray bursts - The energetics of bursts and the nuclear fuel reservoir in the envelope. ApJ, 319:902–915, August 1987.

[135] E. Anders and N. Grevesse. Abundances of the elements - Meteoritic and solar. Geochim. Cosmochim. Acta, 53:197–214, January 1989.

[136] R. Buccheri, J. van Paradijs, and A. Alpar. *The many faces of neutron stars*, volume 515 of *NATO Advanced Science Institutes (ASI) Series C*. 1998.

[137] L. Keek and A. Heger. Carbon production on accreting neutron stars in a new regime of stable nuclear burning. MNRAS, 456:L11–L15, February 2016.

[138] Y. Matsuo, H. Tsujimoto, T. Noda, M. Saruwatari, M. Ono, M. Hashimoto, and M. Y. Fujimoto. Effects of a New Triple-α Reaction on X-Ray Bursts of a Helium-Accreting Neutron Star. *Progress of Theoretical Physics*, 126:1177–1186, December 2011.

[139] L. Keek and J. J. M. in't Zand. On burning regimes and long duration X-ray bursts. In *Proceedings of the 7th INTEGRAL Workshop*, page 32, 2008.

[140] M. Y. Fujimoto, T. Hanawa, I. Iben, Jr., and M. B. Richardson. Thermal evolution of accreting neutron stars. ApJ, 278:813–824, March 1984.

[141] D. Galloway. MINBAR / Thermonuclear burst observations for model comparisons: a reference sample. https://burst.sci.monash.edu/reference, 2017.

[142] J. Chenevez, D. K. Galloway, J. J. M. in 't Zand, J. A. Tomsick, D. Barret, D. Chakrabarty, F. Fürst, S. E. Boggs, F. E. Christensen, W. W. Craig, C. J. Hailey, F. A. Harrison, P. Romano, D. Stern, and W. W. Zhang. A Soft X-Ray Spectral Episode for the Clocked Burster, GS 1826-24 as Measured by Swift and NuStar. ApJ, 818:135, February 2016.

[143] A. Turlione, D. N. Aguilera, and J. A. Pons. Quiescent thermal emission from neutron stars in low-mass X-ray binaries. A&A, 577:A5, May 2015.

[144] X. L. Yan, H. S. Xu, Y. A. Litvinov, Y. H. Zhang, H. Schatz, X. L. Tu, K. Blaum, X. H. Zhou, B. H. Sun, J. J. He, Y. Sun, M. Wang, Y. J. Yuan, J. W. Xia, J. C. Yang, G. Audi, G. B. Jia, Z. G. Hu, X. W. Ma, R. S. Mao, B. Mei, P. Shuai, Z. Y. Sun, S. T. Wang, G. Q. Xiao, X. XU, T. Yamaguchi, Y. Yamaguchi, Y. D. Zang, H. W. Zhao, T. C. Zhao, W. Zhang, and W. L. Zhan. Mass Measurement of ^{45}Cr and Its Impact on the Ca-Sc Cycle in X-Ray Bursts. ApJ, 766:L8, March 2013.

[145] H. Schatz and W.-J. Ong. Dependence of X-ray Burst Models on Nuclear Masses. *ArXiv e-prints*, October 2016.

List of Figures

List of Tables